

**Some pages of this thesis may have been removed for copyright restrictions.**

If you have discovered material in Aston Research Explorer which is unlawful e.g. breaches copyright, (either yours or that of a third party) or any other law, including but not limited to those relating to patent, trademark, confidentiality, data protection, obscenity, defamation, libel, then please read our [Takedown policy](#) and contact the service immediately (openaccess@aston.ac.uk)

**Multi-frequency segmental  
bio-impedance device:  
design, development and  
applications.**

**Joeal Subash**

**Doctor of Philosophy**

**Aston University**

**ARCHA & Bio-medical research group.**

**December 2013**

© Joeal Subash, 2013.

Joeal Subash asserts his moral right to be identified as the author of this thesis.

This copy of the thesis has been supplied on condition that anyone who consults it is understood to recognise that its copyright rests with its author and that no quotation from the thesis and no information derived from it may be published without proper acknowledgement.

## **Abstract:**

Bio-impedance analysis (BIA) provides a rapid, non-invasive technique for body composition estimation. BIA offers a convenient alternative to standard techniques such as MRI, CT scan or DEXA scan for selected types of body composition analysis. The accuracy of BIA is limited because it is an indirect method of composition analysis. It relies on linear relationships between measured impedance and morphological parameters such as height and weight to derive estimates. To overcome these underlying limitations of BIA, a multi-frequency segmental bio-impedance device was constructed through a series of iterative enhancements and improvements of existing BIA instrumentation. Key features of the design included an easy to construct current-source and compact PCB design. The final device was trialled with 22 human volunteers and measured impedance was compared against body composition estimates obtained by DEXA scan. This enabled the development of newer techniques to make BIA predictions. To add a 'visual aspect' to BIA, volunteers were scanned in 3D using an inexpensive scattered light gadget (Xbox Kinect controller) and 3D volumes of their limbs were compared with BIA measurements to further improve BIA predictions. A three-stage digital filtering scheme was also implemented to enable extraction of heart-rate data from recorded bio-electrical signals. Additionally modifications have been introduced to measure change in bio-impedance with motion, this could be adapted to further improve accuracy and veracity for limb composition analysis. The findings in this thesis aim to give new direction to the prediction of body composition using BIA

The design development and refinement applied to BIA in this research programme suggest new opportunities to enhance the accuracy and clinical utility of BIA for the prediction of body composition analysis. In particular, the use of bio-impedance to predict limb volumes which would provide an additional metric for body composition measurement and help distinguish between fat and muscle content.

**INDEXING TERMS:** Segmental bio-impedance analysis, body composition, body-volume indexing, bio-electrical instrumentation.

*Dedicated to the eternal force that  
will rise to bring equality and  
justice to this world.*

## ❖ Acknowledgments:

Firstly I would like to express my sincere gratitude for my supervisor Professor Clifford Bailey for his support and guidance throughout this project, he has been a source of inspiration to me and many other students. I would also like to thank my associate supervisors Dr Nagi Fahmi, Dr Xianghong Ma and Professor Ian Nabney for their support.

My parents in India and my brother & family in the U.K (Shelvin, Manju, Adwith and Arpith) for being patient and helpful throughout this PhD. Also Swarna and her better half Abhishek for giving me unconditional backing.

Sue Cattell from the Heartlands Hospital, Birmingham for her help during the data collection phase.

Dr Srikanth Bellary for his valuable contribution throughout the ethical approval stage.

Members of [www.edaboard.com](http://www.edaboard.com) and [comp.dsp](http://comp.dsp) (Google group) who enthusiastically replied to my many DSP and electronics related queries.

Aston research centre for healthy ageing (ARCHA) for funding this project.

Fellow ARCHA colleagues and fellow bio-medical scientists in MB171.



# Contents

Chapter 1	Introduction.....	20
1.1	Medical body imaging:.....	22
1.1.1	X-ray imaging:.....	23
1.1.2	DEXA scan:.....	24
1.1.3	CT scan: .....	24
1.1.4	MRI Scan:.....	25
1.1.5	Isotopic dilution and mass spectroscopy to determine body water content: .....	26
1.1.6	Advantages of BIA over standard techniques: .....	26
1.2	Body compartments:.....	27
1.2.1	Total body water (TBW), extracellular water (ECW) and intracellular water (ICW):28	
1.2.2	Fat free mass (FFM) and Fat Mass: .....	29
1.2.3	Body cell mass (BCM): .....	29
1.3	Current Conduction:.....	29
1.3.1	Basic bio-materials: .....	30
1.3.2	Major tissues & organs:.....	34
1.3.3	Flow of current - a microscopic and a macroscopic view: .....	36
1.3.4	Bio-potential electrodes:.....	37
1.4	Resistance, reactance and impedance:.....	40
1.5	Current BIA devices and previous studies:.....	40
1.6	Bio-impedance measurement (device version 1): .....	43
1.6.1	Current source:.....	44
1.6.2	Electrodes and placement:.....	45
1.6.3	Volunteer tests and results: .....	46
1.7	Tissue electrical models: .....	46
1.7.1	The Fricke model: .....	47
1.7.2	The Cole-Cole model: .....	49
1.8	Body composition estimation: various approaches:.....	50
1.8.1	Regression: .....	50
1.8.2	Cole-Cole analysis:.....	53
1.8.3	Cole-Cole and Hanai's mixture theory: .....	54
1.9	BIA Variants: .....	55
1.9.1	Multi-frequency BIA: .....	55

1.9.2	Bio-Impedance spectroscopy (BIS):.....	56
1.9.3	Segmental BIA (SBIA):.....	56
1.10	BIA errors and body composition estimation variability: .....	57
1.11	Patient and volunteer trials:.....	59
1.12	Electrical safety: .....	63
1.12.1	Physiological effects of electricity:.....	64
1.12.2	Neuromuscular stimulation and fibrillation:.....	65
1.12.3	Physiological effects of electricity:.....	66
1.12.4	BS EN 60601 and device versions 1, 2 and 4:.....	66
Chapter 2	Essential theory.....	73
2.1	Introduction: .....	73
2.2	Signal analysis:.....	73
2.2.1	Signal sampling and anti-aliasing filters:.....	74
2.2.2	Fundamentals of FFT based signal analysis:.....	75
2.2.3	Low pass filtering in the digital domain: .....	79
2.2.4	Designing a digital LPF to filter bio-electrical signals: .....	80
2.2.5	Savitzky-Golay moving average filter: .....	86
2.3	Statistical techniques: .....	88
2.4	Learning from data:.....	90
2.4.1	Brief History of neural networks:.....	91
2.4.2	Description: .....	92
2.4.3	Training neural networks using back-propagation: .....	93
2.4.4	Splitting data: .....	95
2.5	Estimating body volumes with KinectFusion algorithm:.....	95
2.5.1	Depth map conversion:.....	98
2.5.2	Camera tracking: .....	98
2.5.3	Volumetric representation and integration:.....	99
2.5.4	Raycasting for rendering: .....	101
2.5.5	The Polygon file format:.....	102
2.6	Aims and objectives: .....	103
2.7	Summary: .....	104
Chapter 3	Segmental bio-impedance measurement: a primer .....	105
3.1	Initial evaluation of current commercial technology:.....	105
3.1.1	Features:.....	106

3.1.2	Body composition estimates from Tanita BC-545:.....	109
3.2	Segmental bio-impedance measurement:.....	112
Chapter 4	Implementation of S-BIA protocol .....	115
4.1	Voltage control current source (VCCS) switching: .....	116
4.2	Electrode pair selection for impedance measurement: .....	117
4.3	Integrated system function:.....	118
4.4	Summary: .....	121
Chapter 5	System components and testing: V1 to V4. ....	122
5.1	Introduction: .....	122
5.2	Voltage measurement setup:.....	125
5.3	The Voltage controlled current source (VCCS):.....	126
5.3.1	The XR2206, sinusoidal function generator: .....	126
5.3.2	The Howland current pump: .....	127
5.4	Electrodes for the system: .....	134
5.5	Phase measurements:.....	136
5.6	Summary: .....	137
Chapter 6	Single frequency SBIA Prototype development (version 2).....	138
6.1	Transferring the prototype circuit to the Proteus suite:.....	138
6.2	PCB design with Proteus ARES: .....	139
6.3	PCB manufacturing:.....	141
6.4	Through-hole drilling, board testing and soldering: .....	142
6.5	Leakage current tests: .....	143
6.6	Summary: .....	144
Chapter 7	Development of Multi-frequency S-BIA system (version 3 and version 4) .....	145
7.1	Improved segmental multi-frequency bio-impedance device (version 4):.....	146
7.2	Improved current source: .....	147
7.3	New electrode switching scheme: .....	150
7.4	Improvements in PCB manufacturing technique:.....	155
7.5	Leakage current tests: .....	157
7.6	Summary: .....	158
Chapter 8	Matlab for device control and signal analysis.....	159
8.1	Introduction: .....	159
8.2	Matlab to save body-impedance signals and extract impedance:.....	159
8.3	Patient trial application:.....	160

8.4	Controlling the data acquisition device: .....	163
8.5	Extracting bio-impedance from saved signals:.....	165
8.6	Summary: .....	167
Chapter 9	Evaluation of impedance measurements.....	168
9.1	Introduction: .....	168
9.2	Testing with precision resistors:.....	171
9.3	Repeatability of bio-impedance measurements:.....	172
9.4	Whole-body impedance; compared to sum from arm, leg and trunk: .....	173
9.5	Validity of segmental BIA measured; comparison with Tanita BC-545 body composition estimates:.....	174
9.6	Summary: .....	175
Chapter 10	Other applications of obtained bio-impedance signals .....	176
10.1	Introduction: .....	176
10.2	Extracting heart rate from segmental-bio-electrical signals:.....	176
10.2.1	Initial approach: .....	177
10.2.2	Three stage digital-LPF to determine volunteer heart rate: .....	179
10.2.3	Eliminating baseline drift: .....	181
10.2.4	Extracting the heart-rate from baseline rectified signal: .....	183
10.3	Estimating volume of body sections using the KinectFusion algorithm in PCL:.....	185
10.4	Summary: .....	189
Chapter 11	Results .....	190
11.1	Whole body composition: .....	195
11.1.1	Whole-body lean mass:.....	196
11.1.2	Whole-body bone mass: .....	197
11.1.3	Whole-body fat mass (WBFM):.....	198
11.1.4	Conclusion: .....	199
11.2	Composition of the arms:.....	201
11.2.1	Lean mass:.....	201
11.2.2	Bone mass: .....	202
11.2.3	Fat mass:.....	202
11.2.4	Conclusion: .....	204
11.3	Composition of the legs and measured bio-impedance: .....	204
11.3.1	Lean mass:.....	204
11.3.2	Bone-mass:.....	205

11.3.3	Fat mass:.....	206
11.3.4	Conclusion: .....	207
11.4	Composition of the body trunk: .....	207
11.4.1	Lean mass: .....	208
11.4.2	Bone mass: .....	209
11.4.3	Fat-mass: .....	211
11.4.4	Conclusion: .....	211
11.5	Bio-impedance variation during motion and body composition: .....	212
11.6	3D body volume and bio-impedance: .....	215
11.7	Neural-networks to learn from BIA data:.....	217
11.7.1	Data pre-processing: .....	218
11.7.2	Network structure and training: .....	218
11.7.3	Results .....	219
11.8	Summary: .....	222
Chapter 12	Discussion .....	223
12.1	Chronology of the presented study: .....	225
12.2	Major challenges addressed: .....	229
12.3	Major advances and findings: .....	230
12.4	Major shortcomings: .....	232
12.5	Future work: .....	233
12.6	Conclusion: .....	235

## ❖ List of figures:

Figure 1-1: Shows the five compartment human body model relevant to BIA(Kyle, De Lorenzo, et al. 2004).....	28
Figure 1-2: Shows the polar structure of a water molecule.....	31
Figure 1-3: Shows the bilayer lipid membrane (BLM) formed of polar lipids.....	33
Figure 1-4: Shows the potential difference between intracellular and extracellular space around a cell.....	33
Figure 1-5: Shows the structure of an amino acid, R is side chain.....	34
Figure 1-6: Shows a cubical biomaterial with insulating implant.....	36
Figure 1-7: Shows the simple electrical model of the electrode-tissue interface.....	38
Figure 1-8: Shows typical sectional resistance of a body in Ohms from palm to foot on the right side(values obtained from Organ & Bradham 1994).....	39
Figure 1-9: Shows the impedance vector which is formed of resistance and reactance.....	40
Figure 1-10: Shows the blocks of the basic bioimpedance measurement system. Z is the impedance of the tissue under observation.....	44
Figure 1-11: Shows the electrode placement for whole body BIA.....	45
Figure 1-12: Shows cell walls which act as capacitors to the flow of current. Also shown is the use of a low and high frequency current to bypass the effect of cell wall capacitance. An equivalent circuit deduced from this behaviour is also shown.....	48
Figure 1-13: Typical Cole-Cole plot for impedance measured at various frequencies. This also illustrates extrapolation (shown in red) to derive resistance at ideal frequencies. Cole-Cole plot adopted Thomas et al. 1998.....	50
Figure 1-14: Human body depicted as a cylinder for purposes of the general principles underlying BIA calculations.....	52
Figure 1-15: Shows the segmentation into 5 segments viz. four limbs and trunk (left) and placement of electrodes to measure impedance for SBIA procedure.....	57
Figure 1-16: Shows the macroschock condition (subfigure a) and the microschock (subfigure b). Adopted from Grimnes & Martinsen 2014.....	65
Figure 1-17: Shows the generic structure of the BIA devices used to collect data from subjects. Please note that only the BIA devices in direct contact with the subject. The function generator (V1 only) and the data acquisition card are IEC 61010 compatible.....	67
Figure 1-18: Shows the human body circuit model used for BS EN 60601 leakage and auxiliary current tests. The values of the components and their tolerances are shown next to their symbol. V is a true RMS voltage measurement unit.....	70
Figure 1-19: Shows the simplified version of leakage current test measurement setup proposed in BS EN 60601. S5 toggles the device between normal operating condition and single fault (reversed supply) condition. S1 simulates the open earth SFC. MD represents human body model shown in Figure 1-18. Adopted from BS EN 60601.....	71
Figure 2-1: Shows a sinusoid, in black and its reconstruction, in green. The reconstructed signal is obtained from samples of the original signal sampled at a rate lower than the Nyquist sampling rate.....	74

Figure 2-2: Shows a sum of three sinusoids of different frequencies in the time domain and their respective contributions in the frequency domain, adopted from the National Instruments website ( <a href="http://www.uk.ni.com">www.uk.ni.com</a> ). .....	77
Figure 2-3: Two sided FFT spectrum of the voltage signal from the whole-body used to measure whole-body impedance. The two sections show signals scaled differently to expand lower magnitude peaks. ....	78
Figure 2-4: Single-sided FFT spectrum of the voltage signal from the whole-body used to measure whole-body impedance. The two sections show signals scaled differently to expand lower magnitude peaks. ....	79
Figure 2-5: Shows the 'brick wall' response of an ideal LPF as opposed to that of a real LPF. Note: there exists a transition band between cutoff and stop band frequencies in the real case. ....	81
Figure 2-6: Shows a real FIR LPF with ripples in the passband and the stopband. ....	82
Figure 2-7: Shows a view of the 'fdatool' in Matlab used to design a FIR LPF using the windowing technique. Note the minimum order required for the specifications filled in is 951. ..	83
Figure 2-8: Shows the magnitude response of the 801 order FIR LPF designed using the equiripple method and lest-squares method. ....	85
Figure 2-9: Shows the linear phase response of the equiripple filter chosen above for the extraction of heart rate signals. ....	87
Figure 2-10: Shows linear regression model. The predicted values (in red) are on the line of best-fit. The residuals are the difference between the predicted and the actual values. ....	89
Figure 2-11: Shows a single node ('neuron') of a MLP, it includes inputs, their corresponding weights and an activation function. ....	91
Figure 2-12: Shows a MLP network with neurons connected as input, hidden and output nodes. ....	93
Figure 2-13: Shows an image of the Kinect depth stream. A colour gradient is used to represent depth where closer objects appear white gradually changing to blue as distance from the camera increases. ....	96
Figure 2-14: Illustrates the four major steps involved in obtaining 3D scans from Kinect depth stream. Adopted from Newcombe et al. 2011. ....	98
Figure 2-15: Illustrates how ICP is utilized to align two lines. From the initial (unaligned, left) and final state (aligned, right) the transition of view (camera movement) with 6 DOF can be calculated. ....	99
Figure 2-16: Shows how a 3m cube-space is divided into smaller cubes called voxels in 3D computational geometry. For computational efficiency they take values which are powers of two. Adopted from <a href="http://www.pointclouds.org">www.pointclouds.org</a> . ....	100
Figure 2-17: Shows a cross section of the TSDF method. Values approach zero closer to the surface (silhouette) which then transit to negative values within the surface. Adopted from <a href="http://www.pointclouds.org">www.pointclouds.org</a> . ....	101
Figure 3-1: Shows the Tanita BC-545 and 8 foot and hand electrodes (two hand electrodes hidden from sight). ....	107
Figure 3-2: Position of 8 electrodes for SBIA measurement. ....	108
Figure 3-3: Shows the linear plot between bone mass and lean body mass predicted by the Tanita BC-545. The results presented here are from 81 volunteers who participated in a previous study at the university (n = 81). A strong linear relationship with Rsq of 0.96 was observed. ....	110
Figure 3-4: Shows the linear plot between percentage body water and percentage body fat predicted by the Tanita BC-545. A strong linear relationship with Rsq of 0.89 was observed. ....	111

Figure 3-5: Shows the correlation between total muscle-mass predicted by Tanita BC-545 and muscle-mass in the left arm and left leg. There appears to be a strong correlation between the two predicted quantities (segmental data from 14 volunteers, n = 14). .....	112
Figure 3-6: Shows electrode placement on palms and feet of individual for S-BIA measurements. Stars (in red) represent current source electrodes and triangles (in blue), the voltage sensing electrodes.....	113
Figure 4-1: Shows functional diagrams of SPDT switch (left) and multiplexer (right). .....	116
Figure 4-2: Two SPDT switches connected to VCCS to allow VCCS switching between two pairs of electrodes (E1;E5 and E3;E7). .....	117
Figure 4-3: Shows two 4:1 multiplexers used for electrode pair selection with their outputs connected to a differential DAQ channel.....	118
Figure 5-1: Shows the schematic for the VCCS switching and measurement electrode multiplexing scheme. ....	124
Figure 5-2: Shows the major blocks in the designed segmental bio-impedance measurement system. ....	125
Figure 5-3: Shows the circuit utilizing XR2206 to generate a 50 kHz sinusoid for bio-impedance measurement. ....	127
Figure 5-4: Shows the basic Howland current pump where current flows through load $Z_L$ .....	129
Figure 5-5: Shows the modified Howland current source constructed using two op-amps. This circuit has higher output current capability and efficiency than the basic Howland circuit shown in the previous figure. ....	130
Figure 5-6: Schematic of the modified Howland current pump (VCCS) used in this project; designed using Proteus ISIS software. ....	131
Figure 5-7: Shows the clipping of the output current from VCCS at loads above 10k $\Omega$ . Note: voltage shown in figure is arbitrary; figure only represents the clipping phenomenon which was observed.....	133
Figure 5-8: Shows the current supplied by the Howland current source with changing input frequency (x axis is logarithmic).....	133
Figure 5-9: Shows the electrodes used in the present system and their labels on a subject's palms and underside of their foot. In essence the subject would stand on the foot electrodes and grab the hand electrode attachment. Note: electrodes E4 and E1 are hidden from view. ....	135
Figure 5-10: Shows the setup used to measure electrode-skin interface impedance. E3 and E7 are the two types of electrodes that were tested, T is the temporary electrode used to assist the measurement.....	135
Figure 5-11: Shows the impedance variation of the hand and foot electrodes with changing frequency (between 1kHz and 200kHz). ....	136
Figure 6-1: Shows the prototype of the single frequency SBIA system on a bread board. ....	139
Figure 6-2: Shows the top side and bottom side of the PCB layout used to house the SBIA circuit. ....	140
Figure 6-3: Shows failed attempts to manufacture the SBIA PCB layout in Figure 6-2. ....	142
Figure 6-4: Designed single frequency SBIA system on a PCB board with its components labelled. ....	143
Figure 7-1: Shows the PCB design of the top layer of version 3 of device. As compared to top layer of version 2 in Figure 6-2, a DIL switch with 4 selectable resistors are added for multi-frequency operation.....	146

Figure 7-2: Shows the functional diagram of the INA110 instrumentation amplifier by Texas instruments; adopted from INA110 datasheet. A gain of 10 was selected for current purpose. .	148
Figure 7-3: Shows the simplified version (without A1, A2) of the new current constructed using the INA110. The internally connected 10kΩ resistors make this current source easier to construct as opposed to the previous current source used this project. ....	149
Figure 7-4: Version4 (final version) of the device constructed for this project. ....	150
Figure 7-5: Shows the functional configuration of the new current source switching using a single SPDT switch. The control signal IN connects the current source either to the left-side of the subject or right-side of subject. ....	152
Figure 7-6: Shows the electrode configuration for the new switching scheme (a). (b) shows the truth table for the AD436. (c) shows the digital inputs to the AD436 and electrode pairs selected. ....	153
Figure 7-7: Shows the constructed version 4 of device with its various components labelled. ....	154
Figure 7-8: Shows the PCB layout of the final version of the device used for patient trials.....	156
Figure 7-9: Shows the simple bubble etch device made using a computer fan, lab glove and rubber tubing. ....	156
Figure 7-10: Shows top side and bottom side of PCB board designed (circuit in Figure 7-4) for version 4 of the device. This was manufactured using the 'toner-transfer' method. ....	157
Figure 8-1: Shows flowchart for the patient trial program used to acquire subject information and acquire bio-electrical signals. ....	161
Figure 8-2: Three major functions of the volunteer trial application 'databasetrial.m'. Arrow heads represent exchange of control between functions and the digits show the sequence of this exchange. ....	162
Figure 8-3: Shows the FFT spectrum of a bio-electrical signal acquired from an individual's left arm. The two FFT plots belong to the same data but have been scaled differently to show low magnitude of noise close to the 50kHz peak. ....	166
Figure 9-1: Shows the S-BIA (version 4) measurement setup. Main sections include the device & battery pack housing, the electrode rig, the DAQ card, wires which connect electrodes and digital control lines to control device. Also required is a computer with Matlab (not shown in picture). Please note that the original circuitry from the Tanita device is removed and the electrodes alone are used.....	169
Figure 9-2: Shows a subject undergoing impedance examination on the device (version 4). ....	170
Figure 9-3: Shows the strong correlation between whole-body lean mass predicted by Tanita BC-545 and whole-body impedance coefficient measured using the constructed device (version 2). ....	174
Figure 10-1: Shows regular dips observed in bio-electrical signals acquired over five second duration. It also provides an insight into the sensitivity of the device. Here the signal is sampled at 200kSa/s and recorded for 5 second duration.....	177
Figure 10-2: Shows the block of a basic AM synchronous demodulator. The input AM signal is mixed (multiplied) with a locally generated carrier and the passed through a low pass filter stage(s) to retrieve the original message signal.....	178
Figure 10-3: Shows the three filtering stages the input bio-electrical signal goes thorough before the output with distinguishable heart-rate peaks is obtained. ....	180
Figure 10-4: Input signal along with the output from each filtering stage. The original signal (subfigure 1) is sampled at 2MSa/s. Also the heart rate dips are marked with red boxes.....	181

Figure 10-5: Shows the R peaks of a real ECG signal, the time difference between the two R peaks is the time difference between two heart-beats. ....	182
Figure 10-6: Shows the smoothing procedure which generates a signal following the baseline drift of the original signal. After subtracting the smoothed signal from the input the baseline rectified signal is recovered as shown in the lower sub-figure. ....	183
Figure 10-7: The bust which was reconstructed using the KinectFusion algorithm. ....	185
Figure 10-8: Shows the reconstructed bust as a point cloud and its point normal (upper two images) and as a mesh and face normals (lower two images). Notice there exist holes at the top and bottom of the bust. ....	186
Figure 10-9: Shows the bust surface reconstructed using the Poisson surface reconstruction. Notice that the holes in the previous figures have been successfully filled. ....	188
Figure 11-1: Shows a volunteer undergoing bio-impedance examination on device version 4. As stated in section 9.1 the internals of the Tanita device pictured is replaced with device V4. ....	192
Figure 11-2: Shows the typical split of a subject's body into left and right limbs and the trunk. The lines are used to separate different sections and body composition of each of these sections is presented in a DEXA result scan summary. ....	195
Figure 11-3: Shows a linear model between whole-body lean mass and whole-body impedance coefficients measured at 10kHz and 100kHz. The whole-body lean mass is obtained from DEXA scan reports and is presented here in grams. ....	196
Figure 11-4: Shows linear association between whole-body impedance coefficient and whole-body combined lean-mass. The whole-body lean-mass and bone-mass is obtained from DEXA scan reports and is presented here in grams. ....	200
Figure 11-5: Shows the scatter plot between impedance coefficient of left arm and the whole-body with the left arm lean mass. A linear trend can be observed in the two graphs. The left-arm lean-mass is obtained from DEXA scan reports and is presented here in grams. ....	201
Figure 11-6: Shows the scatter plot between the impedance coefficient of right arm at 50kHz and 75kHz and the combined right arm lean mass. The right-arm lean-mass and bone-mass is obtained from DEXA scan reports and is presented here in grams. ....	203
Figure 11-7: Shows the scatter plots between right leg lean mass and whole body impedance coefficient from right (a) and the impedance coefficient of the right leg (b) measured at 75kHz. The right-leg lean-mass is obtained from DEXA scan reports and is presented here in grams. ....	205
Figure 11-8: Shows the correlation and $R_{sq}$ values when lean-mass of the trunk is modelled with impedance of the trunk (b) and whole-body (a). The trunk lean-mass is obtained from DEXA scan reports and is presented here in grams. ....	208
Figure 11-9: Shows the correlation between trunk bone-mass and whole-body impedance coefficient measured at 10kHz. The trunk bone-mass is obtained from DEXA scan reports and is presented here in grams. ....	210
Figure 11-10: Shows the volunteer undergoing impedance measurement while his arm is flexed. Note the elastic band around the wrist and the change in area of cross section of the arm before and after flexing the arm. The procedure utilized V4 of the bio-impedance device and the signals are recorded using Agilent U2531A. ....	214
Figure 11-11: Shows a typical example of variation of impedance across a subject's arm as the subject flexes and relaxes his/her arm. $Z_{max}$ is the maximum value of impedance before start, $Z_{min}$ is the minimum value of impedance after flexing, $Z_{diff}$ is the change in impedance due to flexing. The signal is sampled at 1MSa/s using the U2531A for duration of 5 Seconds. ....	215

Figure 11-12: Subfigure 1, 2 and 3, 4 show the original and reconstructed (with no holes) legs of two volunteers, whereas subfigure 5 shows the rear view original leg in 3..... 216

Figure 11-13: Shows scatter plot between left-leg volume measured using KinFu algorithm and impedance coefficient of the left-leg..... 217

Figure 11-14: Shows the performance metrics of a neural-network with 5 neurons in the hidden layer..... 221

Figure 11-15: Shows the performance metrics of a neural-network with 5 neurons in the hidden layer..... 221

## ❖ List of tables:

Table 1-1: Shows the advantages and limitations of common methods used to determine body composition.....	27
Table 1-2: Shows typical concentrations of electrolytes in body fluids expressed in milliequivalents per litre. Adopted from Grimnes & Martinsen, 2008. ....	30
Table 1-3: Shows the electrical conductivity of various human tissues. Adopted from Grimnes & Martinsen, 2008a. ....	35
Table 1-4: Lists six commercially available bio-impedance analysers, their technology and the body composition parameters they are able to predict. Here SF, MF, WB stand for single frequency, multi-frequency, whole-body, segmental BIA is described in section 1.9.3. For BC parameters refer section 1.2.....	41
Table 1-5: Lists 5 prominent studies which explore the ability of BIA to predict body composition parameters in various subject types. ....	42
Table 1-6: Lists the data collected from human volunteers for this project along with the type of study the volunteers participated in. ....	62
Table 1-7: Shows the upper limits of allowable leakage and auxiliary currents through a subject in normal and single fault conditions for both AC and DC currents. All values are reported in microamps.....	69
Table 1-8: Shows the auxiliary and leakage currents measured in V1 using SPICE simulations. The values are lower than upper limits for these currents set by BS EN 60601. Values reported in microamps.....	71
Table 2-1: Shows the comparison of important characteristics of the 801 order filters designed using equiripple and least-squares method and the Kaiser window filter of order 951. ....	86
Table 2-2: Lists the main differences between programming approach and neural computing approach to problems. ....	92
Table 3-1: Shows the most likely assignment of electrodes on the Tanita BC-545. ....	109
Table 3-2: Shows electrode pair configuration for measuring voltage across different segments. ....	114
Table 4-1: Shows the truth table for SPDT switch.....	115
Table 4-2: Shows the truth table for 4:1 multiplexer.....	115
Table 4-3: Shows the truth table for control bits of two SPDT switches. ....	117
Table 4-4: Shows the significance and order of bits used to control the switches and multiplexers. ....	119
Table 4-5: Shows the eight digital control states to obtain segmental bio-impedance. ....	119
Table 5-1 : Shows the developmental stages and versions of the BIA device. Also listed are the details on various components of the device. ....	123
Table 5-2: Shows the output current from the designed VCCS at loads varying between 0 and 10kΩ at two different frequencies; 5kHz and 100kHz. ....	132
Table 5-3: Lists the phase difference measured in a series RC circuit. Measurements were made using device V2 and were inconsistent with theoretical estimates of the same.....	137
Table 6-1: Shows the auxiliary and leakage currents measured in V2. The values are lower than upper limits for these currents set by BS EN 60601. Values reported in microamps.....	144

Table 7-1: Shows the digital states required to make segmental bio-electrical measurements from 8 segments of the human body in version 4 of the device. ....	153
Table 7-2: Shows the auxiliary and leakage currents measured in V4. The values are lower than upper limits for these currents set by BS EN 60601. Values reported in microamps. ....	158
Table 9-1: Ten consecutive impedance estimates of 100, 250,500, 1000Ω test loads at 50kHz with corresponding mean, standard deviation and mean error (all units in Ohms). ....	171
Table 9-2: Shows the relative standard deviation for different segments from 8 consecutive bio-impedance measurements at 50kHz. ....	172
Table 9-3: Show the mean absolute percentage error between measured whole-body impedance and whole-body impedance found by adding impedances from the arm, trunk and leg which was observed in device version2 (single-frequency) and version 4 (multi-frequency). ....	173
Table 10-1: Shows the cutoff frequency, stopband frequency, stopband attenuation and order of the three filters used to extract heart-rate from bio-electrical signals. ....	179
Table 11-1: Shows the mean and standard deviation for the age, height, weight and BMI for participants in this study. ....	190
Table 11-2: Shows the body composition summary from a DEXA. The 'Region' column lists the section of the body and the top row lists the body composition parameters in grams. Last column represents percentage fat in the particular region. ....	193
Table 11-3: Shows mean and standard deviation of bio-impedance measured from various body sections (from 22 volunteers) at four different frequencies, viz. 10,50,75,100 kHz. ....	193
Table 11-4: Shows the mean and standard deviations of body composition parameters measured using DEXA scan (22 volunteers). ....	194
Table 11-5: Shows the significance value for body composition parameters in whole-body lean-mass linear regression model. ....	197
Table 11-6: Shows the significance value for body composition parameters in a whole-body bone mass model. GenderM represents male volunteers. ....	198
Table 11-7: Shows the significance value for body composition parameters in the left arm lean-mass model. ....	202
Table 11-8: Shows the P-values for the right leg lean mass prediction model. ....	205
Table 11-9: Shows the P-value for the regression model to predict bone mass in the left leg. This model is to be optimized by excluding the non-significant parameters. ....	206
Table 11-10: Shows the optimised model to predict bone mass in the left leg with parameters and their significance. ....	206
Table 11-11: Shows the optimised linear model to fit lean-mass in the trunk with different parameters and their significance. ....	209
Table 11-12: Shows the significance of the various parameters used to produce the linear model for the trunk bone mass. 'GenderM' stands for the inclusion of male gender as a parameter in the prediction model. ....	211

## ❖ List of abbreviations:

AM : Amplitude modulation.....	179
BCM : Body cell mass. ....	29
BIA : Bio-impedance analysis. ....	20
BIS : Bio-Impedance spectroscopy. ....	56
BM : Bone mass.....	29
BW-EH : Body-weight excluding the head. ....	200
CMRR : Common-mode rejection ratio.....	38
CT : Computerized tomography. ....	20
DAQ : Data acquisition card. ....	116
DDS : Direct digital synthesis.....	235
DEXA : Dual-energy X-ray absorptiometry.....	22
ECW: Extracellular water.....	28
EIT : Electrical impedance tomography.....	128
FFM : Fat-free mass.....	29
FM : Fat mass. ....	29
IC : Integrated circuit.....	149
ICW : Intracellular water ....	28
KinFu : Kinect Fusion. ....	73
LBM : Lean body-mass. ....	29
MFBIA : Multi-frequency bio-impedance analysis. ....	55
MLP: Multi-layer perceptron.....	92
MM : Muscle mass. ....	29
MRI: Magnetic resonance imaging.....	20
PCB: Printed circuit board. ....	140
Rsq : Coefficient of determination.....	88
S-BIA : Segmental bio-impedance analysis. ....	105
SD : Standard deviation.....	173
SFBIA : Single-frequency BIA. ....	55
SPDT : Single-pole double-throw. ....	116
TBW: Total body water. ....	26
VCCS : Voltage control current source. ....	117
VCCS : Voltage-controlled constant current source.....	43
WB-CLM : Whole-body combined lean-mass. ....	200
WBFM : Whole-body fat mass. ....	200
WHO : World health organisation.....	23

# Chapter 1 Introduction

This thesis describes a programme of research to refine bio-impedance analysis methodology for the investigation of human body composition. The programme includes the construction and testing of a bio-impedance measurement device and also explores additional applications of bio-impedance in human physiology. This chapter will introduce essential concepts of BIA and cover other topics which are relevant to this study.

Body-composition assessment is an effective method to predict nutritional and health status of an individual and also to detect, monitor and helps treat different diseases. For clinical diagnostic purposes and disease monitoring it is highly advantageous to be able to image the body qualitatively and quantitatively. Assessing the size and composition of the main body compartments and mass of major organ and tissue structures is a valuable clinical tool. The standard methods to assess body-composition data are MRI, CT scan and DEXA scan, which retain high accuracy. However use of these standard methods is compromised in various ways, for example these procedures are time consuming and require expensive equipment with substantial operational costs. Bio-impedance analysis (BIA) however offers quick, low cost body composition estimation, although there is lower accuracy and precision. Nevertheless devices based on bio- impedance analysis (BIA) can provide close approximations of the masses of various tissues in an individual in less than 30 seconds with the added convenience that the measurements can be made in a GP surgery or home, at the fraction of the cost of an MRI or CT scan. Also BIA is non-invasive and can be repeated any number of times unlike standard methods which involve radiation or other health risks (Kanai et al. 1987; Grimnes & Martinsen 2008d). Due to its cost effectiveness and non-invasive nature there has been keen interest in BIA in the last three decades.

BIA is based on measuring impedance of the human body and predicting the masses of different tissues in the body from these measurements (Jackson et al. 1988). Modern BIA devices (like the Tanita BC-545 considered in detail herein) are not only capable of estimating overall body composition but can also provide approximate information on composition (% fat, muscle mass etc.) of each limb and trunk separately. The BC-545 can also estimate very approximately the amount of visceral fat, high amounts of which have been associated with increased risk of heart disease and diabetes (Despres & Lemieux 2006).

The primary drawback of BIA is that it is an indirect method of estimation. After the body impedance is measured the body composition estimates are made with regression equations which are based on composition data collected from a large number of test subjects. Alternatively mathematical models and/or emulsion mixing theory equations are used to predict body fluid volumes. Both these approaches have merits and demerits but fundamentally these results do not represent real user tissue volumes because these equations are based on substantial underlying assumptions (Jaffrin & Morel 2008). At present the accuracy of this technique is not sufficient to be used as a standard method for clinical applications. For example the standard error for estimating percentage body-fat has been reported to be around 5-6% (Jackson et al., 1988). Such a large variance cannot always be tolerated in a clinical scenario. Presently the equations used for BIA estimates are based on normal healthy subjects and cannot necessarily be used in cases of significantly altered hydration or physical abnormalities (Misc, 1996). Also the prediction methods are not adjusted for different ethnic groups because body composition differs with ethnic origin (Tanaka et al., 2003). The potential applications of BIA, with improved accuracy are many. Osteoporosis for example can be detected at an early stage if a low bone density is measured and shows a decreasing trend over time (Schiper et al. 2011). Nutrition related disorders such as loss of muscle mass (sarcopenia), and excess adiposity which is associated with development of diabetes and heart disease risk

could also be detected at an early stage. Some studies have used BIA to monitor progression of AIDS (Schwenk et al. 2000). There are many more possible applications of this technique as a diagnostic aid and for monitoring disease progression or the efficacy of treatment. But before we start exploring BIA technologies an introduction to essential concepts of body tissue types, their broad segregation, current conduction within these tissues and tissue electrical models used for BIA prediction is necessary. The following sections are aimed at providing a brief overview of essential concepts but first we shall look at other body imaging techniques which can be used for body composition assessment.

## **1.1 Medical body imaging:**

Body imaging techniques like MRI, CT or DEXA scan could be used to determine body composition. However their repeated use involves radiation risks and concerns regarding patient well-being due to over-exposure to radiation. Also the expense of performing techniques such as MRI, CT scan is high since equipment is expensive and operational costs are involved. Patient compliance is another issue because some patients do not understand or accept the requirements for undergoing a particular technique or repeated investigation and treatment. Since body composition imaging is our primary concern we will focus on comparing prominent body composition estimation techniques viz. X-rays, CT scan, DEXA scan and MRI with BIA. BIA prediction equations require real body composition estimates using standard body composition techniques like DEXA scan (Donadio et al. 2008). Also many studies have used isotopic dilution techniques to estimate water distribution in the body (Gonzalez et al. 2002; Ellis & Wong 1998; Thomas et al. 1998). It is useful to understand these techniques and weigh them against BIA.

### **1.1.1 X-ray imaging:**

The ability of X-rays to show the inside of objects was first observed by German physicist Wilhelm Conrad Roentgen in 1895. His proposal of the use of this technique to view the inside of objects was greeted by the scientific community which earned him the first Noble prize for physics in 1901. The frequency of X-rays is between  $3 \times 10^{16}$  to  $3 \times 10^{19}$  Hz, and their energies range from 0.12keV to 12keV. X-rays are generated by bombarding high energy electrons with a metal surface (mostly Tungsten or a Tungsten alloy). When X-rays with sufficient energy are subject to the surface of an object they pass through the objects and its contents within (Bushberg 2012). The rays emitted through the object have varied energies depending upon the material they interact with. The resultant rays are imposed on a detector that originally was photographic plates, which have been replaced by digitized detectors in recent times. In the case of body tissues, X-rays are partially blocked by hard tissue like bone but pass readily through soft tissue like most organs. On the detector, areas where X-rays strike darken when developed, this causes bones and other calcified tissues in X-ray images to appear lighter than surrounding soft tissue (Carlton et al. 2006). X-rays can give accurate 2-D images of tissue structures within the human body and can be used to see the changes in tissue structure over time. But with health risks involved, fewer exposure routines are advised (de González & Darby 2004). Also the procedure requires specialized equipment, an isolated room to avoid involuntary exposure and a trained radiologist to carry out the process. Also the cost of maintenance and specialized film per acquisition is involved. Diagnostic X-rays increase the risk of developmental problems during growth and also cancer (Calabrese & Baldwin, 2003). X-ray radiation and other ionizing radiation (radiation capable of removing electrons from atoms) are classified as carcinogens by the world health organisation (Mohr et al. 1999). It is estimated that additional exposure increases the cumulative risk of getting cancer by 0.6% to 1.8 % by the age of 75 (de González & Darby, 2004).

### **1.1.2 DEXA scan:**

The potential use of X-rays to estimate bone density was established in years close to the discovery of X-rays itself. It is the advancement in technology which later led to the practice of this idea. Dual Energy X-ray Absorptiometry uses two different X-ray beams of different energies targeted at the subject's area of interest. Since the two different beams are absorbed differently by the same tissue the resultant beam energies provides an estimate of the density of bones. DEXA is also used to measure lean body tissue and fat mass. The fat content is the difference in the weight between the bone mass and fat free mass estimated by DEXA (Bushberg 2012). Although the radiation dose for DEXA is about 1/30th the dose for a single chest X-ray, it still poses radiation risk to the user and is a potential carcinogen. Additionally, the radiation is exposed on the entire body rather than a specified area. DEXA scan requires dedicated hardware equipment and expertise to operate it, in a similar fashion that X-ray imaging methods do. The results from a scan usually require an expert in the field of orthopaedics or body composition to interpret fully. The maintenance cost of the equipment is a factor to be considered (Carlton et al. 2006).

### **1.1.3 CT scan:**

Computerized tomography (CT scan) uses X-ray imaging and computerized tomography to generate a 3D image of an object with 2D images taken around a single rotational axis. Italian radiologist Alessandro Vallebona first proposed the use of projective geometry to 2D X-ray images in 1900 (Bushberg 2012). The advancement in microcomputers aided the enhancement of this initial idea leading to the merging of multiple 2D images to make a 3D structure of the area of interest. The data generated by a CT can be manipulated to show the different structures in the body depending on how each attenuates X-ray radiation. Although a CT scan has several advantages over traditional 2D radiography, it is carcinogenic since X-ray exposure is involved and the amount of exposure to make a 3D map of a body part is far higher than a single X-ray shot 2D image (de González & Darby 2004). Although lead (Pb) filters are used to avoid exposure to unnecessary body

parts it is unable to avoid vestigial exposure when looking at parts with complex structures such as the ball and socket joint. CT scans can give accurate 3-D images of the body part of interest and data manipulation is used to enhance certain tissue visibility in the image to make an estimation of tissue volumes of the different parts of the body. Like X-ray imaging CT scan requires specialized equipment, trained staff and also has maintenance costs involved. The patient undergoing a scan needs to remain still for accurate results and the confined space does not suit many patients.

#### **1.1.4 MRI Scan:**

Magnetic resonance imaging is a medical imaging technique for viewing the internal structure of the body. MRI uses the property of materials known as Nuclear Magnetic Resonance (NMR) to produce detailed images of the human body (Carlton et al. 2006). To make an MRI image of a section a radio frequency transmitter is turned on for a short interval, which generates a large electromagnetic field. Since living tissue is composed of water (which has two hydrogen atoms and a proton) under the influence of such a field the protons in body water start to spin in the opposite direction. The number of protons that flip depends upon the duration of the exposure to the field. When the field is turned off the protons spin down to their original state the energy shift in the protons are detected by the scanner (Bushberg 2012). This relationship between frequency of photons and magnetic field strength is used to produce MRI images. Protons of different tissues return to their equilibrium at different rates, this property of tissues along with four others namely; spin density, relaxation times, flow shifts and spectral shifts are used to construct MRI images. By altering one or more of these parameters contrast between different tissues can be achieved. Like the other body composition estimation techniques described earlier, MRI also has its limitations and risks. First, MRI cannot be used with patients with surgical implants such as pacemakers since large magnetic fields are involved. Such devices may fail under a strong magnetic field leading to instant death (Medicines and Healthcare products Regulatory Agency (MHRA) 2007). The large radio

frequency energy can cause localized heating which could lead to hyperthermia. The contrast agents administered to improve contrast in MRI images possess risk to individuals having specific conditions such as kidney diseases and could lead to renal failure. MRI equipment is expensive and requires dedicated staff for operation and maintenance. The costs per scan are also large and require the individual to go to a dedicated scan centre. MRI is a very accurate method for estimating body composition and is the gold standard for correlative studies with body composition (Carlton et al. 2006).

### **1.1.5 Isotopic dilution and mass spectroscopy to determine body water content:**

Total body water (TBW) can be measured using deuterated water ( $2\text{H}_2\text{O}$ ) and mass spectroscopy. In order to perform this measurement a dose of deuterated water is administered to the subject and allowed to circulate throughout the entire body water space. The body water pool size is determined by the level of dilution of this dose after equilibration of the dose throughout the TBW space (Schoeller & Santen 1980). The mass spectroscopy to quantify dilution is quick, but it takes a long time (two to three hours) for the administered dose to spread evenly across the TBW space. Also a large dose of deuterated water is reported to cause changes in metabolism and behavioural changes in small mammals. Alternately tritiated water can be used, but radiation risks are involved with its usage and its use is unsuitable in large amounts. Several BIA studies have used this technique to quantify body water and correlate it against measured impedance (Lukaski et al. 1985) but this method is inconvenient and has risks involved.

### **1.1.6 Advantages of BIA over standard techniques:**

The advantages BIA offers over the standard methods to determine body composition are summarized in the Table 1-1. All the standard methods have health risks involved but BIA is comparatively safe although companies, such as Tanita and Biospace (Table 1-4),

advise pregnant women and people with pacemakers to avoid using BIA instruments. BIA can also be performed at the convenience of one's home whereas the other techniques require expensive equipment and the individual to travel to the site where the equipment is present. Also BIA equipment is relatively cheap compared to the equipment for the other techniques and requires low maintenance. Although there are several advantages of BIA over standard methods its accuracy is relatively poor and the composition of different segments of the human body cannot be segregated with the same level of detail as it is possible with the other techniques.

**Table 1-1: Shows the advantages and limitations of common methods used to determine body composition.**

	Principle	Safety	Accuracy	Convenience	Cost/Time
DEXA	X-rays	Radiation risks	Fair	On site	Equipment & Maintenance
MRI	Electromagnetic Field	Field exposure risks	Good	On site	Equipment & Maintenance
CT Scan	X-rays	Radiation risks	Good	On site	Equipment & Maintenance
BIA	Low electric current	None established	Relatively poor	At home	Low equipment cost

## 1.2 Body compartments:

BIA can estimate the volume of different compartments in the human body. So it is appropriate to consider the human body as a 5 compartment human body model and composition of each compartment (Organ & Bradham 1994). Figure 1-1 shows this model and identifies the 5 compartment human body model.



**Figure 1-1: Shows the five compartment human body model relevant to BIA(Kyle, De Lorenzo, et al. 2004).**

### **1.2.1 Total body water (TBW), extracellular water (ECW) and intracellular water (ICW):**

BIA estimates of body composition rely on accurate estimation of body water (from impedance) and its distribution within the intracellular (within the cells) and extracellular (around the cells) compartments also known as intracellular water (ICW) and extracellular water (ECW) respectively. Many BIA methods aim to estimate the total body water (TBW) which is the volume of all the water that is present in an individual (sum of ICW and ECW). It is important from a BIA perspective since the conduction of the current takes place via the electrolytes dissolved within TBW. If two of these quantities are estimated the third can be calculated as their difference. Generally in a healthy individual with 40 litres of TBW, 25 litres (62.5%) is ICW and 15 litres (37.5%) is ECW (Guyton 1981).

### **1.2.2 Fat free mass (FFM) and Fat Mass:**

As the name suggests FFM is the volume of everything in the human body except fat, also known as lean body mass (LBM). It includes the bone mass (BM), muscle mass (MM), TBW and also the metabolically inactive tissues. Empirical equations have been derived which can predict the FFM from impedance measurements; these equations are formulated by regression analysis of impedance data from healthy populations and may be adjusted for different parameters such as age, height, weight and gender (Guyton 1981). Sometimes the extremities of any of these parameters such as weight could be used to improve the prediction capability. Fat mass (FM) is the volume of total fat (adipose tissue) which is present in the body. It is the difference between the total body mass and the FFM in an individual. FM has low electrical conductivity whereas FFM readily conducts due to presence of ions which migrate to conduct.

### **1.2.3 Body cell mass (BCM):**

Body cell mass (BCM) is generally regarded as the mass of the protein rich compartment of the body. BCM includes muscle tissue, organ tissue, intracellular and extracellular water, and bone tissue. In a normally nourished individual, muscle tissue accounts for approximately 60% of the BCM, organ tissue accounts for 20% of BCM, with the remaining 20% made up of red cells and tissue cells. The BCM also contains the large majority (98-99%) of the body's potassium. It has been reported to be good indicator of an individual's health status since it accommodates all of the metabolically active tissue in an individual (Guyton 1981).

## **1.3 Current Conduction:**

BIA relies hugely on accurate measurement of body impedance by passing a known current through the subject. The current flows through tissues which exhibit properties of both electrolytes and dielectrics. Conduction of current in an electrolyte happens with the

migration of ions present within its volume (Grimnes & Martinsen 2008a). In living tissues electrolytes are present within ICW and ECW (Table 1-2); these ions (mainly Na<sup>+</sup>, Cl<sup>-</sup> and K<sup>+</sup>) migrate in the electric field of a current and contribute to conduction. To appreciate the flow of current through the body it is appropriate to examine electrical properties of basic bio-materials, cells and major tissues.

**Table 1-2: Shows typical concentrations of electrolytes in body fluids expressed in milliequivalents per litre. Adopted from Grimnes & Martinsen, 2008.**

	<b>Cations (meq/L)</b>		<b>Anions (meq/L)</b>		
	<b>Plasma</b>	<b>Intracellular</b>	<b>Plasma</b>	<b>Intracellular</b>	
Na <sup>+</sup>	142	10	Cl <sup>-</sup>	103	4
K <sup>+</sup>	4	140	HCO <sub>3</sub> <sup>-</sup>	24	10
Ca <sup>2+</sup>	5	10 <sup>-4</sup>	Protein <sup>-</sup>	16	36
Mg <sup>2+</sup>	2	30	HPO <sub>4</sub> <sup>2-</sup> + SO <sub>4</sub> <sup>2-</sup> + organic acids	10	130
H <sup>+</sup> (pH = 7.4)	4 × 10 <sup>-5</sup>	4 × 10 <sup>-5</sup>	Sum	153	180
Sum	153	180			

### 1.3.1 Basic bio-materials:

#### 1.3.1.1 Water:

Water is essential to sustain life and around 70% of a healthy human body is water. Water is a polar liquid with a relative permittivity (the ratio of the amount of electrical energy stored in a material by an applied voltage) of about 80 at 20°C (Grimnes & Martinsen 2008a). Figure 1-2 shows the polar structure of the water molecule: the high permittivity of water is the reason for its dissociative property. Due to its polar nature water molecules closely surround any charged ion and effectively neutralize its charge. A living cell has aqueous electrolytes in and around it. The major intra and extracellular ions and their concentrations are listed in Table 1-2.

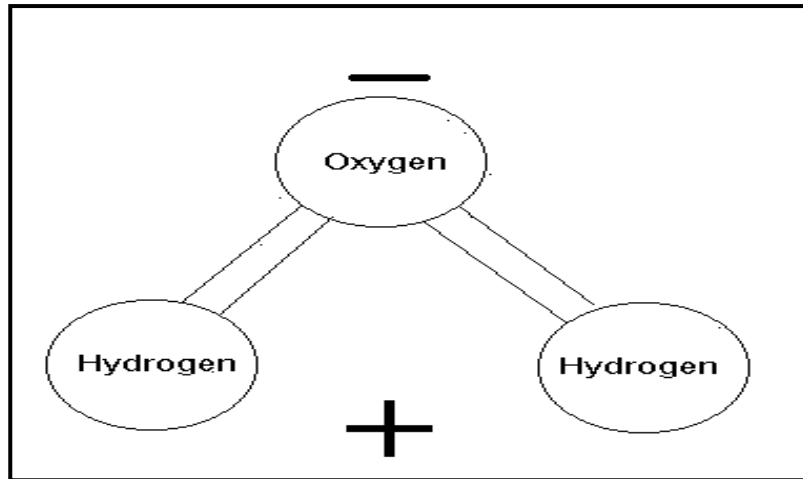


**Figure 1-2: Shows the polar structure of a water molecule.**

### ***1.3.1.2 Lipids and cell membranes:***

Lipids are oily organic substances which are water insoluble. In our context a group of lipids known as polar lipids are of interest. These are hydrocarbons which have a hydrophobic tail and hydrophilic heads (Figure 1-3). When in water these lipids form a layer on the surface with the hydrophobic tails pointing towards air away from the water, thus cells are surrounded by a membrane formed of a double layer of polar lipids called the Bilayer Lipid Membrane (BLM) (Grimnes & Martinsen 2008a). The BLM is constituted of a close arrangement of polar lipids with their tails facing away from the extra- and intracellular water (Figure 1-3). The thickness of this membrane is around 7nm and is absolutely essential to sustain the integrity of a cell. The BLM is selectively permeable because controlled gaps (pores and transporters) are the only paths of entry into and exit from a cell (Grimnes & Martinsen 2008a). Therefore the membrane controls movement of electrolytes and water in and out of the cell. The BLM usually maintains a healthy resting potential of around 70mV (negative on the inside) between the extra- and intracellular part (Figure 1-4). To maintain a resting potential of -70mV across a 7nm wide membrane means the membrane has to withstand a field strength of 10MV/m which is the reason for the large capacitance, low conductivity and large dielectric strength of the BLM. Its capacitance is in the order of 1 $\mu$ F per square centimetre (Alvarez 1978). Therefore cell

membranes are the main source of capacitive reactance within the human body. When an AC flows through the body the capacitive reactance of all the cells introduces a phase shift between the input current and the detected voltage. This phase difference is directly related to the BCM and is used to predict the amount of healthy living cell mass or BCM (Schwenk et al. 2000).

### ***1.3.1.3 Proteins & carbohydrates:***

All proteins in the human body are composed of 20 amino acids combining with each other to form proteins. All amino acids are made from a common chemical structure (Figure 1-5); here R represents the side chain which characterizes the properties of the amino acid. Eight of the 20 amino acids are hydrophobic and seven are hydrophilic, hence they are polar. Two have negatively charged R groups and two have positively charged R groups, therefore they have a net negative and positive charge respectively. In their dry form amino acids are crystalline and have dielectric properties but in an aqueous solution they have properties of an electrolyte (Grimnes & Martinsen 2008a). Small groups of amino acids form peptides and complex structures of peptides form proteins. Proteins exist as a strand or as a rigid structure and their electrical properties in water depend on structure, size, rigidity and other features since in water (which is polar) bonds are broken and formed according to the distance of atoms and charges. Carbohydrates are also common in cells: they give energy and have other functions such as solubilisation of drugs. Some saccharides are attached to proteins in cell membranes but overall carbohydrates do not contribute largely to conduction tissues (Grimnes & Martinsen 2008a).

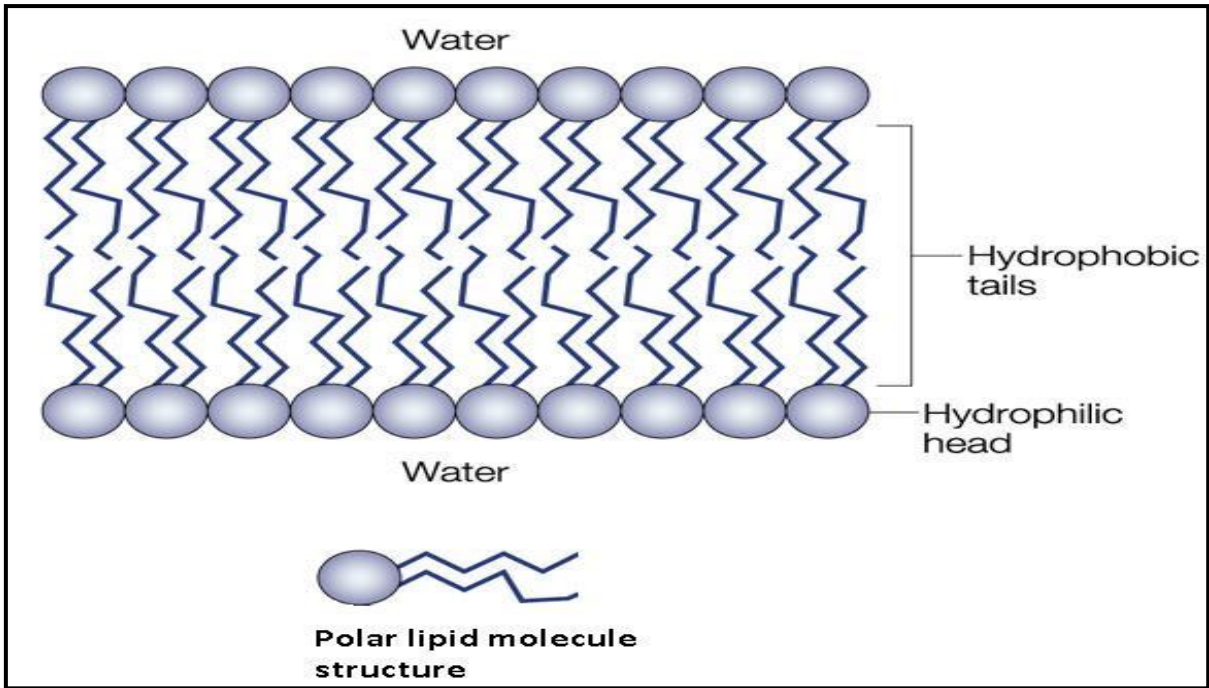


Figure 1-3: Shows the bilayer lipid membrane (BLM) formed of polar lipids.

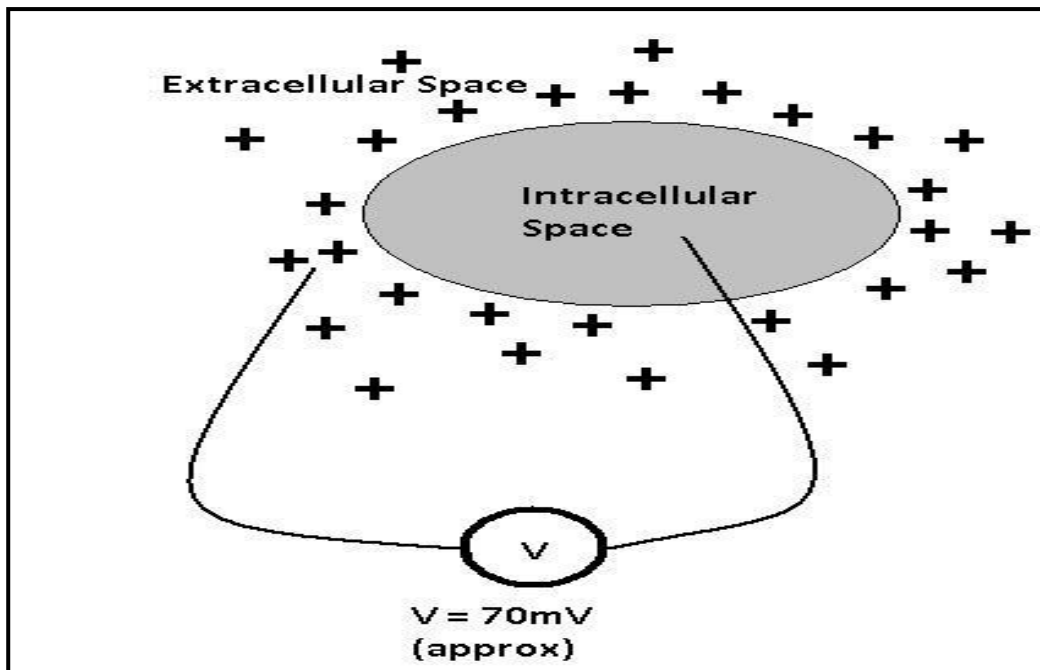
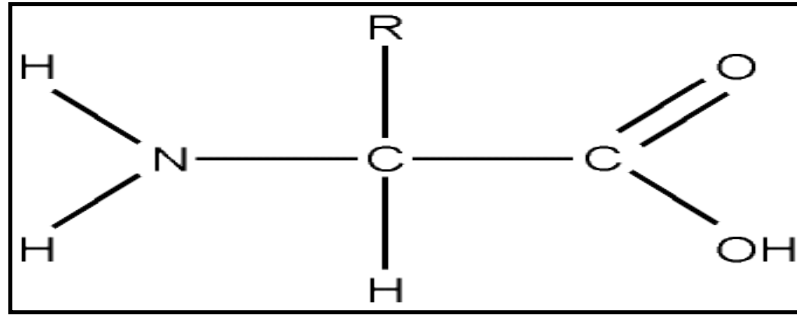


Figure 1-4: Shows the potential difference between intracellular and extracellular space around a cell.



**Figure 1-5: Shows the structure of an amino acid, R is side chain.**

### **1.3.2 Major tissues & organs:**

Living tissue is a heterogeneous medium from an electrical perspective since it is constituted of cells of various sizes, composition and resistivity. Also many tissues are electrically anisotropic. Most organs in humans have multi-layer membranes and the concentration of ions inside gives rise to voltage gradients which affect the flow of current. Table 1-3 shows electrical conductivity and other electrical properties of major human tissues. The problem with tissue conductivity is that it can change extensively (in order of a few decades) depending on the placement, insertion depth of electrodes, level of hydration of tissue under study and various other factors. Below frequencies of 10MHz (range of our interest) tissue conductivity is predominantly electrolytic (Kyle, De Lorenzo, et al. 2004).

**Table 1-3: Shows the electrical conductivity of various human tissues. Adopted from Grimnes & Martinsen, 2008a.**

<b>Tissue</b>	$\sigma$ (S/m) 1 Hz–10 kHz	$\sigma$ (S/m) ca 1 MHz	$\varphi_{\max}$ @<10 MHz	<b>anisotropy</b>
Human skin, dry	$10^{-7}$	$10^{-4}$	80°	?
Human skin, wet	$10^{-5}$	$10^{-4}$	30°	?
Bone	0.005–0.06		20°	Strong
Fat	0.02–0.05	0.02–0.05	3°	Small
Lung	0.05–0.4	0.1–0.6	15°	Local
Brain (grey matter)	0.03–0.4	0.15	15°	Small
Brain (white matter)	0.03–0.3			Strong
Liver	0.2	0.3	5°	?
Muscle	0.05–0.4	0.6	30°	Strong
Whole blood	0.7	0.7	20°	Flow dependent
Urine	0.5–2.6	0.5–2.6	0°	0
CSF	1.6	1.6	0°	0
Saline, 0.9%, 20°C	1.3	1.3	0°	0
Saline, 0.9%, 37°C	2	2	0°	0
Seawater	5	5	0°	0

For tissues with a higher density of cells (like keratin) conductivity is lower, and conductivity is lowered further with reduced input frequency. Also the conductivity of the upper layer of the skin (stratum corneum), hair, fat etc. are dependent on their location in the body and their water content at time of measurement. Muscle tissue which forms a large part of the human body is largely anisotropic and the ratio of conductance when measured along and across the tissue gradient can be as large as 8:1. The conductivity of muscle tissue is found to rise from 0.3 to 1 between frequencies of 10 Hz to 100MHz. Nerve tissue is found mainly in the human brain, the conductivity of the brain rises fairly steadily from 0.05 to 0.8 between 10Hz to 100MHz (Grimnes & Martinsen 2008b). Conductivity of adipose tissue and bone marrow is very low and varies depending upon the amount of blood and other fluids in and around them. The conductivity of the human skin is very versatile and depends on the area of the body under interest. The majority of impedance of the skin at frequencies below 10 kHz is offered by the stratum corneum (top layer), but depends hugely on the level of hydration and the type of electrode used for measurement. Stratum corneum contributes about 50% of skin impedance about 10 kHz and about 10% at 100 kHz (Grimnes & Martinsen 2008a). Indeed skin impedance varies with different body surface regions of the same individual and also from person to person and is considerably affected by humidity level, time of day and perspiration (McAdams et al. 1996).

### 1.3.3 Flow of current - a microscopic and a macroscopic view:

The microscopic view was briefly covered in the previous section but one additional emphasis is to be brought to anisotropy of tissues. Cells in tissues are of various sizes, shapes and vary in their pattern of morphological arrangement. Macroscopically usually they are assumed to be homogenous, but this is not always representative (Grimnes & Martinsen 2008a). For example a cubical bio-material with two pairs of electrodes (Figure 1-6) with an insulating implant within itself will experience less current flow between the vertical pair of electrodes than the horizontal pair. In a tissue with ellipsoidal cells oriented in one direction the current flow (at low frequency) in the horizontal direction will be lower than in the vertical direction because the cell membrane capacitance causes low conductivity, hence the current has to flow around the cells forcing it to take a longer flow path.

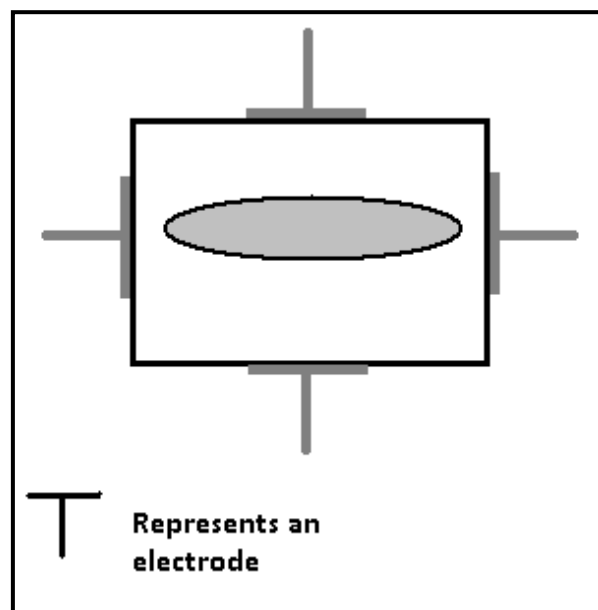


**Figure 1-6: Shows a cubical biomaterial with insulating implant.**

From a macroscopic perspective as mentioned earlier the resistance of different parts of the body depends largely on the area of cross section of the region of interest. From equation (5) as the cross sectional area is reduced the resistance increases. Figure 1-8 shows the sectional resistance of current flow path that may be illustrative of flow from right hand to the

right leg. Note that the contribution of lower cross sectional area such as finger and legs is far greater than that of a larger cross section such as the chest.

### **1.3.4 Bio-potential electrodes:**

Accurate acquisition of bio-electrical signals is necessary in BIA applications. Therefore it is important that the measured electrical signal is not distorted during the measurement process and is noise free. Since electrodes play a vital role in sending signals (into the subject) and relaying back recorded response to the measurement system; if not chosen correctly bio-potential electrodes can give rise to significant problems in the system (Yoo 2011). Charge carrying ions carry current inside the patient's body whereas electrons carry the current in the electronic device connected to the subject. The charge transfer mechanism between electrons to ions happens at the electrode/skin interface and is of great importance when designing electrical systems which involve electrodes (Yoo 2011). The electrode itself and the skin under the electrode give rise to potentials and impedances (which is known as contact impedance) which can adversely affect the measured bio-electrical signal. The focus here is primarily on BIA hence external bio-electric electrodes. A major problem with external electrodes is the skin impedance which is usually large and has unstable potential (Marquez et al. 2011; Spach et al. 1966). This can cause the difference between the two contact potential to add along with the acquired bio-electrical signal. If this potential mismatch is high the measurement system (particularly the input stage which is usually a differential amplifier) cannot cope and will saturate, this can mask the voltage changes occurring within the underlying tissue (Yoo 2011). Another major issue with skin impedance is its variability with frequency. The frequency dependence of electrode impedance can be attributed to parallel capacitances in the electrode-electrolyte interface and the skin below the electrode (McAdams et al. 1996). Figure 1-7 shows the basic electrical model of an electrode here  $C_A$  and  $R_A$  represents the impedance associated with the electrode tissue interface.  $R_S$  is the resistance of the tissue and  $V_i$  is the potential build up at the electrode-skin interface. The values of these parameters are dependent on the electrode type. At high input frequencies

the contact-impedance is very small and there is minimal attenuation of high frequency signals.

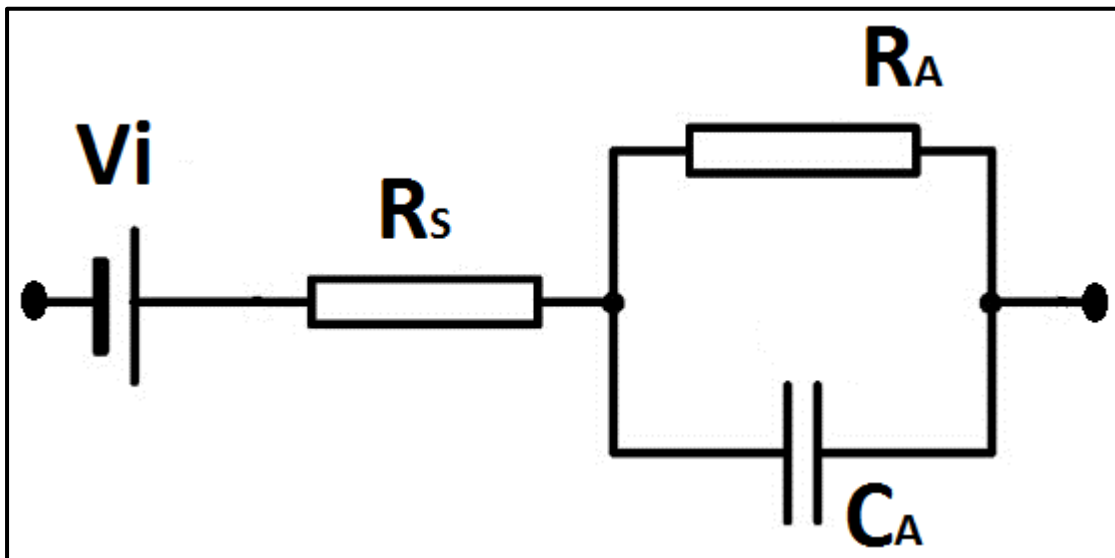


**Figure 1-7: Shows the simple electrical model of the electrode-tissue interface.**

It has been noted that decreasing the electrode size increases the contact impedance. In bio-impedance analysis contact impedance can arise in both the current injection circuit and the voltage recording system (Grimnes & Martinsen 2008c). It has been shown theoretically the large impedance mismatches can result in errors in perceived impedance (Grimnes & Martinsen 2008c). Contact-impedance mismatch in the current injection circuit will lead to a common-mode voltage on the body. A mismatch will also lead to a reduced common mode rejection ratio (CMRR) in the voltage recording system and prevent elimination of common mode voltage. A four-electrode system (in which one pair is used to inject current and the other to measure voltage) should be insensitive to problems arising from contact impedance because the measurement system does not measure contact impedance along with tissue impedance (McAdams et al.1996). Therefore all systems designed during this project were four electrode systems. The desired electrical properties for electrodes are low offset potential, low matched interface impedances and low polarization. Low interface impedance depends largely on the surface topography of the electrode. Silver Silver-chloride (Ag Ag-Cl)

electrodes fit these criterion quite well, but are cumbersome and need to be stuck on to the skin surface (McAdams et al.1996). Standardizing the position of Ag Ag-Cl electrodes is difficult, causing low repeatability of measurements. To avoid the problems which arise with the use of Ag Ag-Cl electrodes, the electrode from a commercial bio-impedance measurement system (Tanita BC 545) were used throughout this project. This will be discussed in detail in later sections. The electrodes were in contact with the subject's palms and the underside of their feet (soles). This made it easy to ensure that the subjects were in contact with the electrodes in a proper manner and also ensured fixed electrode contact positions. The electrode used in this project had large surface area and a rough topography. This ensured that the contact impedance was low. Further studies on electrode-impedance are presented and the subsequent chapters.

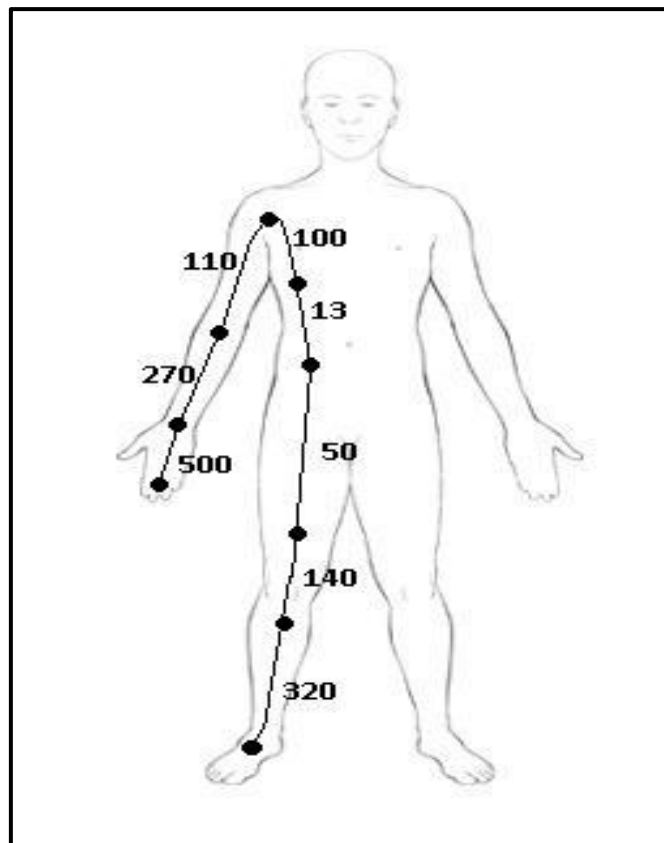


**Figure 1-8: Shows typical sectional resistance of a body in Ohms from palm to foot on the right side(values obtained from Organ & Bradham 1994).**

## 1.4 Resistance, reactance and impedance:

With regard to bio-impedance it is pertinent to consider the relevant aspects of electrical impedance. Ohm's law states that the current flowing across a conductor is directly proportional to the potential difference (voltage) across the conductor and inversely proportional to the resistance across the conductor; this law applies to both DC & AC circuits. The obstruction to the flow of current offered by a resistor is resistance. In practical circuits current flows through a combination of resistance, inductance and capacitance. When current flows through either an inductance or capacitance the obstruction to the flow of current offered is known as reactance (Bird 2010). As an AC current flows through a human body it is obstructed by both resistance and capacitive reactance. Impedance ( $Z$ ) is a vector function of both these components (Figure 1-9).  $X$  represents the reactance,  $R$  the resistance and  $\theta$  is the phase angle.

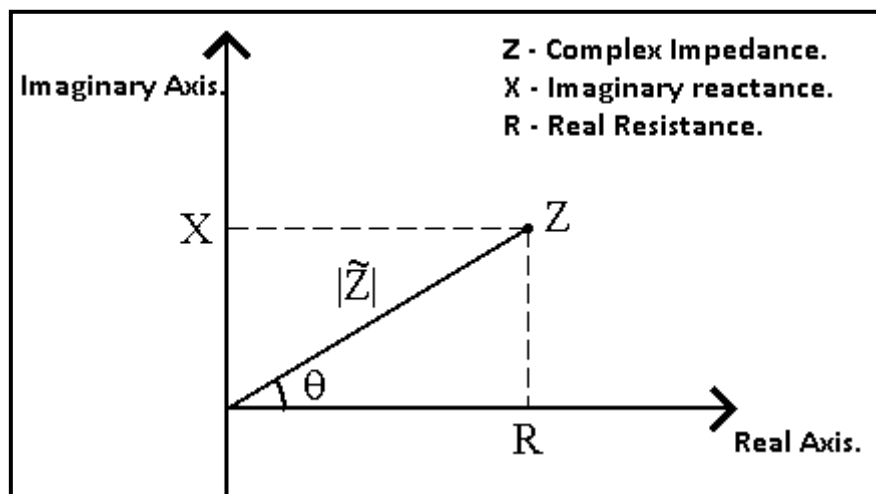


**Figure 1-9: Shows the impedance vector which is formed of resistance and reactance.**

## 1.5 Current BIA devices and previous studies:

There are several BIA devices available in the market with varied functionalities. Table 1-1 notes a few advanced BIA devices along with the technology they are based on and the body composition parameters they are able to predict. Here a variety of methods are

employed by different manufacturers to determine body composition parameters, some of these methods are undisclosed or patented. Throughout this thesis the Tanita BC-545 body composition monitor is utilized to estimate the body composition in volunteer subjects. It is hypothesised that a significant advance in BIA predictions can be made if information on the volume of the body section under study was available. If a visual of the same segment was available, its length could be evaluated, which can be used to evaluate impedance coefficient of individual limbs (impedance coefficient introduced in section 1.8) instead of normalizing the impedance with the subject's height. In order to do this an attempt to add a 'visual aspect' to BIA is made by utilizing 3D scans of limbs to predict their composition.

**Table 1-4: Lists six commercially available bio-impedance analysers, their technology and the body composition parameters they are able to predict. Here SF, MF, WB stand for single frequency, multi-frequency, whole-body. Segmental BIA is described in section 1.9.3. For BC parameters refer section 1.2**

Device	Type	Current type	BC parameters
<b>Akern BA-101</b>	SF, WB	50kHz, 400 $\mu$ A	TBW, BCM, ECW, ICW, FFM, FM, MM
<b>Tanita SC331S</b>	SF, Segmental	50kHz, 90 $\mu$ A	TBW, FFM, FM, S-MM, BM, BMR, MA, VFR
<b>InBody 770</b>	MF, Segmental	Undisclosed	TBW, FFM, FM, S-MM, BM, Protein content
<b>Maltron Bioscan916</b>	WB	Undisclosed	BCM, ECW, ICW, FFM, FM, Protein content
<b>RJL Quantum IV</b>	SF, Segmental	50kHz	FM, FFM, LM, TBW
<b>Tanita BC-545</b>	MF, Segmental	50kHz, 6.25kHz, 100 $\mu$ A	TBW, FFM, S-FM, S-MM, BM, BMR, MA, VFR

Table 1-5 lists some prominent studies in the field of BIA in various subject groups. All of the studies listed use DEXA scan as their reference method and have applied bio-impedance in different population types, most of these studies report inaccuracies in the predicted BC parameter. In order to help improve BIA predictions we aimed to construct multi-frequency

segmental BIA device and compare body segment impedance with body composition obtained using a DEXA scan. The results will be used to model prediction equations for FFM, FM, muscle mass and bone mass in subjects. Additionally the DEXA scan results will be combined with previously collected body composition data collected using the Tanita BC-545. This will be done using neural networks to produce equations able to better predict body composition. Impedance changes in limbs during flexing will be modelled with composition of the limbs to verify the ability of impedance change to predict limb composition.

**Table 1-5: Lists 5 prominent studies which explore the ability of BIA to predict body composition parameters in various subject types.**

<b>Research group</b>	<b>Subject type, number, reference</b>	<b>BC parameter</b>	<b>Comments</b>
<b>(Kotler et al. 1996)</b>	HIV AIDS, 266, DEXA	FFM, BCM, FFM	BIA overestimated FFM in subjects with large FM.
<b>(Kyle et al. 2001)</b>	Heart, lung and liver transplant, 245, DEXA	FFM	No significant difference between pre and post-transplant patients.
<b>(Dey &amp; Bosaeus 2003)</b>	Elderly, 106, DEXA	FFM	Needs to be validated in population under study.
<b>(Bedogni et al. 2003)</b>	Anorexia nervosa, 35, DEXA	FFM	Lower BIA accuracy due to greater ECW:ICW ration variability
<b>(Haapala et al. 2002)</b>	Elderly women, 93, DEXA	FFM	Equations are to be adjusted with age.

## **1.6 Bio-impedance measurement (device version 1):**

BIA relies on accurate impedance measurement of the tissue under observation. Initially a whole body impedance measurement system was constructed which was further developed into a segmental and multi-frequency system. In order to provide essential understanding of the body impedance measurement process the first bio-impedance measurement device (version 1, V1) conceived during this project is presented here. This would provide an initial idea on components and working for a more elaborate bio-impedance measurement system presented in this project.

The most basic BIA measurement system constitutes a voltage-controlled constant current source (VCCS) which passes a small sinusoidal current through the body section of interest and a voltage sensing device to measure the response to this current (Figure 1-10). It is to be noted that a constant current source is required because it feeds a fixed current through load (impedance of tissue under test) even if there are load variations (tissue impedance variations), excessive current through the human body is can damage body tissue and in extreme cases lead to fatality. A constant voltage source on the other hand draws more current with increasing load and is unsuitable for this purpose since the current flow is not regulated (refer section 1.12 for discussion on electrical safety). This approach is in place to ensure a limited amount of safe current flows through the tissue under observation to avoid any harm to the subject. The VCCS is composed of a sinusoidal signal generator and a modified Howland current source circuit (Aroom & Harting 2009; Pease 2008). The Howland circuit utilizes the sinusoid from the generator to output a constant sinusoidal current. The circuit provides approximately 800 $\mu$ A (RMS) constant current which is delivered to the subject via a pair of current source electrodes Figure 1-11. The analysis and working of the Howland circuit is detailed in the methods section.

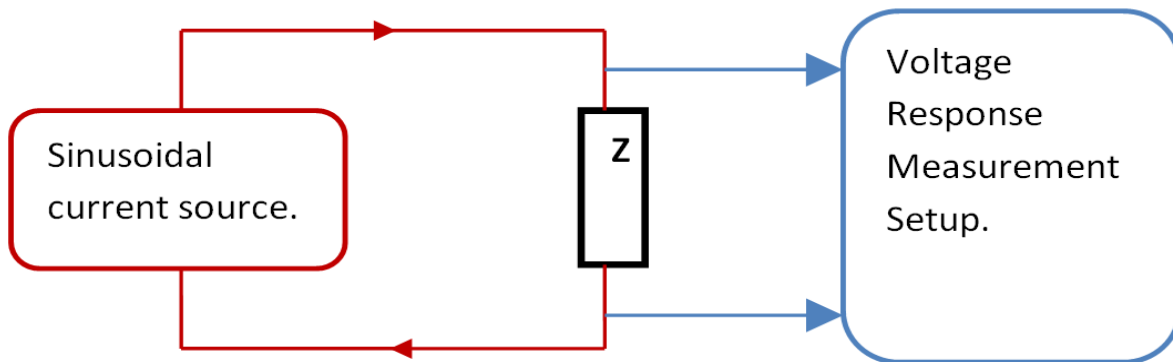


**Figure 1-10: Shows the blocks of the basic bioimpedance measurement system.  $Z$  is the impedance of the tissue under observation.**

The subject's voltage response to the current from the Howland circuit is acquired using a different pair of voltage sensing electrodes (Figure 1-11) using an analogue to digital (A/D) converter. The converter is connected and controlled by a computer which acquires the signal for analysis using Matlab.

### **1.6.1 Current source:**

The LF/1 function generator by Farnell, Wetherby, UK was chosen to drive the Howland circuit. It is capable of generating sinusoidal, square and triangular waveforms from 10 Hz up to 1MHz. An OPA2107 precision dual operational amplifier by Burr-Brown Corporation, USA was used to realize the Howland circuit (using 0.01% tolerance 10k $\Omega$  resistors). The frequency of input was 50kHz, this frequency was preferred because most single frequency BIA analysers operate at this frequency and current at this frequency is reported to flow through ECW and partly through ICW (Ellis & Wong 1998; Kyle, De Lorenzo, et al. 2004). The proportion of current through ICW and ECW is tissue dependent because different tissues have different cell types. The circuit was designed to deliver a current to 800 $\mu$ A.

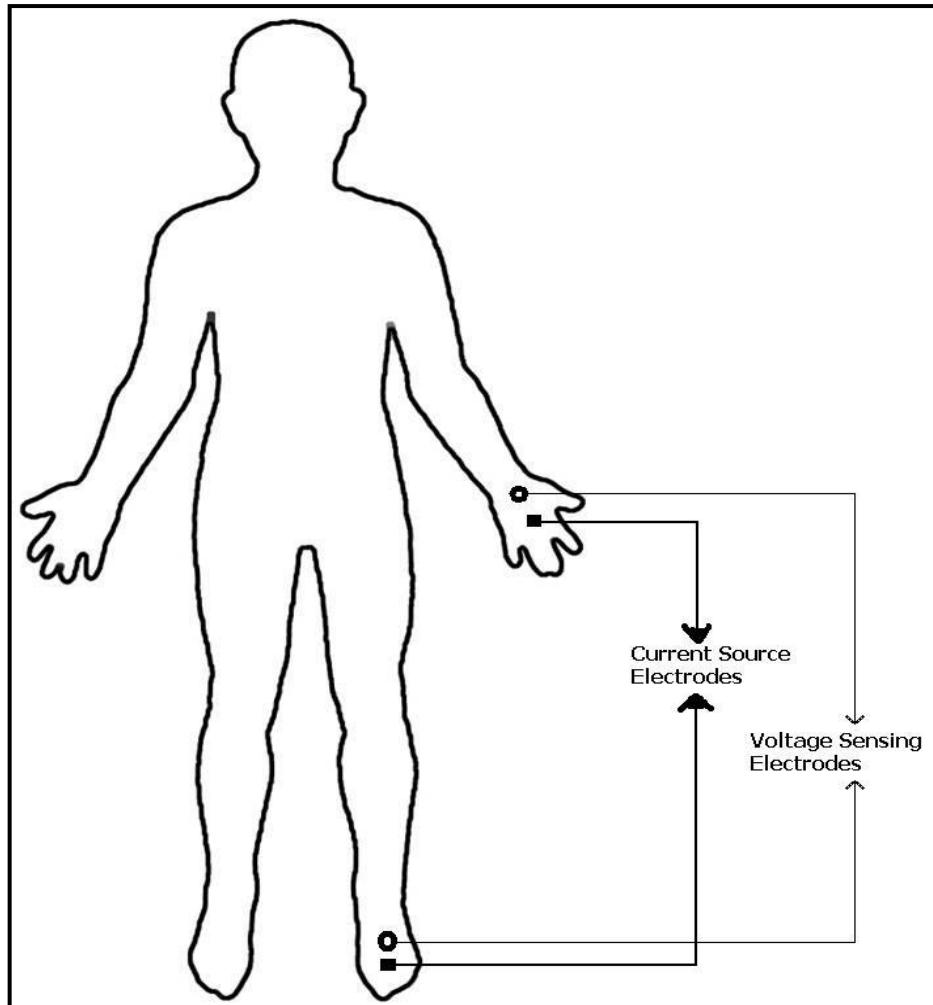


**Figure 1-11: Shows the electrode placement for whole body BIA.**

### **1.6.2 Electrodes and placement:**

Standard Ag:Ag-Cl ECG electrodes were used to deliver the current to the subject and to detect the voltage response. Their use is common practice for the measurement of BIA (Hoffer 1969; Hannan et al. 1998; Organ & Bradham 1994). Figure 1-11 shows the electrode placement adopted for whole-body impedance measurement on the left hand side of the subject (Thomas et al. 1998; Yanovski et al. 1996). The data acquisition card (A/D converter) used to acquire voltage signals was the DAQ6015 by National Instruments Corporation, Austin, Texas, USA. It has 8 analog input channels capable of sampling analog signals at 200 kilo-samples per second (kSa/sec) if a single channel is used (if two channels are used simultaneously the sampling rate is halved to 100 kSa/sec). The voltage sensing electrodes

were connected to an input channel on the DAQ (selectable through Matlab) and the sampled signal was transferred to Matlab for further processing. The data acquisition device acquired the voltage response from the subject which was processed in Matlab to extract impedance. Matlab's data acquisition toolbox running on a Windows XP computer at 2.8 GHz was used to control the data acquisition device. The acquisition time is set to five seconds (at 200 kSa/sec); a random one second sample is extracted from the five second sample, after allowing a one second settling time. The RMS voltage of a single time period from this random (voltage response from the subject) is extracted and then divided by the 800 $\mu$ A constant current to obtain the impedance.

### **1.6.3 Volunteer tests and results:**

The bio-impedance measurement system described above was used to measure the impedance of precision resistor (0.1% tolerance) of 100 $\Omega$  and 250 $\Omega$ , 500 $\Omega$  and 1k $\Omega$ . When measurement error from 10 consecutive impedance measurements (for resistor of each type) was averaged an error of 0.73% was observed. This setup was used to measure whole body impedance from 7 volunteers this yielded a mean and standard deviation of 647.67 $\Omega \pm 128.48\Omega$ . This is in agreement with results presented by others (Organ et al., 1994 and Hoffer, 1969).

## **1.7 Tissue electrical models:**

In order to understand, interpret and study the effects of current flowing through tissues a model which accounts for and closely approximates electrical behaviour of tissues is required. Various electrical models have been proposed to model human tissues. It is not possible to build an exact electrical model of tissues because lumped components (like resistors, capacitors) do not mimic the physical (distributed as opposed to lumped) or chemical properties of biological tissues. In BIA tissue models are necessary to evaluate impedance at infinite and zero frequencies as will be detailed below. If the body is composed

of cells surrounded by extracellular space and enclosing intracellular space, the resistance  $R_e$  of the extracellular space is assumed to be parallel with the series combination of intracellular resistance  $R_i$  and cell membrane capacitive reactance  $X_c$  (Figure 1-12). This is also called the Fricke's model. The resistance and reactance can be measured at a range of frequencies but most single frequency bio-impedance devices use a sinusoidal signal at 50kHz (Kyle, De Lorenzo, et al. 2004). At 50 KHz the current passes through both intra- and extracellular compartments but the extent to which it passes through different tissues is dependent on the type of tissue, especially the size and orientation of the cells, proportions of the intra and extracellular fluids and the amount of lipids (Kushner & Schoeller, 1986). As will be discussed in the next section, it is in our interest to be able to evaluate impedance at zero and infinite frequency since they characterise impedance of extracellular and intracellular components of the tissue under observation. Practically the use of infinite and zero frequencies for bio-impedance measurement is not possible (because relaxation mechanisms in living tissues prevent impedance to reach the real axis), hence we resort to extrapolating the measured impedance to these ideal frequencies. Various models have been proposed to represent body tissue as an equivalent circuit such as the series-model where tissue impedance is represented by a resistor and a capacitor connected in series (Gudivaka 1999). A study of 7 such models in volunteers with normal hydration and induced altered hydration is presented in by Gudivaka (1999). The Fricke model and the Cole-Cole model are presented here as they have been the most widely used (Gudivaka 1999).

### **1.7.1 The Fricke model:**

An important property of body cells is that their walls behave like capacitors to the current flow. The fluids in and around the cells behave as resistors: when this capacitance and resistances are lumped together one can draw a simplified equivalent tissue model circuit (Figure 1-12). Capacitive reactance is inversely proportional to the frequency of measurement and capacitance value as shown in equation (1).

$$X_c = \frac{1}{2 * \pi * f * C} \quad (1)$$

From the circuit one can infer that when a zero or low frequency current is passed for bio-impedance measurement the current primarily flows through the extracellular compartment of tissues ( $R_e$  in model circuit). At infinite or high frequencies, since the reactance of a capacitor is inversely proportional to frequency; the cell walls offer very low or no resistance to the flow of current hence the current flows through both the intracellular and extracellular compartment of tissues (both parallel branches in the circuit, represented as  $R_\infty$  in this discussion). This is also known as the Fricke's model which assumes that cellular impedance is represented by a resistance  $R_i$  in series with cell wall (membrane) capacitance  $C$  both of which are in parallel with resistance of the extracellular component  $R_e$  (Fricke 1925). The equivalent impedance of the whole circuit is described by equation (2).

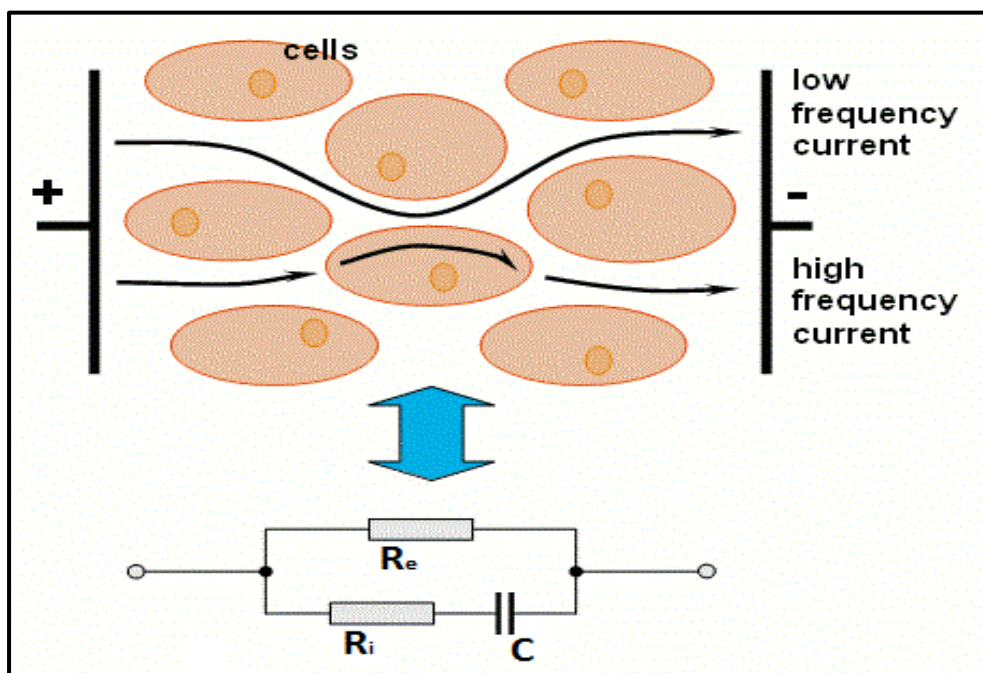


**Figure 1-12: Shows cell walls which act as capacitors to the flow of current. Also shown is the use of a low and high frequency current to bypass the effect of cell wall capacitance. An equivalent circuit deduced from this behaviour is also shown.**

$$Z = \frac{Re(1 + j\omega CRi)}{1 + j\omega C(Re + Ri)} \quad (2)$$

From the above equation if  $Z_i$  and  $Z_r$  are the imaginary (reactance) and real (resistance) part of the complex impedance  $Z$  by elimination of  $\omega$  yields:

$$Z_r^2 + Z_i^2 - Z_r(R_\infty + R_e) = R_\infty(R_\infty - R_e) \quad (3)$$

where  $R_\infty$  is the resistance of the circuit model at infinite frequency (intracellular and extracellular) and  $R_e$  is the resistance of the model at zero frequency (extracellular only). This represents a circle centred on the  $Z_r$  axis with centre at  $Z_r = (R_\infty + R_e)/2$ . Hence  $R_e$  and  $R_\infty$  can be recovered by extrapolation.

### 1.7.2 The Cole-Cole model:

It was noted that this model was valid to represent blood which primarily was composed of erythrocytes (Kanai et al. 1987) and was not valid in the presence of other cell/tissue types. The article went on to state that in the case of mixed cell types the Cole-Cole model was more appropriate (Cole & Cole 1941) where a Gaussian distribution term was included to account for different cell types in parallel. The simplified equation to the Cole-Cole model is

$$Z = R_\infty + \frac{R_e - R_\infty}{1 + (j\omega T_o)^{1-a}} \quad (4)$$

Here  $T_o$  is the average Gaussian distributed time constant (every RC circuit has a time constant) and the value of  $a$  is chosen to give the best fit of experimental data (Jaffrin et al. 1997; Thomas et al. 1998). The Fricke model can be recovered from equation (4) when  $a$  is substituted to zero. Here the locus of impedance measured at different frequencies forms a part semi-circle (Figure 1-13) with the centre below the resistance ( $Z_r$ /real) axis. Here also  $R_e$  and  $R_\infty$  can be recovered by finding the intercepts of impedance locus on the real axis. It is to be noted that when  $a = 0$  the Fricke's model can be obtained.

## 1.8 Body composition estimation: various approaches:

As pointed out earlier body composition estimates made by BIA is deduced from the measured impedance of tissue under observation. Measured impedance is then translated into volumes of one or more body compartments as mentioned in the previous section. There is more than one method to convert impedance to compartment volumes. Three major methods of doing this will be discussed here viz. regression, Cole-Cole analysis and Cole-Hanai mixture theory because these have been discussed extensively in previous studies.

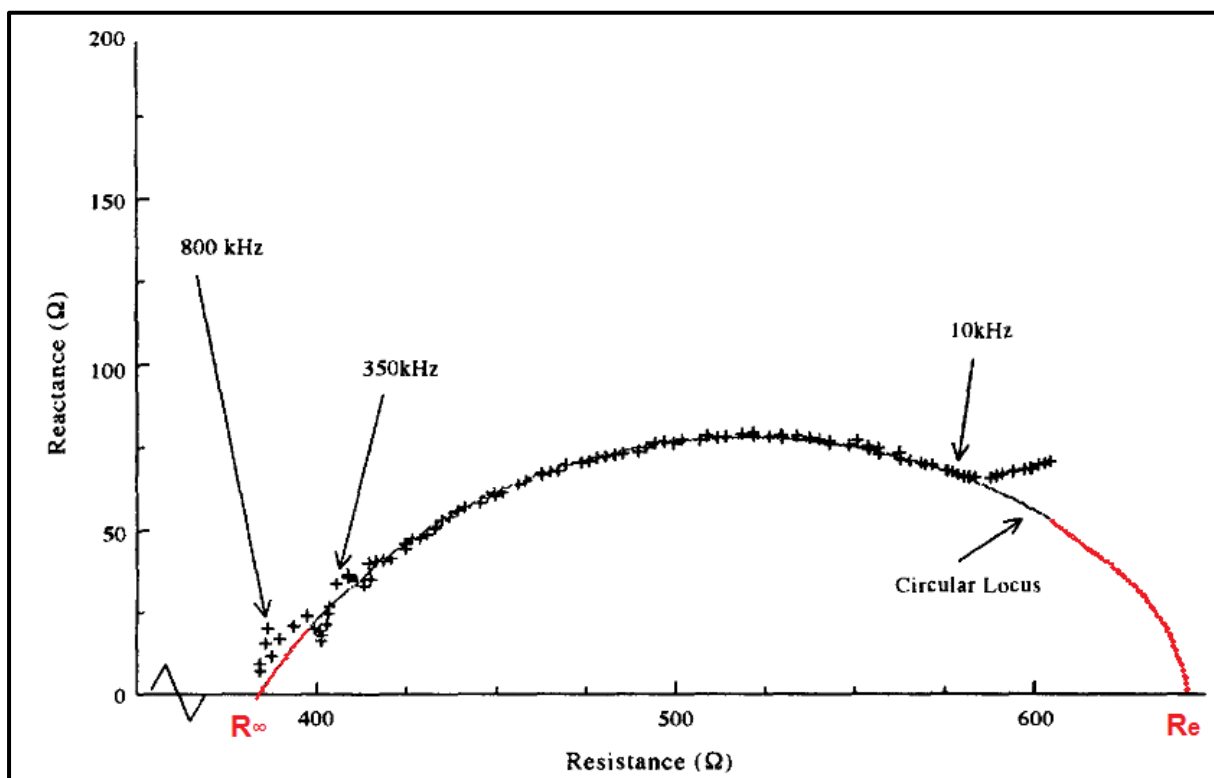


**Figure 1-13: Typical Cole-Cole plot for impedance measured at various frequencies. This also illustrates extrapolation (shown in red) to derive resistance at ideal frequencies. Cole-Cole plot adopted Thomas et al. 1998.**

### 1.8.1 Regression:

An empirical relationship between body impedance and TBW was established by Hoffer in 1969 (Hoffer 1969). Most early BIA estimates were based on such relationships. A brief overview to volume conduction is provided next to understand the underlying ideas.

According to the theory of volume conduction the impedance of a uniform conductor of length  $l$  is,

$$Z = \frac{\rho l}{A} \quad (5)$$

Where  $\rho$  is the resistivity of the conductor and  $A$  is the area of cross section. Multiplying  $l$  on the numerator and denominator we obtain,

$$Z = \frac{\rho l^2}{V} \quad (6)$$

Rearranging we get,

$$V = \frac{\rho l^2}{Z} \quad (7)$$

The human body can be broadly divided into two compartments viz.: FFM, which readily conducts electricity and fat tissue which acts as an insulator. Assuming the human body to be a uniform volume cylindrical conductor composed of these two compartments (Figure 1-14); the majority of current passed will flow through the FFM (due to ions inside water in FFM). Let the length of the conductor be equal to the height ( $H_t$ ) and the resistivity is assumed to be uniform throughout, it has been shown in several studies that  $\frac{H_t^2}{Z}$  (impedance coefficient, which is measured) can closely predict the volume of water in the FFM using regression. Therefore an empirical relationship between the impedance coefficient and TBW can be deduced. A correlation of 0.92 between TBW and impedance coefficient was achieved by Hoffer, (1969).

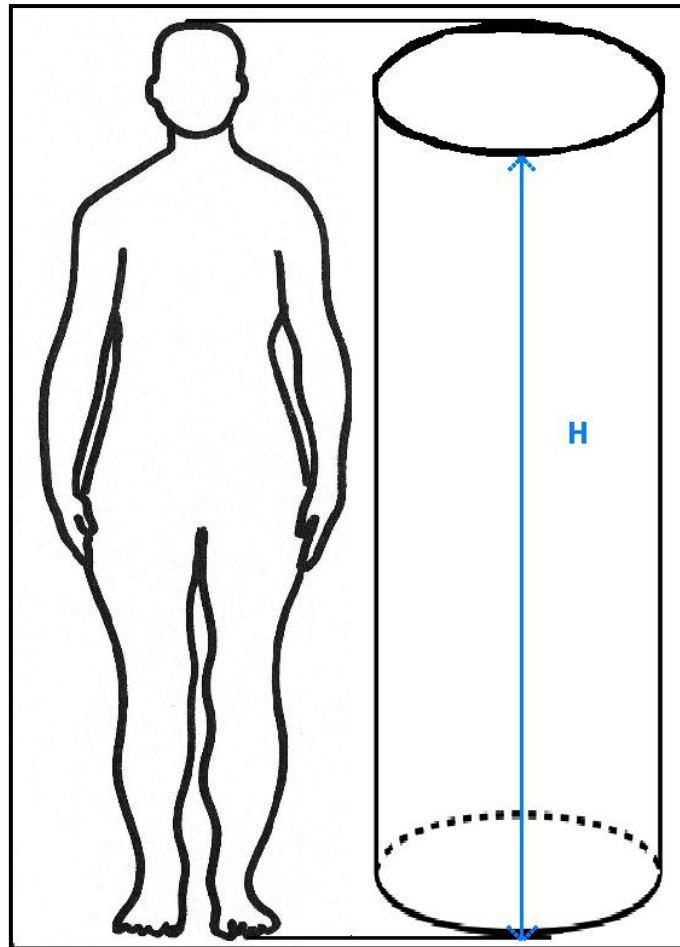


**Figure 1-14: Human body depicted as a cylinder for purposes of the general principles underlying BIA calculations.**

The coefficient of determination reported of 0.95 has been reported by Lukaski, Johnson, Bolonchuk, & Lykken, 1985. Volume estimates of FFM can also be obtained in a similar way. Later studies showed inclusion of more person specific parameters such as gender and weight aided better prediction. An elaborate list of such equations from various studies is provided in Kyle, De Lorenzo, et al. 2004. Since numerous independent studies across the globe have looked at such relationships with a varying number of people and also have followed different protocols the lack of standardisation seems to be a major handicap of BIA.

As mentioned earlier, empirical equations are used to make tissue volume estimates from measured impedance. After the impedance coefficient is obtained it is calibrated against real volume estimates, this is done in large numbers of subjects using standard methods such as

isotopic dilution (for TBW). Statistical regression is used to formulate equations relating impedance coefficient and body compartment volumes like TBW (Baumgartner et al., 1989). The general form of the equation for the case of TBW is,

$$TBW = x \frac{Ht^2}{Z} + z \quad (8)$$

To improve the accuracy of the estimate additional terms such as weight, age, and gender are added as shown in equation (9),

$$TBW = x \frac{Ht^2}{Z} + yWt + z \quad (9)$$

Here an extra weight term is added to improve estimate accuracy and many are guarded to some extent for commercial interests. Equation (9) represents only a basic form of BIA equations. Modern devices use equations which are more complicated than the ones presented here. A large list of equations which can estimate volumes assimilated from different studies can be found in Kyle, De Lorenzo, et al. 2004. Some studies have utilized impedance coefficient and benchmark data on body tissue masses such as muscle mass (Pietrobelli et al. 1998; Nunez et al. 1999) and found strong relationships between the two. The benchmark body composition and tissue mass data is obtained from standard methods notably MRI, CT and DEXA scan.

### **1.8.2 Cole-Cole analysis:**

Another method to predict body compartment volumes from measured impedance is using the Cole-Cole analysis which models tissues as a combination of resistive and reactive components. Two important electrical models used in BIA were introduced previously (section 1.7.2). The following discussion will continue based on these electrical models. The extrapolated values of resistances  $R_e$  and  $R_\infty$  are then used as predictors of ECW and TBW. Alternately the impedance at the characteristic frequency (frequency at which reactance is maximum) has been shown to be a good predictor of TBW (Thomas et al. 1998).

### 1.8.3 Cole-Cole and Hanai's mixture theory:

The body compartment volume of interest can be represented in terms of extrapolated ideal frequency resistances (discussed in previous section) like in equation (10)

$$V_b = \frac{K_b \rho H t^2}{R} \quad (10)$$

Here  $V_b$  is the body volume and  $R$  is the extrapolated resistance at one of the ideal frequencies derived from the Cole-Cole plot.  $K_b$  is the dimensionless shape factor determined from length and perimeter measurements. A value of 4.3 has been reported for  $K_b$  in literature and has been obtained from statistical anatomical measurements (Jaffrin & Morel 2008). Since non-conducting tissues are present in the volume of interest their effect must be accounted for. This is done with Hanai's emulsion or 'mixture' conduction theory which says the apparent resistivity is changed due to the presence of such non-conducting tissues and the value of this apparent resistivity can be obtained from equation (11).

$$\rho_a = \frac{\rho}{(1-c)^{3/2}} \quad (11)$$

This apparent  $\rho_a$  must be substituted in equation (10) to compensate for the increased resistivity. At low frequencies,  $c$  a constant, is derived as  $\left(1 - \frac{V_e}{V_b}\right)$  because only ECW volume  $V_e$  is conducting ( $V_b$  is obtained from the previous equation). After a few manipulations the low frequency volume of ECW is given by equation (12).

$$V_e = k_e \left( \frac{H t^2 W^{1/2}}{R_e} \right)^{2/3} \quad (12)$$

Here  $W$  is the weight of the individual and  $k_e$  takes value of 0.306 as presented by Michel Y. Jaffrin & Morel, (2008). An equation to estimate the volume of ICW is also provided which can be calculated after determining  $V_e$ . A number of variants of these equations from

independent studies can be found in the literature and a comparison of these equations is presented in Jaffrin & Morel 2008.

A recent development in the field has shown that the impedance measured at 50KHz could be directly used to extrapolate impedance at infinite frequency with very little effect on overall prediction (Morel & Jaffrin 2008). This as the title of the paper states has 'bridged' the gap between regression techniques and the ones based for impedance extrapolation.

## **1.9 BIA Variants:**

Increasing interest in bio-impedance has led to its rapid development and variants of the technology have emerged in recent years. In its most basic form this involves using two pairs of surface electrodes (one pair injects current and the other detects the voltage response to this current) between the hand and foot (Figure 1-11). Some devices use other locations such as foot to foot or hand to hand configurations. The frequency of choice is usually 50kHz: theoretically at this frequency the current passes through both the extracellular and intracellular compartments but in practice the impedance at this frequency typically accounts for 75% of extracellular and about 25% of intracellular resistivity (Jaffrin & Morel, 2008). This method estimates TBW and predicts other tissue volumes as explained previously.

### **1.9.1 Multi-frequency BIA:**

Further with the advancement of the field, multi-frequency bio-impedance analysis (MFBIA) came into being. Unlike single frequency BIA (SF-BIA) multi-frequency BIA (MFBIA) measures impedances at different frequencies to evaluate body compartment values. In the case of MFBIA, benchmark body compartment volumes or tissue masses are compared to impedances at different frequencies and the frequency which provided the best prediction (using regression technique) is sought and utilized (Thomas et al. 1998). Usually frequencies between 5 kHz and 200 kHz are used since beyond this range poor reproducibility of impedance is observed. It has been shown that SF-BIA is a better predictor of TBW than

MFBI in critically ill patients but MFBI is more accurate and less biased in the prediction of ECW (Deurenberg et al. 1996).

### **1.9.2 Bio-Impedance spectroscopy (BIS):**

BIS takes a different approach to evaluation of body compartments, it uses mathematical models and/or Hanai's mixing theory to directly predict compartment volumes (Jaffrin & Morel, 2008). The impedances at zero and infinite frequencies are predicted from measured impedance using a Cole-Cole plot. Predictions are made using empirically derived equations from these values or Hanai's mixing theory described earlier. The equations are found to be a good predictor of ECW but the validity of this model to predict ICW is questionable (Ellis & Wong 1998). This can be attributed to the cumulative error inherited by  $R_i$  (Figure 1-12) when derived from  $R_e$  and  $R_\infty$  which have their own prediction errors. It also depends on the validity of the electrical model used for analysis. This method needs refinement since the modelling techniques are complicated and not accurate, but with further improvement this method has scope to be a promising approach to BIA.

### **1.9.3 Segmental BIA (SBIA):**

This method is based on making composition estimates of the different segments of the body. The impedance of different segments is measured separately and the composition estimate of each segment is made independently. Usually the body is divided into five segments, the four limbs and the trunk (Figure 1-15) (Organ & Bradham 1994; Bedogni et al. 2002). For a whole-body impedance measurement, say a value  $500\Omega$  was observed; typically the contribution of the arm, trunk and leg would be around  $230\Omega$ ,  $70\Omega$  and  $200\Omega$ . If we look at inverse proportionality in equations (8) and (12), a much larger change in trunk water volume (which contributes to only 14% of whole body impedance) is required to register a 10% change in whole body impedance as compared to arm water volume (which contributes to 46% of whole body impedance). The advantage of this technique over whole body measurements is that the usual bias in the impedance measurements due to variations

in area of cross sections along the current path is reduced (refer (5), low area of cross-section increases impedance). This reduces the overall bias in compartment volume estimates. Segmental impedance measurements are mostly performed using 8 electrodes (2 on each limb). Figure 1-15 shows the eight (E1 through E8) electrodes in contact with the subject for measuring impedance of five different segments: this will be the electrode configuration for SBIA used throughout this manuscript. Composition estimates of each segment are made using regression or Cole-Cole methods in the same way as traditional BIA except that the equations are adjusted for each segment.

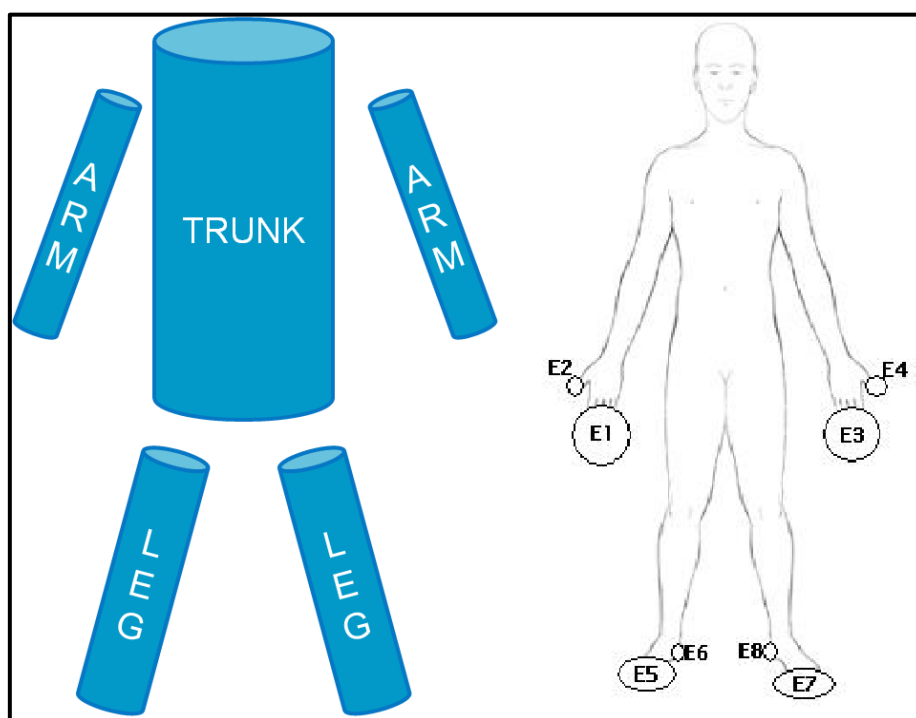


**Figure 1-15: Shows the segmentation into 5 segments viz. four limbs and trunk (left) and placement of electrodes to measure impedance for SBIA procedure.**

### **1.10 BIA errors and body composition estimation variability:**

The errors in estimates of body volumes by BIA can be mainly attributed to impedance measurement error and estimation error. Body composition estimates could become erroneous if the perceived impedance is different from the actual impedance. This could

occur due to a number of reasons for example poor connection of electrodes, measurement equipment malfunction and altered hydration during measurement or due to health condition. Measurement errors can be effectively minimized with the use of a standard calibrated measurement system and following a proven measurement protocol such as the one provided here (Gonzalez et al. 2002). Estimation errors on the other hand can be attributed to prediction equations which are inherently compromised due to the assumptions made to obtain the empirical relationships that BIA is based on. Various studies have used BIA to monitor hydration and body composition in states of good health and disease, in different age groups and ethnic populations. A number of factors can alter body impedance measurements which will inevitably affect composition estimates. It is relevant to review the major factors which influence BIA measurements. Since most BIA estimates take into account the subject's height and weight these are to be accurately determined at the time of measurement. Dietary intake, measurement position and recent exercise are reported to influence body impedance measurements. Body impedance measurements after food intake is reported to reduce by 4-15 $\Omega$ . Errors of one to one and a half litres in TBW have been reported when subjects were lying down for several hours before measurements, while equations derived from upright subjects were used (Kyle, Bosaeus, et al. 2004). Some studies have also observed that equations derived by observing subjects of a particular ethnic group may be prone to bias when used with subjects from different ethnic backgrounds; this could be partly due to difference in limb lengths between ethnicities. BIA equations derived from a specific group of young and healthy individuals may be biased when used with elderly and obese populations mainly due to change in hydration levels and variation of cross-sectional areas of limbs. The distribution of water between ECW and ICW has also been noted to vary with age, gender and pregnancy. BIA equations derived from healthy volunteers cannot be effectively used for subjects with specific disease conditions which severely effect body composition such as malnutrition, anorexia and post-traumatic paraplegia. Hence the variation of body impedance and body composition is largely altered by subject specific factors, health conditions and the population under study (Kyle, Bosaeus,

et al. 2004). Current BIA equations and methods are probably not suitable for such a large variety of situations and care has to be taken when using equations from a specific cohort on a different set of individuals.

### **1.11 Patient and volunteer trials:**

In order to test the SBIA system developed, as described in this thesis, studies were undertaken on healthy human subjects. But it was necessary that the study was compliant with the declaration of Helsinki introduced at the 18th World Medical Assembly, Helsinki, Finland in 1964 which was subsequently updated several times with the last update published in 2008 (Slavicek & Forsdahl 2009). The principles of this declaration require that bio-medical research must conform to accepted scientific standards and should be based on thorough knowledge of scientific literature and fully informed consent of the subject. Every experimental procedure in the study must be laid down in the study protocol and later be reviewed by an independent unbiased review (ethics) committee. The study must be conducted by scientifically qualified persons under the supervision of a qualified medical practitioner. The object of the study must in be in proportion to the risk to the subject, with appropriate assessment of the risks involved. Informed consent must be given by the subject, wherein the subject is sufficiently aware of the aims, methods, anticipated benefit and potential hazards or discomfort that the study may entail. In this respect the declaration notes that research on human subjects in the interest of science and society should never take precedence over the well-being of the subject.

The present studies involved testing a newly developed SBIA device on human subjects and obtain their body composition using a DEXA scan. The use of bio-impedance is non-invasive and has no reported adverse effects; however its use still needed to be approved by relevant ethics committees. A DEXA scan on the other hand utilizes low energy X-rays which is classified as ionising radiation and its use on human subjects for scientific research required detailed permission. To achieve this, an amendment to a previously obtained NHS ethical

approval was sought. The original approval allowed the use of BIA devices on patients, collection of blood samples and acquisition of morphological measurements. The proposed amendment sought approval for the use of DEXA scans on volunteers as well as patients. These should reflect in the associated documents namely; study protocol, patient invitation letter, patient information sheet and patient consent form (ethics documents included in Appendix 1).

Within the U.K, NHS research ethics governance is a complex structure of interlinked bodies under the Research Governance Framework (IRAS U.K). Any study involving Clinical Trial of Investigational Medicinal Product (CTIMP) has to filter through a stricter regime of rules and formalities as compared to non-CTIMPs. Since our study did not involve testing a medicinal product it was classified as a non-CTIMP. The main criteria to be observed to conduct the study were:

- Obtain a favourable ethical opinion from a regional NHS research ethics committee (REC).
- Obtain approval from the R&D at the host NHS site and host university.
- Have a clear audit trail and comply with Good Clinical Practice guidelines.
- The study must also identify a sponsor and be adequately funded.

Hence for the study to be carried forward a favourable opinion to the proposed ethical amendment was attained which consequently received acceptance by the host R&D which in this case was the Heart of England Foundation Trust (HEFT), Birmingham. Apart from HEFT initial evaluation of the device was to be performed at Aston University by calibrating the designed device against a commercially available bio-impedance device. This part of the study had to be approved by local ethics committees at Aston University. To undertake the study at HEFT an initial amendment application was made in October 2010 which enabled collection of DEXA scan information from patients due to undergo DEXA scan as part of their

clinical care. Since a DEXA scan is normally used for bone densitometry an additional ethics amendment application was necessary to obtain body composition information from DEXA scans because body composition from DEXA required a separate scan which would expose the volunteers to additional ionising X-Rays. This application was submitted in June 2012 and since the R&D at HEFT required more information regarding DEXA scans in the volunteer information sheet a third application was presented in August 2012.

All three ethical amendment applications secured favourable opinion from the Coventry and Warwickshire REC (REC reference 08/H1210/17 AM03) and the relevant documents which include a revised study protocol, updated volunteer invitation letter, information sheet and consent form are presented in Appendix 1. This thesis will discuss the development of four versions of a bio-impedance measurement system. The first version (V1) has been discussed in section 1.6. The following sections will discuss the development and testing of subsequent three versions of bio-impedance measurement systems viz. V2, V3, V4. All versions except V3 (which was a proof of concept) were tried on human subjects. Table 1-6 lists the number of volunteers who participated in different studies carried out during this project. Also listed are the types of studies each set of volunteers participated in. In the study type column T-BC stands for body composition obtained from the Tanita BC-545, BC-DXA stands for body composition obtained from DEXA scans, BV stands for body limb volume obtained using the KinFu algorithm and BI-Vx stands for bio-impedance measured using a particular version of the BIA device, for example BI-V2 stands for bio-impedance measured using version 2 (V2) of the device.

<b>Number of subjects</b>	<b>Study type</b>	<b>Age range in years</b>	<b>Gender division</b>	<b>Description</b>	<b>Ethics reference number</b>	<b>Outcome</b>
7	BI-V1	23 - 29	3F, 4M	06/2010, done to evaluate bio-impedance measurement feasibility	08/H1210/17	Established feasibility of bio-impedance measurements.
14	BI-V2, T-BC	20 - 26	9F, 5M	06/2011, done to compare segmental bio-impedance with Tanita BC-545 body composition estimates	08/H1210/17	Established relationships between bio-impedance from V2 and T-BC.
81	T-BC	22 - 73	48F, 33M	Data collected before current project commenced	08/H1210/17	Developed neural network models.
22	BI-V4, BC-DXA, T-BC	24 - 64	18F, 6M	08/2013, done to evaluate relationships between segmental bio-impedance and actual body composition.	08/H1210/17 AM03	Developed models to predict body composition from bio-impedance.
9	BV, T-BC	24 - 34	4F, 5M	08/2013, done to evaluate relationship between limb volume and bio-impedance.	08/H1210/17 AM03	Established relationship between body volume and bio-impedance.

Table 1-6: Lists the data collected from human volunteers for this project along with the type of study the volunteers participated in.

## 1.12 Electrical safety:

Safety of the subjects is of prime importance in the design and development of any medical device. The three bio-impedance devices tried on human subjects utilize an alternating sinusoidal current to evaluate the impedance of the body (segments). The frequency range of the current utilized to evaluate impedance was between 10 kHz and 100 kHz. Additionally the device was designed to deliver a maximum current of 800 $\mu$ A (in V1, V2 and 250 $\mu$ A in V4). The safety of 800 $\mu$ A for impedance evaluation can be verified with reference to BS EN 60601, IEC 60479-1 and Dalziel & Lee 1968. The 60601 sets a limit to the AC current through the subject at 100 $\mu$ A for frequencies below 1 kHz. This limit is to be compensated by a tenth for every decade (logarithmic) increase in frequency. Therefore the 800 $\mu$ A current compensated at 10 kHz is 80 $\mu$ A and 8 $\mu$ A at 100 kHz. These values are well below 100 $\mu$ A limit set by the 60601. Additionally Dalziel & Lee 1968 present a graph where an RMS current of 5mA is deemed safe at 10kHz. It is also observed that the allowable current rises with increasing frequency of the current suggesting that the highest current (800 $\mu$ A) chosen is safe at frequencies well below and beyond 10 kHz. This is related to the exponential decrease in body impedance with increasing frequency of current as reported in IEC 60479-1, where body impedance at 2 kHz is reported to be around 750 $\Omega$ , this at 800 $\mu$ A would mean a power dissipation of 0.5mW across the current flow path. The current flow path in the all bio-impedance devices constructed during this project (V1 to V4) is from the hand to the foot on each side of the subject. The IEC 60479-2 notes that the impedance of the skin (which forms a significant part of total body impedance) can be considered to be inversely proportional to the input frequency in the order of tens of volts, i.e., skin impedance at 60 Hz is ten times its value at 600 Hz. This holds particularly true at higher frequencies and along with cell membrane bypass phenomenon explained in 1.3.1.2, causes the decrease in body impedance with increasing frequency. Also according to IEC60479-2 the threshold of perception at frequencies between 10 kHz to 100 kHz rises from 10mA to 100mA, the

highest current used during this project is 800 $\mu$ A which is less than a tenth of the threshold of perception at 10 kHz. Hence it can be concluded that the current used to evaluate bio-impedance during this project is safe and non-invasive.

For the constructed devices the subject is at a risk of electric hazard from other parts of the device as well, this includes accidental contact with exposed live parts/metal surfaces. Therefore the safety of the devices during normal operation and fault conditions is to be evaluated. The BS EN 60601 sets out guidelines for medical electric equipment and its key concept is the safety of the subject under single-fault conditions, which specifies that the subject is safe if any one component of the system fails. The limits stipulated by this standard to various aspects of medical devices reduce the risk of a hazard to acceptable levels. Before the compatibility of the constructed devices to BS EN 60601 the physiological effects of electricity on the human body is to be studied.

### **1.12.1 Physiological effects of electricity:**

The flow of electricity through the human body can be classified into two shock types viz. microshock and macroshock. Figure 1-16 shows the two scenarios, a macroshock is when the current enters and exits the body through the skin and the current path is not directly through an organ (the heart is the organ most susceptible to failure due to an electric current). A microshock occurs when the current passes directly through the organ of interest. The occurrence of microshock is highly unlikely in bio-impedance devices constructed during this current study, since the chances of a direct connection close to the heart when the subjects are fully clothed is very low in controlled laboratory conditions. Also microshock condition occurs when the contact electrode surface is small leading to area of large current density around a body organ such as the heart (Grimnes & Martinsen 2014). The electrodes used for bio-impedance measurement in this project have a large contact area which in all versions is greater than 2cm<sup>2</sup> and have no direct contact with the chest area (close to the heart). In macroshock conditions the current is essentially spread out uniformly through the

region of interest (Grimnes & Martinsen 2014). The primary risk of exposing the human body to macroshocks beyond acceptable limits is the risk of fibrillation due to neuromuscular stimulation; this will be discussed in the following section.

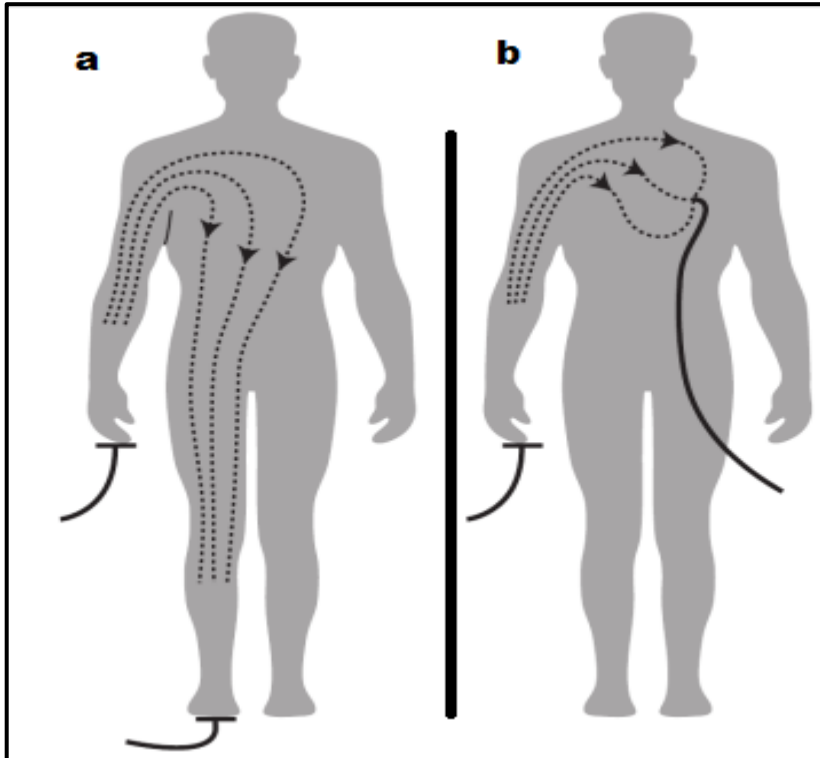


**Figure 1-16: Shows the macroshock condition (subfigure a) and the microshock (subfigure b). Adopted from Grimnes & Martinsen 2014.**

### **1.12.2 Neuromuscular stimulation and fibrillation:**

An alternating current can stimulate muscles and nerves directly. Motor-nerve stimulation can also cause involuntary muscular activity. The neural membrane potential is about 70mV, which, if reduced for a duration greater than 20 $\mu$ s can lead to the propagation of a nerve action potential. A similar stimulus could be delivered to muscles as well, both resulting in muscular contraction. A high degree of risk is associated with cardiac muscle stimulation at frequencies below 1 kHz. The internationally accepted allowable current through the heart is 10 $\mu$ A, current beyond this safe limit can disrupt its coordinated pumping and if the current is large, the disruption can prevail after the current has been removed (IPEM, Report 90,

2004). This uncoordinated contraction is known as fibrillation. The heart is most susceptible to fibrillation at power generation and distribution frequencies of 50-60Hz. Increasing the frequency reduces the sensitivity to stimulation since only lesser time is available in each half cycle of the current, to change the voltage across the membrane capacitance, which is required for an action potential.

### **1.12.3 Physiological effects of electricity:**

In macroschock conditions, on average, a 70kg human starts to perceive current through his body at about 1mA (at 50/60 Hz). The let-go current (maximum current allowing voluntary release) is about 6mA. At 22mA one starts to experience respiratory paralysis. Between 75-400mA fibrillation occurs. From 6A and above tissue damage and tissue burns are observed (IPEM, Report 90, 2004).

### **1.12.4 BS EN 60601 and device versions 1, 2 and 4:**

The 60601 stipulates limits on the amount of current that can flow through the subject and in this section the compatibility of devices constructed with these limits will be established. For the appropriate safety tests to be applied on the constructed devices the device is to be classified firstly based on the type of protection against electric shock (the CLASS of the device). Secondly, based on the degree of protection against electric shock, the TYPE of the device is to be determined (BS EN 60601-1, 3<sup>rd</sup> edition). This applies to devices which come into direct contact with the subject to perform its function (referred to as APPLIED PART in 60601). A third criterion of classification would categorize the device based on its protection against the ingress of water, but since the patients are dealt with in controlled laboratory environments the risk due to water spillage and subsequent risk is low. In order to classify the devices the structure of the device shall be studied first. Figure 1-17 presents the generic structure of the BIA devices, it has two major parts the device itself and the data acquisition card (V1 had an additional function generator). According to the 60601 a non-medical device(s) (data acquisition card in our case) may be present in the patient environment but in

itself should not have an applied part. The medical device must be inserted between the patient and the non-medical device(s).

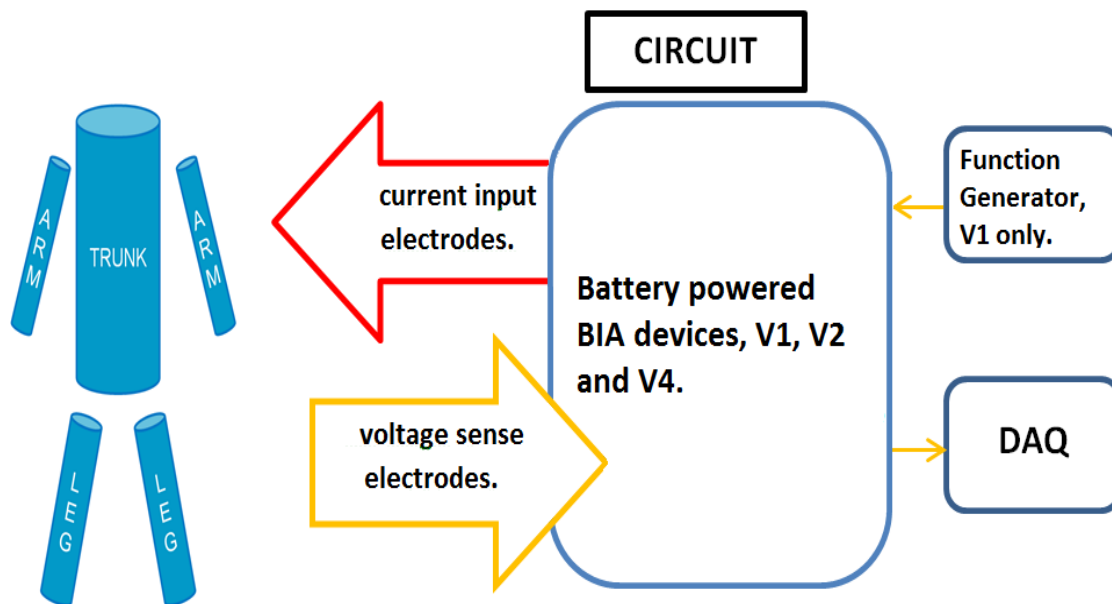


**Figure 1-17: Shows the generic structure of the BIA devices used to collect data from subjects. Please note that only the BIA devices in direct contact with the subject. The function generator (V1 only) and the data acquisition card are IEC 61010 compatible.**

This is acceptable when the leakage current of the non-medical device(s) is lower than  $500\mu\text{A}$ . The BIA device itself is battery powered and is connected to a data acquisition card. The power supply to the data acquisition card is a double insulated external unit which would put the current device into the CLASS II category, in accordance to the 60601 (please refer to datasheet in Appendix 2). The data acquisition cards and function generator used during this project were compatible with the IEC 61010 (international standard for laboratory equipment) which stipulates that the leakage current remain well within  $500\mu\text{A}$ . The IEC 61010 also stipulates the inclusion of current and voltage limiting hardware within the device along with double insulation (between hazardous part and user accessible parts) and automatic disconnection of supply when current/voltage limits are exceeded. Hence their use around the patient can be considered safe; additionally it was ensured that the patient would not

come into direct contact with the non-medical equipment and RCDs (residual-current device) were inserted between the non-medical devices and the mains socket for added safety. The BIA device has 8 applied parts (8 electrodes in V2 and V4 and 4 electrodes in V1). Now since the device is battery powered and has its separate ground its degree of protection against electric shock will be classified as type B according to the 60601. The risk from incorrect battery connection to the device can be considered to remain low since, a strict protocol was followed before the applied parts were connected to the subject. This included, checking battery voltage polarity on the device(s) and testing the output current of the device(s) before the electrodes were connected to the subject.

As mentioned earlier the 60601 has set limits to the amount of current that can flow through the subject when the device is in use. To comply with the 60601 the following currents are to be evaluated:

- **Earth leakage current:** this is the current flowing from the protective earth pin of the non-medical device (data acquisition device in V2 & V4; data acquisition device and function generator in V1).
- **Enclosure leakage current:** this is the current flowing to the earth through a person by touching the medical device or a part of it. The risk that is presented by enclosure leakage is low because the devices do not have an exposed conductive surface (except the electrodes which would be considered as an applied part and their risk will be dealt with separately) and the bio-impedance measurements are carried out under controlled laboratory conditions.
- **Patient leakage current:** this is the current flowing through a person to earth from an applied part. The patient leakage current is the most important leakage current measurement in a medical device since the applied part is readily and in direct contact with the subject.

- **Patient auxiliary current:** is the current that flows between applied parts in normal and fault conditions. These measurements are made between an applied part and all other applied parts connected together.

**Table 1-7: Shows the upper limits of allowable leakage and auxiliary currents through a subject in normal and single fault conditions for both AC and DC currents. All values are reported in microamps.**

Type B device		
Currents	Normal condition	Single fault condition
Earth Leakage	5000	10000
Patient leakage(DC)	10	50
Patient leakage(AC)	100	500
Patient auxiliary(DC)	10	50
Patient auxiliary(AC)	100	500

These current have to be evaluated in normal operating conditions and single fault conditions. Table 1-7 lists the allowable patient leakage and auxiliary current set out by the 60601 during normal and fault conditions for type B device. These currents are to be evaluated using a human body model presented in the 60601; this has been reproduced in Figure 1-18. This model takes into account the human body and its risk of fibrillation and is a cumulative result of various studies performed in the field.

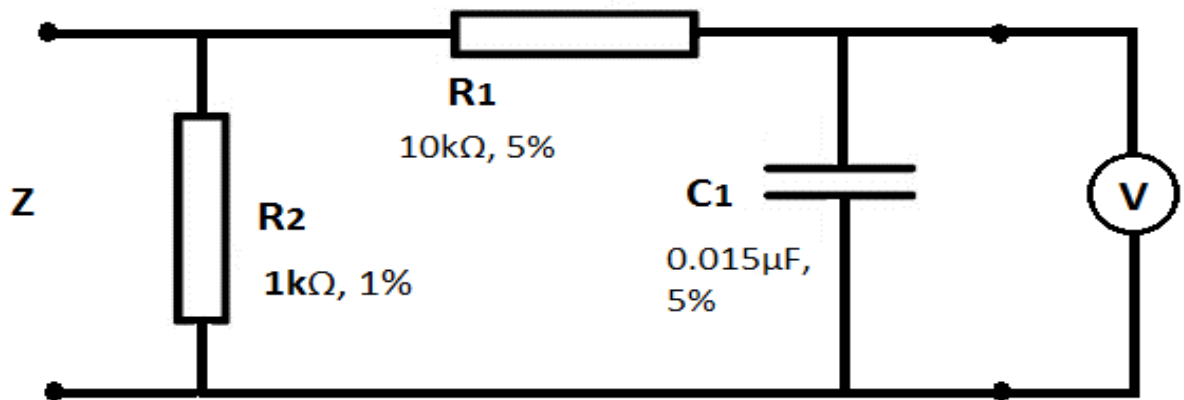


**Figure 1-18: Shows the human body circuit model used for BS EN 60601 leakage and auxiliary current tests. The values of the components and their tolerances are shown next to their symbol. V is a true RMS voltage measurement unit.**

**1.12.4.1 Device current safety tests:**

The following tests are to be performed to ensure that the device(s) is compliant with the 60601. The tests relevant for a CLASS II type B device according to the 60601 are earth leakage in normal and supply open (single fault) condition, patient leakage in normal and supply open (single fault) condition and patient auxiliary current in normal and supply open (single fault) condition (the safety of 800μA auxiliary current in normal condition has been established). Since the auxiliary currents are to be measured with all combinations of applied parts connected together only the highest value observed has been reported to keep the results concise. The AC and DC values of these currents flowing through the body model (Figure 1-18) is to be measured, therefore 10 current measurements are required for each device version. Figure 1-19 shows the earth leakage current measurement setup. MD in Figure 1-19 represents the human body model shown in Figure 1-18. In order to measure the earth leakage current in normal conditions the current through MD is measured with S1 closed and S5 both in normal and reversed connection (simulates reversed supply condition which is considered as normal operating condition in 60601). To simulate a single fault

condition S1 is opened and the current through MD is measured with S5 in both normal and reversed condition. Similar circuit configurations were developed to quantify the various currents flowing through the human body model in normal and single fault conditions for devices V1, V2 and V4.

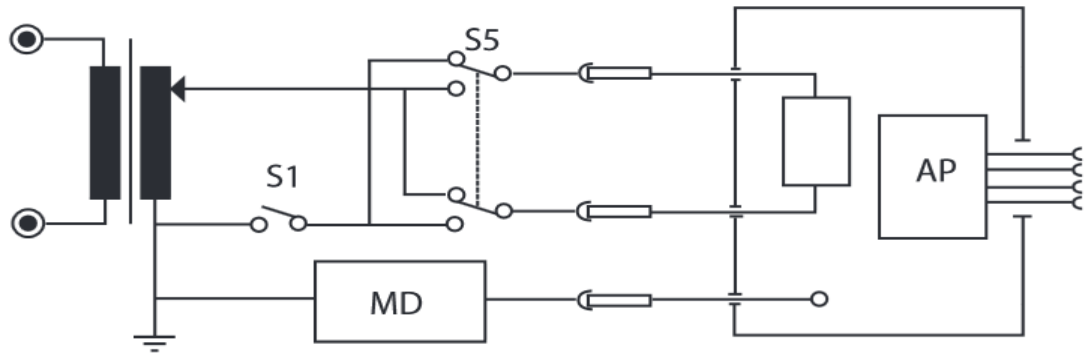


**Figure 1-19: Shows the simplified version of leakage current test measurement setup proposed in BS EN 60601. S5 toggles the device between normal operating condition and single fault (reversed supply) condition. S1 simulates the open earth SFC. MD represents human body model shown in Figure 1-18. Adopted from BS EN 60601.**

**Table 1-8: Shows the auxiliary and leakage currents measured in V1 using SPICE simulations. The values are lower than upper limits for these currents set by BS EN 60601. Values reported in microamps**

BIA device version 1 (V1)		
Currents	Normal condition	Single fault condition
Earth Leakage	73	117
Patient leakage(DC)	<1	36
Patient leakage(AC)	<1	<1
Patient auxiliary(DC)	<1	7
Patient auxiliary(AC)	80 (compensated)	80(compensated)

BS EN 60601 Annexe E presents an exhaustive list of the circuit configurations that could be used to evaluate auxiliary and leakage currents. With V1 of the device, due to unavailability at the time of testing, SPICE simulations were utilized to make the estimates of the leakage and auxiliary currents. Table 1-8 lists the leakage and auxiliary currents measured in device V1 using SPICE simulations. As can be seen the values reported are much lower than the stipulated limits by the 60601 shown in Table 1-7. From this, along with controlled laboratory conditions under which the subject bio-impedance was measured, it can be concluded that the risk with using device V1 is under control. Similar tabulated values for V2 and V4 will be presented after their description.

## **Chapter 2    Essential theory**

### **2.1 Introduction:**

The objective of this chapter is to introduce uncommon concepts which have been used in this project. This will be useful when understanding certain methods used later on in this thesis. Firstly signal analysis techniques will be described followed by sections on statistical analysis, neural-networks and finally the Kinect Fusion (KinFu) method for 3D scanning will be introduced.

### **2.2 Signal analysis:**

Since this project deals with aspects of digital signal processing (DSP) particularly low pass filtering and low pass filter (LPF) design using Matlab, an introduction to these concepts relevant to this project is included here. The underlying concepts of DSP is considered elsewhere (Oppenheim 1975), and a formal understanding of DSP is assumed. We will also briefly consider Fast Fourier transform and its applications in the current project. The moving average filtering technique particularly the Savitzky-Golay smoothing filter used in this study to extract heart-rate from bio-electrical impedance signals will be presented. To help better understand ideas in the context of the present work, examples from the present study will be used throughout this section to examine the application of DSP. Before we explore DSP further an introduction to Matlab is provided since it has been widely used in this project, mainly for the purposes of device control (present device), analysing the acquired signals to evaluate impedance and to store the acquired signals for further analysis. Matlab (Matrix Laboratory) is widely used for numerical computing in science and industry. Matlab enables matrix manipulations, plotting data and implementing algorithms. It also provides a plethora of built-in functions and algorithms for data analysis and manipulation. Matlab itself is a programming language; it can be readily interfaced with programs written in other

programming languages notably C, C++, Java and FORTRAN, but has been utilized directly in the present study. Matlab is packaged with various 'toolboxes' which enable the user to build applications for specific purposes and provide an interface with external hardware. Specific to this study functions from the signal processing toolbox have been utilized to process the acquired body impedance signals, and the data acquisition toolbox has been used to control the signal acquisition device and acquire signals from the same.

### 2.2.1 Signal sampling and anti-aliasing filters:

The Nyquist sampling theorem states that an analog signal can be effectively reproduced if it is sampled at a rate two times the highest frequency component of the signal being sampled. In practice usually for good reconstruction of the sampled signal the sampling frequency is often 4 to 8 times the highest frequency component. Sampling at such high sampling gives rise to the problem of aliasing. Consider Figure 2-1 where the original signal (in black)

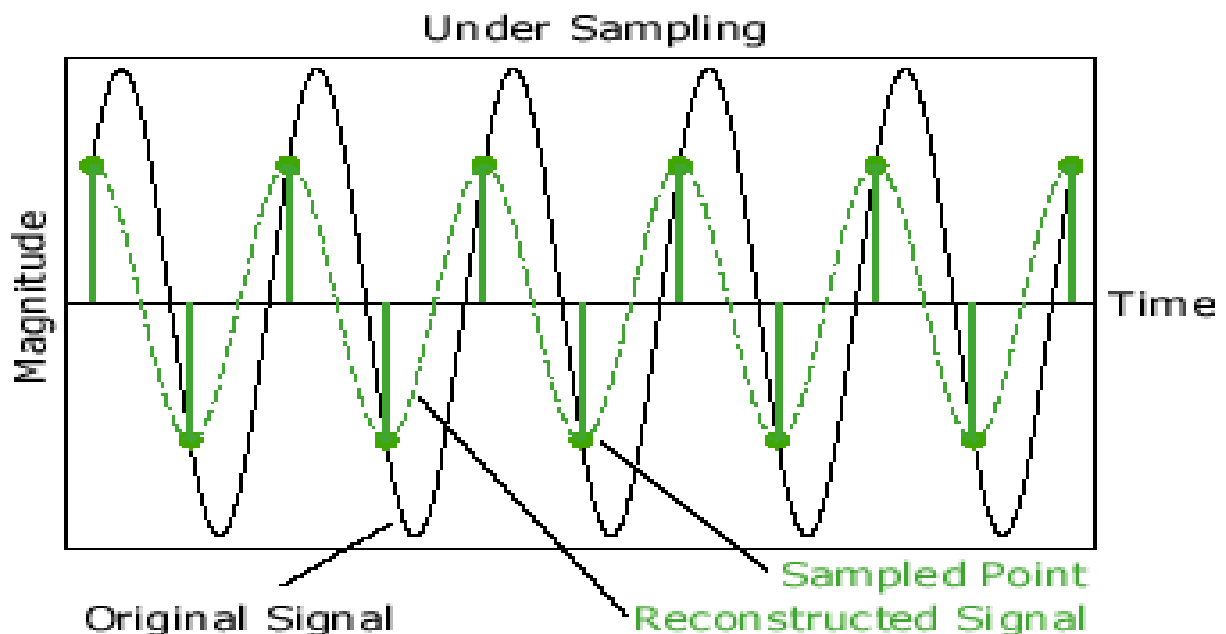


**Figure 2-1: Shows a sinusoid, in black and its reconstruction, in green. The reconstructed signal is obtained from samples of the original signal sampled at a rate lower than the Nyquist sampling rate.**

is under sampled (less than Nyquist rate), this results in the sample points shown in green. When reconstructed, as shown by sinusoid in green, one can see that the reproduced signal (in green) is lower in amplitude than the original signal and hence is not a good representation of the original signal.

Now consider a similar (but alternate) case where a signal is being sampled at a rate much higher than the Nyquist frequency but the signal is corrupted with noise whose frequency is higher than half the sampling frequency. This noise will be under sampled (as explained above) and added to the samples of the desired signal and corrupt the samples of the desired signal permanently. Therefore it is important in data acquisition systems that the signal being sampled is band limited to half the sampling frequency. This is achieved with the use of anti-aliasing filters. Anti-aliasing filters are low pass filters which limit the bandwidth of the sampled signal to one half of the sampling frequency, therefore negating the problems which may arise due to aliasing.

The three versions of the device presented in the following chapters use the Agilent U2531A data acquisition card to record signals. The device is capable of sampling at 2MSa/s across its four analog input channels. The device is internally band limited to 400kHz (datasheet page 5, Appendix 1). So if the signals are sampled at sampling rate higher than 800kSa/s (as was the case throughout the rest of this thesis) the problems that could arise due to aliasing were avoided.

### **2.2.2 Fundamentals of FFT based signal analysis:**

FFT, standing for Fast Fourier Transform is the name given to algorithms which rapidly perform Discrete Fourier Transform (DFT). DFT is performed over discrete time domain signals in the present project. The concepts behind Fourier transform and DFT can be found in Oppenheim, (1975). Computing DFT from its original definition is often too slow for practical uses hence it is appropriate to resort to FFT algorithms since they are computationally efficient. The most commonly used FFT algorithm is known as the Cooley-

Tukey algorithm which recursively divides the DFT of size  $N$  into many smaller DFT's of sizes  $N_1$ ,  $N_2$  etc. essentially implementing the divide and rule policy to simplify the problem (Cooley & Tukey 1965).

The power spectrum obtained from a FFT returns an array that contains a two sided spectrum centred on the maximum frequency. Within Matlab FFT is performed using the 'fft' function which takes in a discrete time-domain signal and outputs an array with the values of its sinusoidal components at different frequencies ( Figure 2-2, an illustration to visualise Fourier transform). The values of the peaks at different frequencies are proportional to the square of the amplitude of each frequency component making the time domain signal (MathWorks 2002). Figure 2-3 shows the two sided FFT spectrum with the positive and negative frequencies. Note that the positive and negative frequency peaks that occur at a height of  $A_k^2/4$  are mirror images of each other. Generally only one side of this two sided spectrum is required for analysis (shown in Figure 2-4). However the power is spread equally among the two halves. Therefore while displaying the positive half of interest all the values in the positive half of the array are to be multiplied by two except the zero frequency (DC) component which occurs only once. Hence while displaying the single-sided spectrum, the non-DC values in the spectrum the values are to be multiplied by two making the frequency peak height to be  $A_k^2/2$  which is the square of the root mean squared (RMS) value of frequency component  $K$ . This is a valuable conversion because the magnitude of AC voltage or current is usually represented in RMS units (Oppenheim 1975). The frequency range and resolution depend (Figure 2-3 and Figure 2-4) on the sampling rate and duration of acquisition. If  $N$  number of samples is acquired within a specific time duration, the single sided FFT spectrum would contain  $N/2$  points (Oppenheim 1975). But in the present case the length of the sampled signal is padded (with zeroes) to the nearest power of 2 because the Cooley-Tukey algorithm is much more efficient when the length of signal is a power of 2 (typically for this project signals are sampled for 2 seconds at 2000kSa/sec, hence the length of the signals is 4000kSa and the nearest power of 2 for this is 4194304).

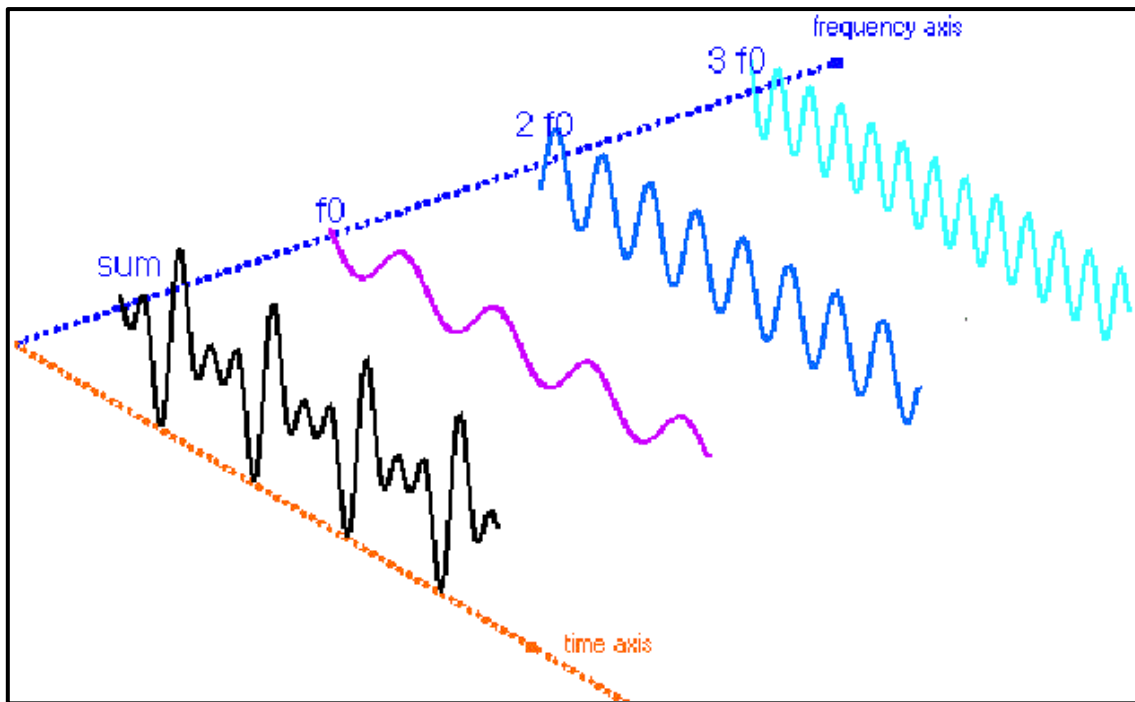


**Figure 2-2: Shows a sum of three sinusoids of different frequencies in the time domain and their respective contributions in the frequency domain, adopted from the National Instruments website ([www.uk.ni.com](http://www.uk.ni.com)).**

Also, FFT operation returns spectral values in complex form ( $X + iY$ ), and this needs to be converted to polar form to obtain magnitude and phase. The 'abs()' function in Matlab enables us to perform this wherein the function takes in any complex form and returns it in polar form (MathWorks 2002). Since magnitude of a peak in the single-sided FFT spectrum represents its RMS amplitude in the time domain FFT was utilized to extract the voltage and current peaks from bio-electrical signals to find impedance.

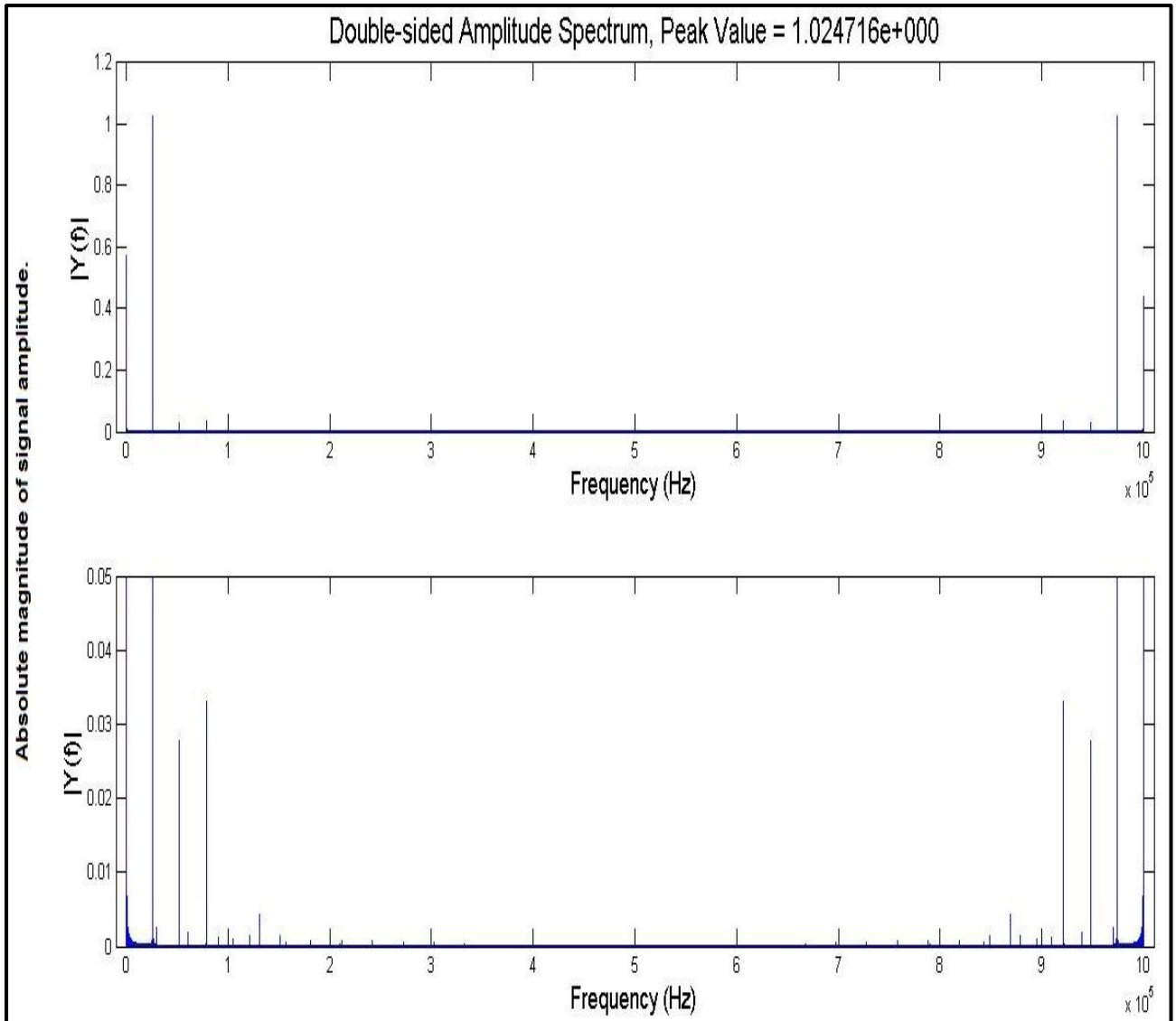


**Figure 2-3: Two sided FFT spectrum of the voltage signal from the whole-body used to measure whole-body impedance. The two sections show signals scaled differently to expand lower magnitude peaks.**

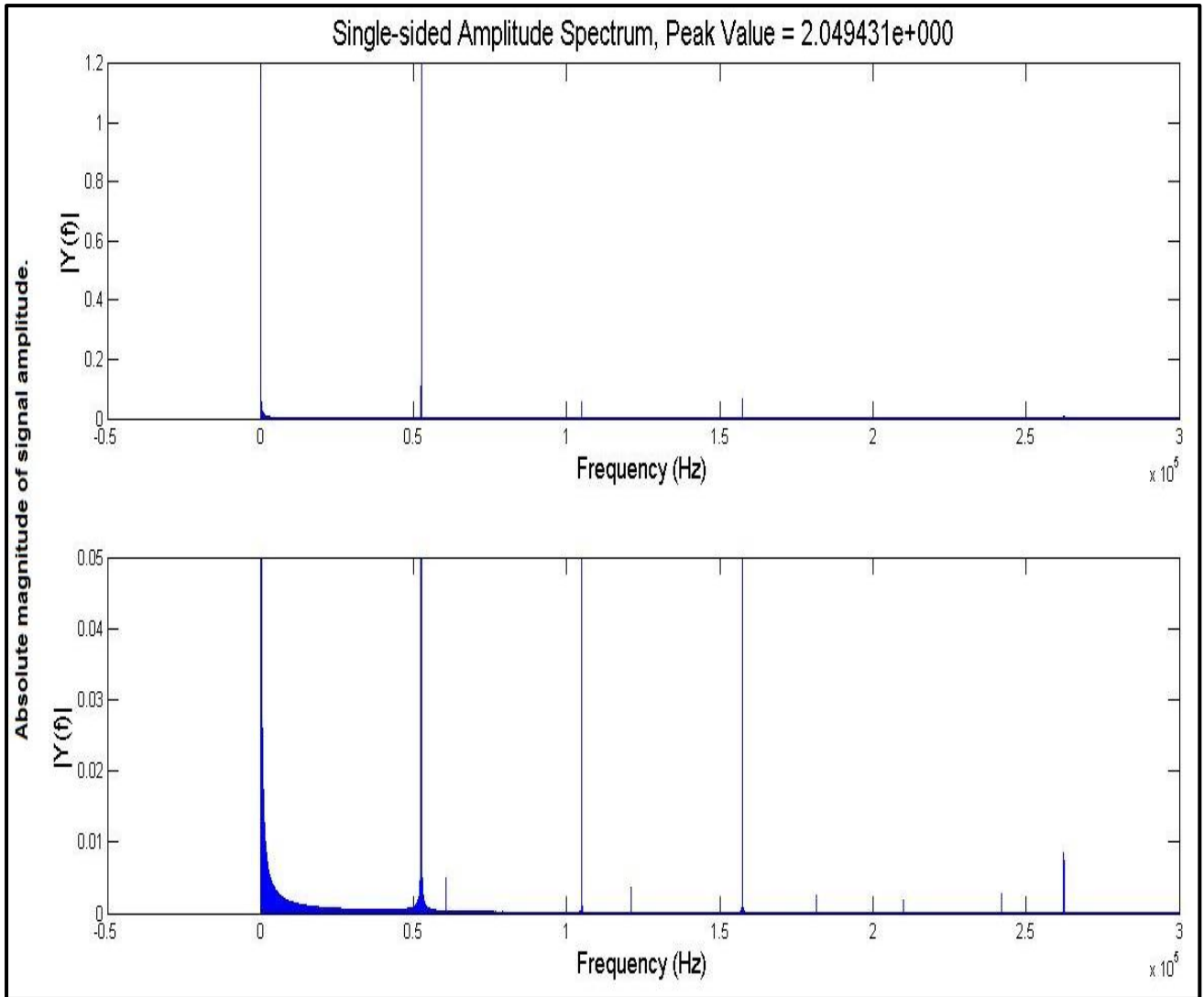


**Figure 2-4: Single-sided FFT spectrum of the voltage signal from the whole-body used to measure whole-body impedance. The two sections show signals scaled differently to expand lower magnitude peaks.**

### **2.2.3 Low pass filtering in the digital domain:**

An ideal low pass filter in theory allows all frequency components of a signal below a designated cut-off frequency to pass uninterrupted and completely rejects all frequencies above the cut-off (also called stopband frequencies). Figure 2-5 shows the frequency response of an ideal LPF together with that of a real LPF. The gain (ratio of output from the filter to the input at a particular frequency) is usually represented in decibels (dB). The frequency can either be normalized (with respect to the sampling frequency) or represented in hertz (Hz). The ideal response shows how the filter acts as a 'brick wall' to frequencies

beyond the cut-off frequency. But real low pass filters are unable to provide such a brick wall response and have a transition band between passband and stopband frequencies.

As filters become more complex (hardware complexity in analog domain and computational cost in digital domain) they approach the ideal filter response. The filter design task can be thought of as an optimization problem, between filter complexity and desired filter response. Certain trade-offs have to be made between filter complexity and desired filter response (e.g. transition band width) to obtain a filter fit for a specific purpose (Losada 2008). For the current purpose digital low pass filtering was desired to filter the obtained bio-impedance signals.

#### **2.2.4 Designing a digital LPF to filter bio-electrical signals:**

Filters in the digital domain can be of two types

1. Infinite impulse response (IIR) filters.
2. Finite impulse response (FIR) filters.

The specific differences and features of each of the above can be found in Oppenheim, (1975). For this project we restrict our scope to FIR filters only, primarily because they are simple, easy to design and robust.

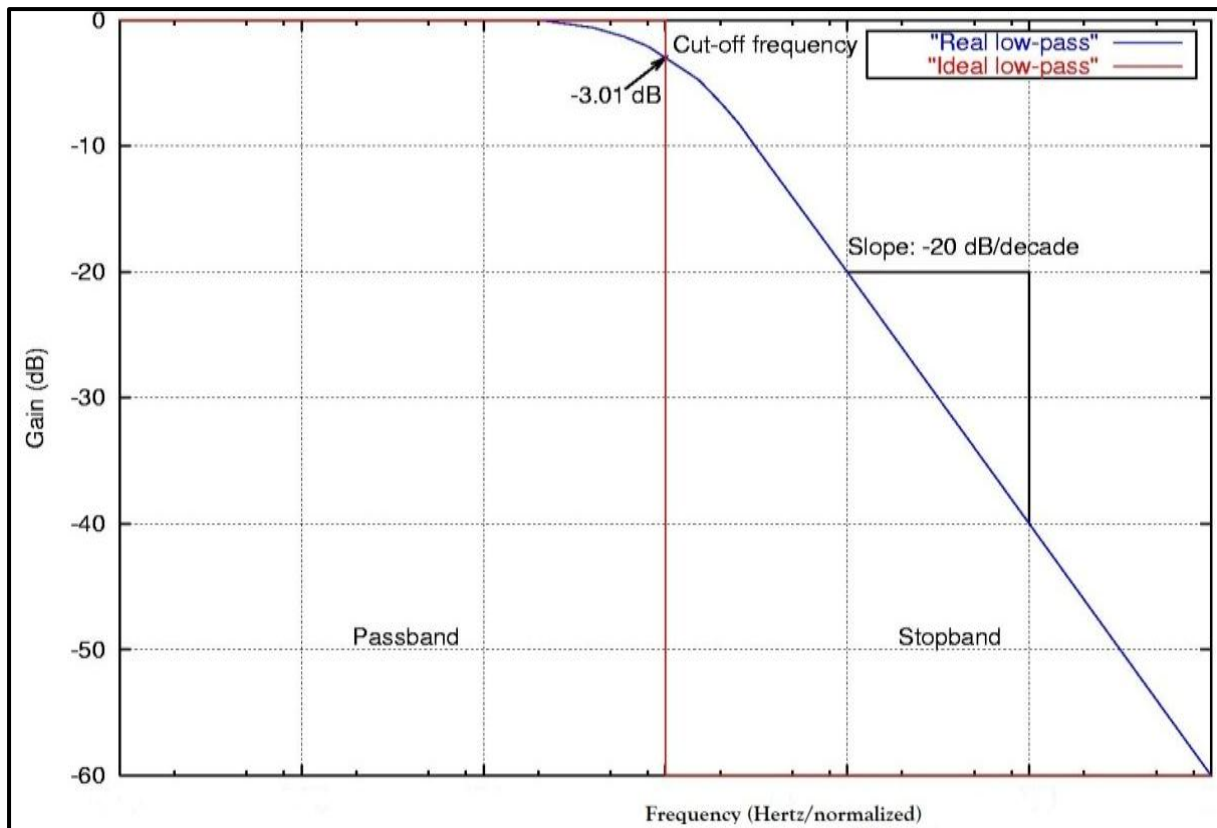


**Figure 2-5: Shows the 'brick wall' response of an ideal LPF as opposed to that of a real LPF. Note: there exists a transition band between cutoff and stop band frequencies in the real case.**

They also can be designed to have a linear phase response and preserve phase information. This means the phase response of the filter is a linear function of the frequency, this causes all the frequency components of the input signal to be delayed (shifted in time) by the same amount. When a sinusoid  $\sin(\omega t + \theta)$  is passed through a filter with constant phase delay  $\tau$ , the result is the signal  $A(\omega)\sin[\omega(t - \tau) + \theta]$ . For bio-impedance signals this might not be a huge concern since we are concerned with the response to a single input frequency to the filter, but linear phase is preferred to extract additional information from bio-impedance signals. To implement ideal low pass FIR filters, the filter lengths are to be of infinite length which is not plausible. So instead we truncate the length to a finite number which introduces ripples in the passband and stop band (Figure 2-6).

It is useful to think of FIR filter design as the angles of a triangle with each angle corresponding to filter order, transition width and peak passband/stopband ripple (Losada 2008). Like the angles of the triangle we are free to choose two angles but the third will inherit itself from the other two. For the present project the order of the filter is not our biggest concern because the signals acquired are being post-processed to acquire desired impedance and other information.

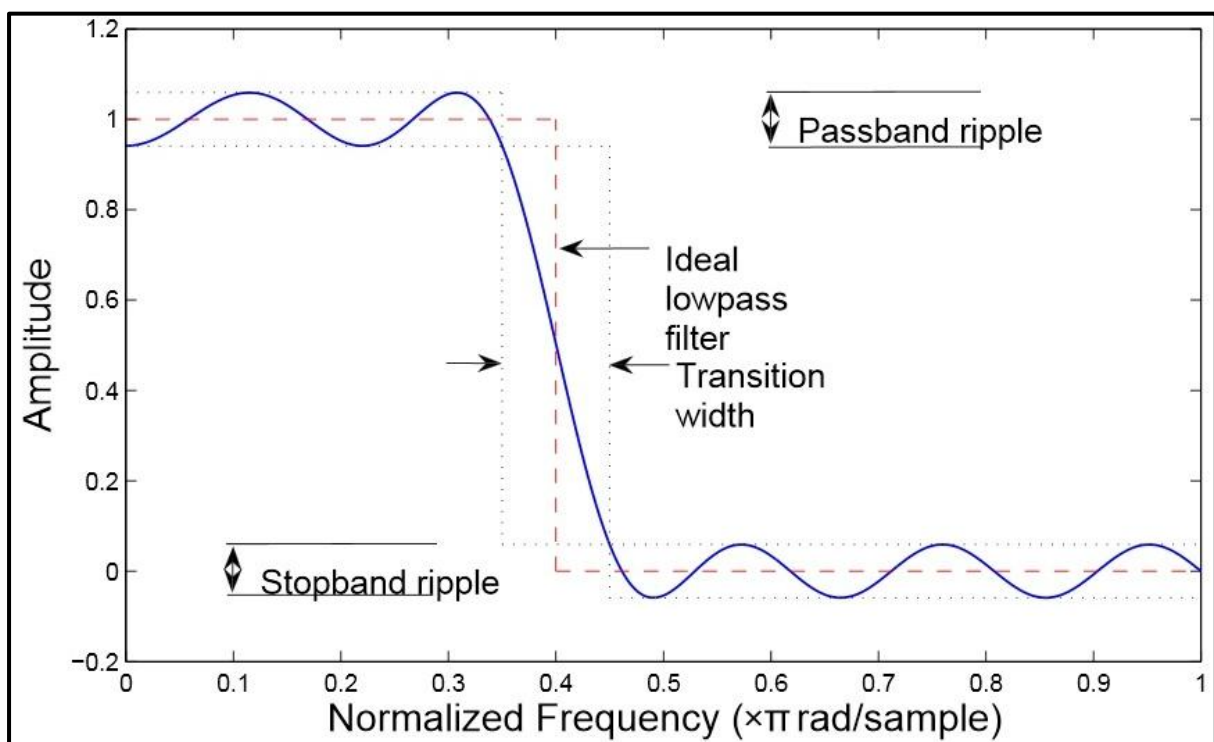


**Figure 2-6: Shows a real FIR LPF with ripples in the passband and the stopband.**

However, we impose performance requirements on the filter to obtain the clean signal of interest. The following example will illustrate the LPF design technique adopted in this project. As mentioned in section 1.6.1, the 50 kHz was the original choice for frequency of operation. To extract the heart rate peaks (caused by heart beats during signal acquisition, reasons explained in section 10.2) the 50 kHz carrier is to be filtered out. In order to do this we pass the original signal through a filter with a cut-off frequency of 10 kHz and a transition bandwidth of 2.5 kHz. Our aim is to design a FIR LPF fit for this purpose. Assuming the cut-

off frequency is half way in the transition band, the transition starts at 8.75 kHz ( $10 \text{ kHz} - 2.5 \text{ kHz}/2$ ) and ends at 11.25 kHz ( $10 \text{ kHz} + 2.5 \text{ kHz}/2$ ). We also impose a stopband attenuation of 25 dB (0.01 in linear units). Using the 'fdatool' (filter design and analysis tool) in Matlab one can design a filter with the above specifications using a Kaiser window (windowing technique described in Oppenheim 1975). As can be seen in Figure 2-7 we can choose to design a lowpass FIR filter using the windowing technique. We need the tool to determine the minimum order required for a Kaiser window filter to meet the above specifications. This returns the LPF magnitude response seen in Figure 2-7 and the order of the filter required was 951.

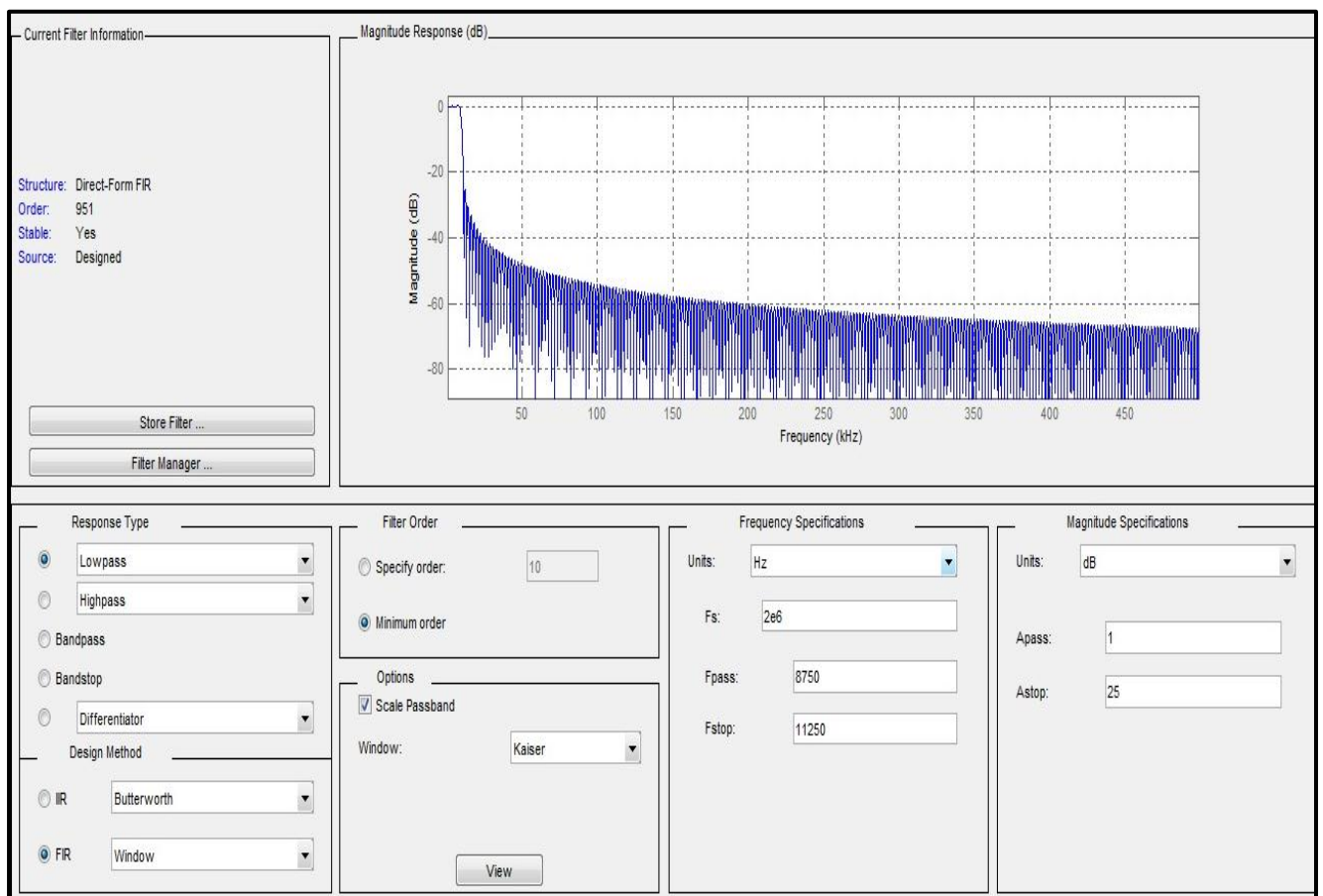


**Figure 2-7: Shows a view of the 'fdatool' in Matlab used to design a FIR LPF using the windowing technique. Note the minimum order required for the specifications filled in is 951.**

Windowing is a standard filter design technique for FIR filters but generally returns inferior filters for the given order, and usually a filter of much lower order can be designed with a similar response using better methods (Losada 2008). Hence more advanced techniques with certain optimization criteria are to be used. Such optimized designs can be used to lower some measure(s) of deviation between the designed filter and the ideal filter response. The choices we have for optimization are the equiripple method and the least squares method. Equiripple filters are desirable because they have the lowest deviation from the ideal filter response for any other filter design technique with the same order. Least squares filter aims at minimizing the energy of error in the stopband/passband. For the above specifications an equiripple and a least-squares filter can be designed using the following Matlab commands:

```
Hf1=fdesign.lowpass('N,Fp,Fst',801,8750,11250,2e6);  
  
Hff1=design(Hf1,'equiripple');  
  
Hff2=design(Hf1,'firls');  
  
fvtool(Hff1,Hff2)
```

'fdesign.lowpass' returns a set of specifications that can be used to design lowpass filters and takes the following parameters.

1. N is the order of the filter, order 801 is used as will be detailed later.
2. Fp is the passband frequency which is 8.75 kHz.
3. Fst is the stop band frequency which is 11.25 kHz.
4. Followed by the sampling frequency of the signals (2 MSa/Sec).

The 'design' function can be used to return filter coefficients of specifications which are stored in 'Hff1' for the equiripple case and 'Hff2' in the least-squares case.

'fvtool(Hff1,Hff2)' returns the magnitude response of both filters (Figure 2-8) (further details in Matlab program 'ecg\_bia\_hilbert.m' given in Appendix 3).

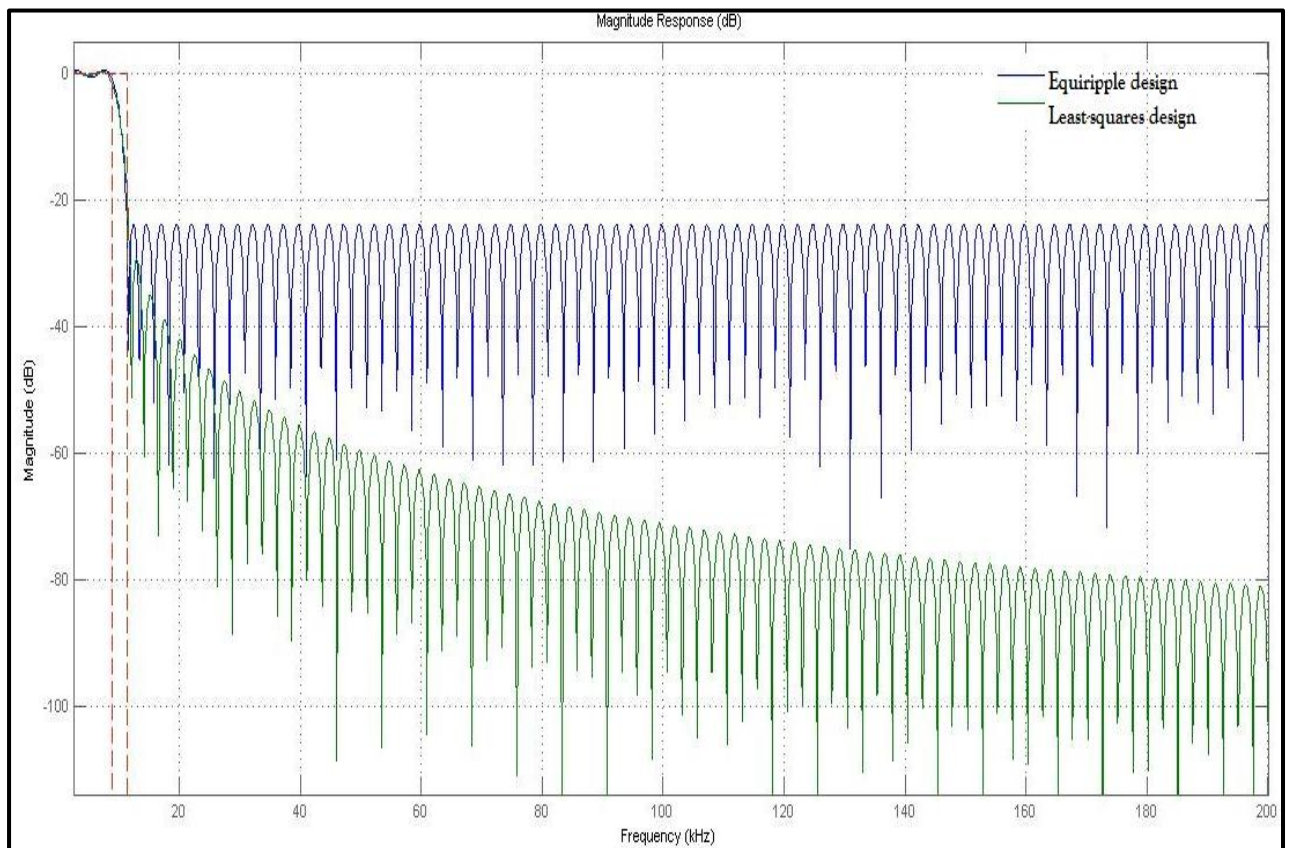


**Figure 2-8: Shows the magnitude response of the 801 order FIR LPF designed using the equiripple method and lest-squares method.**

The 'measure' command can be used to measure the different characteristics of the designed filter (e.g. `measure(Hff1)`; would return the characteristics of the equiripple filter). The parameters of the above design realized using equiripple, least-squares and Kaiser Window method are shown in Table 2-2. As mentioned earlier FIR filter design is an optimization task, although the Kaiser window filter has least passband ripple and highest stopband attenuation (Table 2-1), its order (951) is much higher than when compared to optimized filter design orders (801) with similar performance. In this case the equiripple filter was chosen for its lower passband ripple since we do not want large interference in the

signal of interest caused by the filter and also because it has larger stop band attenuation (23.64 dB) than the least-squares case (18.26 dB).

**Table 2-1: Shows the comparison of important characteristics of the 801 order filters designed using equiripple and least-squares method and the Kaiser window filter of order 951.**

	<b>Equiripple method (order 801)</b>	<b>Least-squares method (order 801)</b>	<b>Kaiser window (order 951)</b>
<b>Sampling Frequency</b>	2 MHz	2 MHz	2 MHz
<b>Passband Edge</b>	8.75 kHz	8.75 kHz	8.75 kHz
<b>3-dB Point</b>	9.4801 kHz	9.2872 kHz	9.4742 kHz
<b>6-dB Point</b>	10.0052 kHz	9.9305 kHz	9.9791 kHz
<b>Stopband Edge</b>	11.25 kHz	11.25 kHz	11.25 kHz
<b>Passband Ripple</b>	1.1225 dB	1.751 dB	0.90456 dB
<b>Stopband Attenuation</b>	23.6369 dB	18.2569 dB	25.3455 dB
<b>Transition Width</b>	2.5 kHz	2.5 kHz	2.5 kHz

The Kaiser Window order is used as a guide to indicate maximum order required for given specifications. Order 801 for equiripple and least-squares designs is obtained by trying different orders below 951 and picking the lowest order which gives an acceptable passband ripple and stopband attenuation. In this manner we can design FIR lowpass filters for our desired purpose.

### **2.2.5 Savitzky-Golay moving average filter:**

The concept of moving average filters is well established, for given a fixed set of numbers the moving average is given by, averaging a subset of the initial set, then moving the subset in succession to the next element and averaging again until a set of averaged values equal in length to the initial set is obtained. Different averaging techniques can be used to obtain

the averaged value (Surhone et al. 2010). One such technique is the Savitzky-Golay method which performs polynomial regression on the values of each subset to obtain the averaged value of each point. The primary advantage of this averaging technique is that it preserves the features of the original set including its maxima and minima; features which can be compromised when using other averaging techniques. The 'smooth' function in Matlab enables users to apply moving average on datasets. For example a dataset N with 1000 elements, the Savitzky-Golay moving average can be applied for a subset of 100 elements of N using the following command

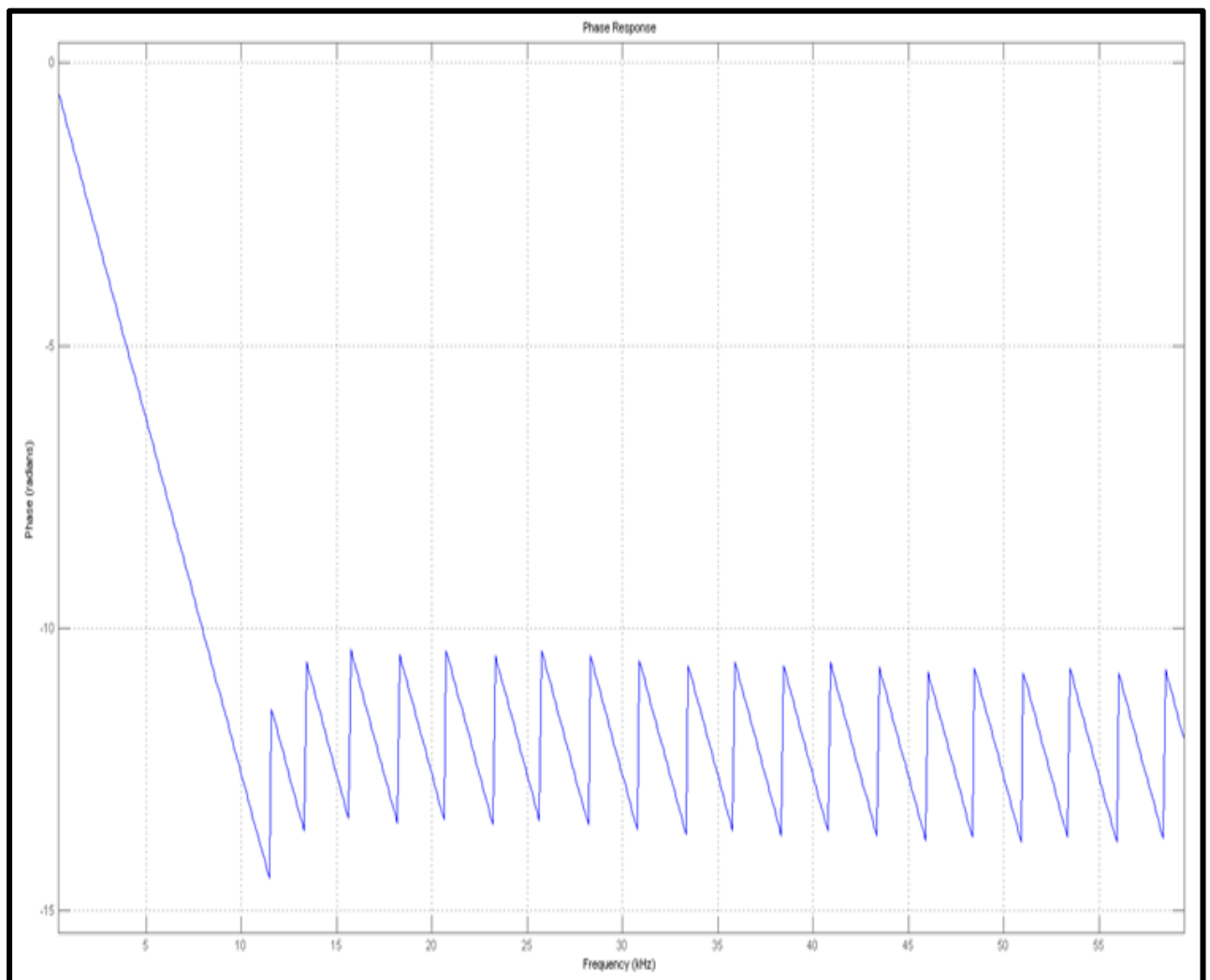


**Figure 2-9: Shows the linear phase response of the equiripple filter chosen above for the extraction of heart rate signals.**

```
MAvg=smooth(N,100,'sgolay',4);
```

Where N is the dataset, 100 is the span or length of the subset for which the average is to be determined, 'sgolay' specifies the use of the Savitzky-Golay technique and 4 specifies the order of the polynomial to be used for polynomial regression. Other averaging techniques can also be used like 'moving' which uses the normal averaging technique. For this study we utilize the 'sgolay' technique and its use on bio-electrical impedance signals to extract heart rate will be shown in the methods section.

## 2.3 Statistical techniques:

As mentioned in section 1.8.1 linear/multiple regression is generally used for making bio-impedance estimates. In general regression is a statistical analysis tool used for assessing the association between two variables. It is used to find the relationship between two variables. For example we could expect a linear relationship between grades-obtained by students in a class to the hours of lectures attended by the students. Here grades-obtained is the dependent variable (or response variable) and number of hours of lectures attended is the independent variable (or explanatory variable). This can be expanded further using more independent variables like grades obtained in previous year to improve on the original association. When two or more independent variables are used in attempt to improve association as compared to a single independent variable it is known as multiple-regression (Boslaugh 2008). Regression model quality is evaluated using a parameter called the coefficient of determination (Rsq). To illustrate Rsq further consider Figure 2-10, here the observed values are represented by the black points. The line of best fit (blue) in most cases is plotted using the ordinary least-squares method (where the sum of squared vertical distances between the observed and predicted values is minimized) and the vertical distance or error between the predicted and observed values (in green) are called the residuals (Boslaugh 2008). If  $\bar{Y}$  is the mean of the observed values,  $Y_i$  (black dots) are the observed

values and  $F_i$  (red dots) are the values predicted by the linear model, the following equations hold:

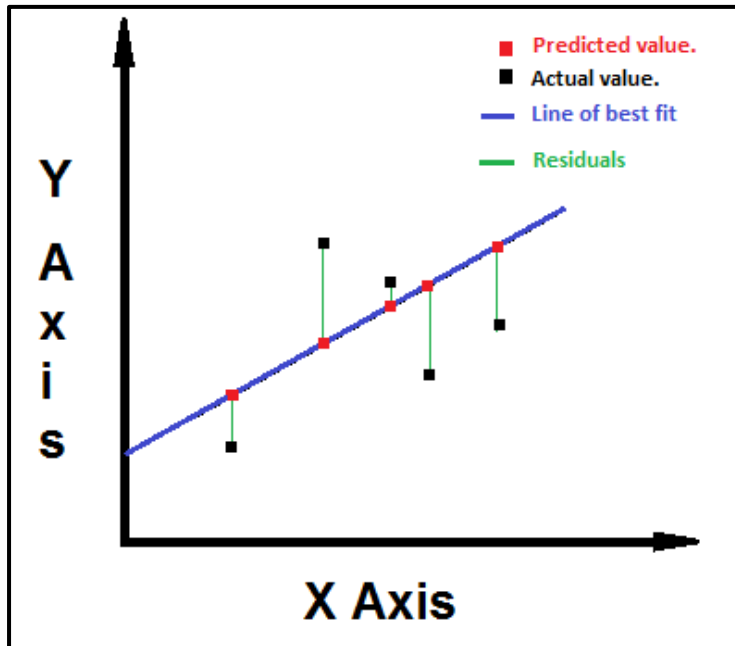


**Figure 2-10: Shows linear regression model. The predicted values (in red) are on the line of best-fit. The residuals are the difference between the predicted and the actual values.**

$$S_{tot} = \sum (Y_i - \bar{Y})^2$$

$$S_{res} = \sum (Y_i - F_i)^2$$

Where  $S_{tot}$  is the total sum of squares and  $S_{res}$  is the residual sum of squares (because it is the squared sum of residuals). The coefficient of determination  $R_{sq}$  is given by

$$R_{sq} = 1 - \frac{S_{res}}{S_{tot}}$$

and since  $S_{tot}$  is always greater than  $S_{res}$ ,  $R_{sq}$  will be less than one and zero for perfect models where all variation in the response variable is explained by the explanatory variable(s). Another important aspect of regression is the significance of the predictor

variables in the model; this is estimated by the significance p-value. P-value stands for the probability value based on which we accept or reject the null-hypothesis. For the above example based on the p-value obtained for each independent variable (most statistical software packages provide p-values in the summary of a model) one can accept or reject whether 'previous grades' is significantly contributing to the model or not. Our decision to include or reject 'previous grades' in the final model will be based on the significance obtained using the p-value. Generally if a variable has a p-value less than 0.05 it is regarded to be statistically significant to the model. With regards to multiple regression models the f-statistic p-value is regarded to provide insight into the significance of the entire regression model (which includes all explanatory variables). This is a method used to perform a hypothesis test on the entire model which helps make a decision on the overall significance of the model (Boslaugh 2008). These are the main statistical concepts used in analysis of results in this project.

## **2.4 Learning from data:**

BIA predictions have largely relied on linear and multiple regressions because there is high degree of correlation between impedance coefficients and their respective water space (Gudivaka 1999). But the capability of regression to model non-linear relationships is questionable. Alternately one can view BIA predictions as a pattern recognition problem wherein tissue impedance is used as a predictor for body composition. In recent years neural computing has emerged as a practical method for pattern recognition and has been successfully applied in several fields. Neural networks are widely used in robotics, image processing, data and speech recognition, and increasingly in new areas of mathematics and physics including pattern recognition. A few studies have explored the usability of neural networks for BIA and have found it to be a better predictor than multiple regression (Hsieh et al. 2008). Hence the interest in applying neural network based methods for the evaluation on

BIA data. The following is a brief introduction to the neural computing field and its applications in BIA will be explored further in the methods section.

### 2.4.1 Brief History of neural networks:

McCulloch & Pitts (1943) suggested information processing by means of interconnected simplified neurons provided a model for learning from data using artificial neural nodes. Around 15 years after the neuron models was proposed by McCulloch & Pitts, Rosenblatt proposed the idea of 'perceptron' for supervised learning (Figure 2-11). The disadvantages of the perceptron model from a mathematical point of view was reported by Minsky in 1988. A renewed interest in neural networks emerged in early 1980's after some important theoretical results were proposed, and advances in computing provided increased processing made practical applications of neural networks feasible. This meant that neural computing became attractive for many applications outside computer sciences (Bishop 2007).

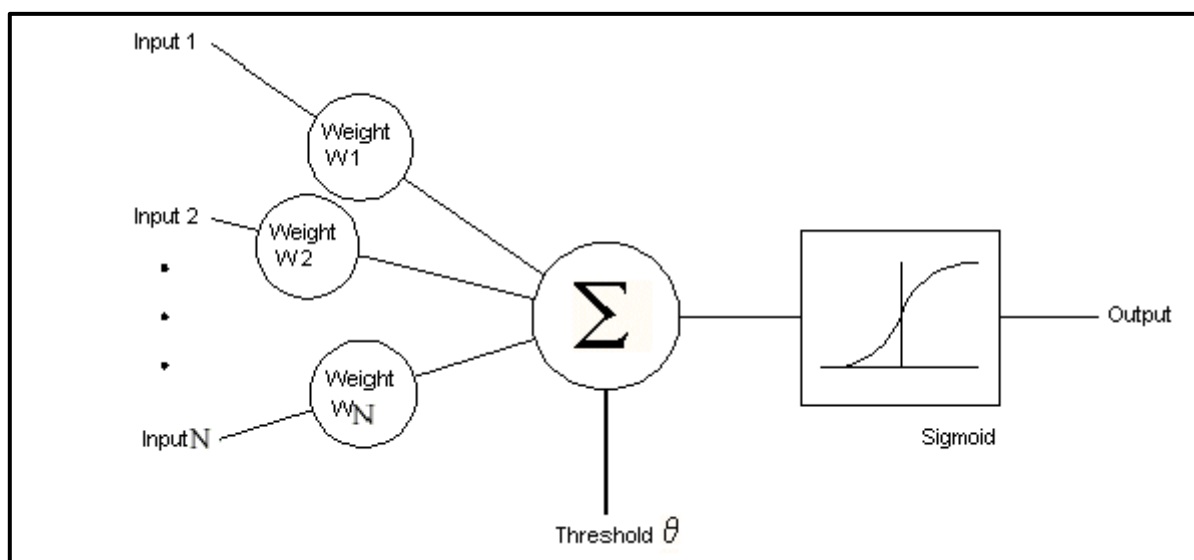


**Figure 2-11: Shows a single node ('neuron') of a MLP, it includes inputs, their corresponding weights and an activation function.**

## 2.4.2 Description:

Neural networks are used to solve problems where the mathematical relationships between inputs and the outputs of a system are not known, but a minimum amount of data is available so that the network can infer a potential relationship. A neural network uses training data (complete sets of input data for which the corresponding complete output data are known) to build a model which links the input and output variables. The resulting model is consistent in that the same input pattern will always produce the same output but contains no explicit rules. Neural networks can be applied when problems are too complex to be modelled mathematically, and are widely used in pattern recognition. Traditional techniques utilizing mathematical equations are reserved for situations where the exact rules linking the inputs and outputs of a system are known. The functions inferred by neural networks are non-linear and are particularly powerful; for categorisation tasks (Table 2-2). A neural network's ability to generalise means that it is able to 'learn' from noisy or incomplete data.

**Table 2-2: Lists the main differences between programming approach and neural computing approach to problems.**

<b>Programming approach</b>	<b>Neural computing approach</b>
Follow rules	Learns from data
Solution formally specifiable	Rules are not pre-specified
Cannot generalise	Able to generalise
Not error tolerant	Tolerates noisy data

The mathematical model built by a neural network is made up of simple functions linked together by weight. The weights describe the effect that each input (or unit) will have on the overall model. A typical example of a neural network is the multi-layer perceptron (MLP). A MLP has a set of input units, to which input values are fed, a set of output units which report the final answer, and a set of hidden processing units which link the inputs to the outputs (Figure 2-12). Each node is essentially a summing junction which calculates the weighted

sum of its inputs, followed by an activation function. The activation function can take a variety of forms, including linear or various kinds of threshold function. The weights  $W_1$ ,  $W_2$ , etc., are scalars whose values are optimised during the network training stage. These principles are applicable to data analysis in the present project since only basic statistical methods like linear regression has been used for body-composition predictions.

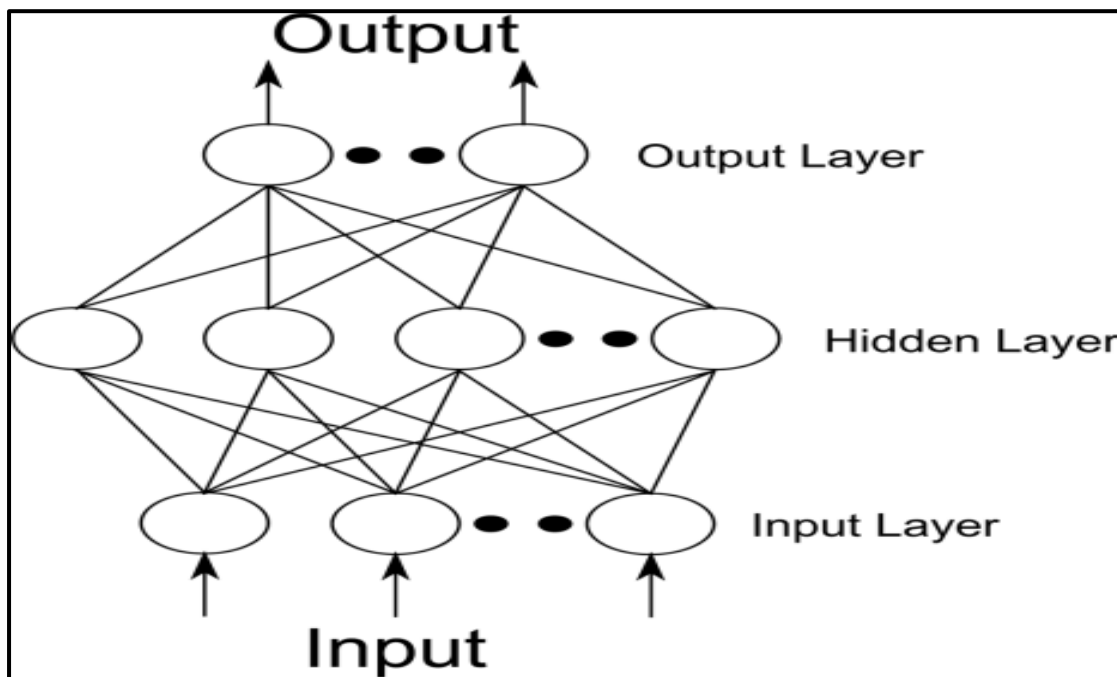


Figure 2-12: Shows a MLP network with neurons connected as input, hidden and output nodes.

### 2.4.3 Training neural networks using back-propagation:

A popular algorithm to train MLP's called the back-propagation algorithm, which involves calculating the error at each output and changing the values of the weights which caused the error. The training data set and the validation data set are both sets of measured outputs. These are propagated through the neural network and an error value is generated. This error value represents the difference between the neural networks output in response to the validation inputs and the actual validation outputs. Training a neural network is an iterative process in which the values of weights are optimised so that the training error is minimised. This process of learning is known as gradient descent. A problem with gradient descent is

that local minima which are dips in error space and are not the universal minimum. An algorithm designed to always reduce error will not be able to climb out of a local dip to continue descent to the true lowest point. The standard back propagation algorithm uses two parameters which control the rate at which the learning takes place. A momentum term which causes the weight changes to be affected by the size of the previous weight changes to be affected by the size of the previous weight changes is used to avoid local minima. The learning rate tells the network how slowly to progress. The weights are updated by a fraction of the calculated error each time to prevent the network making large changes about the best values without ever achieving optimisation.

There are two types of training:

1. Train with a single pattern of data and update weights after each pattern (online learning).
2. Train with a whole set of data patterns and update weights after each batch (batch learning).

Errors are calculated and saved after each pattern, and then weights are recalculated at the end of each batch. The batch mode is faster and calculates a more accurate weight change, but needs more memory to store the error values over an entire batch. In the methods section we show the application of neural networks approach to the analysis of a particular BIA dataset. The concepts described here will be utilized to obtain body composition prediction results. For our analysis in this project a variant of the back-propagation algorithm known as the Levenberg-Marquardt back-propagation is used because it is a fast learning algorithm and is readily available to be used with the neural-network toolbox with Matlab. The learning method of choice in this project was batch learning since it produces quicker results(Bishop 2007).

#### **2.4.4 Splitting data:**

By convention data used to train and characterize neural-networks is split into training data, validation data and test data. Training data is used to train an initialized neural-network through several iterations of the training-set. Validation data is used to evaluate the performance of the network as training progresses. Training is usually stopped when no improvement is seen in the error between predicted validation-set and actual validation-set. Testing dataset is used to evaluate the performance of the trained neural-network and determines the behaviour of the network when fresh data is presented to the network. The error produced by the network when being tested gives an idea of the generalization to the problem achieved by the network (Bishop 2007). Generally the split percentages are 70% entire dataset for training, 15% for validation and 15% for testing (Witten et al. 2011).

#### **2.5 Estimating body volumes with KinectFusion algorithm:**

While waiting for the ethics committee to approve the clinical component of the present study at the Heartlands hospital the opportunity arose to extend the project to consider the potential application of BIA in conjunction with estimates of body volume. Body volume scanning is a challenging and expensive prospect and normally involves complex equipment to be used. Taking advantage of newly available hardware and software our idea was to undertake a study which directly compared S-BIA and volumes of the segments under question which would help us to explore possible relationships between these two quantities.

In the last quarter of 2010 Microsoft Corporation introduced the Kinect motion sensing device which was based on scattered infrared light which enabled sensing everyday environments by providing depth information of the sensor's view. Although originally introduced for gesture control of games with the Xbox gaming console, through continued efforts of enthusiasts and reverse engineers open source drivers to access sensed data on a computer were soon available through the OpenNI (Open Natural Interaction) framework

(Anon 2010). The device also enclosed within a RGB (Red, Green, Blue; normal digital camera) and a multi-array microphone (Anon n.d.). The focus of this study is around the depth sensing capabilities of this device. The depth sensor consists of an infrared laser projector which scatters an array of infrared points into the environment and detects the reflection from these pointers as a monochrome video stream of  $640 \times 480$  pixels with 11 bit depth providing 2048 levels of sensitivity (Figure 2-13).



**Figure 2-13: Shows an image of the Kinect depth stream. A colour gradient is used to represent depth where closer objects appear white gradually changing to blue as distance from the camera increases.**

This video stream is converted into depth maps based on the grayscale levels in the video. The sensor is reported to have a field of view of  $57^\circ$  horizontally and  $43^\circ$  vertically and has a viewing distance of 6m (Anon 2013). After its introduction researchers were provided with a

new quick and easy way to obtain depth streams and work on various algorithms which would utilize consecutive depth streams and combine them (register) to reconstruct objects in 3 dimensions (3D). A particular software project to become available was called the Point Cloud Library (PCL) which is free, open source and programmed by researchers and enthusiasts in the field. A feature of this project is the KinectFusion (KinFu) algorithm which registered depth maps from Kinect-like devices in real time. The methods section of this thesis describes how this feature was utilized to scan body volume.

3D reconstruction is a vast field of on-going research and development, but to understand how it was utilized in the present study a brief introduction of the essential concepts will be provided in the following section. Figure 2-14 shows the raw output (raw depth in figure) from a Kinect sensor. As mentioned earlier different colours or grayscale levels are used to represent the distance of an object from the camera, where the darker the object the closer it is to the camera. The KinFu algorithm works through four major steps to convert raw Kinect depth stream to a 3D surface which will be covered briefly below. But before, it is to be noted that KinFu is a real-time 3D reconstruction algorithm which implies that it comes with a very larger computational cost and requires parallel computation over multiple execution threads. Traditional central processing units (CPUs) are not able to provide multiple execution threads (generally one thread on one CPU core). Graphical processing units (GPUs) however have several cores each of which can be assigned an execution thread. We have employed the Nvidia GTX570 graphics card with 536 cores for this project. The four steps are implemented for GPU execution using the NVIDIA CUDA (Compute Unified Device Interface) platform which unlike other programming platforms is optimized for parallel computing on GPUs.

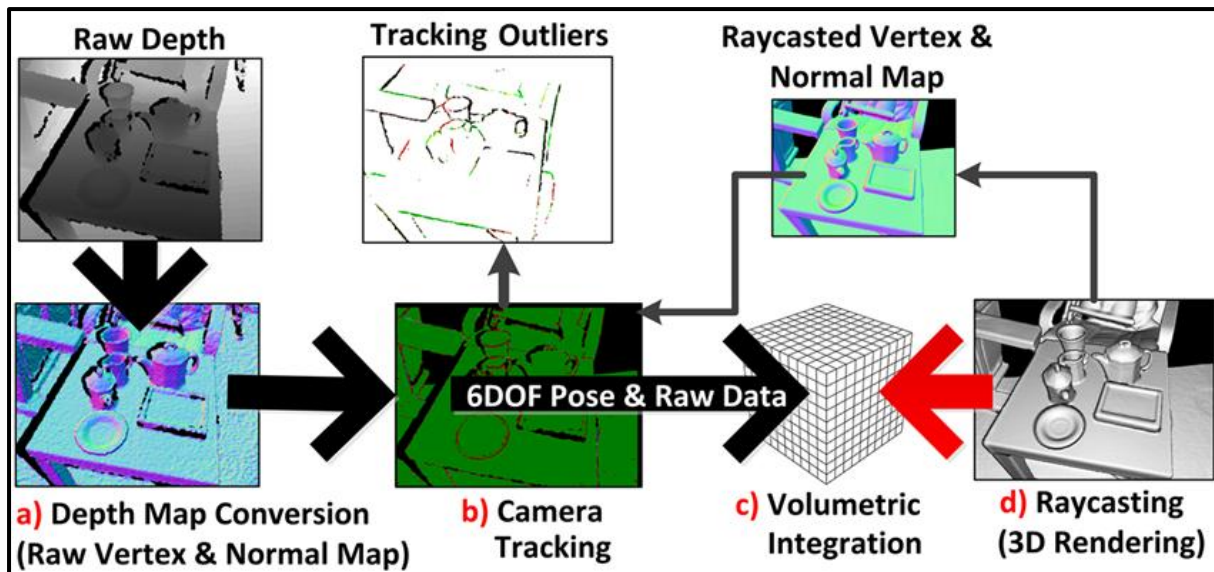


**Figure 2-14: Illustrates the four major steps involved in obtaining 3D scans from Kinect depth stream. Adopted from Newcombe et al. 2011.**

### 2.5.1 Depth map conversion:

To convert the raw depth stream into 3D points each CUDA GPU thread operates in parallel on a separate pixel to convert the incoming depth stream into a 3D vertex map (Figure 2-14)(Izadi et al. 2011).

### 2.5.2 Camera tracking:

Camera tracking (knowing the camera's current position) is essential to obtain reconstructed 3D surfaces from consecutive depth frames when the camera moves around the object of interest. The current pose of the camera which has 6 degrees of freedom (6 DOF) is predicted based on the current depth map and previous depth map. This is done using a well-studied algorithm for 3D shape alignment called the Iterative Closest Point (ICP) algorithm. In brief this minimizes the Euclidean distance between feature points of two adjacent frames iteratively. Figure 2-15 shows how ICP has been used to align two lines, now after alignment the 6 degrees of movement of these two lines can be calculated (Newcombe et al. 2011).

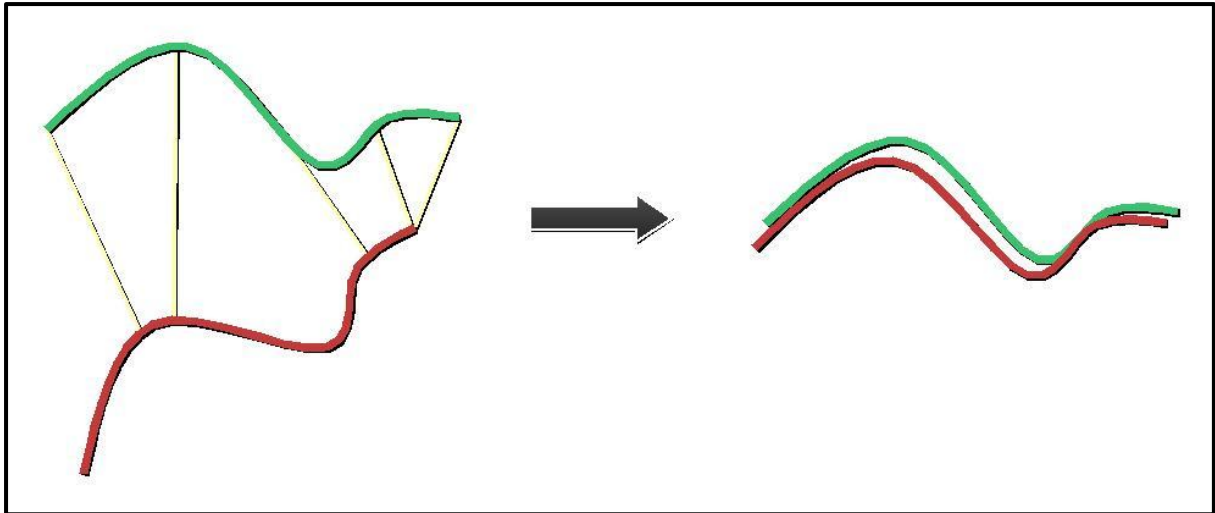


**Figure 2-15: Illustrates how ICP is utilized to align two lines. From the initial (unaligned, left) and final state (aligned, right) the transition of view (camera movement) with 6 DOF can be calculated.**

Thus when applied to consecutive frames from the Kinect camera ICP would essentially detail the motion of the camera between two consecutive. The individual steps in this process is described fully elsewhere (Besl & McKay 1992).

### **2.5.3 Volumetric representation and integration:**

With the pose of the camera known from the previous step any depth measurement coming in from the Kinect camera can be converted into a single consistent 3D coordinate space (3D surface). This information is integrated into a 3D volume, the 3D resolution of which is predefined and represented as a uniform grid of 3D (pixels in 2D) voxels (Figure 2-16) (Newcombe et al. 2011).

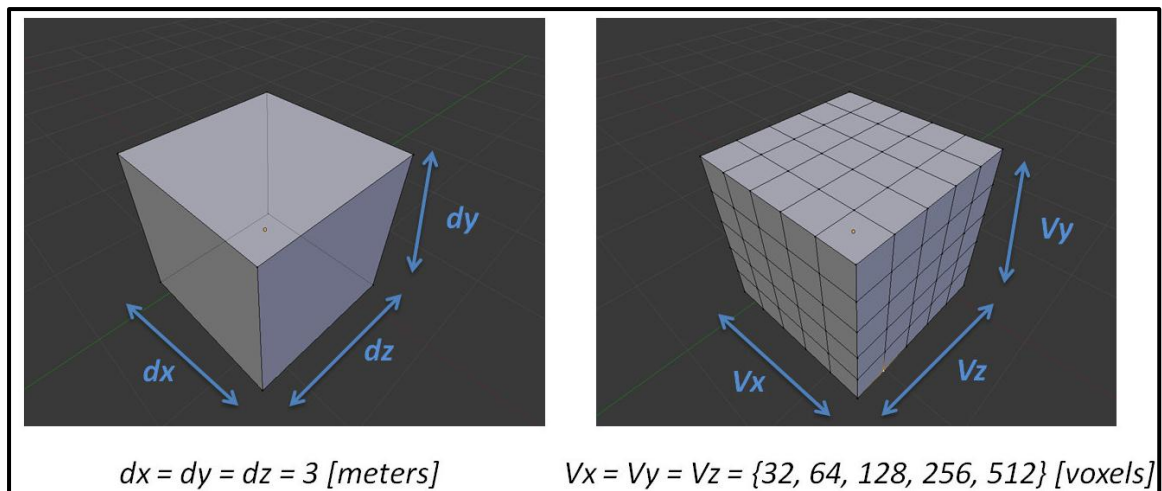


**Figure 2-16: Shows how a 3m cube-space is divided into smaller cubes called voxels in 3D computational geometry. For computational efficiency they take values which are powers of two. Adopted from [www.pointclouds.org](http://www.pointclouds.org).**

The 3D vertices computed after ICP are integrated into the 3D grid of voxels using the Truncated Signed Distance Function (TSDF). Figure 2-17 shows a cross section (of 3D grid) with TSDF values, here values in front of the surface are positive and approach zero as we move towards the surface. The values within the surface are negative. The TSDF value is the distance to the nearest surface. For memory efficiency only values which have deviated from 1 are stored on the GPU since values of 1 represents empty space (Izadi et al. 2011). In this manner the TSDF function is used to represent surfaces in a global 3D volumetric grid. The elegance and a prime advantage of this method is that, as the camera moves in the scene new depth data is integrated into this 3D volumetric grid since the camera's position with respect to the grid is known. Ideally we would like to assign a GPU thread per voxel in the volumetric grid, but there is larger number of voxels than threads. Hence the KinFu program allocates one thread per voxel along the x and y axis (refer Figure 2-14) and a parallel GPU thread sweeps through the volume moving along each x, y slice in the z axis and integrates new information coming from the Kinect sensor in the process (Izadi et al. 2011).

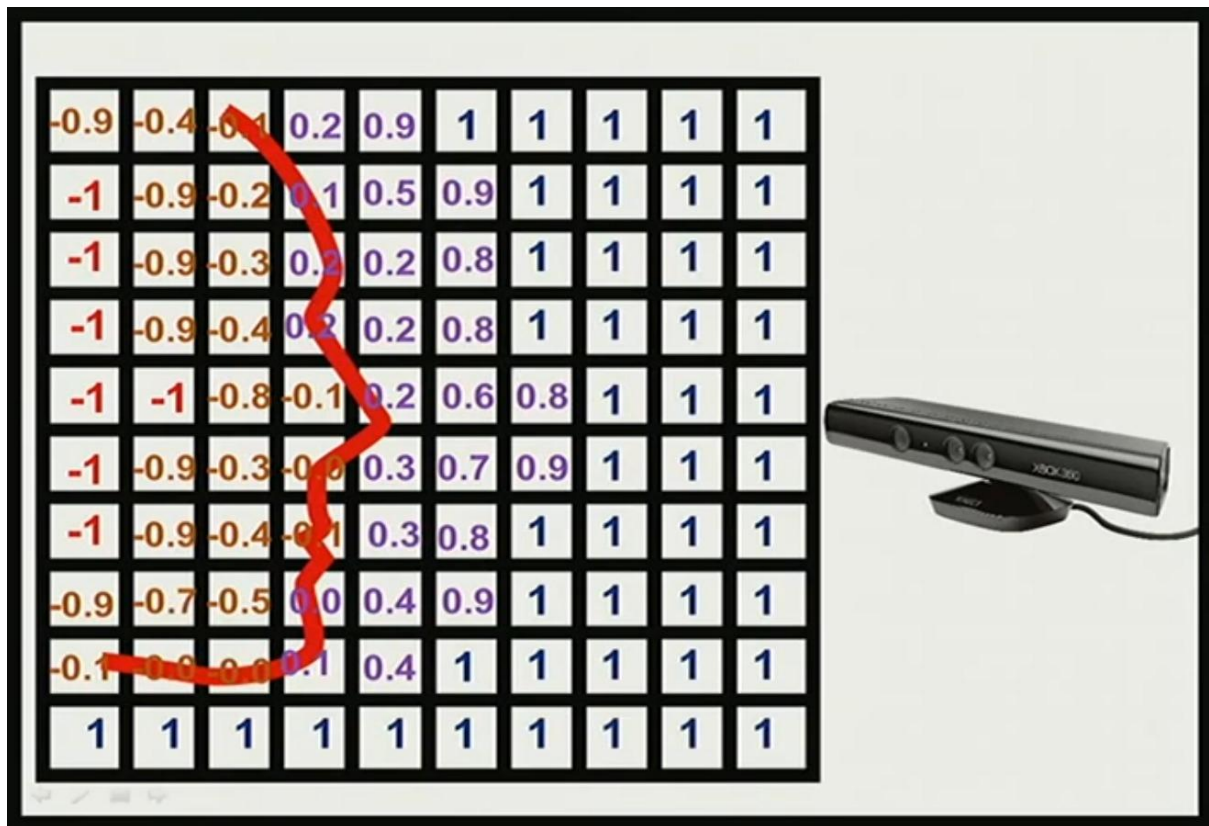


**Figure 2-17: Shows a cross section of the TSDF method. Values approach zero closer to the surface (silhouette) which then transit to negative values within the surface. Adopted from [www.pointclouds.org](http://www.pointclouds.org).**

### 2.5.4 Raycasting for rendering:

In order to generate views (2D views) of the constructed surface a technique called raycasting is used. Here each GPU thread traces an imaginary ray to render a pixel in the output image (note, we say image because although the generated surfaces in 3D when we view the surface on a computer screen it is still in 2D). Detailed information on raycasting can be found elsewhere and will not be described here (Newcombe et al. 2011).

The above is a concise description of a highly complex algorithm to reconstruct 3D surfaces. Full details regarding solutions to specific mathematical and programming challenges to realize this reconstruction algorithm are described in Izadi et al., 2011; Newcombe et al., 2011.

### **2.5.5 The Polygon file format:**

Since we are interested in the volume of the object we are scanning further analysis of the generated volume is in order. This will be done using MeshLab which is an advanced 3D volume processing software with various options including volume estimation. MeshLab uses the polygon file format (amongst many others) to process 3D data. PCL conveniently allows acquired 3D models to be saved in this format; it goes with the extension '.ply'.

## **2.6 Aims and objectives:**

Having studied the theory and previous work behind BIA technologies this research programme aimed at designing and constructing a more accurate bio-impedance measurement system. Since there exist several variants of BIA, some of which predict certain aspect of body composition better than others, one objective was to incorporate features of whole body, segmental and multi-frequency body impedance measurement. To be able to study other possible applications of body impedance we chose to construct a highly flexible bioelectrical signal acquisition system which could be customised to fit many such applications with minimum modification. A typical example for an alternate use of BIA methodologies is the use of change in bio-impedance with the movement of left and right shoulders to direct wheelchairs in either direction(Yunfei et al. 2009). Therefore we envisaged objectives that would provide a customisable bio-electrical signal acquisition system capable of measuring segmental, whole body bio-impedance at various frequencies from bioelectrical signals; the system should also be customisable to allow usage for exploring other applications of BIA.

Various applications of bioelectrical signal acquired using this system have also been explored and also new ways of interpreting BIA data have been sought. This mainly includes the use of bio-impedance measurements along with body volume scans to improve body composition estimation and the use of bio-impedance signals to extract heart rate of the subject during the scan. We were also able to show a reduction in bio-impedance during the flexing of an arm and the use of neural networks to fuse bio-impedance measurements with body composition data to improve bio-impedance based body composition predictions.

## **2.7 Summary:**

In this chapter we introduced some essential concepts required to understand the work done in this thesis. Introduced were concepts of aliasing (and anti-aliasing filters) FIR digital low – pass filters (their design), data analysis techniques which included linear regression and neural networks. Also presented were the steps involved in obtaining 3D volumes of objects using the Xbox Kinect controller and the Point cloud library. These concepts will be further applied in subsequent chapters to obtain the results presented in this thesis.

## **Chapter 3      Segmental bio-impedance measurement: a primer**

The main aim of this project as described earlier was to construct an SBIA measurement system. After having successfully built a whole-body impedance measurement system (version 1) the natural extension to this initial system was to add the ability to measure the impedance of the limbs and body trunk separately. In order to do this; first the functioning of a commercial BIA device, the Tanita BC-545, was evaluated and is described in this chapter. Followed by an in depth analysis of segmental bio-impedance analysis (SBIA). Finally a description of the procedure to obtain prior permission from ethics and regulatory bodies to use the developed device on human subjects is presented. The following sections will describe the above mentioned steps in further detail.

### **3.1 Initial evaluation of current commercial technology:**

As described in the introduction BIA based devices are available commercially. Tanita is a market leader in bio-impedance devices and the BC-545 from Tanita is the particular device this study will focus on. The reason being; other studies in our group have utilized this device and as will be shown in this section, the data from these studies will be used to evaluate its (BC-545) performance; this was particularly useful to form the basis for interpretation of results from the device constructed for this project. Assessment of the various internal and external elements of this device was performed as an initial investigation in order to understand its components, construction, and circuitry. The outcome of this analysis was compared to bio-impedance procedures in theory.

### **3.1.1 Features:**

The BC-545 is one of the first of what is anticipated to become a new generation of segmental bio-impedance devices capable of determining the total-fat percentage and muscle-mass of the whole-body and each of the 5 segments described in section 1.9.3. The device additionally determines body weight, percentage of TBW, and estimates basal metabolic rate (energy required for an individual per day when resting) in kilocalories and kilojoules based on lean body mass, metabolic age (the age equivalent for basal metabolic rate depending upon the rate at which energy is being used), bone mass of the body, and visceral fat rating (calculated on a scale from 1-59, 1 being lowest and 59 being the highest based on trunk segmental fat: rating below 13 is considered to show low visceral fat mass, the algorithm for this is not disclosed). The device is capable of storing information from 4 individuals and can display changes in body composition over time on a graph.

Externally as shown in Figure 3-1 the BC-545 has 8 electrodes, four of which are in contact with the foot (a pair with each foot) and four are in contact with the hands (a pair for each hand). Figure 3-2 shows the position of the different electrodes when the device is in use. The device also has buttons for selection of data inputs (gender, age and height) and output is displayed on a LCD screen. When the device is opened, internally this reveals four force transducers on which the device rests. These are evidently used for determining the weight of the user. The transducers and the 8 electrodes are connected to a circuit board which is the crux of the device and has various discrete and integrated circuits (IC's) to control the device, make composition estimates and display and save user results. As indicated in section 1.6 whole-body BIA requires a pair of electrodes to facilitate passage of current through the subject and another pair to enable recording the voltage response to this current. SBIA on the other hand requires two pairs of electrodes to aid the passage of current and several voltage sensing pairs to enable voltage recording (further details in section 3.2).



**Figure 3-1: Shows the Tanita BC-545 and 8 foot and hand electrodes (two hand electrodes hidden from sight).**

To test the working of the device the electrode determined to be the signal source for measurement was connected to an oscilloscope and the device operated. It was established that the device operates at a single frequency of 50kHz sinusoidal signal. Before investigating the flow of current through the electrodes it was noted that when the device is working it displays the segment for which the current estimate is being made. The sequence of its segmental estimation is right arm, left arm, right leg, left leg and lastly the whole body. Blocking each electrode with an insulator (paper) stopped the device from operating as normal and the device showed an error or a wrong estimate. When each electrode was blocked in turn and in pairs, the following current input and the voltage sensing designation of electrodes was established.

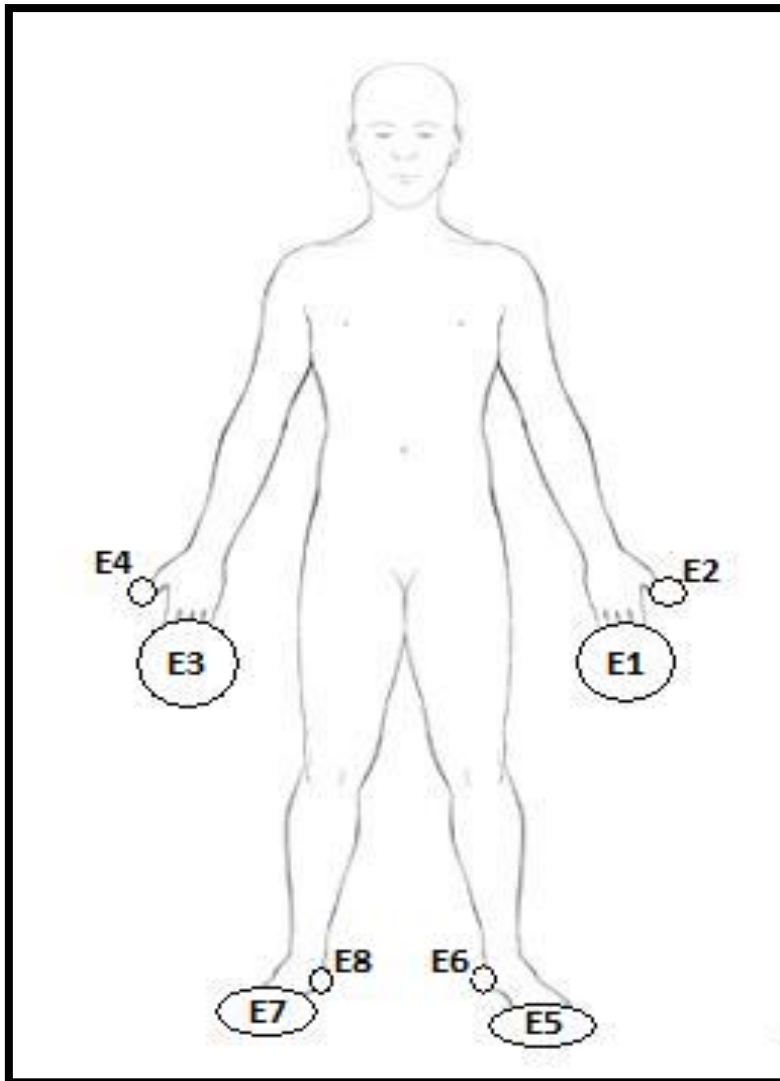


**Figure 3-2: Position of 8 electrodes for SBIA measurement.**

The device showed an error when electrode E1 and E2 (Figure 3-2) were covered when the estimate of the right arm was being made. The same was observed when E3 and E4 were covered during the estimate of the left arm. This shows that any of these 4 electrodes is the source of current (one on each side). When the estimate on the right leg was being made and E1 was blocked the device showed an error but a correct estimate of the right leg was given when E2 was covered. The same pattern was observed with E3 and E4. Therefore it can be concluded that E1 and E3 are the current sources and E2 and E4 are the voltage pickup electrodes. This is in line with

the segmental impedance approach proposed in Organ & Bradham 1994 and will be detailed exhaustively in section 3.2. Hence to make an estimate of the arm segments the BC-545 passes a current from hand to the foot and records voltage between the two hands (Table 3-1). A similar approach was taken to determine the sink electrodes out of E5, E6, E7 and E8, however, although wrong estimates of segments were observed the sink and voltage pickup electrodes could not be distinguished conclusively, but the most likely arrangement of electrodes is indicated in Table 3-1.

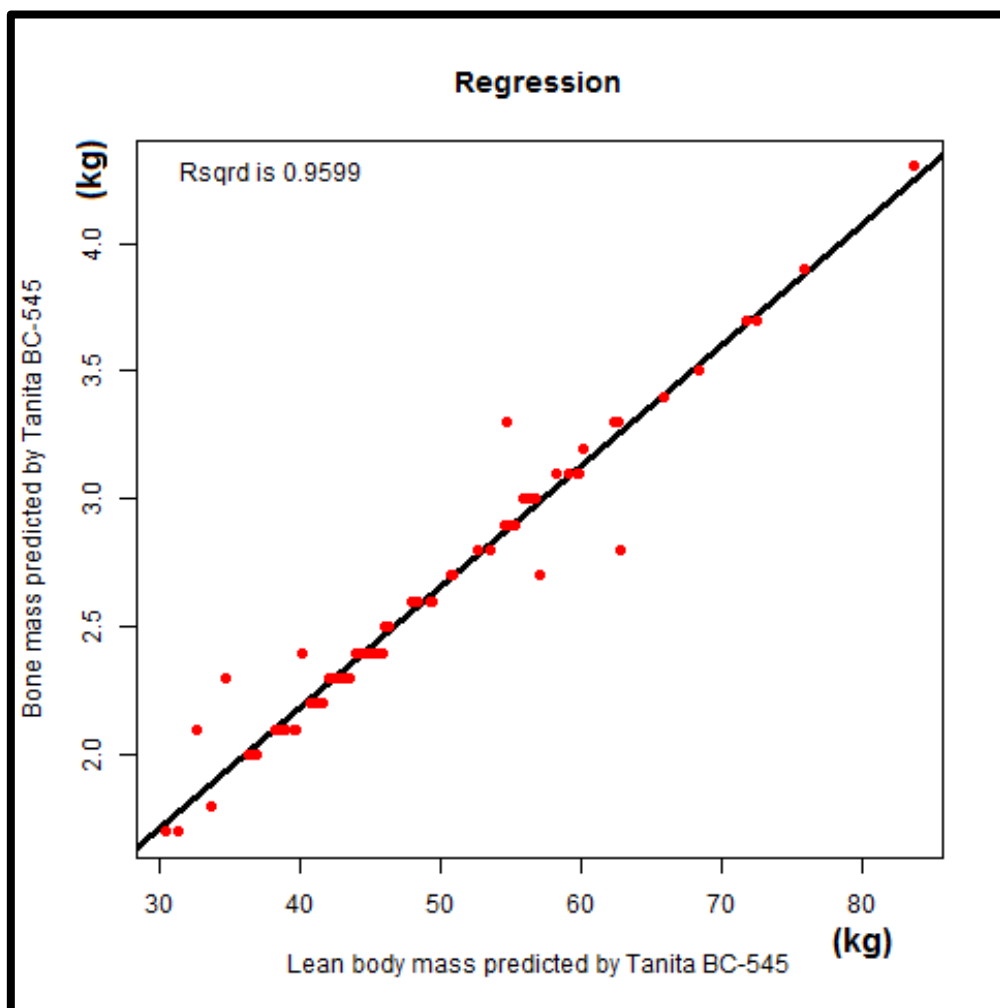
**Table 3-1: Shows the most likely assignment of electrodes on the Tanita BC-545.**

<b>Electrode label (Figure 3-2)</b>	<b>Electrode function</b>
<b>E1</b>	Current source positive on left side.
<b>E2</b>	Voltage sense on left arm.
<b>E3</b>	Current source positive on right side.
<b>E4</b>	Voltage sense on right arm.
<b>E5</b>	Current source negative on left side.
<b>E6</b>	Voltage sense on left leg.
<b>E7</b>	Current source negative on right side.
<b>E8</b>	Voltage sense on right leg.

### **3.1.2 Body composition estimates from Tanita BC-545:**

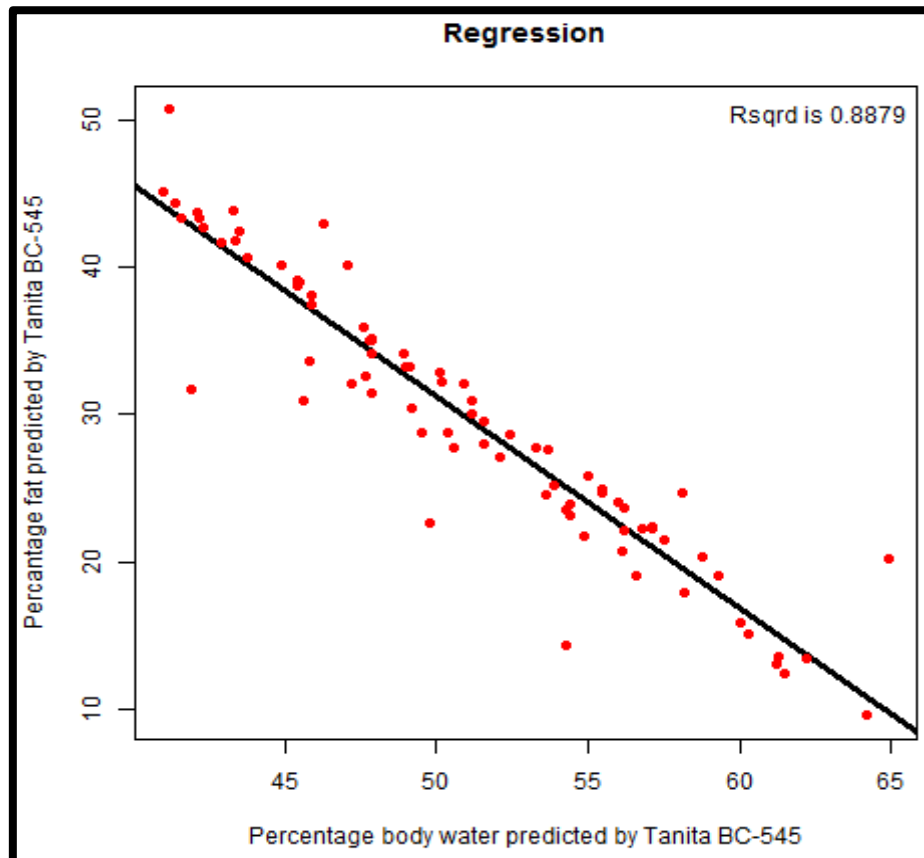
Analysing the body composition estimates from the BC-545 provided some vital insights into the functioning of the device as is presented here. In order to do this previously collected body composition estimates (81 volunteers, ethical approval reference REC08/H1210/17) from the BC-545 were analysed. Analysis of the body

composition results showed that the device used a direct linear relationship to predict bone-mass from lean-mass or vice versa (although the former is more likely to be the case) this is illustrated in Figure 3-3 with an Rsq of 0.96. A similar direct linear relationship was revealed between percentage TBW and percentage fat-mass estimates as shown in Figure 3-4 and has an Rsq of 0.89 (with a negative slope). The negative slope indicates that there is an inverse relationship between TBW



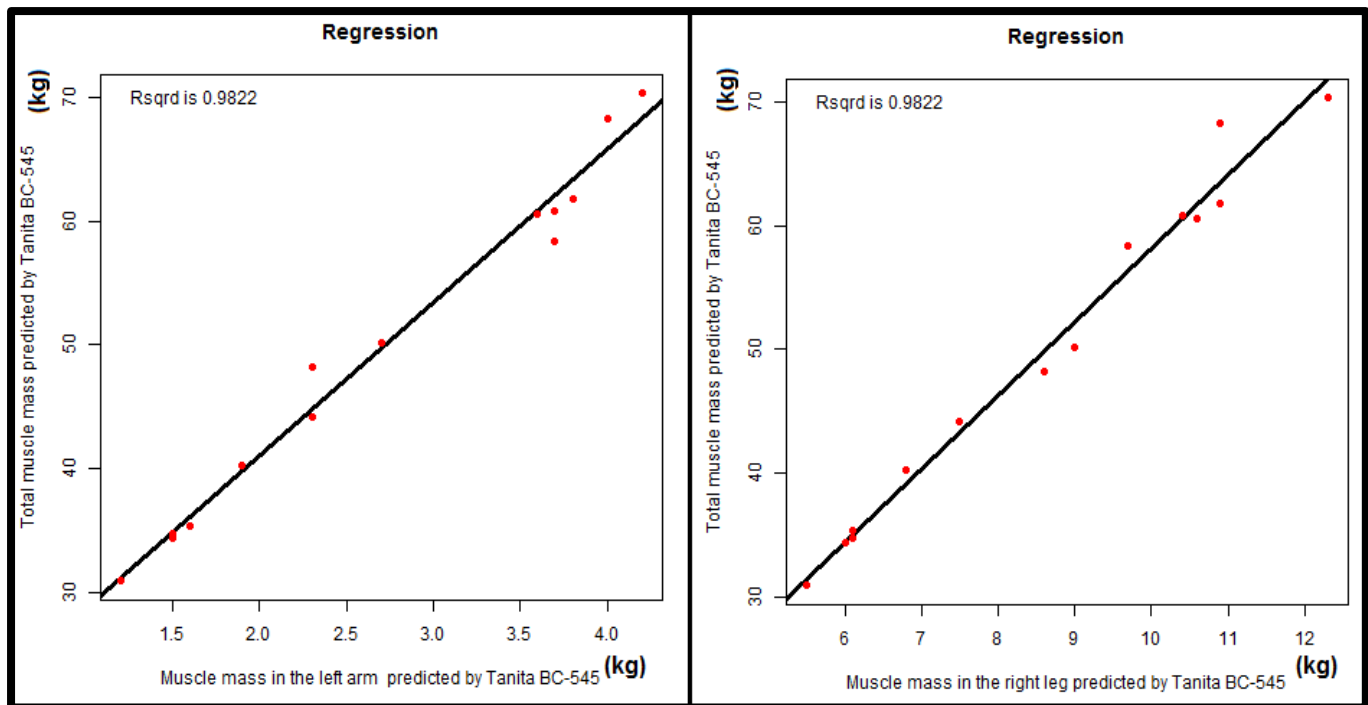
**Figure 3-3: Shows the linear plot between bone mass and lean body mass predicted by the Tanita BC-545. The results presented here are from 81 volunteers who participated in a previous study at the university (n = 81). A strong linear relationship with Rsq of 0.96 was observed.**

and fat-mass. Hence the device assumes fat-mass has no water, this method has been described in section 1.8.1. This also explains the reason for percentage estimates for fat-mass (given by the device) as opposed to kilogram estimates for lean-mass.



**Figure 3-4: Shows the linear plot between percentage body water and percentage body fat predicted by the Tanita BC-545. A strong linear relationship with Rsq of 0.89 was observed.**

Other moderate relationships ( $0.85 > \text{Rsqr} > 0.7$ ) were observed between bone-mass & height, weight and lean-mass & height, weight. But in essence it can be seen that some body composition parameters estimated by the BC-545 are obtained from other parameters using linear relationships most likely involving just one predictor variable. Segmental composition (tissue-mass in the limbs and trunk) results from the device also followed a similar trend.



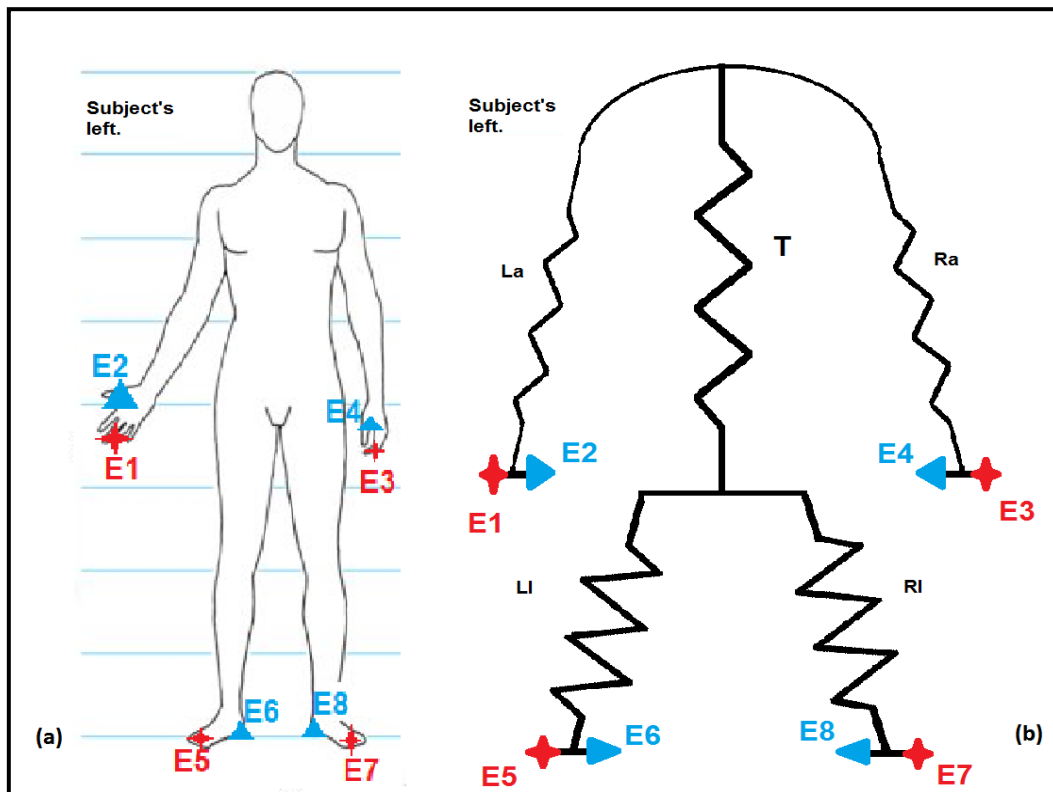
**Figure 3-5: Shows the correlation between total muscle-mass predicted by Tanita BC-545 and muscle-mass in the left arm and left leg. There appears to be a strong correlation between the two predicted quantities (segmental data from 14 volunteers, n = 14).**

Figure 3-5 illustrates this, a substantial correlation ( $R_{sq} 0.98$ ) can be observed between the segmental muscle estimates and the whole-body muscle-mass estimates showing a possible use of whole-body estimates to make segmental estimates. The study of the functioning of the Tanita BC-545 provided an insight into the operating procedure of commercial SBIA devices and also showed a high degree of agreement between SBIA procedures and estimation methods in literature and in practice.

### **3.2 Segmental bio-impedance measurement:**

The procedure to obtain impedance from the five body segments of interest is detailed here. In order to perform SBIA measurement a set of eight electrodes are required. As described

earlier in section 1.6 whole-body BIA uses two pairs of surface electrodes, one pair to introduce current into the subject and the other to sense the voltage response to this current flow. SBIA requires two pairs of current source electrodes (shown in red Figure 3-6) and four voltage sensing electrodes (shown in blue Figure 3-6) with selectable pairs to determine the impedance of the 5 segments.



**Figure 3-6: Shows electrode placement on palms and feet of individual for S-BIA measurements. Stars (in red) represent current source electrodes and triangles (in blue), the voltage sensing electrodes.**

Electrodes E1; E5 is the first current source pair and E3; E7 the second. The labels Ra, La, RI, LI, T correspond to the impedances of the right arm, left arm, right leg, left leg and trunk respectively. The electrodes (Figure 3-6) are in contact with the subject's palms and soles. To measure the impedance of the left arm (La) a current is passed from E1 to E5 and the voltage measured between E2 and E4. The path between E2 and E4 is a single conductor and the voltage along this path in theory should remain constant (Organ & Bradham 1994) provided the input impedance of the voltage recording device is a few hundred mega ohms.

Therefore the voltage between E2 and E4 can be approximated to be between the right shoulder and E2. This gives the voltage across the left arm, and impedance La can be determined since current (I) is known (Organ et al., 1994). A similar approach can be applied to the measured voltage between E4; E8, E6; E8 and E2; E6 to obtain impedances T, LI and total body impedance (Wb1; first estimate of whole-body impedance measured from left) respectively. An analogous method when repeated when current flows between E3; E7 (second current source pair passes current through subject's right) gives us the impedances Ra, RI and a second estimate of T and Wb2 (second estimate of whole body impedance measured from right) (Organ et al., 1994). Table 3-2 summarizes the procedure described above. It is to be noted that, in theory, the impedances from the arm, trunk and leg behave as impedances connected in series (La+T+LI) and form whole-body impedance from the same side Wb1 (Figure 3-6).

**Table 3-2: Shows electrode pair configuration for measuring voltage across different segments.**

<b>VCCS connected between.</b>	<b>Voltage measured between.</b>	<b>Impedance measured for</b>
<b>E1 &amp;E5</b>	E2&E4	Right arm (Rh).
	E4&E8	Trunk impedance 1 (T).
	E6&E8	Right leg (RI).
	E2&E6	Whole body 1 (Wb1).
<b>E3&amp;E7</b>	E4&E2	Left arm (Lh).
	E2&E6	Trunk impedance 2 (T).
	E8&E6	Left leg (LI).
	E4&E8	Whole body 2 (Wb2).

## Chapter 4 Implementation of S-BIA protocol

The scheme presented in the previous section can be implemented with the use of two electronic components; an single-pole double-throw (SPDT) switch (to direct the current between the current source pairs, E1;E5 and E3;E7) and multiplexers (to select voltage measurement pairs). Figure 4-1 shows their functional diagrams. The SPDT switch connects one of the inputs S1 or S2 to the output COM depending on the control signal (D) given to the device. The 4:1 multiplexer connects one of the 4 inputs (A, B, C or D) to the output M depending upon the control signal given to it. It is noted that both these devices are digitally controlled. The data acquisition card (DAQ) used in this system (device described later in this chapter) provides the necessary digital output to control the multiplexer and the SPDT switch. The truth tables for an SPDT switch and the multiplexer are given in Table 4-1 and Table 4-2 respectively.

**Table 4-1: Shows the truth table for SPDT switch.**

Control Signal (D).	Output (COM).
0	L1
1	L2

**Table 4-2: Shows the truth table for 4:1 multiplexer.**

Control signal (S1, S2).	Output (M).
0, 0	A (E2)
0, 1	B (E4)
1, 0	C (E6)
1, 1	D (E8)

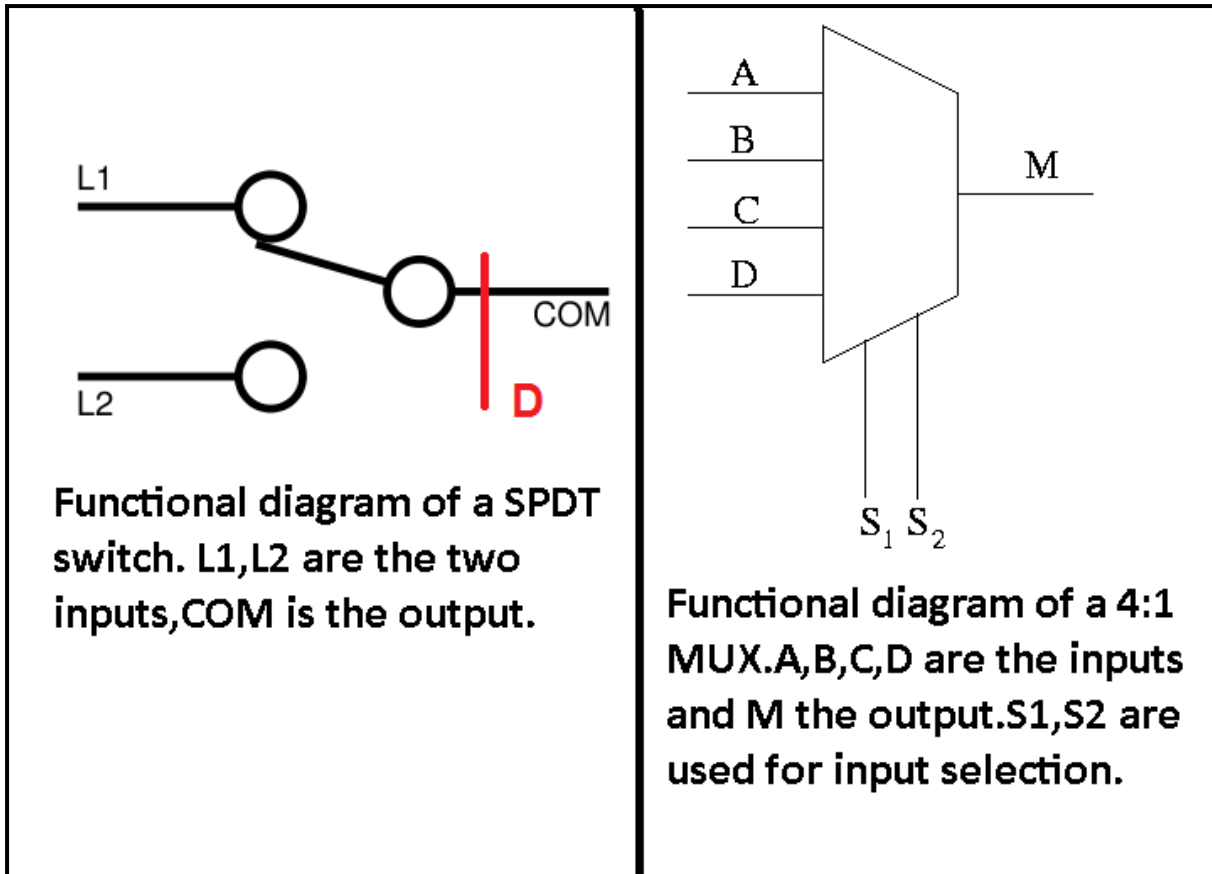


**Figure 4-1: Shows functional diagrams of SPDT switch (left) and multiplexer (right).**

**4.1 Voltage control current source (VCCS) switching:**

To switch the current between the two electrode pairs E1;E5 to E3;E7 two SPDT switches are used and connected with the VCCS as shown in Figure 4-2. When the control signals DA and DB are both 0, the VCCS is connected between E1; E5 hence allowing the current to flow through the left arm to the left foot of the subject. When the control signals are both 1, the SPDT switches change state for the current flow to occur between E3 and E7 forcing current to flow from the right arm to the right foot (Table 4-3). Hence switching the VCCS between two pairs of contact electrodes is accomplished.

Table 4-3: Shows the truth table for control bits of two SPDT switches.

Control digital inputs to SPDT switches (DA, DB)	Current flow pair.
0 0	E1,E5
1 1	E3,E7

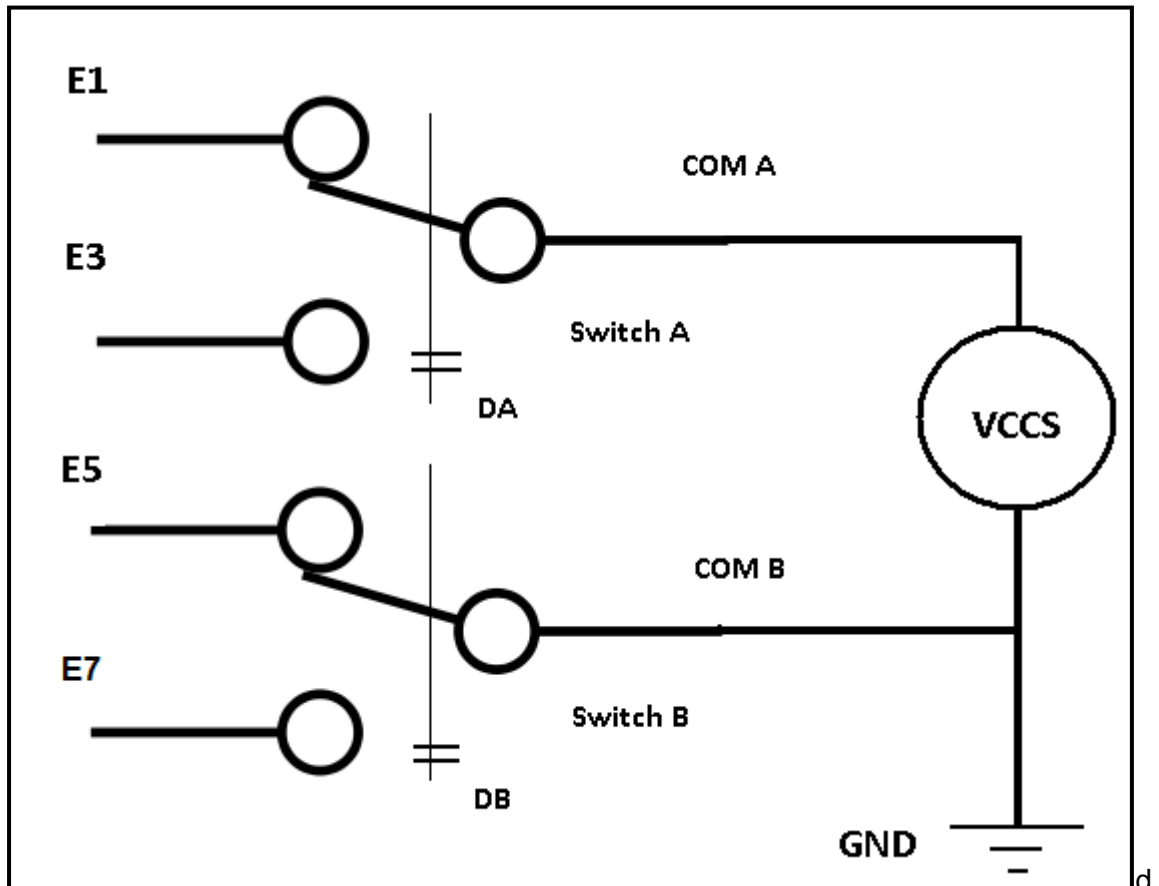
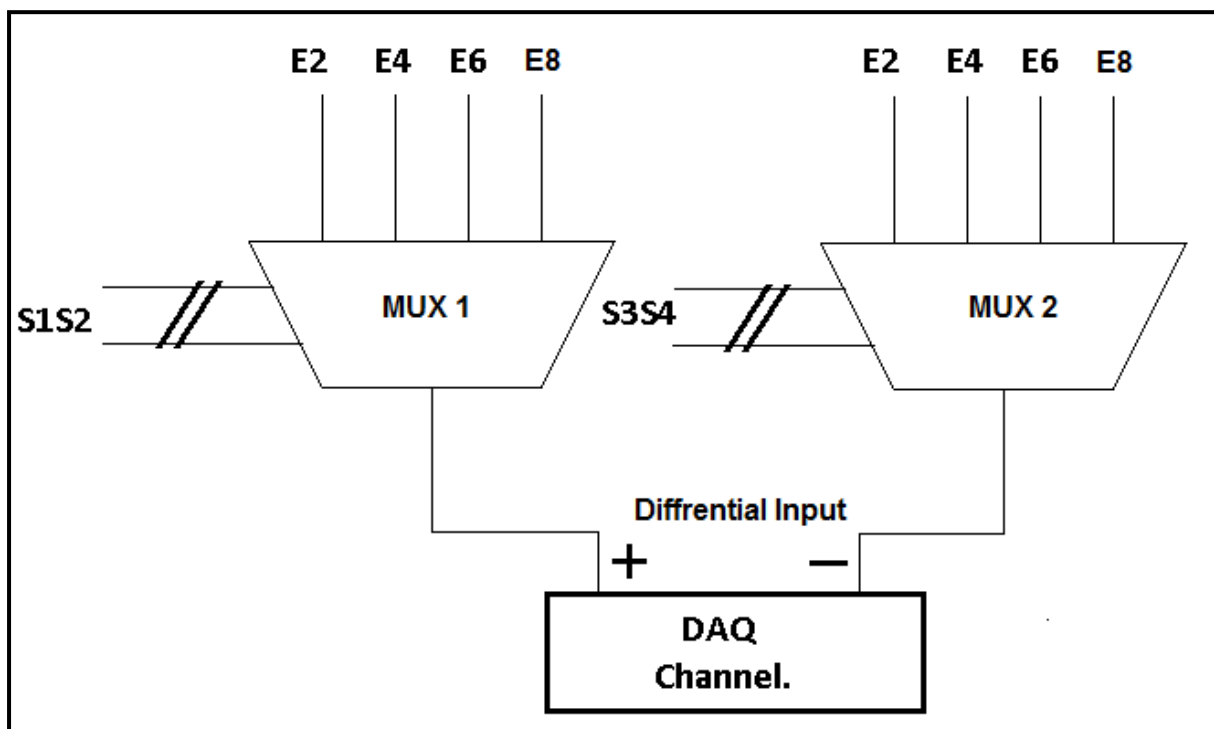


Figure 4-2: Two SPDT switches connected to VCCS to allow VCCS switching between two pairs of electrodes (E1;E5 and E3;E7).

## 4.2 Electrode pair selection for impedance measurement:

In the previous section the switching of the VCCS was shown, in this section the selection of electrode pairs (while current flows through one of the current source electrode pairs) for voltage measurements using multiplexers will be illustrated. Consider Figure 4-3, in which two 4:1 multiplexers have their respective inputs tied (connected or shorted) to one another, also these inputs are connected to the remaining electrodes. Therefore each the four voltage

measuring electrodes (E2, E4, E6, E8) is connected to inputs of both multiplexers (MUX1 and MUX 2 in Figure 4-3). With the aid of the truth table (Table 4-2) and bearing in mind two multiplexers are used (hence four digital control signals are required) any combination of electrodes can be selected for voltage measurement, e.g. to select E6; E8 control signal (S1,S2) 1,0 is given to the first multiplexer and 1,1 to the second (S3,S4). Similarly with the aid of appropriate digital control signals any combination of voltage measuring electrodes can be selected for impedance measurements across the segment of interest.



**Figure 4-3: Shows two 4:1 multiplexers used for electrode pair selection with their outputs connected to a differential DAQ channel.**

### 4.3 Integrated system function:

With reference to the previous sections the whole system is implemented using ICs (integrated circuits). The working version of the VCCS will be described subsequently and also the function generator providing the 50 kHz sinusoidal signal fed to the VCCS. In this section the emphasis will be on the SPDT switches and the multiplexers. To implement the VCCS switching the AD436B dual SPDT package by Analog Devices, U.S.A is used. It is a

16 pin DIP and houses two SPDT switches in one IC which is ideal for this system since it requires two SPDT switches. AD436 takes two digital inputs (one for each switch it houses). To implement the electrode selection for impedance measurement two AD509F multiplexers by Analog Devices, U.S.A are used. The AD509 takes three digital control bits, one which enables (EN) the IC to function and two other bits for input selection (Table 4-4). Two AD509 ICs are required to implement the voltage-sense electrode pair selection. Hence 8 bits are required altogether to execute control over the switches and the multiplexers. The significance and order of the bits are shown in Table 4-4.

**Table 4-4: Shows the significance and order of bits used to control the switches and multiplexers.**

Bit 0 (DA)	Bit 1 (DB)	Bit 2 (EN1)	Bit 3 (EN2)	Bit 4 (S1)	Bit 5 (S2)	Bit 6 (S3)	Bit 7 (S4)
Control bit for first SPDT	Control bit for second SPDT	Enable bit for first multiplexer	Enable bit for second multiplexer	2 Control bits for first multiplexer.		2 Control bits for second multiplexer.	

**Table 4-5: Shows the eight digital control states to obtain segmental bio-impedance.**

VCCS connected between.	Bit 0 (DA)	Bit 1 (DB)	Bit 2 (EN1)	Bit 3 (EN2)	Bit 4 (S1)	Bit 5 (S2)	Bit 6 (S3)	Bit 7 (S4)	Electrode pair selected.	Impedance measured
E1&E5	0	0	1	1	0	0	1	0	E2,E4	Right arm.
	0	0	1	1	1	0	1	1	E4,E8	Trunk impedance 1.
	0	0	1	1	0	1	1	1	E6,E8	Right leg.
	0	0	1	1	0	0	0	1	E2,E6	Whole body 1.
E3&E7	1	1	1	1	1	0	0	0	E4,E2	Left arm.
	1	1	1	1	0	0	0	1	E2,E6	Trunk impedance 2.
	1	1	1	1	1	1	0	1	E8,E6	Left leg.
	1	1	1	1	1	0	1	1	E4,E8	Whole body 2.

Table 4-5 illustrates the digital sequence used to acquire the impedance measurements of the 8 different segments of the subject's body. During the first four digital states (DA, DB are 0, 0 respectively) of the device the VCCS is connected between E1;E5 (Figure 3-6, Table 4-5) hence the current flows from the left arm to the left foot. While the current is still flowing between E1;E5 various combinations of multiplexer control bits (S1&S2 for multiplexer 1 and S3&S4 for multiplexer 2) are used to select any pair of the voltage measuring electrodes, like for selecting E4; E8 to obtain 'Trunk impedance 1', S1, S2, S3, S4 are 1,0,1,1. Now for the next four digital states (DA, DB are 1, 1 respectively) the VCCS is connected between E3; E7 which forces the current through the right arm of the subject to his right foot, again various combinations of multiplexer control bits are used to measure the impedance of the segments of interest. When comparing Table 4-5 to Table 3-2 it can be seen how the concept for segmental BIA has been transformed into an actual implementation using ICs and their control bits. But transforming this idea to an actual circuit required additional steps, the first one being designing a schematic with the current source connected to SPDT switches such that current direction (through the subject) can be switched between E1; E5 and E3; E7. Also electrodes E2, E4, E6 and E8 need to be connected to the four inputs of both multiplexers; this can be seen in Figure 5-1. The VCCS is connected between pin 3 and pin 11 (ground via. 100Ω resistor) of the SPDT IC, thus the input current to be directed between E1; E5 first followed by E3; E7. When IN1 (pin1) and IN2 (pin 9) are both low (logic 0) electrodes E1 and E5 are connected to the VCCS (pin 3) and ground (pin 11), whereas E3 and E7 are connected to the VCCS and ground when IN1 and IN2 are high (logic 1). The 100Ω series resistor (R12) connected between pin 11 and circuit ground helps to measure the current flowing through the segment of interest to provide more reliable impedance estimates. As can be seen for the multiplexers (MUX1 and MUX2) the inputs are shorted (pin 4, pin5, pin 10 and pin11) and connected to each of the voltage measurement electrodes (E2, E4, E6 and E8). The output of the multiplexers (pin 6 on both) is connected to the voltage recording system (DAQ card) detailed next. It is to be noted that the schematic does not include an anti-aliasing filter because the DAQ card was bandlimited to

400kHz and the signals were sampled at a minimum sampling rate of 1MSa/s (higher than Nyquist sampling rate of 800kSa/s for upper bandlimit of 400kHz, refer 2.2.1).

#### **4.4 Summary:**

In this chapter we have described the segmental bio-impedance measurement protocol and implemented this protocol using readily available components. Also discussed is the translation of this protocol into digital control bits to acquire bio-impedance voltage and current signals from 8 different segments of a subject's body.

## **Chapter 5      System components and testing: V1 to V4.**

### **5.1 Introduction:**

The protocol described previously can be utilized to measure segmental body impedance but the performance of different sections of this measurement was to be evaluated. Figure 5-2 shows the major parts of the segmental bio-impedance measurement system. Here the switching scheme is realised using multiplexers and SPDT switches, their performance can be deduced from their respective data sheet. On the signal acquisition side the datasheet of the DAQ (data acquisition card) used will dictate its performance. The card utilized to achieve signal acquisition in versions 2 through 4 is the Agilent U2531A. The datasheets for various components used for this system are listed in Appendix 2. This leaves two sections of the designed system whose performance needs to be evaluated, namely the VCCS and the electrodes. Since both of these are project specific their performance characteristics (particularly the VCCS) are vital to the overall system. The details on various components of the devices can be found in Table 5-1. As a second step to the development of the device, a single frequency S-BIA system was realised (V2, chapter 6) and the multi-frequency operation feature was added as a third developmental step (V3, Chapter 7). V3 of the device was further enhanced and is presented as V4 (section 7.1), the final version of the device. The single frequency S-BIA system like the whole body BIA system (section 1.6) will operate at 50kHz. The following sections will illustrate the design, selection of components and test performance of the VCCS and electrodes used for the system at hand.

**Table 5-1 : Shows the developmental stages and versions of the BIA device. Also listed are the details on various components of the device.**

	<b>Sinusoid source</b>	<b>Current source (VCCS)</b>	<b>VCCS switching</b>	<b>Voltage sense electrode switching</b>	<b>Data acquisition</b>
<b>Version1 (Whole body system section 1.6)</b>	LF/1 function generator unit	Howland using matched resistors and OPA2107	N/A	N/A	NI DAQ6015
<b>Version 2 (Segmental single frequency system, Chapter 6)</b>	XR2206 IC	Howland using matched resistors and OPA2107	SPDT, AD436	MUX1 & MUX 2 using AD509	Agilent U2531A
<b>Version 3 (Segmental multi frequency system, Chapter 7)</b>	XR2206 IC	Howland using matched resistors and OPA2107	SPDT, AD436	MUX1 & MUX 2 using AD509	Agilent U2531A
<b>Version4 (improved version 3, section 7.1 )</b>	XR2206 IC	Howland using only INA110KP	SPDT, AD436	SPDT, AD436	Agilent U2531A

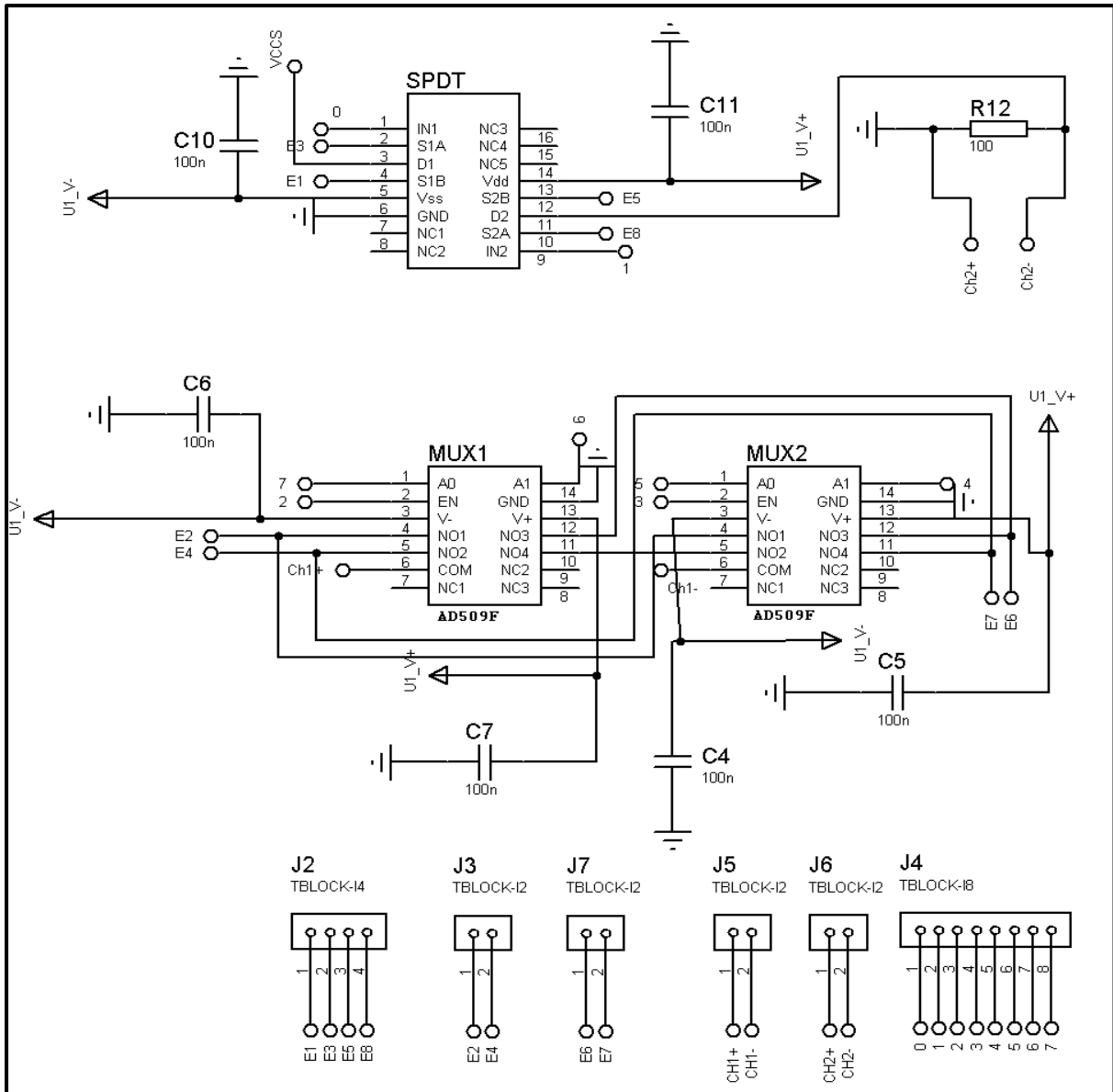


**Figure 5-1: Shows the schematic for the VCCS switching and measurement electrode multiplexing scheme.**

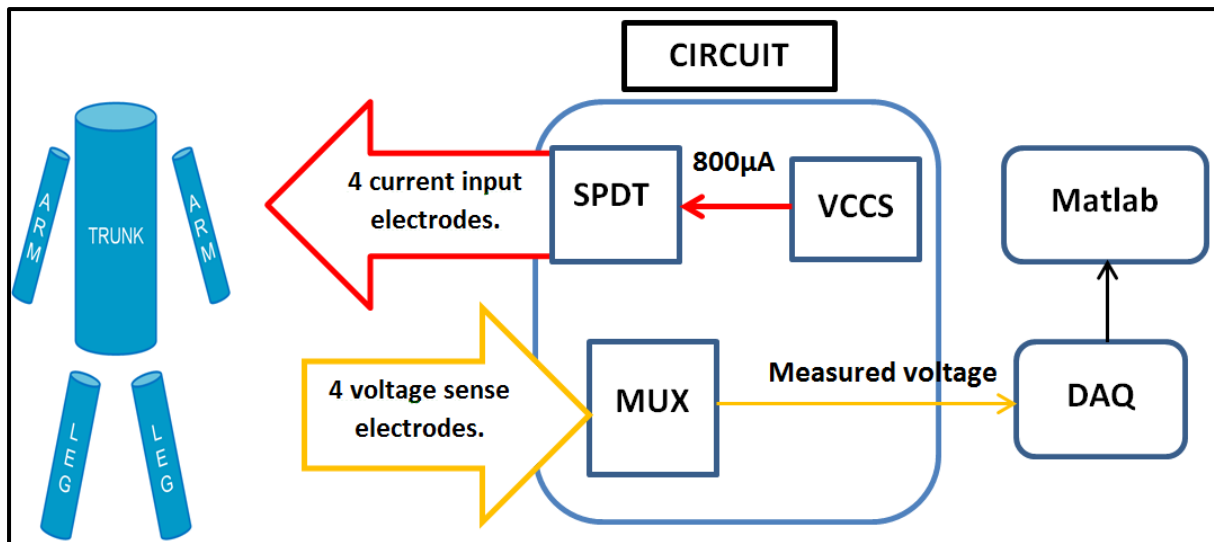


**Figure 5-2: Shows the major blocks in the designed segmental bio-impedance measurement system.**

## 5.2 Voltage measurement setup:

The whole-body BIA system is elucidated in the section 1.6 and is presented as version 1 (V1) of the device. V1 used a National instruments data acquisition card to acquire signals. Figure 5-2 shows the major blocks in the envisaged SBIA system. For acquiring voltage responses to the current (current passed by VCCS) through the segment of interest in the SBIA system a more advanced data acquisition card was used. The analog input channels to most data acquisition cards, (like the DAQ6015 used with V1) the inputs are multiplexed therefore their sampling rate (per channel) is halved with the use of each additional input channel. For the SBIA system we need two input channels one to record the voltage at the multiplexer outputs (pin 6 in MUX1 and 2; labelled as CH1+ and CH1- in Figure 5-1) and the other to measure the current flowing through (R12) the segment of interest (connected across R12; labelled as Ch2+ and Ch2- in Figure 5-1). Also a high sampling rate was desired which remained unchanged with addition of new channels and the multi-frequency system (maximum frequency of operation 100kHz, described in later chapters) means a higher sampling rate than that provided by DAQ6015 was required (200kSa/s). An Agilent U2531A data acquisition card manufactured by Agilent technologies fit this profile. It had four

simultaneous sampling channels (not multiplexed) and had a sampling rate of 2 MSa/sec, 14-bit input resolution, input impedance of  $1\text{G}\Omega$  coupled with  $100\text{pF}$  capacitor and CMRR of 64 db. It also had 24 digital output channels which were used to generate the digital bits necessary to control the SBIA device (Table 4-5). Its inputs and outputs could be readily controlled from the Matlab environment with the data acquisition toolbox. Additionally to the Agilent U2531A is band-limited to 400kHz which would negate the problems which would arise due to aliasing (explained in 2.2.1) because the signals are sampled at least 1MSa/sec. Hence the U2531A unit was used for the purposes of acquiring voltage signals and producing digital signals to control the envisaged SBIA device.

### **5.3 The Voltage controlled current source (VCCS):**

The VCCS is a vital component of any bio-impedance measurement system and its performance will dictate the selection of parameters for the designed system, such as input current magnitude and supply voltage range, such aspects will be detailed in this section. The VCCS (current source) needs a sinusoidal signal source which is fed to a Howland current pump. In section 1.6.1 the sinusoidal source was a separate unit requiring separate mains power supply. But for the new segmental system an IC signal source was used which enables battery power operation and incorporation on a compact PCB board. As for the actual current source, a Howland current pump circuit is utilized, both of which will be scrutinised in the following two sections.

#### **5.3.1 The XR2206, sinusoidal function generator:**

The XR2206 is a tuneable function generator IC developed by Exar corporation which is capable of producing sinusoidal, sawtooth and triangular signals from 0.01Hz to several megahertz. For the single frequency SBIA prototype the frequency of choice was 50kHz. The circuit utilizing an XR2206 to generate the desired sinusoid (at a magnitude sufficient to cause the Howland pump to push  $800\mu\text{A}$  through the tissue under observation, chosen

experimentally) is shown in Figure 5-3. Here the output voltage is set by resistor R9 in the circuit connected to pin 3 of the IC (replaced by variable resistor on PCB to allow current magnitude adjustment in VCCS). The frequency of the output is set by timing components C13 (connected between pin 5 and 6) and R1 (connected between pin 7 and circuit ground). The output frequency as reported in the datasheet is the inverse of the product of R1 and C13. The output of the IC (pin 2) labelled as 'Csin' is connected to the input of the Howland current pump (Figure 5-6). When tuned and tested the circuit provided a stable 50kHz sinusoid at an amplitude required to allow the Howland current pump to generate 800 $\mu$ A through the load.

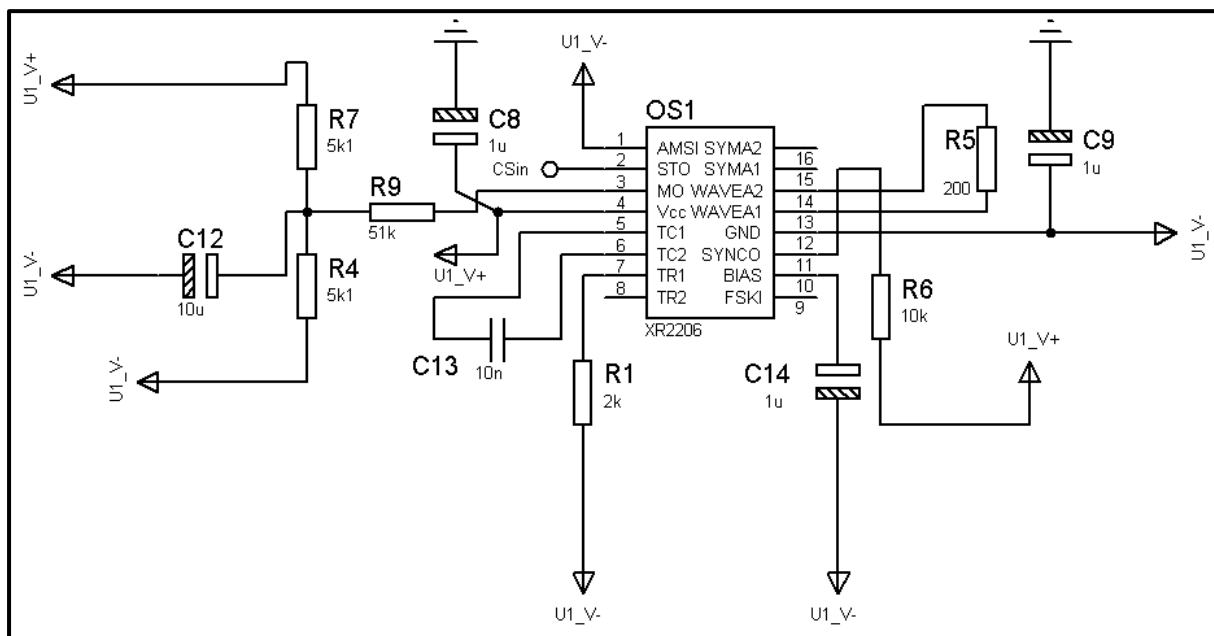


**Figure 5-3: Shows the circuit utilizing XR2206 to generate a 50 kHz sinusoid for bio-impedance measurement.**

### 5.3.2 The Howland current pump:

The Howland current pump is used extensively as a current source circuit in BIA and EIT (electrical impedance tomography). The circuit ensures that a safe constant current passes through the volunteer. It was first reported in 1965 (Pease 2008). Figure 5-4 shows the basic Howland current pump. The circuit can be analysed formally but an intuitive approach will

suffice to understand it's working. As can be seen the output from the op-amp is feedback to the inverting and non-inverting input in equal strength because  $R1/R2=R3/R4$ . This would appear as common mode signal at the op-amp input and will have no effect on the op-amp output (assuming op-amp is ideal). Therefore when the input voltages  $V_{IN+}$ ,  $V_{IN-}$  ( $V_{IN-}$ ,  $V_{IN+}$  are the voltages to the inverting and non-inverting input of the operational amplifier) are the same the output is indeterminate. Now when an offset is introduced between voltages  $V_{IN+}$ ,  $V_{IN-}$ , because of the equal feedback to both input terminals the op-amp output is forced to push a current through  $Z_L$  in order to equate the voltage difference at the input terminals (Hickman 1999). The magnitude of this current is  $(V_{IN+}-V_{IN-})/Z_L$ . Therefore the output current is directly controlled by the input voltage, giving the circuit its name; voltage controlled current source (VCCS). A major problem with this circuit is the resistors are to be very closely matched to ensure high output impedance, which normally degrades at high frequencies (Hong et al. 2007). Typically trim pots are utilized to achieve close resistor matching. Another disadvantage of the basic Howland circuit is its efficiency, because when the load voltage changes are large the op-amp has to work hard to push a constant current through the load increasing power demands from the supply. To circumvent some of these problems the modified Howland current source constructed with two operational amplifiers (Figure 5-5) was adopted. As can be seen (when compared to Figure 5-4), the non-inverting feedback path of the op-amp includes an additional resistor and a voltage follower circuit. Using two resistors in the non-inverting feedback path and connecting the load in between reduces the power consumption at R1 (compared to the basic Howland circuit). The voltage follower circuit after the load ensures that all the current from the op-amp output flows through the load because of its large input impedance. A modified Howland circuit was constructed to fit our purpose and it was tested under varying load and input frequency. This allowed evaluation of the circuit's ability to provide constant current during varying loads and since the output impedance of this circuit is known to vary with increasing input frequency, it was necessary to study the effect of increasing frequency on the output capability of the circuit (to aid extension from single to multi-frequency SBIA system). Figure 5-6 shows a

schematic of the modified Howland current source, this is part of a larger schematic of the entire circuit used to make a PCB board. R5 for the single frequency SBIA device was chosen to remain at  $1k\Omega$  which allowed  $800\mu A$  to pass through the segment of interest at  $50kHz$ . However, to operate at frequencies varying between  $5kHz$  and  $100kHz$  (to accommodate the effect of increased frequency of operation) and reduced supply voltage ( $\pm 9V$ ) the current had to be lowered to  $250\mu A$  for the final multi-frequency SBIA system.  $0.01\%$  tolerance  $10k\Omega$  resistors were used as R1, R2, R3, R4 ensuring close resistor matching which was necessary.

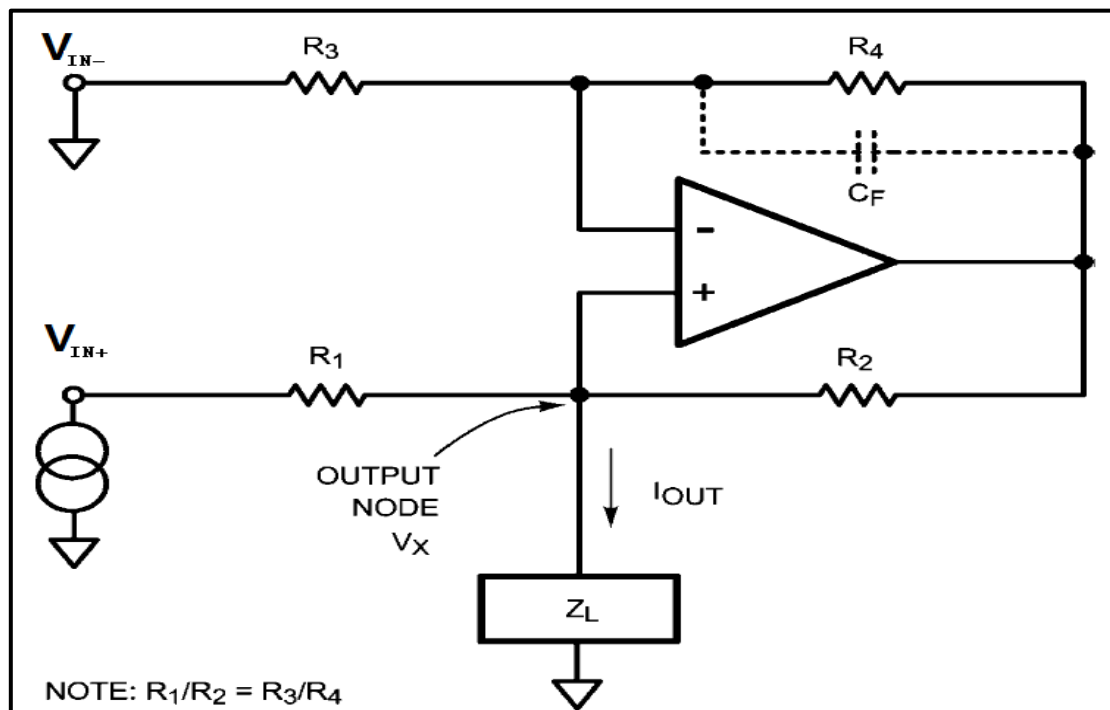


**Figure 5-4: Shows the basic Howland current pump where current flows through load  $Z_L$ .**

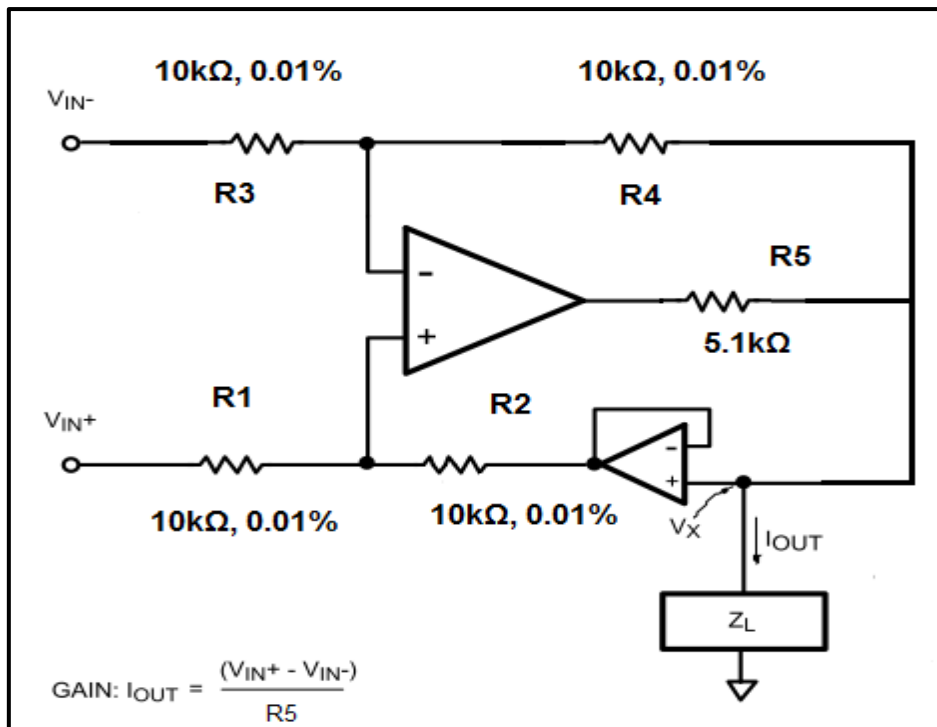


**Figure 5-5: Shows the modified Howland current source constructed using two op-amps. This circuit has higher output current capability and efficiency than the basic Howland circuit shown in the previous figure.**

Since two op-amps were required the low noise OPA2107 dual op-amp IC package by Texas instruments was used. This op-amp has low input bias current, a maximum quiescent current of 2.5mA and a wide supply voltage range of  $\pm 18V$ , these features made this particular op-amp a good choice for this purpose. Labels, 'Csin' and 'VCCS' (Figure 5-6) represent the input (sinusoidal signal) and output node of the circuit respectively. In order to gauge the load bearing capabilities of the circuit, it was connected to loads varying between 0  $\Omega$  to 20 k $\Omega$  with a 100  $\Omega$  shunt resistor connected in series to measure the current. The voltage across the shunt when the load was varying was observed on an oscilloscope. The information in Table 5-2 shows the output current from the VCCS with changing load. The circuit performs optimally when the load varies between 0  $\Omega$  to about 10k $\Omega$ . Beyond 10 k $\Omega$  clipping of the half of the input sinusoid was observed as shown in Figure 5-7. To mimic the effect of a discharged battery (because the final system was battery operated) the circuit was tested at a fixed supply of  $\pm 7.5V$ . The frequency characteristics of the circuit was

evaluated with a  $10\text{k}\Omega$  load and using the input sinusoid from a function generator unit was varied between 100 Hz and 1 MHz, while the current was measured using the same method utilized to evaluate load characteristics of the circuit.

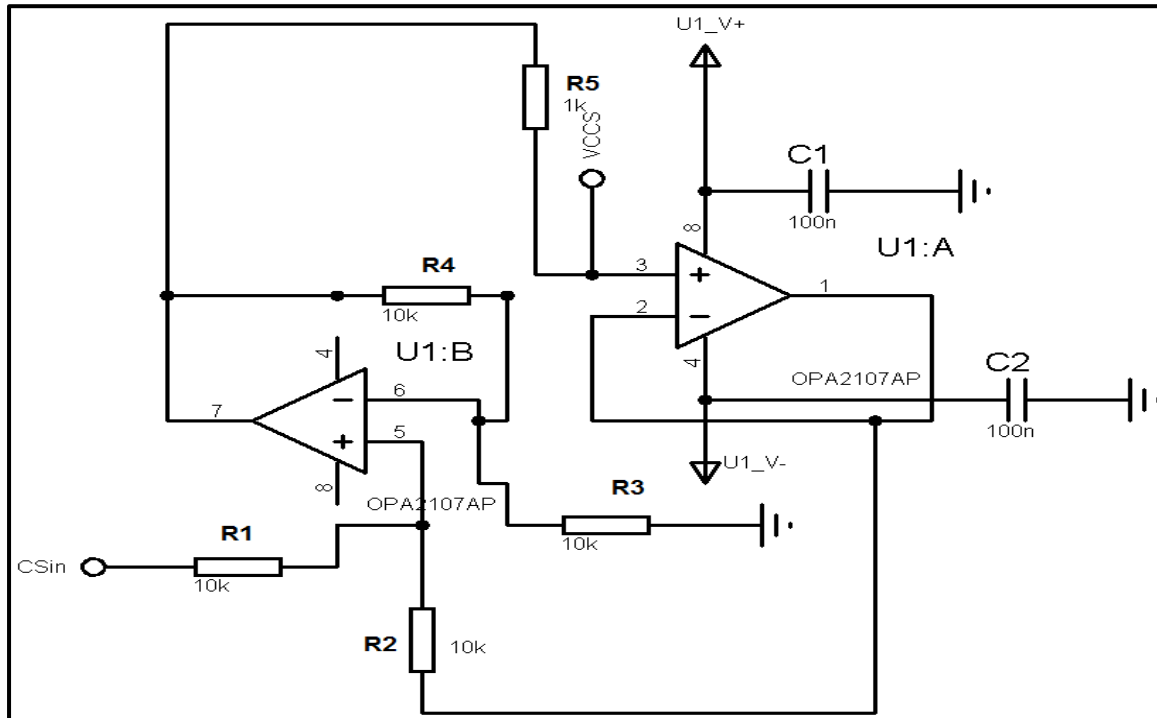


**Figure 5-6: Schematic of the modified Howland current pump (VCCS) used in this project; designed using Proteus ISIS software.**

**Results and conclusion:** Figure 5-8 shows the output current flowing through the load when the frequency was varied. As can be seen the circuit provided a steady constant current up to 100kHz after which the performance of the circuit degraded. This was expected as the output impedance of the circuit is affected at high input frequencies (Hong et al. 2007). Hence 100kHz can be set as the upper limit for the multi-frequency SBIA system that is envisaged.

**Table 5-2: Shows the output current from the designed VCCS at loads varying between 0 and 10k $\Omega$  at two different frequencies; 5kHz and 100kHz.**

Load	Input frequency	
	5khz	100kHz
<b>0</b>	250 $\mu$ A	250 $\mu$ A
<b>1.5<math>\Omega</math></b>	250 $\mu$ A	250 $\mu$ A
<b>100<math>\Omega</math></b>	250 $\mu$ A	250 $\mu$ A
<b>250<math>\Omega</math></b>	250 $\mu$ A	250 $\mu$ A
<b>386<math>\Omega</math></b>	250 $\mu$ A	250 $\mu$ A
<b>500<math>\Omega</math></b>	250 $\mu$ A	250 $\mu$ A
<b>1k<math>\Omega</math></b>	250 $\mu$ A	250 $\mu$ A
<b>5.1k<math>\Omega</math></b>	249 $\mu$ A	249 $\mu$ A
<b>10k<math>\Omega</math></b>	248 $\mu$ A	247 $\mu$ A

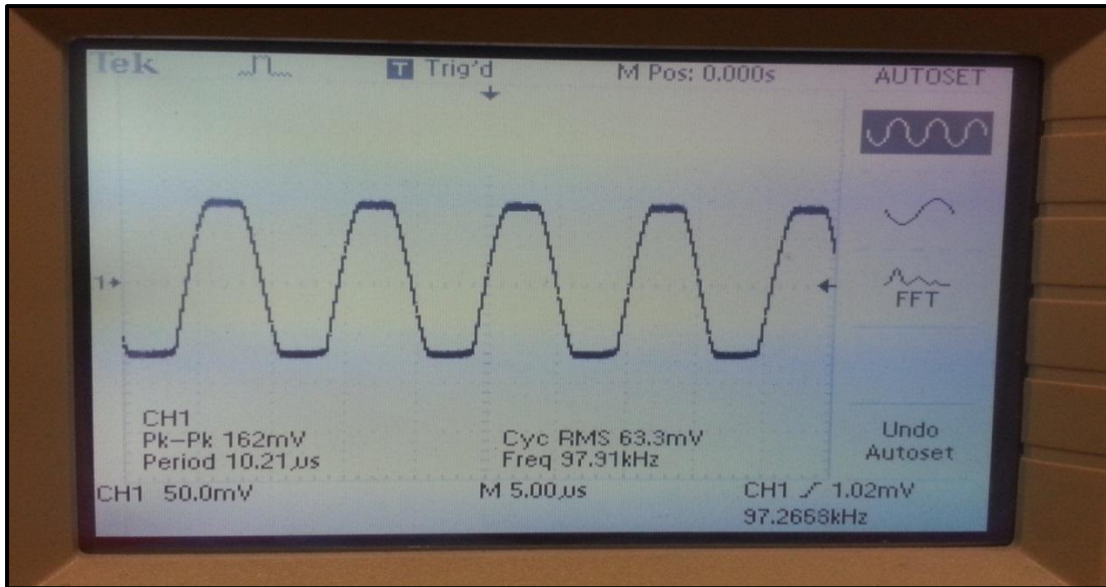


**Figure 5-7: Shows the clipping of the output current from VCCS at loads above 10kΩ. Note: voltage shown in figure is arbitrary; figure only represents the clipping phenomenon which was observed.**

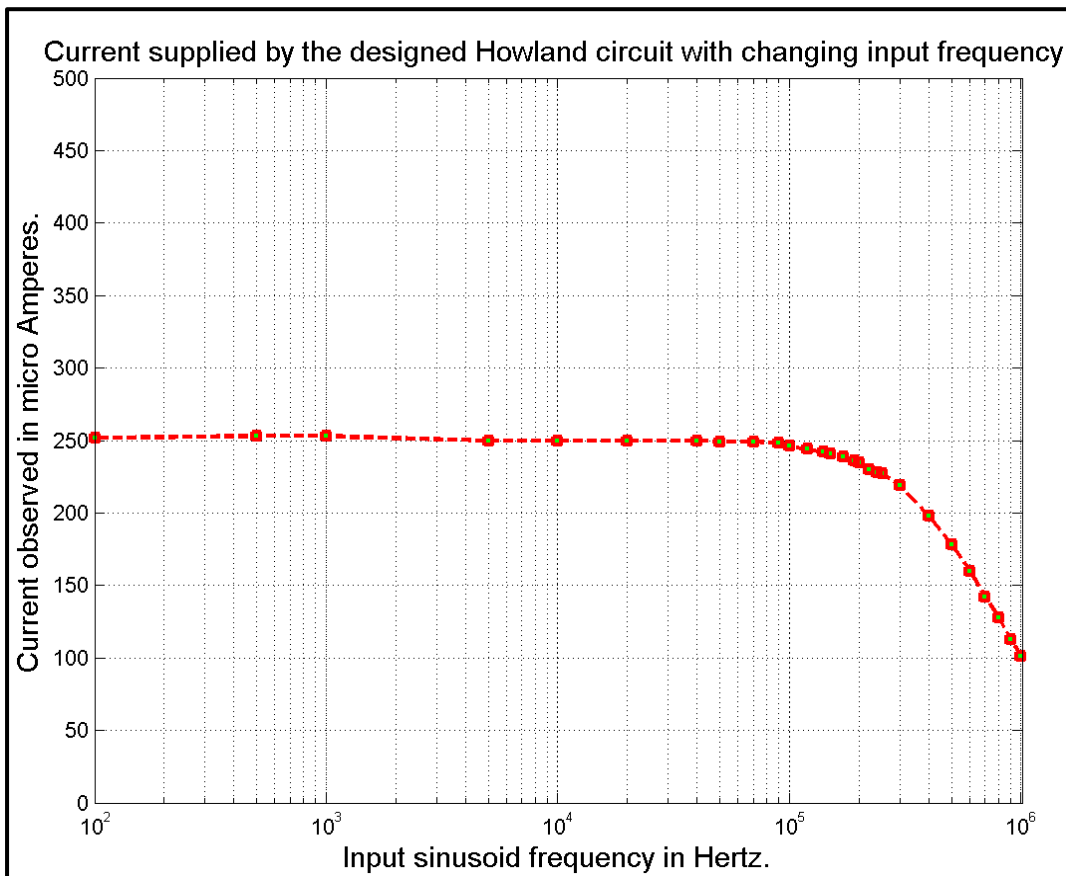


**Figure 5-8: Shows the current supplied by the Howland current source with changing input frequency (x axis is logarithmic).**

## 5.4 Electrodes for the system:

Another vital part of any bio-impedance measurement system is the kind of electrodes used. If not correctly chosen they can give rise to significant problems that make bio-electrical signal analysis difficult. This is because electrode-skin interface impedance has significant effects on the electronic system used to measure bio-impedance (McAdams et al. 1996) (detailed in 1.3.4). From the start of this project it was aimed to make the measurement system simple to operate and convenient for both the operator and subject. The present system utilizes the eight metal-contact type electrodes (two on each hand and foot) from a commercially available bio-impedance device the Tanita BC-545 (Figure 5-9). These electrodes were selected primarily to avoid the use of Ag-AgCl electrodes which can be cumbersome and their use also enabled data from the present study to be compared directly with studies previously conducted at our institution using the same device. But the suitability of these electrodes under our frequency cap of 100kHz was to be evaluated. The electrode-skin interface impedance is known to vary with frequency of signal used and has significant implications in the design of a bioelectrical device (Spach et al. 1966; Marquez et al. 2011; McAdams et al. 1996; Yoo 2011). In order to ensure this impedance was not very large the handheld (e.g. E3 in Figure 5-9) and foot electrode impedance (e.g. E7 in Figure 5-9) was tested under varying frequency. A modified procedure to the one presented in Spach et al. (1966) was used. To measure the electrode-skin impedance a current (800 $\mu$ A) was passed between the test electrode (E3 or E7) and the temporary electrode (T) using the Howland circuit (Figure 5-10). The temporary electrode T and the Howland current pump together form a current path across the electrode impedance being measured. The voltage across a 100 $\Omega$  series resistor helped determine the magnitude of current flowing between E3 (or E7) and T. The potential drop at E3 (or E7) was recorded using a voltage follower from which the impedance was calculated.

**Results and conclusion:** Figure 5-11 shows the electrode impedance for electrode E3 and E7 between 1kHz and 200kHz. As can be seen from the graph the electrode impedance of

both electrodes drops exponentially until about 10kHz. From around 10kHz the electrode impedance is comparable, therefore 10kHz was set as the lower limit on the frequency range of the multi-frequency S-BIA system to be constructed



**Figure 5-9:** Shows the electrodes used in the present system and their labels on a subject’s palms and underside of their foot. In essence the subject would stand on the foot electrodes and grab the hand electrode attachment. Note: electrodes E4 and E1 are hidden from view.

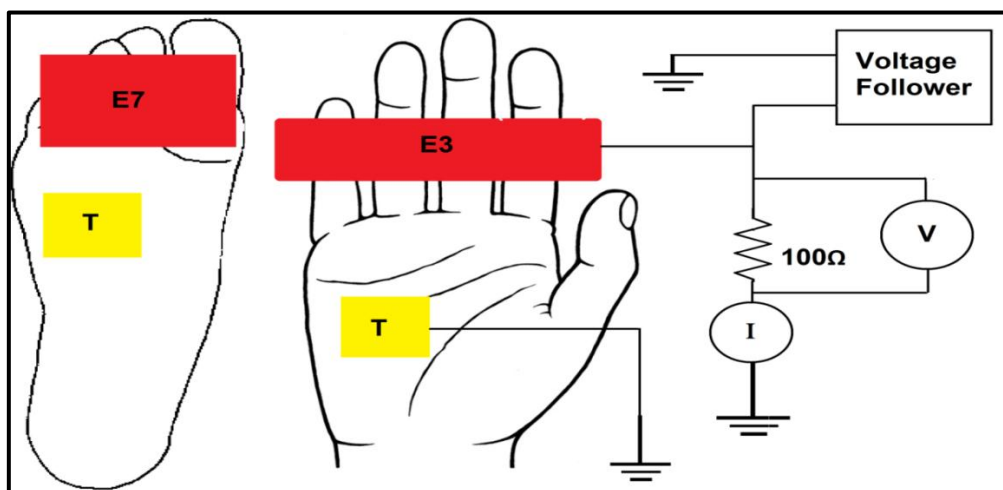


**Figure 5-10:** Shows the setup used to measure electrode-skin interface impedance. E3 and E7 are the two types of electrodes that were tested, T is the temporary electrode used to assist the measurement.

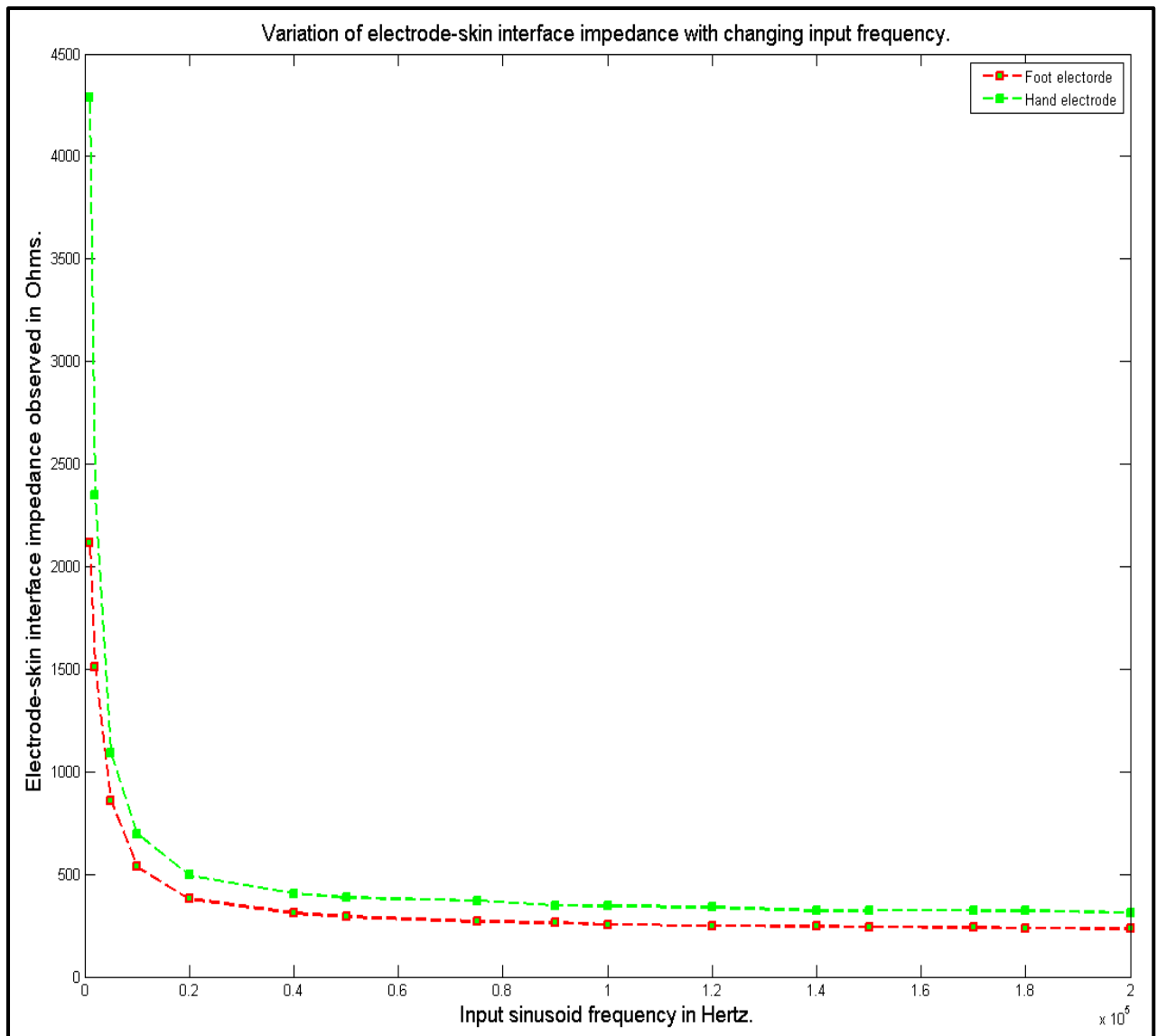


**Figure 5-11: Shows the impedance variation of the hand and foot electrodes with changing frequency (between 1kHz and 200kHz).**

### 5.5 Phase measurements:

It was also of interest to measure the phase shift (refer 1.4) introduced during impedance evaluation because several studies have reported the ability of measured phase to aid body composition estimates (Dittmar & Reber 2001; Kyle, Bosaeus, et al. 2004; Pietrobelli et al. 1998) and other studies have used measured phase as an indicator of body cell health (Schwenk et al. 2000). Therefore it was of our interest to measure the phase change introduced during impedance measurements. In order to evaluate the phase sensitivity of the

device a sinusoidal signal of 500Hz (5V) was used to excite a series RC circuit where  $R = 100\Omega$ ,  $C = 47\mu\text{F}$ . At 500Hz, the capacitive reactance ( $X_C$ ) is  $6.78\Omega$  and the theoretical phase difference should be a lag of  $3.89^\circ$ . When this phase was directly evaluated using two channels in an oscilloscope, an average phase lag of  $3.77^\circ$  was recorded from 10 observations. When the same signal was routed through the voltage measurement section of BIA V2 to the oscilloscope values reported in Table 5-3 were observed. As can be noted the phase readings were varying and are not in agreement with the phase measurements made with the oscilloscope connected directly to the RC circuit. This lead to the conclusion that the device V2 was not phase sensitive and was incapable of preserving phase information. The possible reason for this was the non-linearity in the multiplexer switch ICs used, but no evidence to support this argument was found in the device data sheets.

**Table 5-3: Lists the phase difference measured in a series RC circuit. Measurements were made using device V2 and were inconsistent with theoretical estimates of the same.**

Measured phase in degrees.	-0.68	-0.71	-1.39	-0.57	-2.80	-1.46	-0.52	-0.62	-1.93	-0.70
----------------------------	-------	-------	-------	-------	-------	-------	-------	-------	-------	-------

## 5.6 Summary:

This chapter detailed the construction and working of the Howland current pump, which is a vital component of a bio-impedance system. Also discussed were the selection of the data acquisition device and the construction of the sinusoidal signal source using the XR2206 IC. The VCCS (current source) was tested at various loads and frequencies and is shown to perform satisfactorily. Also tested was the suitability of the electrodes from Tanita BC-545 for measuring bio-impedance. It was found that the electrode impedance was in an acceptable range from around 10kHz, hence was selected as the lower limit to the frequency of operation of the system.

## **Chapter 6     Single frequency SBIA Prototype development (version 2)**

Figure 5-1, Figure 5-3 and Figure 5-6 together form the schematics of the SBIA prototype. Since the individual sections of the system were implemented and tested as shown in the previous sections the next step was to connect the individual sections together. Figure 6-1 shows the SBIA circuit prototype on a breadboard constructed using the schematics shown in the previous sections. The Matlab code used to control the switching, recording voltage and determining impedance will be detailed in subsequent sections. To test this prototype a set of precision load resistors were used similar to the method presented in section 9.2. After testing the prototype on the bread board manufacturing a printed circuit board (PCB) board to hold the circuit was necessary. The following section describes the procedure adopted for developing the circuit board which housed the SBIA device prototype. This section will illustrate stepwise in consecutive subheadings, the process to transfer initial breadboard prototype onto a dual layer PCB board.

### **6.1 Transferring the prototype circuit to the Proteus suite:**

For the PCB design the Proteus suite was used which includes two packages, ISIS, for circuit development and prototyping and ARES for PCB design. This package was chosen because it was readily available at Aston University and is able to design PCB boards containing up to 4 layers.

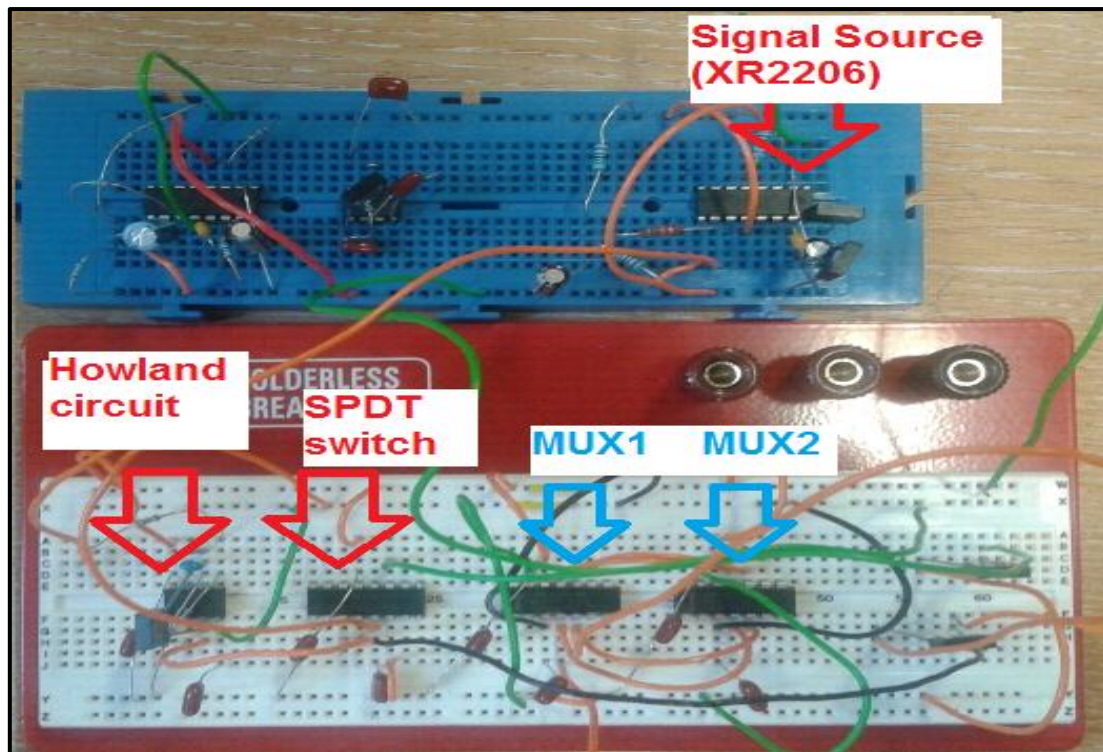


**Figure 6-1: Shows the prototype of the single frequency SBIA system on a bread board.**

ISIS has a component library and a package library with a large dictionary of standard components and ICs one might use for a circuit. Each component has a package assigned to it which dictates the physical configuration and dimensions. For ease during soldering and to keep the costs low, through-hole components with dual in-line packaging (DIP) were chosen. But three ICs used for the prototype were not available in the component library. Therefore the component had to be created and assigned a package. The procedure to achieve this was described in the help guide provided with the software. To connect the electrodes, the input digital control-bits and power, terminal blocks with screw-in connectors were used (labelled as 'J' in Figure 5-1, Figure 5-3 and Figure 5-6).

## **6.2 PCB design with Proteus ARES:**

PCB design in itself is a vast area of study and there are several factors which govern the development of a good PCB design. In this case an inherent low noise design is desired to

keep the signal noise contribution from the board to a minimum. Hence the following design considerations were prioritized.

- Lowest possible interconnect length for the 50 kHz signal carrying lines to reduce track resistance.
- Ground planes were placed extensively on both sides of the board to aid noise drain at its source.
- Also decoupling capacitors were placed adjacent to the power pins of the ICs to shunt noise from other components and supply variations.

Also the design had to be compact because larger design inherently will generate larger noise, undesirable in our design. To ensure a compact design a dual layer PCB (with interconnects on both sides of the board) was adopted. Keeping these factors in mind the following PCB layout was produced. Figure 6-2 shows the topside (component side) and the bottom side of the PCB design used to hold the SBIA device.

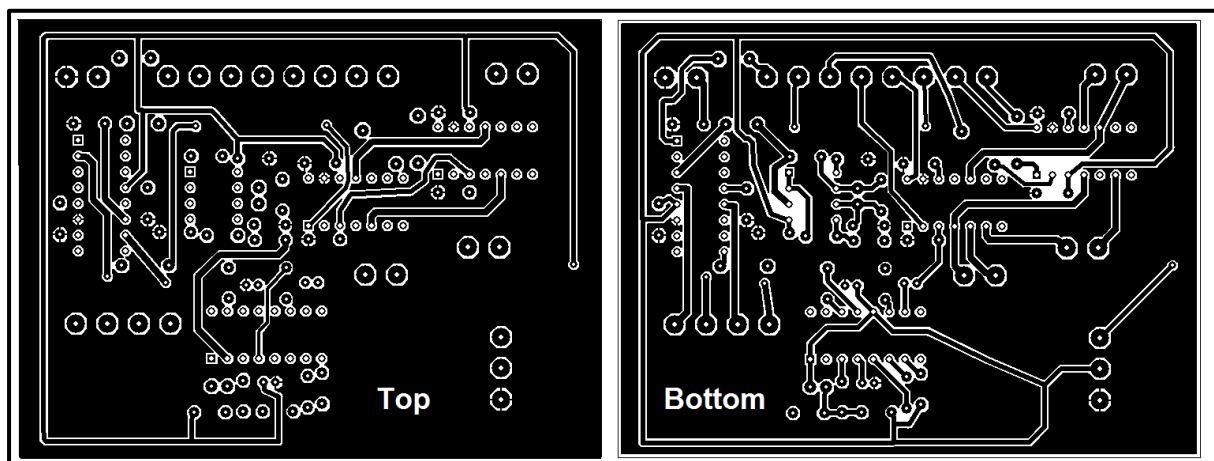


**Figure 6-2: Shows the top side and bottom side of the PCB layout used to house the SBIA circuit.**

### **6.3 PCB manufacturing:**

The manufacturing of PCBs involves three major steps viz. developing the design on the pre-sensitised boards, etching copper off the developed pre-sensitised boards and drilling holes on the board for through-hole components. Pre-sensitised boards are made of a sheet of epoxy covered with a thin layer of metal (0.1 mm copper in present case) which again is covered with photosensitive material. Parts of photosensitive layer which has been exposed to ultra-violet light 'soften'. The softened parts dissolve in a developing revealing the copper layer underneath which can be later etched using a corrosive chemical (ferric chloride solution in our case). The rest of the photosensitive layer ('unsoftened' parts) remains intact during board development preventing the copper under the 'unsoftened' parts to remain intact. For this project a dual layer board with copper and pre-sensitised surface layer on both sides was cut into the right dimensions. The design Figure 6-2 was printed on a transparent sheet and used as masks to expose the photosensitive layer to UV light through these masks. After a few such exposures it was concluded that desired alignment of through-holes cannot be achieved when exposing the two sides individually. Hence each side was exposed on separate single layer pre-sensitised boards and the two were stuck to each other (back to back) using a strong adhesive; this method ensured that desired alignment between the top and bottom layers was achieved. The boards were developed (dissolving 'softened' parts) using a sodium hydroxide (NaOH) solution after exposing the pre-sensitised to UV light through the mask for 150 seconds. The developed design was left overnight to dry and then etched (removing metal from sections which were exposed during development phase) using ferric chloride solution (1 part ferric chloride to two parts water) which took about 20 minutes each. When removed the exposed copper regions were etched giving us the PCB design on a dual-layer board. The remaining photosensitive layer was cleaned using acetone. Figure 6-3 shows few of many failed attempts for properly etching the design on the board. After fine tuning the UV light exposure times and etching solution

concentration a successful PCB was etched. Figure 6-4 shows the finished PCB with all components soldered on.



**Figure 6-3: Shows failed attempts to manufacture the SBIA PCB layout in Figure 6-2.**

#### **6.4 Through-hole drilling, board testing and soldering:**

The holes on the board were hand drilled using standard 0.6 mm and 1 mm PCB drills. Each track and pad on both sides was tested for a short circuit with the ground planes using a multi-meter which otherwise would lead to a malfunctioning circuit. After testing the components were placed in their respective positions as assigned during the PCB design phase (using ARES) and soldered to give the final functional device on a dual layer PCB board. Figure 6-4 shows the single frequency SBIA device with all its components on a PCB board. The manufactured device was used for a trial on 14 volunteers at Aston University as

will be shown in subsequent chapters before it was superseded by a multi-frequency SBIA device.

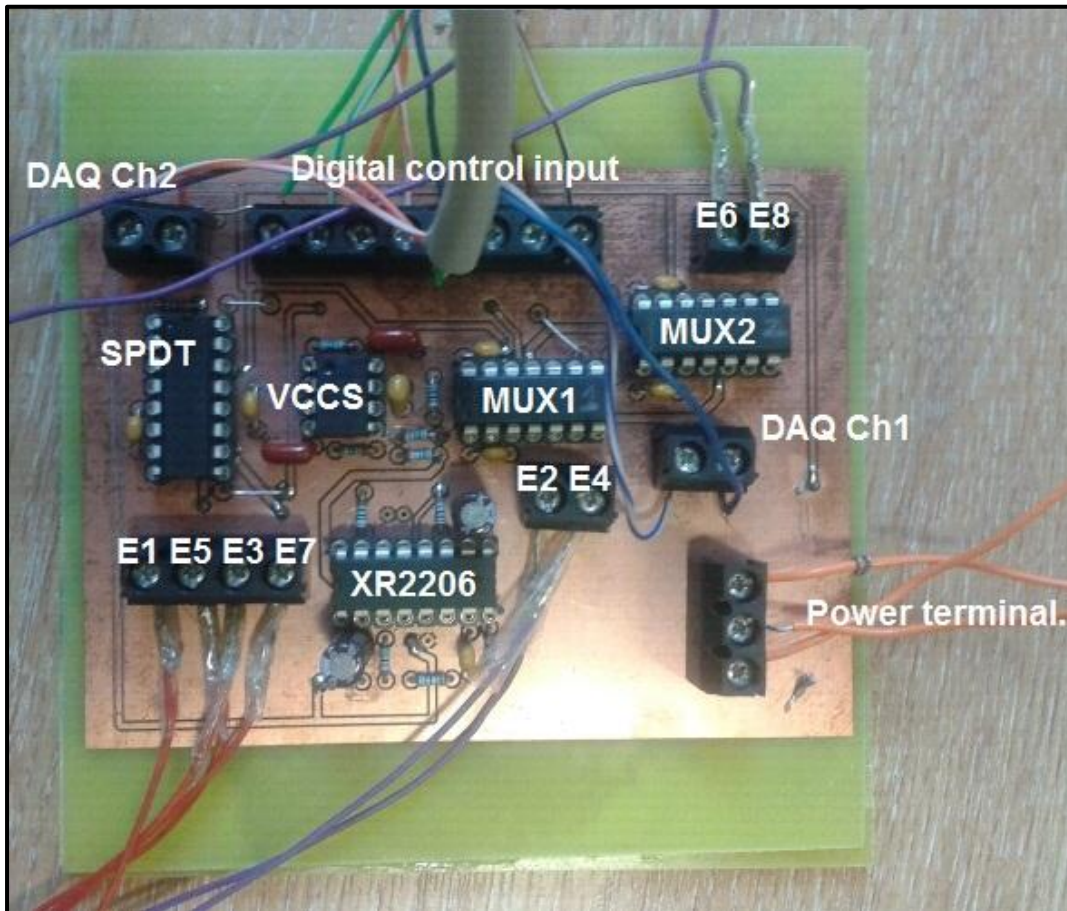


**Figure 6-4: Designed single frequency SBIA system on a PCB board with its components labelled.**

## **6.5 Leakage current tests:**

As previously discussed to ensure the safety of the subject when the device is functioning as normal and under fault conditions, leakage and auxiliary current tests are to be performed on the device to ensure these currents are below limits stipulated by the BS EN 60601. Methods to measure these currents and the current types are detailed in section 1.12. Unlike device V1 these values are measured using a measurement setup specifically designed for this purpose.

**Table 6-1: Shows the auxiliary and leakage currents measured in V2. The values are lower than upper limits for these currents set by BS EN 60601. Values reported in microamps.**

<b>BIA device version 2 (V2)</b>		
<b>Currents</b>	<b>Normal condition</b>	<b>Single fault condition</b>
<b>Earth Leakage</b>	41	57
<b>Patient leakage(DC)</b>	<1	<1
<b>Patient leakage(AC)</b>	80(compensated)	80(compensated)
<b>Patient auxiliary(DC)</b>	<1	<1
<b>Patient auxiliary(AC)</b>	80 (compensated)	80(compensated)

As can be observed the values of auxiliary currents and leakage currents measured for V2 is under the values set by BS EN 60601 and therefore the use of this device can be considered to have low risk of hazard in laboratory settings.

## **6.6 Summary:**

This chapter discussed the translation of the SBIA device V2 from an experimental circuit to a functional circuit on a PCB. Topics of PCB design and development were covered and the SBIA device V2 measurement circuit was realised. Finally auxiliary and leakage current tests were conducted on SBIA device V2 and it was found that the currents are below the limits set according to the BS EN 60601.

## **Chapter 7    Development of Multi-frequency S-BIA system (version 3 and version 4)**

Adding multi-frequency mode of operation to the above mentioned device took a few additional steps. The major revisions required to allow multi-frequency operation (Howland circuit frequency range test and electrode-skin frequency range test) were set out in section 5.3.2. Here we present the changes made to the circuit to allow multi-frequency operation. The signal source IC (XR2206) was capable of producing sinusoids up to a few megahertz and the Howland circuit showed stable operation up to 100kHz. The electrode-skin interface impedances of the two electrode types were comparable from about 10kHz, hence the device would stably operate between 10kHz and 100kHz. The frequency of the XR2206 output can be controlled by varying the resistance connected between pin 7 and ground (R1 in Figure 5-3). To preserve the compactness of the PCB design the decision to add four individually selectable resistors was made, allowing the device to operate at four different frequencies between (but including) 10kHz and 100kHz. These resistors were selected individually via a 4-way DIL switch; variable resistors were used to allow tuning of the available frequencies which meant that the four operating frequencies could be changed if required. Changes were made to the original schematic and a new PCB was designed and developed to incorporate the DIL switch and four variable resistors. Figure 7-1 shows the updated multi-frequency device with the DIL switch and variable resistors which allowed frequency selection.

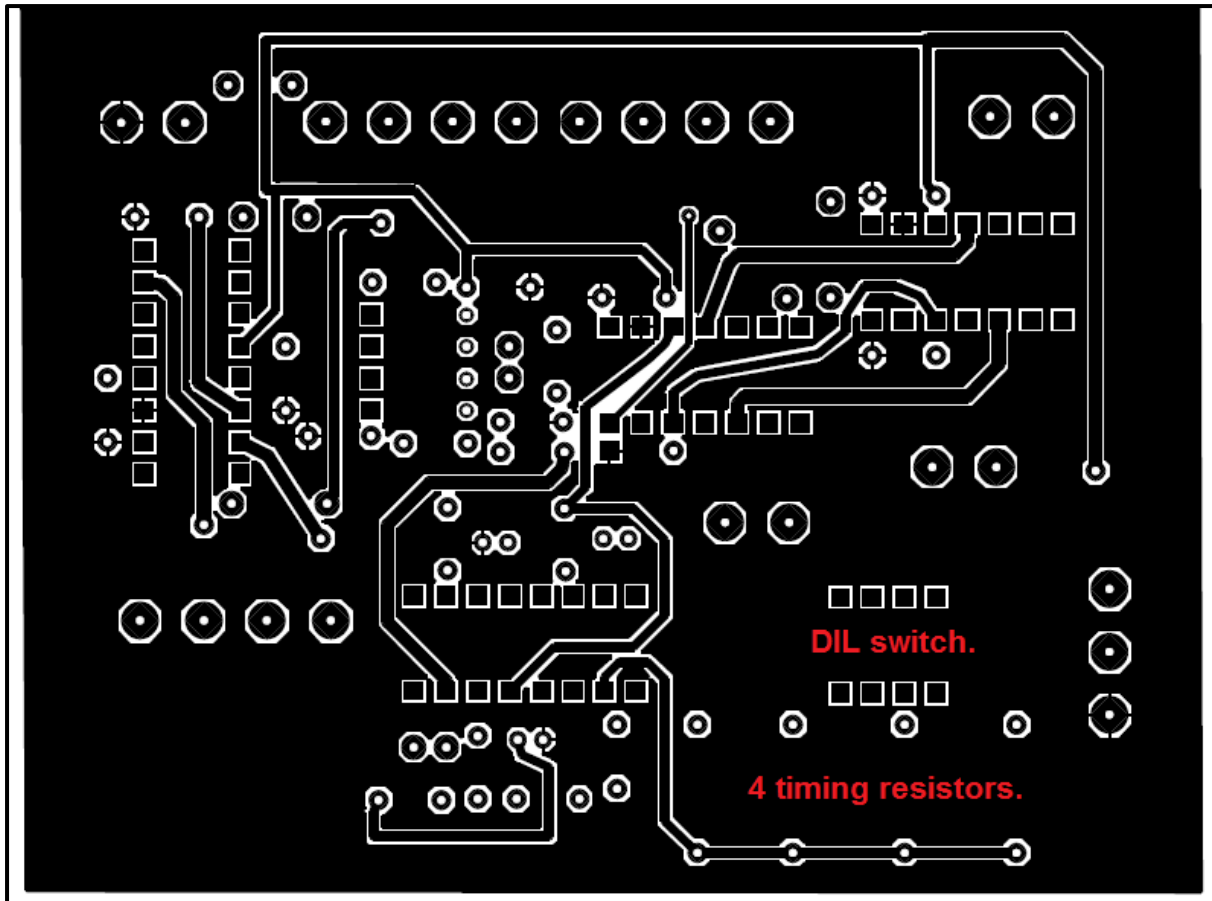


**Figure 7-1: Shows the PCB design of the top layer of version 3 of device. As compared to top layer of version 2 in Figure 6-2, a DIL switch with 4 selectable resistors are added for multi-frequency operation.**

### **7.1 Improved segmental multi-frequency bio-impedance device (version 4):**

Further improvements to the device were explored which led to the development of an improved version of the multi-frequency SBIA device which was more compact, less complex and performed better than its predecessors. This new but final version was built and tested in time before the volunteer trials at the NHS trust commenced. The notable difference between version 4 as opposed to version 3 was primarily related to the construction of the current source. Also adopted in version 4 was an entirely new VCCS & voltage-sense electrode switching scheme. The schematic to the previous version of the device is shown in Figure 5-1, Figure 5-3, Figure 5-6 and the schematic to the new version in

Figure 7-4. When the circuit diagram of the two circuits in V3 and V4 are compared the differences between the two designs is apparent. The signal source implementation in both versions remained the same (OS1 in both designs, realised with the XR2206). The major difference arises with the use of INA110KP (U1, Figure 7-4) to realise the current source, the advantages of using this IC is detailed in the following section. Also the two multiplexers MUX1 and MUX2 (used to switch voltage sensing electrodes) in version 3 (and version 2) to switch voltage sensing electrodes (Figure 5-1) is replaced with a single SPDT switch (SPDT in Figure 7-4) reducing the number of ICs required for in the design by one.

## 7.2 Improved current source:

The Howland circuit has been described in detail in section 5.3, where the importance of resistor matching has also been discussed. Further investigation of technical data sheets from Analog devices (particularly datasheet for differential amplifier AMP03 from Analog devices) showed that the Howland circuit can be constructed with an instrumentation amplifier IC package. The INA110KP instrumentation amplifier was chosen for our purpose. As reported in the datasheet (Appendix 2, page 8) the four  $10\text{k}\Omega$  resistors ( $R_1$ ,  $R_2$ ,  $R_3$  and  $R_4$ , Figure 5-4) are precision matched for high CMRR (laser trimmed resistors, refer datasheet). Hence switching to this IC would mean that the loss of CMRR due to resistor mismatch would be reduced. In case of the discrete Howland circuit realized in section 5.3.2 resistor mismatch is worsened due to varying resistor track lengths on the PCB, this can be avoided with the use of INA110. In order to allow a sufficient voltage to appear at the VCCS input (from the XR2206) the gain in the INA110 is set to 10 (Figure 7-2,  $R_g$  pin 3 connected to X10 pin13). The input buffer stages ( $A_1$ ,  $A_2$ ; Figure 7-2) also ensure that the common-mode signals are suppressed. Since the  $10\text{k}\Omega$  resistors are internally connected, an improved Howland circuit (Figure 5-5) can be realised using a unity gain buffer in the non-inverting feedback path and a single resistor ( $R$  which was chosen by experimentation to  $270\text{k}\Omega$ ) as shown in Figure 7-3.

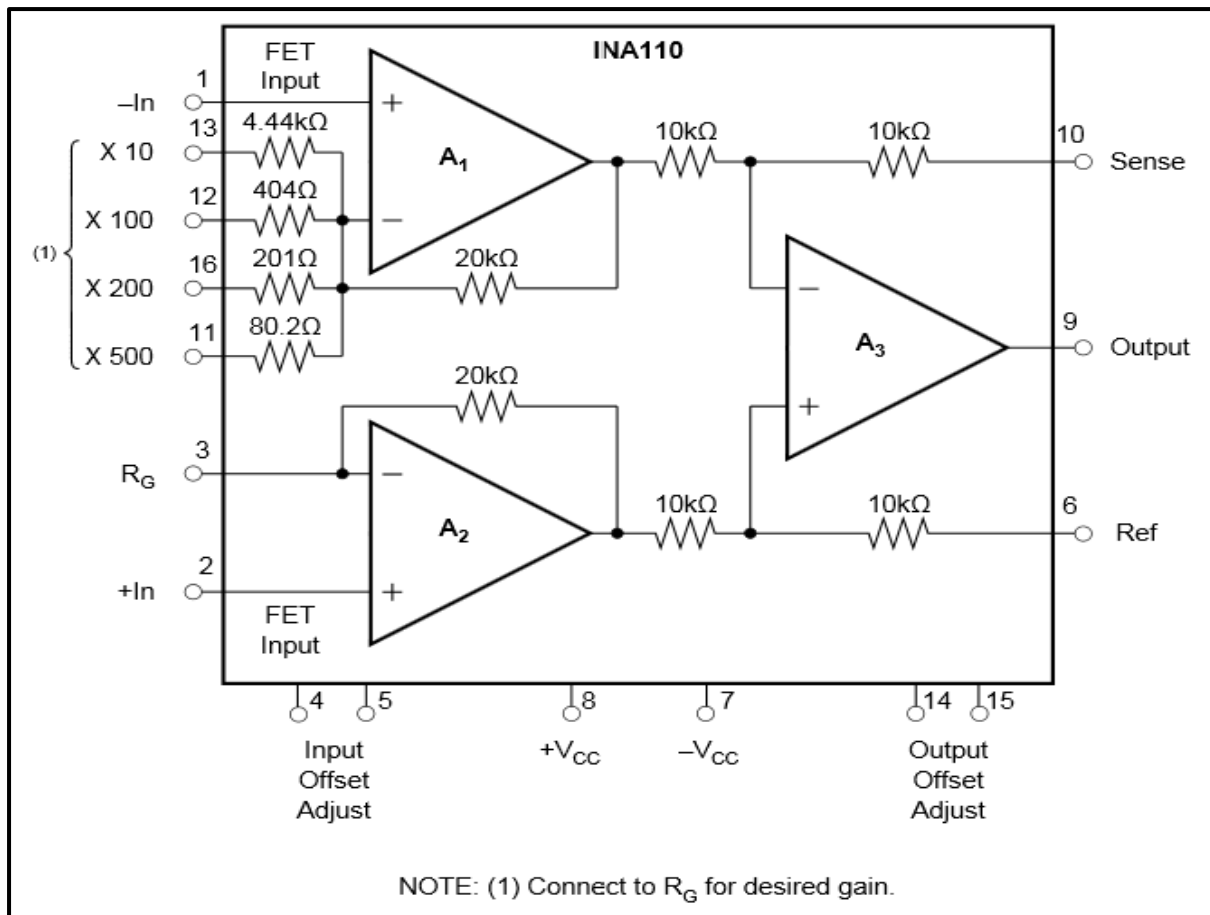


**Figure 7-2: Shows the functional diagram of the INA110 instrumentation amplifier by Texas instruments; adopted from INA110 datasheet. A gain of 10 was selected for current purpose.**

Therefore there was no longer the need to match resistors as was the case for VCCS in section 5.3.2. This automatically reduced the complexity of the circuit. The new current source also had performance improvements when compared to current source used in version 2 (and version 3) of the device (constructed using op-amps and matched resistors) this is detailed below. This current source was highly reliable because the resistor values remained constant. Whereas in case of the previous VCCS the resistor matching in the circuit; whose values; although selected with great care for close matching varied slightly when soldered on a PCB due to varied path lengths.

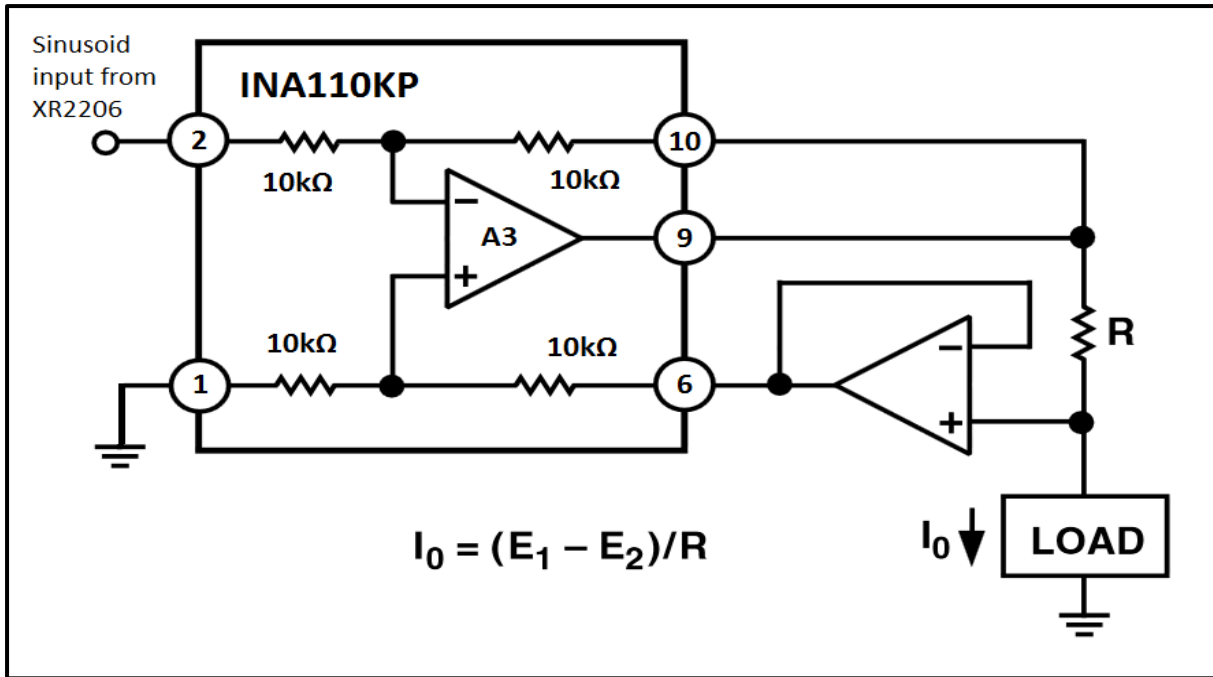


**Figure 7-3: Shows the simplified version (without A1, A2) of the new current constructed using the INA110. The internally connected 10kΩ resistors make this current source easier to construct as opposed to the previous current source used this project.**

This uncertainty was negated in the new VCCS since the resistors were tightly matched within the IC package. U1 and U2 in Figure 7-4 shows the circuit diagram of the VCCS realised in this manner. The new VCCS had a broader frequency range and load range as compared to previous current source. The frequency range was increased 120kHz (which was just over 100kHz for previous current source, Figure 5-8) and the load-bearing range increased to 12.8kΩ (which is lower in previous VCCS, Table 5-2).

**Conclusion:** Therefore the new version of the device had a better VCCS than the previous versions. The VCCS was also easier to construct and had performance improvements over the previous current source.

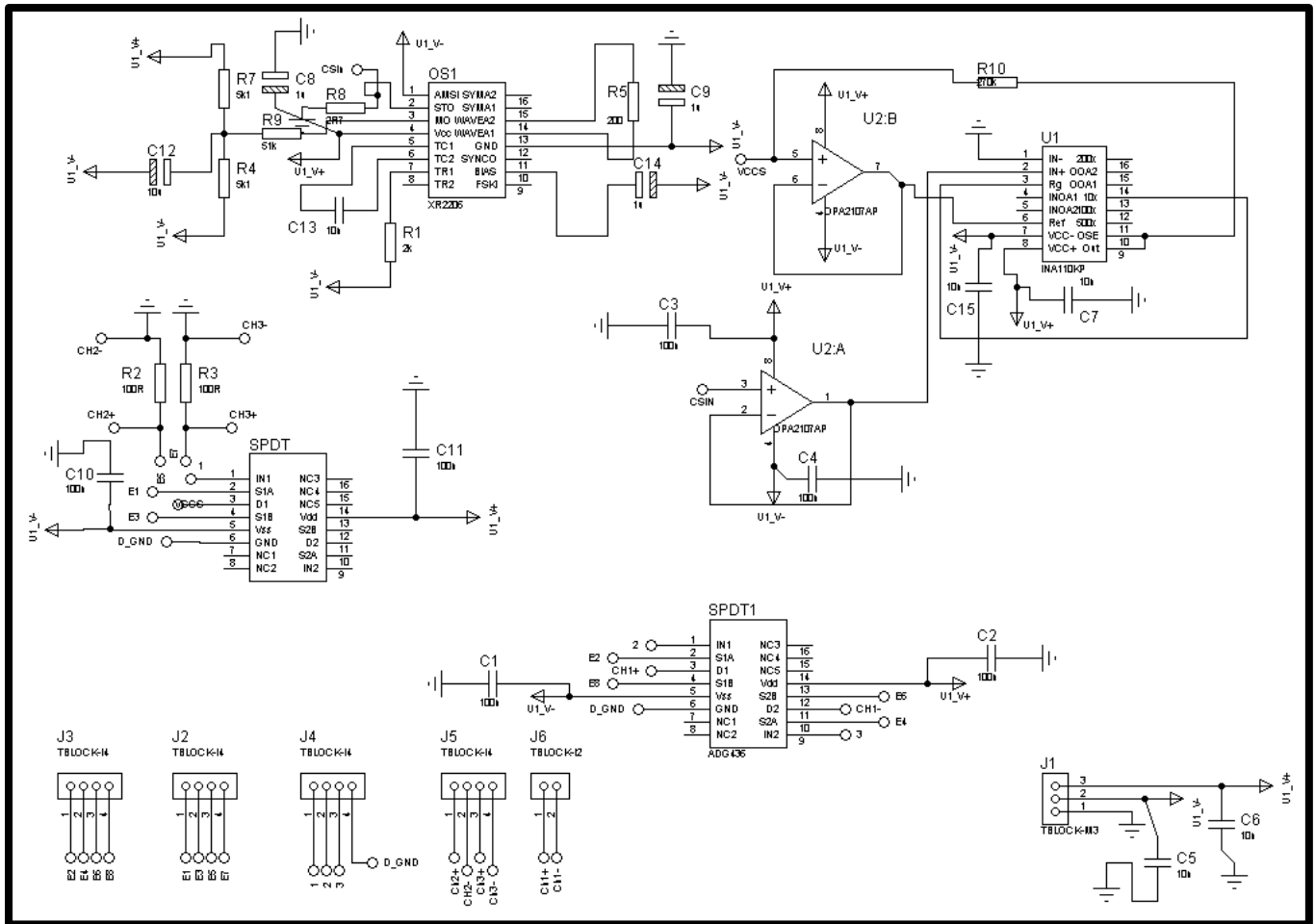


**Figure 7-4: Version4 (final version) of the device constructed for this project.**

### 7.3 New electrode switching scheme:

The switching scheme was completely revised in version 4 of the device. The VCCS switching was done using a single SPDT switch in version 4 (this used two SPDT switches in version 2 & 3). Figure 7-5 shows the single SPDT switching method used to switch the current source across electrode pairs E1, E5 (left side of subject refer to Figure 3-6) and E3, E7 (right side of subject). A 100Ω resistor is used to sense the current flowing across the subject's body (one on each side). As can be seen an additional data acquisition channel is required to sense the current flowing across the two 100Ω (although only the channel corresponding to the particular side to which the VCCS is connected is active one at a time).

The digital input IN determines which electrode-pair the VCCS is connected to, as shown in the truth table in Figure 7-5. This meant that the number of digital inputs required for switching the current source as compared to the previous version was reduced from two to one (in effect a simpler VCCS switching scheme has been implemented). The new device also replaced voltage-sense multiplexers (MUX1 and MUX2) with a single SPDT switch; this made the PCB design for the new circuit less complex. Figure 7-6 shows the voltage sense electrodes connected to the switch and the digital inputs IN1, IN2 required to select electrode pair. The data acquisition device is connected across D1 & D2 (Figure 7-6, (a)) effectively connecting the selected electrode pair to the data acquisition device. The new switching scheme capitalizes on the fact that the order in which the sensing electrode pair is connected to the data acquisition device does not affect the measured voltage. For example voltage measured across E2, E4 is same as voltage measured across E4, E2. Truth Table 7-1 summarizes the new voltage sense switching scheme. The new voltage-sense electrode switching scheme requires only 2 digital inputs from the data acquisition device as opposed to 6 in previous version. This reduced the total number of digital inputs required to control the device from 8 to 3 which in turn made the PCB design simpler. This summarizes the functioning of the final version of the device.

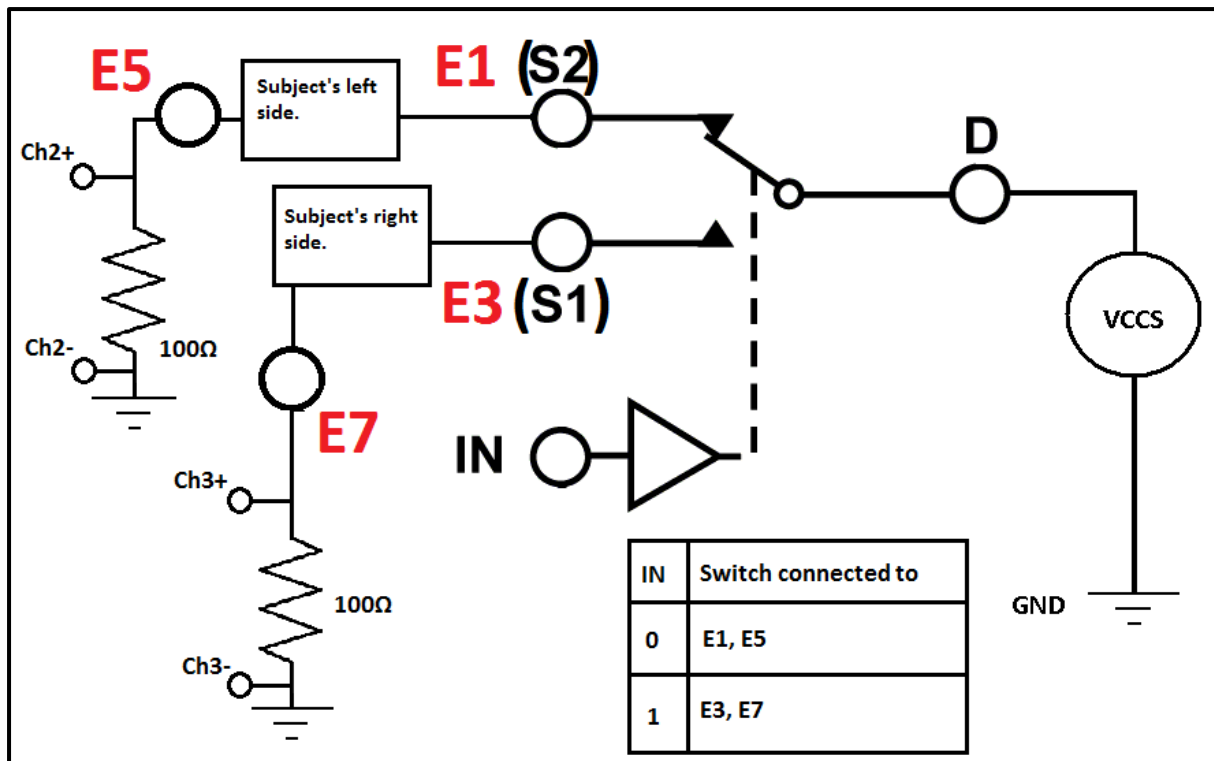


**Figure 7-5: Shows the functional configuration of the new current source switching using a single SPDT switch. The control signal IN connects the current source either to the left-side of the subject or right-side of subject.**

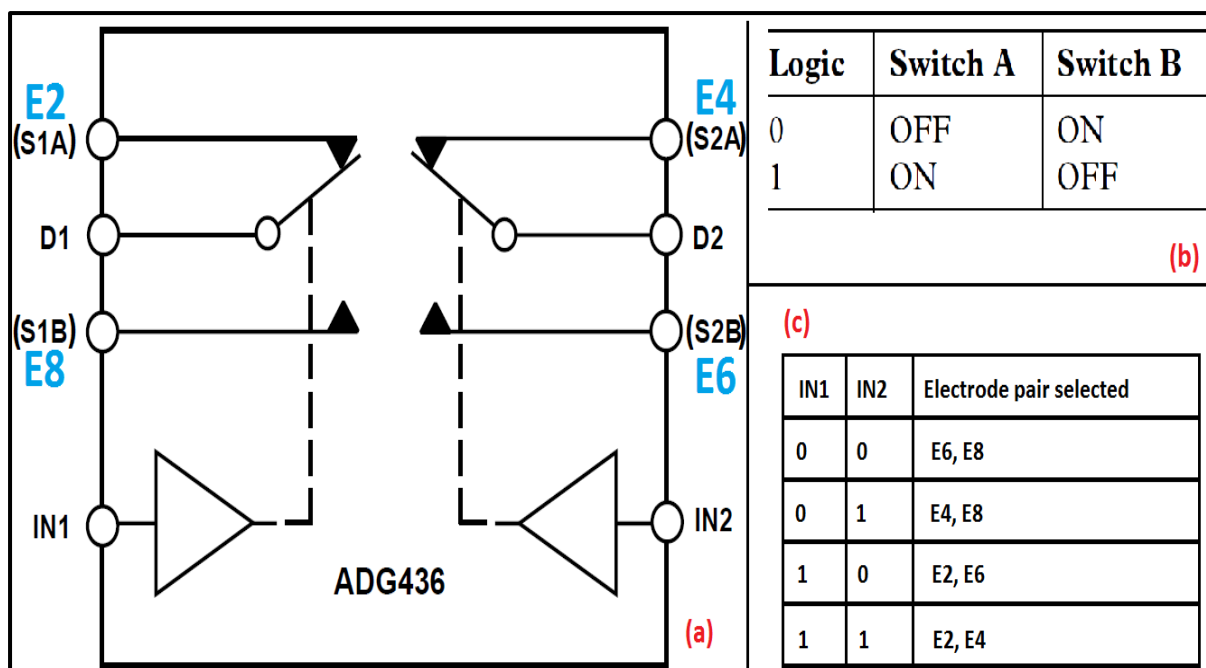


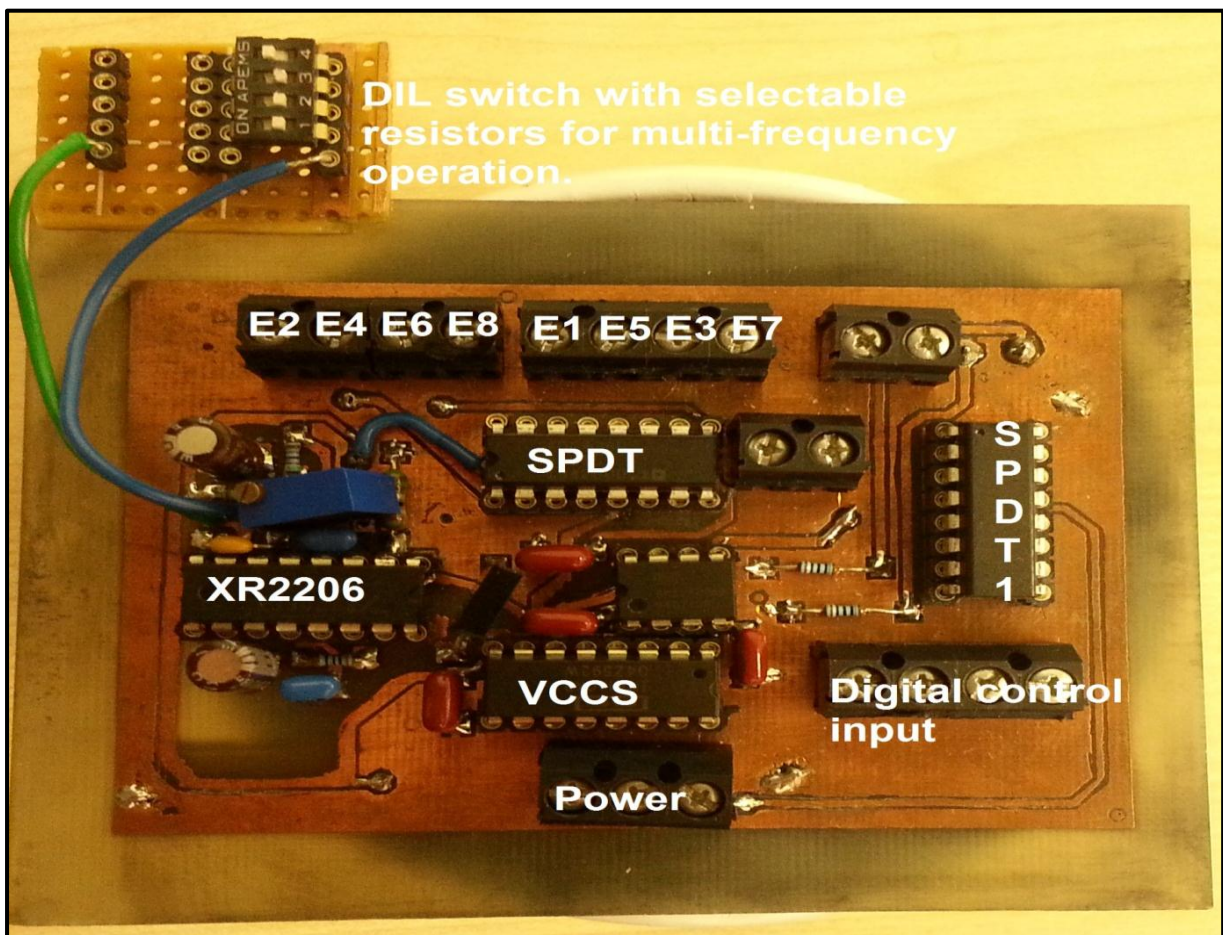
Figure 7-6: Shows the electrode configuration for the new switching scheme (a). (b) shows the truth table for the AD436. (c) shows the digital inputs to the AD436 and electrode pairs selected.

Table 7-1: Shows the digital states required to make segmental bio-electrical measurements from 8 segments of the human body in version 4 of the device.

VCCS connected between.	Bit 0 (IN)	Bit 1 (IN1)	Bit 2 (IN2)	Electrode pair selected.	Impedance measured
E1&E5	0	1	1	E2,E4	Right arm.
	0	0	1	E4,E8	Trunk impedance 1.
	0	0	0	E6,E8	Right leg.
	0	1	0	E2,E6	Whole body 1.
E3&E7	1	1	1	E2,E4	Left arm.
	1	1	0	E6,E2	Trunk impedance 2.
	1	0	0	E6,E8	Left leg.
	1	0	1	E4,E8	Whole body 2.

**Conclusion:** Figure 7-7 shows the final (version 4) of the device with its various components. This device was used for hospital trials and made impedance

measurements from 22 volunteers. Table 5-1 lists the various versions of the BIA device designed and constructed during this project and the manner in which the device evolved from a whole-body impedance measurement system to a compact multi-frequency segmental impedance measurement system. The final version uses the XR2206 IC to generate the sinusoidal signal, improved Howland circuit constructed using INA110KP (instrumentation amplifier to function as VCCS), AD436 to realise VCCS and voltage sense electrode switching. Further improvements are suggested in the future work section of this thesis.



**Figure 7-7: Shows the constructed version 4 of device with its various components labelled.**

## 7.4 Improvements in PCB manufacturing technique:

Version 4 of the device also saw improvement in the PCB manufacturing techniques and methods. A modified version of the 'toner-transfer' method (popular on the internet) for PCB manufacture was used to make PCBs for version 4. Figure 7-8 shows the top and bottom side of PCB design for device version 4. Toner-transfer involves printing the PCB pattern on glossy photographic paper and transferring the toner (printer ink from paper) from the paper to a copper clad PCB board using a hot iron. This is more commonly used for single layer PCBs. For the dual layer board the top and bottom PCB design printed on glossy paper were aligned with a two-side copper clad board sandwiched in between. The alignment was performed using 'alignment holes' shown in red circles in Figure 7-8. The two sides were aligned and held in position by duct tape and the design was ironed on the two side copper-clad board alternately. Also to making etching simpler (which previously involved rocking the dish with the etchant and the PCB manually) a computer fan, lab gloves and tubing was used to make a bubble etch device as shown in Figure 7-9. Figure 7-10 shows PCB manufactured using this method.

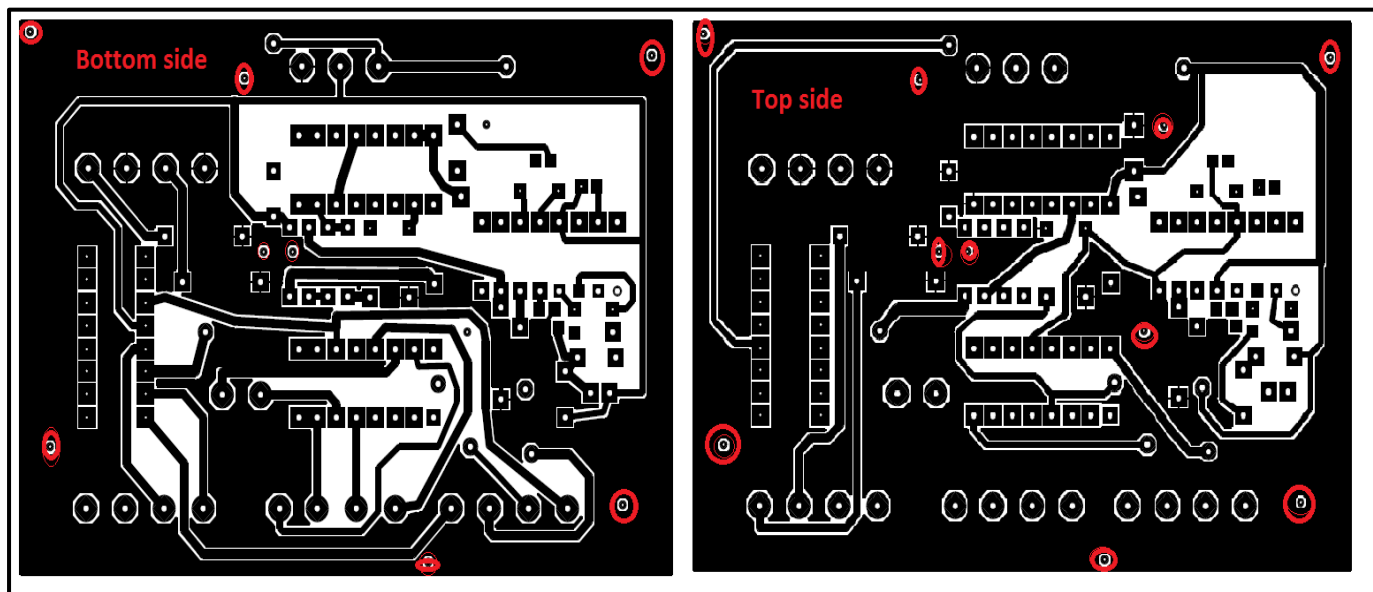


**Figure 7-8: Shows the PCB layout of the final version of the device used for patient trials.**

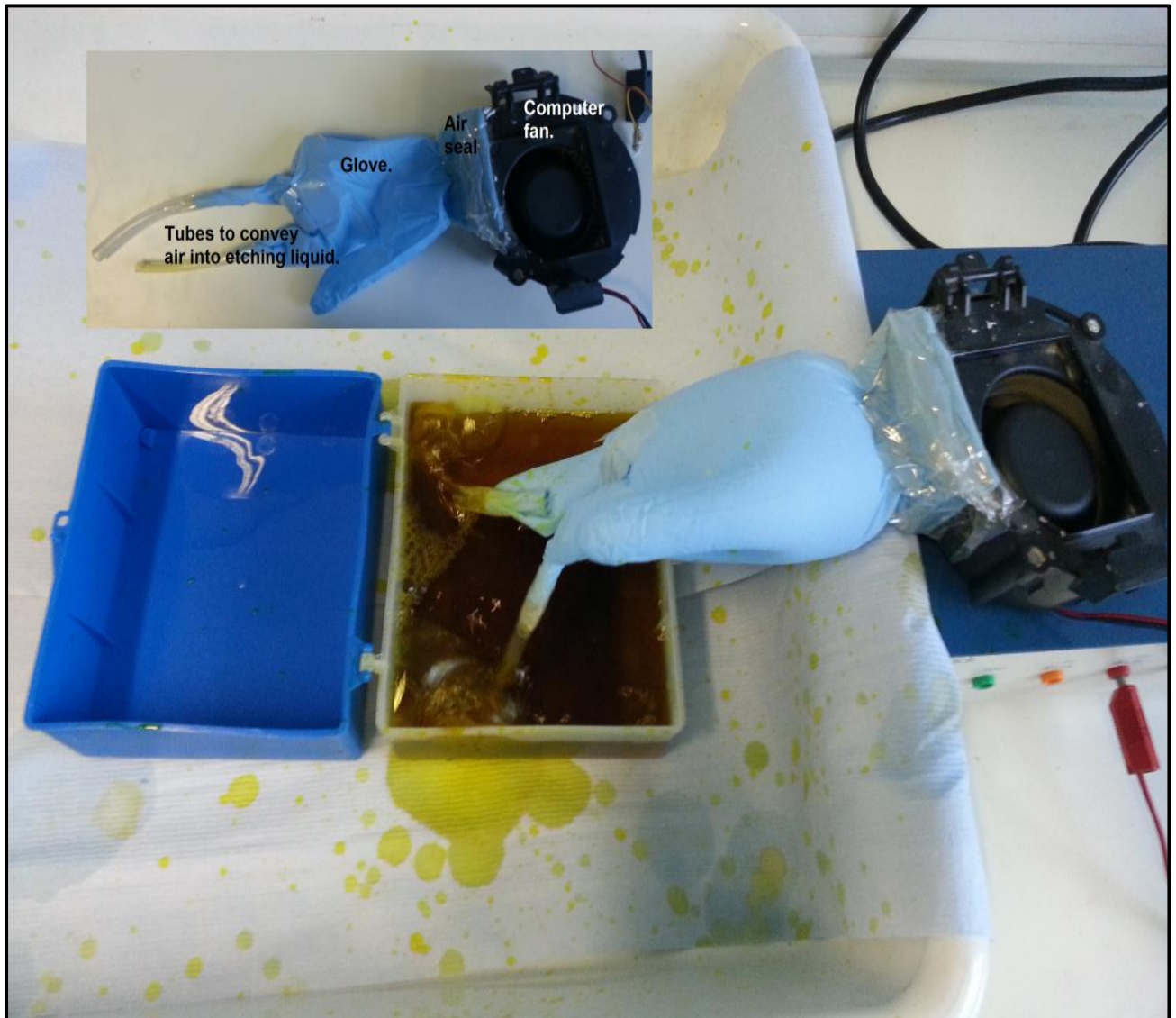


**Figure 7-9: Shows the simple bubble etch device made using a computer fan, lab glove and rubber tubing.**



**Figure 7-10: Shows top side and bottom side of PCB board designed (circuit in Figure 7-4) for version 4 of the device. This was manufactured using the 'toner-transfer' method.**

### **7.5 Leakage current tests:**

V4 was the final version of the device constructed and had some significant design changes when compared to V2 and V3. Also this device was used to acquire segmental

bioimpedance measurements on 22 subjects at Heartlands hospital NHS trust in Birmingham, U.K.

**Table 7-2: Shows the auxiliary and leakage currents measured in V4. The values are lower than upper limits for these currents set by BS EN 60601. Values reported in microamps.**

<b>BIA device version 4 (V4)</b>		
<b>Currents</b>	<b>Normal condition</b>	<b>Single fault condition</b>
<b>Earth Leakage</b>	37	183
<b>Patient leakage(DC)</b>	3	14
<b>Patient leakage(AC)</b>	80(compensated)	80(compensated)
<b>Patient auxiliary(DC)</b>	<1	<1
<b>Patient auxiliary(AC)</b>	80 (compensated)	80(compensated)

As can be seen the values of leakage and auxiliary currents are less than the limits set by BS EN 60601 which are shown in Table 1-7. Hence the risk from using device V4 can be considered low in a controlled hospital setting.

## **7.6 Summary:**

Presented in this chapter is V4 of the bio-impedance device constructed during this project. Discussed here in were the changes and improvements made to V3 of the device particularly the adoption of the INA110 to realise the current source. Also simplified was the voltage-sense electrode switching mechanism which in V4 is achieved using a single AD436 IC as opposed to two AD509 multiplexer IC's.

# **Chapter 8    Matlab for device control and signal analysis**

## **8.1 Introduction:**

Throughout this project Matlab was utilized extensively for the purposes of device control (present device), analysing the acquired signals to evaluate impedance and to store the acquired signals for further analysis. Matlab is packaged with various ‘toolboxes’ which enable the user to build applications for specific purposes and provides interface with external hardware. The two specific toolboxes relevant to the present study are the signal processing toolbox, which were utilized to process the acquired body impedance signals and the data acquisition toolbox used to control the DAQ device.

## **8.2 Matlab to save body-impedance signals and extract impedance:**

Appendix 3 exhaustively includes the Matlab programs written for this study. The entire program and function structure of the patient trial application is summarized in flow chart Figure 8-1. To start the application in the Matlab command window the first program ‘databasetrial.m’ is called which asks patient ‘first name’ and ‘last name’ as the input. After these names are entered the program encrypts this name using a predefined encryption key (encryption feature implemented using AES algorithm to ensure patient anonymity), and compares this against existing folder names. If a match is found the program updates the weight, age and body composition estimates (obtained from Tanita BC545) for this particular volunteer and also acquires the new segmental bio-electrical signals. All this information is saved in a subfolder created with the present date and time. In case a match is not found the

given name is encrypted using the same key and a new folder is created with this encrypted name and the previous step is repeated. After this the control is passed to the 'daqcontrol.m'. This function initially creates a subfolder with current date, sets the acquisition time per segment to two seconds and the sampling rate to 2MSa/sec. The 'daqcontrol.m' function also instructs the DAQ device to provide digital signals to switch the SPDT switch and multiplexers while also saving the two second sampled signal in this subfolder. The saved signals are later analysed to measure bio-impedance of the different segments.

### **8.3 Patient trial application:**

The program-function structure for the volunteer trial application is shown in Figure 8-2. The application 'databasetrial.m' was tailored for the purposes of saving patient information and body-impedance signals in an anonymous fashion. The program has four main sections and control is passed between each of them to save patient information and acquire the desired SBIA. The application is initiated by invoking 'databasetrial.m' application in the Matlab command window. The application itself requests and saves information pertaining to the patient like gender, height, weight and other morphological parameters (exhaustive list can be found within the program listed in Appendix 3). This is followed by a call to 'daqcontrol.m' controls the SBIA signal acquisition superficially by passing the digital bits to control the constructed SBIA device via. The digital output port on the DAQ device and also saves acquired signals in appropriate folders. 'daqset.m' is called to set up the hardware within the Matlab environment. Mainly it sets acquisition parameters i.e. acquisition time and sampling rate. 'imp.m' the last function to be called translates the saved body-impedance signals to actual impedance estimates this procedure is detailed in later sections.

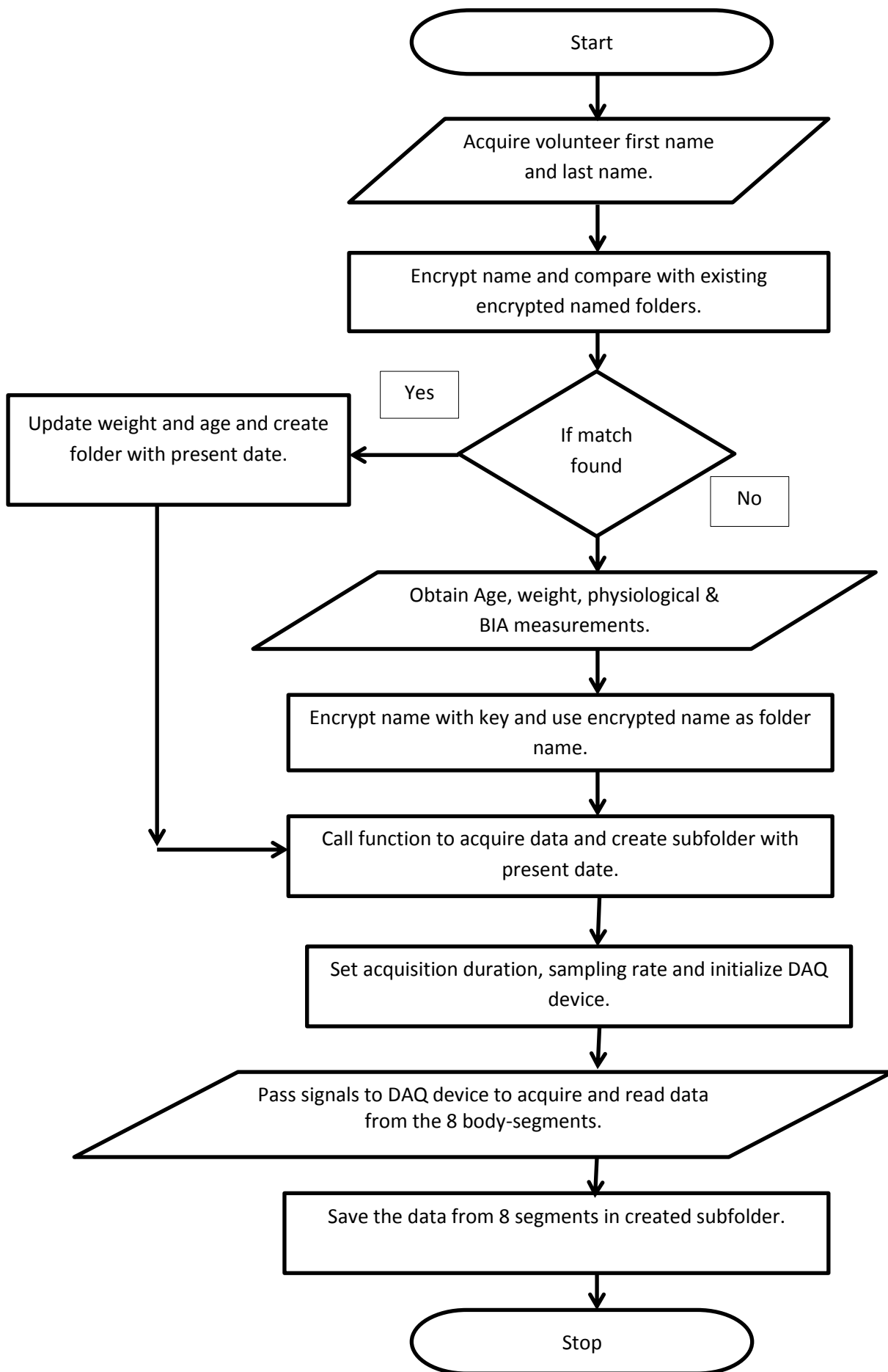


**Figure 8-1: Shows flowchart for the patient trial program used to acquire subject information and acquire bio-electrical signals.**

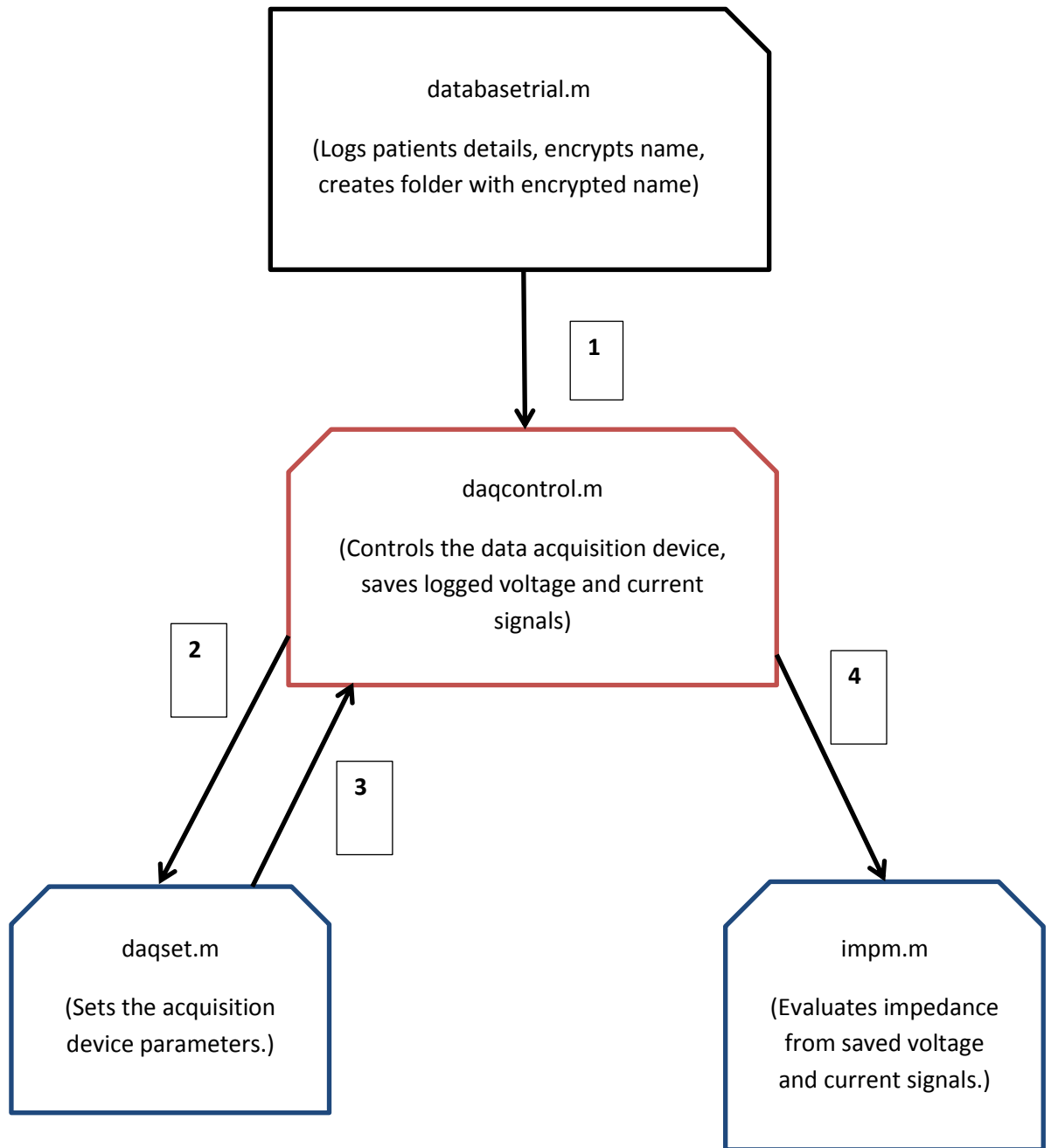


**Figure 8-2: Three major functions of the volunteer trial application 'databasetrial.m'. Arrow heads represent exchange of control between functions and the digits show the sequence of this exchange.**

## 8.4 Controlling the data acquisition device:

The following code snippet from 'daqcontrol.m' shows the Matlab code for acquiring and saving to disk bio-impedance signals from the right-arm.

```
1 nnm=strcat(nnm, '\\', datestr(now, 'yyyy-mm-dd-HH-MM-SS'));
2 mkdir(nnm);
3 dur=2;
4 fs=2e6;
5 [ai,dio]=daqset(dur,fs);
6 start(ai)
7 start(dio)
8 putvalue(dio.Line(1:8),[0 0 1 1 0 1 0 0])
9 pause(1)
10 trigger(ai)
11 pause(2)
12 data0 = getdata(ai);
13 figure(1)
14 plot(data0)
15 save data0;
```

The 'databasetrial.m' passes the encrypted folder name as an argument to 'daqcontrol.m' also passing over control of the application at the same time. 'daqcontrol.m' initially appends the current date and time (line 1) with this encrypted name and creates a folder with the new name, essentially creating a folder with the present date within the subject's folder. Lines 3 and 4 set the acquisition parameters i.e. the acquisition time is set to 2 seconds (dur=2) and the sampling rate to 200k Samples per second. This is followed by a call to 'daqset.m' function in line 5 during which application control is temporarily passed to it. The 'daqset.m' function sets up the data acquisition hardware within the Matlab environment. Following is a code snippet from 'daqset.m' and its description.

```
41-  aii=analoginput('agilentu2500',0);

51-  ch = addchannel(aii,0:1);

71-  set(aii, 'SampleRate',2000e3)

81-  ch.inputrange = [-5 5];

91-  ch.sensor = [-1 1];

101- fs = get(aii, 'samplerate');

102- set(aii, 'SamplesPerTrigger',dur*fs);

102- set(aii, 'triggertype','manual');

103- dioo=digitalio('agilentu2500',0);

104- addline(dioo,0:7,'out');
```

Line 41 defines the data acquisition device object 'aii' within the Matlab environment to the connected Agilent U2531A data acquisition device. Line 51 adds two analogue signals logging channels (0, 1) within the object 'aii'. Two channels are required to log both the voltage and the current signal from the segment of interest as described earlier. Line 71

passes the sampling rate (200 kS/sec) to this object. Line 103 adds a digital output object 'diao' to the Matlab environment and the following line adds an 8-bit wide (0-7) digital output channel. These 8-bits are required to produce the digital control bits to control the SBIA device the bio-impedance device (shown and 'digital control input' in Figure 6-4). After this the control is passed back to line 6 in 'daqcontrol.m' where the analogue object is started followed by the digital object. Line 9 puts the given 8 bit word onto the declared digital object. Referring back to Table 4-5 this digital word is set to acquire the impedance across the right arm. Then the analogue object is triggered to start logging signals across its two channels (hence both voltage and current signals are logged). The 'getdata' function (line 12) saves the data logged by the data acquisition device into a Matlab variable. This variable is then moved to the folder created with current data in line 1. This is repeated 8 times within 'daqcontrol.m' with different digital sequences shown in Table 4-5 to obtain the voltage and current signals across the 8 body-segments with filenames data0 through to data7 in the same folder.

## **8.5 Extracting bio-impedance from saved signals:**

As explained in the introduction FFT can be used to extract magnitudes of a frequency of interest in a signal. For each of the eight saved bio-impedance signals per subject magnitudes of both the measured voltage and current were extracted from their respective FFT spectrum. In order to extract the magnitude of the voltage and current peaks the entire spectrum of the signal response (bandlimited to 400 kHz by the data acquisition device) was imported into Matlab and the peak corresponding to the excitation (input frequency, 50 kHz for V1, V2) was extracted from the entire FFT. The procedure is illustrated in the following code snippet.

```
1 - [~, V] = fft_imp_extract(dataX(:,1)); %V is RMS magnitude of  
voltage signal.
```

```
2 - [~, I] = fft_imp_extract(dataX(:,2));           % I is RMS
magnitude of current signal.
```

```
3 - I = I/100;   %divided by 100Ω to change voltage across R12
(Figure 5-1) to current through R12.
```

```
4 - Z=V/I; %Z is the value of impedance.
```

'fft\_imp\_extract' is a Matlab function written to find the magnitude of the sinusoid signal the segment of interest using FFT (Figure 8-3). For the single-frequency SBIA system FFT peaks corresponding to the 50 kHz input sinusoid were traced from both spectrums directly providing RMS values of current and voltage. This was counter intuitively applied to extract impedance at other frequencies allowing easy expansion to multi-frequency operation. This allowed impedance to be measured without a large signal post-processing overhead.

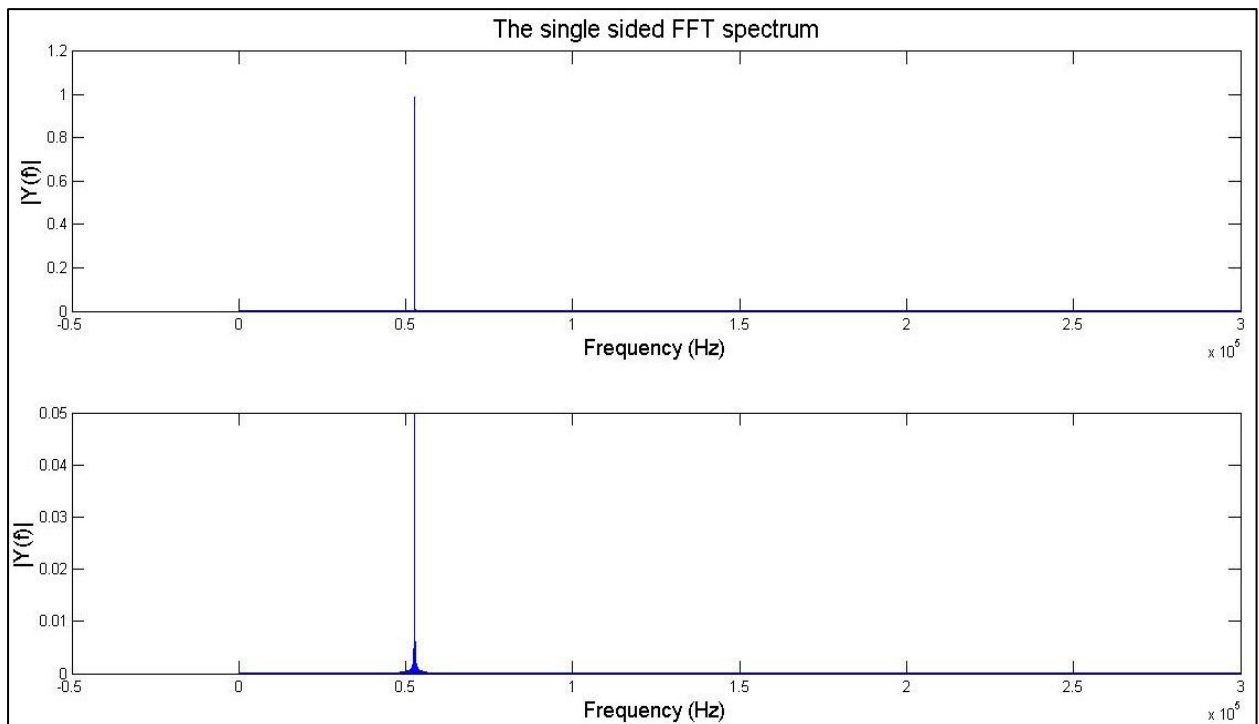


**Figure 8-3: Shows the FFT spectrum of a bio-electrical signal acquired from an individual's left arm. The two FFT plots belong to the same data but have been scaled differently to show low magnitude of noise close to the 50kHz peak.**

**Conclusion:** This way bio-impedance from eight segments at four different frequencies can be obtained. The examples described above apply to version 2 of the device but was extended to acquire bio-electrical signals at 4 different frequencies (in version 3 & 4) of device with minimal modification.

## **8.6 Summary:**

Presented in this chapter was the Matlab application written to acquire volunteer information and obtain bio-impedance signals from the 8 body segments of these volunteers. In order to achieve this various modules in Matlab were invoked, in particular the data acquisition tool box within Matlab was used to set parameters of the Agilent data acquisition device and provide the digital signals required to control the electrode switching within the device. The various functions and programs written to achieve this allowed the patient information and bio-impedance signals from each volunteer to be saved in an encrypted folder.

## **Chapter 9 Evaluation of impedance measurements**

### **9.1 Introduction:**

This section will focus on the impedance measurements from version 2 and version 4 of the device. Figure 9-1 shows the main components of the final (version 4) of the S-BIA system. The developed circuit along with the battery pack is housed in the grey box, the electrode rig has electrodes E1 through E8 attached onto it, the DAQ device (Agilent U2531A) acquires signals and relays the signals back to a laptop computer (not shown in picture). It also produces the digital control signals (three in version 4) to execute control over the constructed device. It is to be noted that the electrode rig comprises of the electrodes E1 to E8 alone, the original circuitry within the Tanita device is removed and the electrodes are connected to the constructed BIA device. Also various connectors connect the electrodes to the circuit and carry signals to and from the DAQ card. Figure 9-2 shows a subject undergoing segmental bio-impedance analysis. Both devices were tested with precision resistors (0.01% tolerance resistors) to evaluate impedance measurement accuracy and repeatability of successive impedance measurements on subjects. In addition as confirmed by Organ & Bradham 1994 (mentioned in section 1.9.3) the sum of impedances from the arm, trunk and leg should closely follow the whole-body impedance measured from the same side (left or right), this is a good indicator of the performance of a SBIA system therefore the error between the sum and measured whole-body impedance was also evaluated. These three metrics gives a good indication of performance of an S-BIA system. Volunteer trials included version 2 of device being tested on 14 volunteers, as part of an undergraduate project and version 4 of the device was trialled in a hospital setting and impedance measurements were compared against body composition results from a DEXA scan

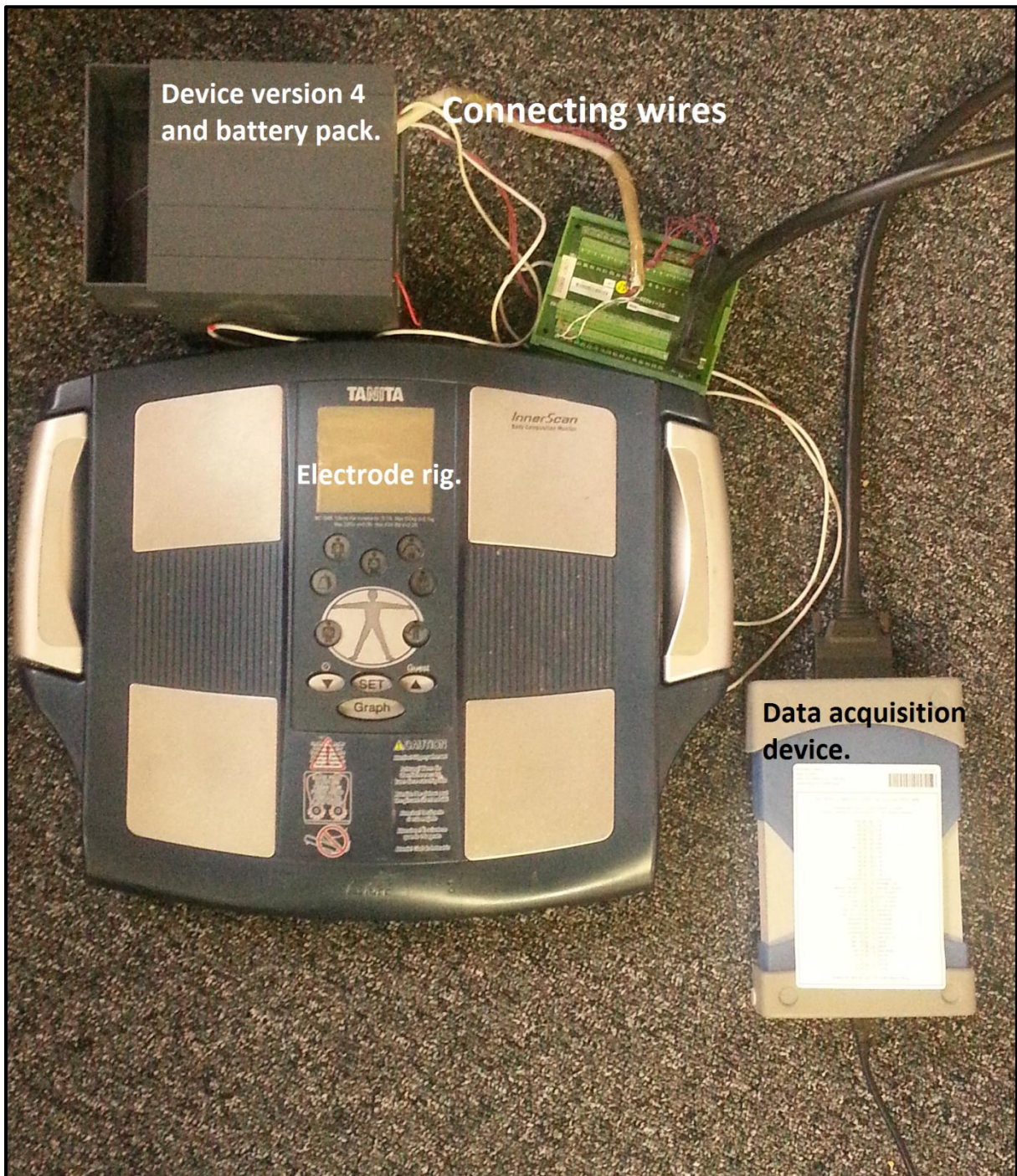


**Figure 9-1: Shows the S-BIA (version 4) measurement setup. Main sections include the device & battery pack housing, the electrode rig, the DAQ card, wires which connect electrodes and digital control lines to control device. Also required is a computer with Matlab (not shown in picture). Please note that the original circuitry from the Tanita device is removed and the electrodes alone are used.**



**Figure 9-2: Shows a subject undergoing impedance examination on the device (version 4).**

## 9.2 Testing with precision resistors:

Table 9-1 shows 10 consecutive impedance estimates across test resistors 100, 250, 500, 1000Ω of 0.01% tolerance. There was a consistent increase in the standard deviation (SD) with increase in the resistor values. The low SD among values shows that the device is capable of making very accurate impedance estimates. The measurement was made at 50kHz using the same method used to make impedance estimates on human subjects except that electrodes were replaced with wired connections to the resistors.

**Table 9-1: Ten consecutive impedance estimates of 100, 250,500, 1000Ω test loads at 50kHz with corresponding mean, standard deviation and mean error (all units in Ohms).**

<b>Actual Value(in Ohms)</b>	<b>100(0.01%)</b>	<b>250(0.01%)</b>	<b>500(0.01%)</b>	<b>1000(0.01%)</b>
<b>Predicted Values (in Ohms)</b>	99.7351	250.4257	501.4222	1001.5740
	99.8088	250.1932	500.9957	1001.6200
	99.7180	250.4475	500.9563	1003.0810
	99.8475	250.2703	501.5149	1002.9530
	99.6175	250.1440	500.9853	1003.6790
	99.7648	250.2316	501.0881	1002.9120
	99.8083	249.9657	500.9182	1003.5460
	99.7578	250.3858	501.0664	1002.6060
	99.7161	250.2932	501.0248	1002.8320
	99.7681	250.1674	501.1967	1002.9700
<b>Mean</b>	99.7542	250.2524	501.1169	1002.7780
<b>Standard Deviation</b>	0.0639	0.1464	0.2020	0.6993

The standard deviation was noted to be less than 1Ω in all cases although there was an increase in the standard deviation (from 0.064 to 0.70Ω) with increase in the test resistor value. A similar increase (from 0.046 to 0.62Ω) was observed for version 4. The slight

decrease in the standard deviation can be attributed to the use of a single SPDT switch for voltage-sense electrode switching in version 4 as opposed to two multiplexers in version 3.

**Conclusion:** Therefore it can be concluded that the impedance estimates from the device are accurate with standard deviation less than 1Ω between measurements which is better than results reported in Goovaerts et al. 1998.

### 9.3 Repeatability of bio-impedance measurements:

Table 9-2 lists the percentage relative SD's from 8 segmental bio-impedance measurements taken from a subject within a span of 20 minutes.

**Table 9-2: Shows the relative standard deviation for different segments from 8 consecutive bio-impedance measurements at 50kHz.**

Body section	Percentage relative SD
Left arm	0.7107
Trunk from left	1.3182
Left leg	0.5217
Whole-body from left	0.5159
Right arm	0.4532
Trunk from right	0.8877
Right leg	0.2714
Whole-body from right	0.2546

For each measurement the subject released contact with the electrodes and came back in touch with the electrodes again. On average it can be observed that the relative percentage error was less than 1%, the highest being for the trunk measurement made from the left hand side. This trend was observed in both versions of the device.

**Conclusion:** This shows that the device is capable of producing highly repeatable results and comparable to those reported in Goovaerts et al. 1998.

## 9.4 Whole-body impedance; compared to sum from arm, leg and trunk:

Table 9-3 lists the mean percentage error between measured whole-body impedance and sum of impedance from arm, trunk and leg.

**Table 9-3: Show the mean absolute percentage error between measured whole-body impedance and whole-body impedance found by adding impedances from the arm, trunk and leg which was observed in device version2 (single-frequency) and version 4 (multi-frequency).**

Frequency	Version 4		Version 2	
	Left	Right	Left	Right
10kHz	0.7351%	0.61997%	N/A	N/A
50kHz	1.4661%	2.241%	0.9448%	0.3182%
100kHz	3.9211%	2.8885%	N/A	N/A

In version 4 of the device it can be seen that the error between the two impedances increases with frequency.

**Conclusion:** The low percentage error shows that the impedance measurements being made by the devices are reliable and the electrode placement is optimal since impedance measurements from wrongly placed electrodes would produce a greater error between measured and summed whole-body impedance (Organ & Bradham 1994).

## 9.5 Validity of segmental BIA measured; comparison with Tanita BC-545 body composition estimates:

In order to validate impedance measurements from the constructed bio-impedance device the impedance measurements was compared with body composition from the BC 545. In order to do this consent was obtained from 14 volunteers to undergo body-composition measurements on the BC-545 and the segmental-impedance measurements on the constructed device as part of an undergraduate project at Aston University. The impedance measurements from the present device provided a convincing positive correlation with the Tanita body composition estimates.

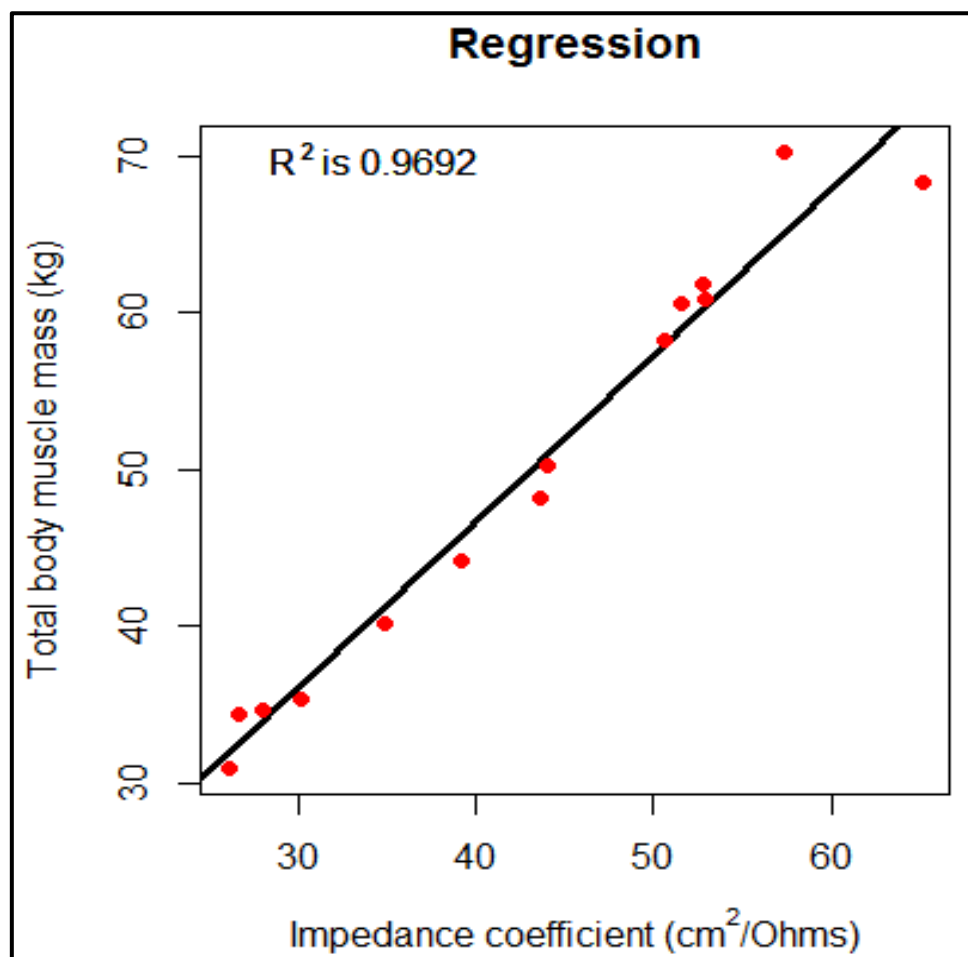


**Figure 9-3: Shows the strong correlation between whole-body lean mass predicted by Tanita BC-545 and whole-body impedance coefficient measured using the constructed device (version 2).**

Figure 9-3 shows the regression plot between whole-body impedance coefficients (ratio of square of subjects height to measured whole-body impedance) measured using the present device compared to the whole-body muscle mass estimated by the Tanita BC-545, here the coefficient of determination ( $R^2$ ) was found to be 0.97. Similar results were seen when impedance estimates from the limbs was compared against the lean mass of the limbs.

**Conclusion:** This gives proof to believe that impedance estimates made by the Tanita BC-545 and the constructed bio-impedance device are similar.

## 9.6 Summary:

In this chapter we tested the constructed bio-impedance device (V2 and V4) with precision resistors and established that the performance of the device was satisfactory. Also performed were tests on the repeatability of SBIA measurements and found that the whole-body impedance closely follows the sum of the impedance of the arm, leg and trunk on each side as reported by Organ & Bradham (1994). A strong correlation was found between whole body impedance measured by the current device and total body muscle mass predicted by the Tanita BC-545.

# **Chapter 10 Other applications of obtained bio-impedance signals**

## **10.1 Introduction:**

From the start of the project we aimed at exploring a few potential applications of bio-impedance signals and measurements. Two such possible applications were explored; one to extract heart-rate from bio-impedance signals and the second to try to establish a possible relationship between limb volumes and measured limb impedance. The following two sections will discuss these potential applications.

## **10.2 Extracting heart rate from segmental-bio-electrical signals:**

Early in the project when the whole body impedance device was conceived, the signal output from this device was visualised before impedance extraction, and it was observed that there were regular dips in the signal envelope when the signal samples were plotted against time as shown in Figure 10-1. The time interval between the dips was roughly quantified, and it matched the heart-rate of a healthy individual which usually is between 60-90 beats per minute (bpm) (between 1 and 1.5 Hz).

The phenomenon of changing electrical impedance due to pulsating blood flow was reported by Shankar et al. (1985). Since all blood vessels are distensible, they provide resistance to blood flow which leads to blood-vessel volume change. A model for impedance variations in limbs due to variations in blood volume and resistivity is provided in Shankar et al. (1985). Previous studies by González-Landaeta et al. (2008) have utilized complicated synchronous demodulation circuitry and further filtering to extract heart rate from changing impedance due

to change in blood volume change. The following investigation will illustrate a less complex method to achieve this utilizing with three digital low pass filtering (LPF) stages, which have been employed to 'clean' the bio-electrical signals in the present study. Similar heart rate signals are also reported in Batra & Kapoor (2010).

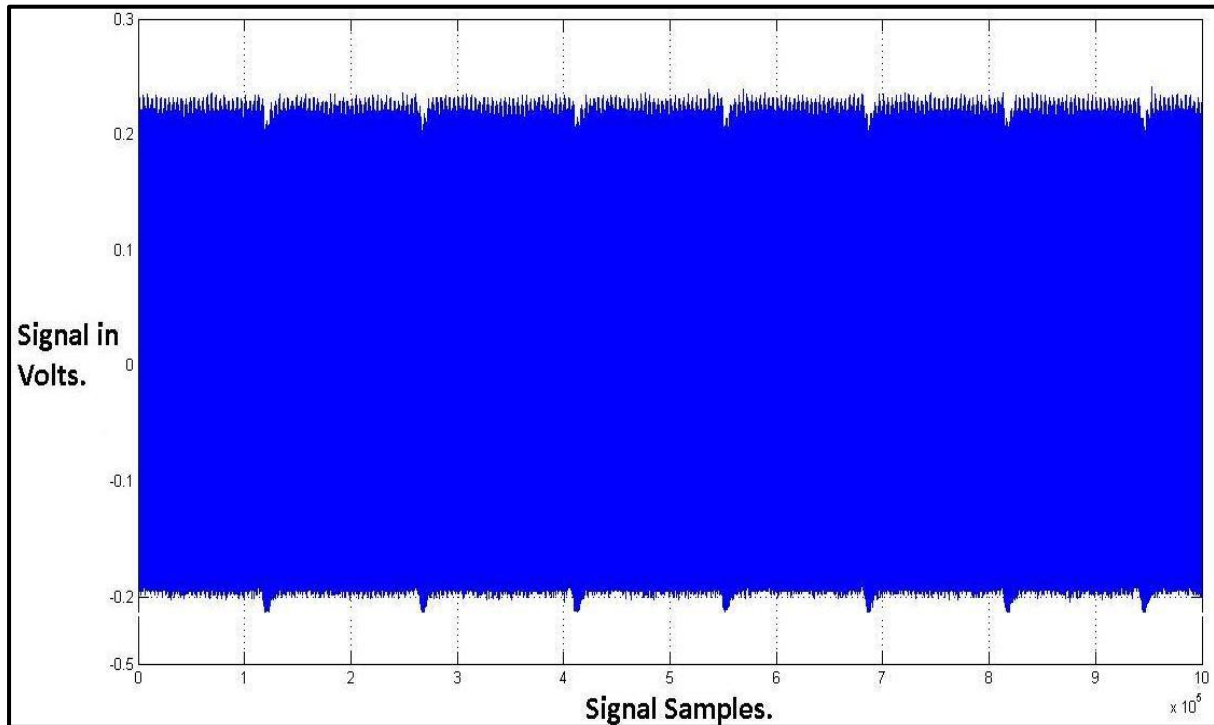


**Figure 10-1: Shows regular dips observed in bio-electrical signals acquired over five second duration. It also provides an insight into the sensitivity of the device. Here the signal is sampled at 200kSa/s and recorded for 5 second duration.**

### **10.2.1 Initial approach:**

Using the general principles set out by González-Landaeta et al. (2008) AM (amplitude modulation) demodulation was opted at first where the 50kHz input sinusoid was the carrier and the signal dip caused by the heart-beat was treated as the message signal. Synchronous demodulation is an effective method to retrieve the message signal (heart rate signal) from the amplitude modulated carrier. In its most basic form it consists of a mixer which multiplies the incoming AM signal with a locally generated carrier (LGC), this LGC needs to be phase locked with the original signal for the message to be effectively retrieved.

Alternately a copy of the original carrier can be used with the mixer to obtain the message signal. The output of the mixer is low pass filtered to remove the high frequency component of carrier from the message to obtain the final message signal. This would be viable if a copy of the input 50kHz sinusoid consistent in phase with the measured bio-electrical signal was available. But by design the circuit layout did not have a connector to retrieve and save a copy of the 50kHz input (carrier) signal.

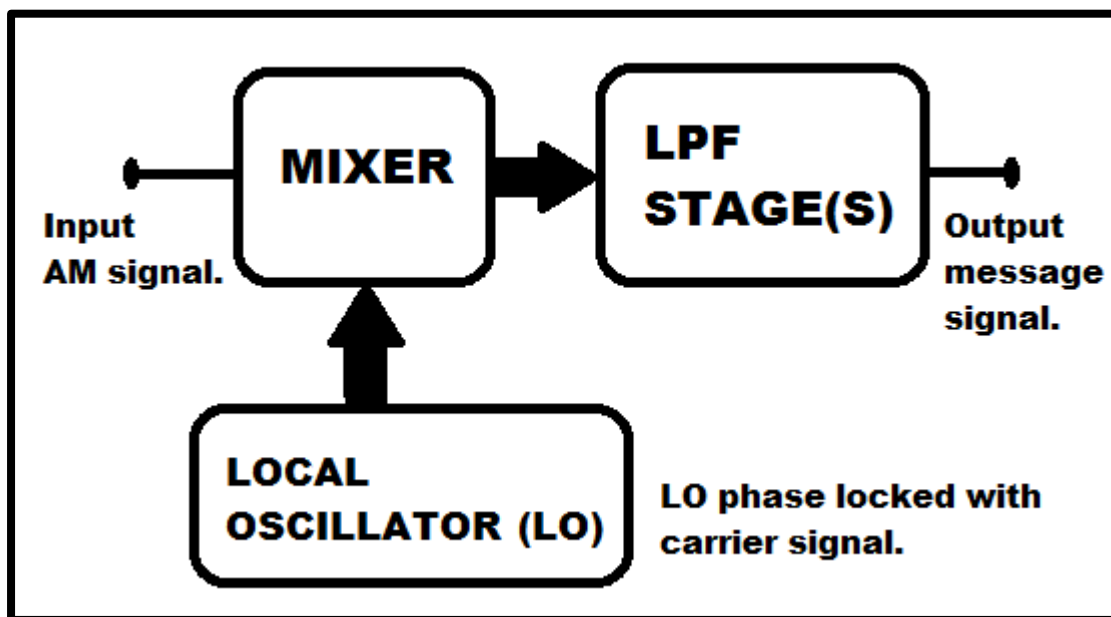


**Figure 10-2: Shows the block of a basic AM synchronous demodulator. The input AM signal is mixed (multiplied) with a locally generated carrier and the passed through a low pass filter stage(s) to retrieve the original message signal.**

Hence AM demodulation by envelope detection was opted. Envelope detection can be performed either by using a signal squaring method, where the input signal is squared, low pass filtered and then the square root of the result taken to recover the message signal. Alternately envelope detection can be performed with Hilbert transform (beyond the scope of this thesis refer to Oppenheim 1975 for specific details). Both these methods were utilized but could not successfully retrieve the heart-rate dips from the bio-electrical signals. The Matlab code used for both these methods is included in the Appendix 3. With both the above

mentioned methods not giving satisfactory results the possibility of low-pass filtering the signals was explored and as will be described in the following section provided satisfactory results.

### 10.2.2 Three stage digital-LPF to determine volunteer heart rate:

Three LPF stages were utilized to retrieve the peaks or dips in bio-electrical signals caused by the functioning of the heart.

**Table 10-1: Shows the cutoff frequency, stopband frequency, stopband attenuation and order of the three filters used to extract heart-rate from bio-electrical signals.**

	Filter stage 1	Filter stage 2	Filter stage 3
<b>Fc (Cutoff frequency)</b>	8750	100	10
<b>Fs (Stopband frequency)</b>	11250	250	100
<b>Stop band attenuation(dB)</b>	23.64	47.57	51.16
<b>Filter order</b>	801	160	300

Table 10-1 lists the important characteristics of the three filters used to retrieve the heart-rate peaks from the bio-electrical signals. Figure 2-5 in section 2.2 shows the frequency response of a non-ideal low pass filter and the interpretation of the characteristics mentioned in Table 10-1. The filter design method described in section 2.2 was used to design the three filter stages. The block diagram (Figure 10-3) illustrates the main steps taken to filter and extract the heart rate signal.

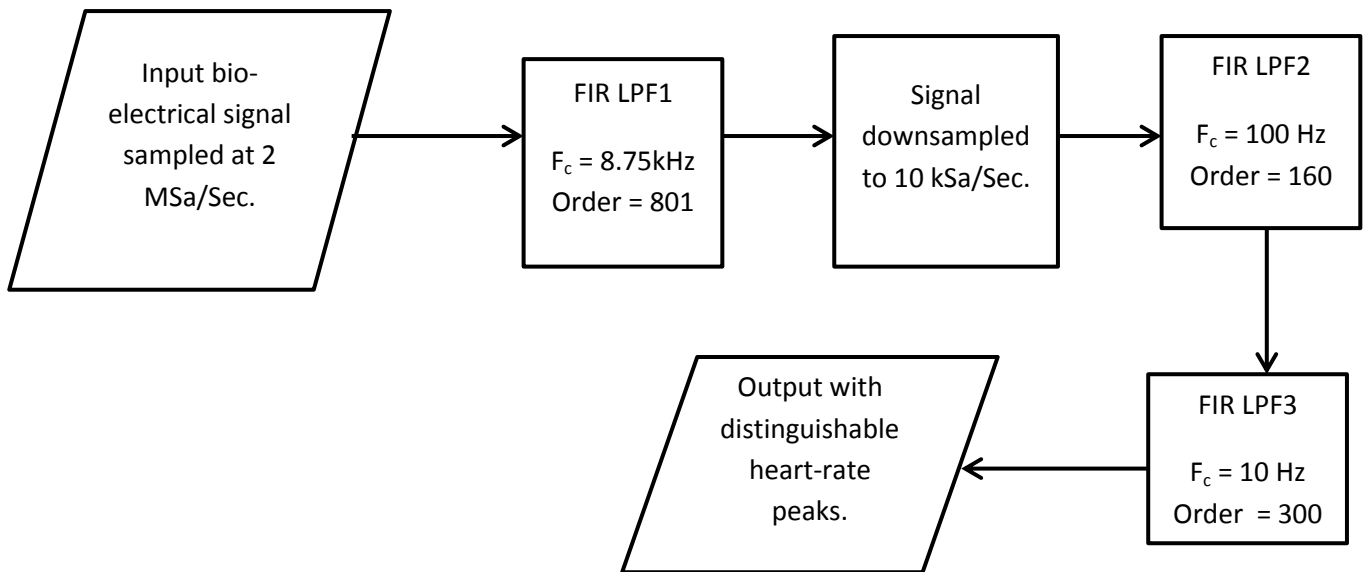


**Figure 10-3: Shows the three filtering stages the input bio-electrical signal goes through before the output with distinguishable heart-rate peaks is obtained.**

As the block diagram in Figure 10-3 shows the input sampled at 2 MSa/sec is first low pass filtered with a stopband frequency and attenuation of 11.25kHz and 23.64 dB. Next the output from the first stage (LPF1) is downsampled 200 times reducing the sampling frequency to 10 kSa/sec, this would still preserve the heart-rate signal we are interested in. The downsampled signal is passed through a second stage (LPF2) with a stopband frequency and stopband attenuation of 250Hz and 47.57 dB. The output from LPF2 is passed through the third low pass filtering stage (LPF3) which has a stopband frequency and stopband attenuation of 100 Hz and 51.16 dB. Figure 10-4 shows a time fragment of two seconds of the bio-electrical signal recorded across the right-arm before and after each filtering stage. The final stage with 10 Hz cutoff ensures the heart-rate signal which in a normal human being is between 0.8 Hz to 1.5 Hz, is preserved and can be analysed. The other alternative to this method was to down sample the signal and then use a single LPF stage after down sampling. This method was applied initially but it was observed that the resulting output was corrupted with noise to a larger extent than the method described above. It was also deduced from experimentation that it is computationally more efficient to

run the signal through two consecutive filters of smaller order than feeding the signal through a single filter whose order is higher, but produced results comparable to the original case.

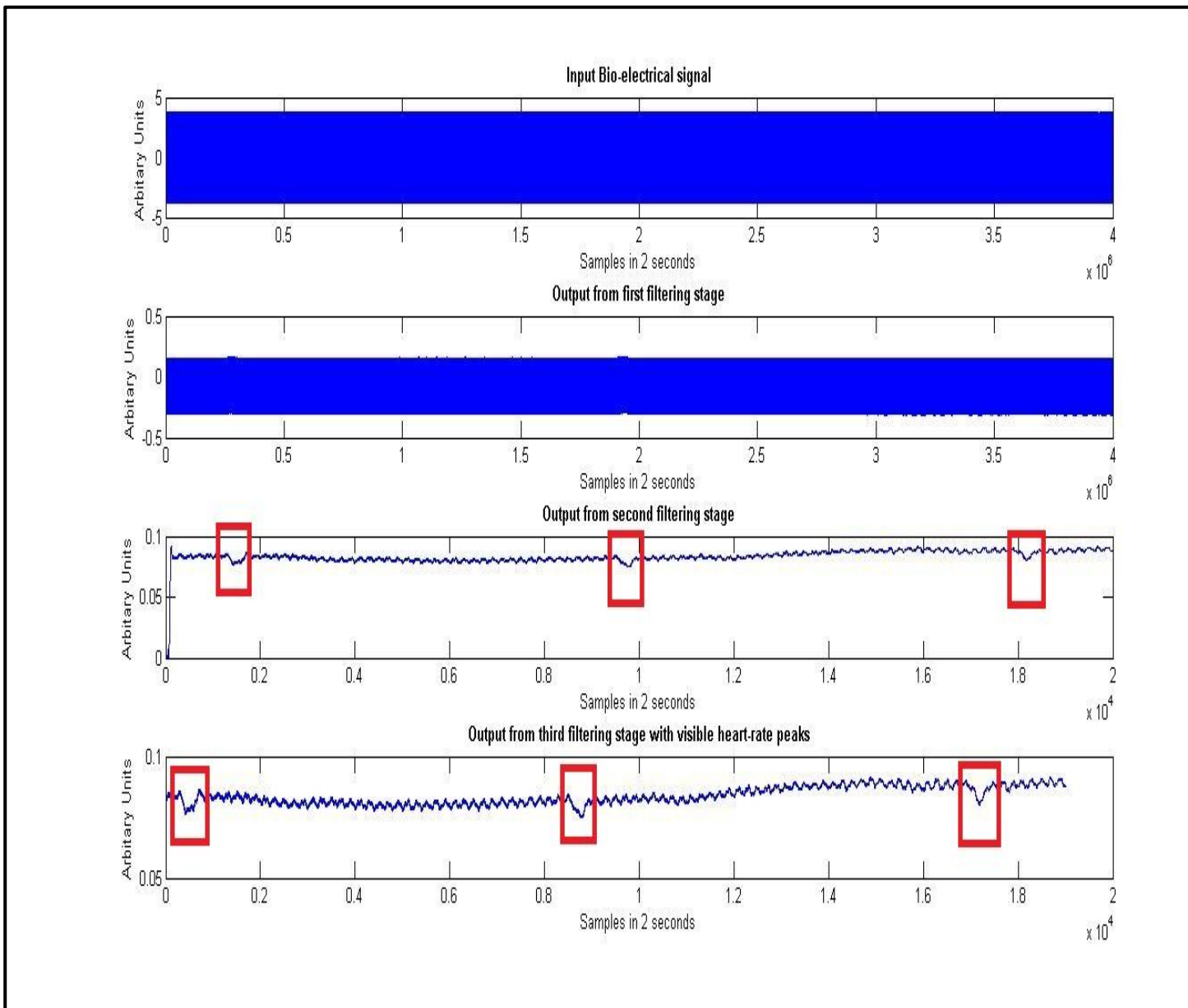


**Figure 10-4: Input signal along with the output from each filtering stage. The original signal (subfigure 1) is sampled at 2MSa/s. Also the heart rate dips are marked with red boxes.**

### 10.2.3 Eliminating baseline drift:

The output of the third LPF stage is the heart-rate signal but as can be observed from Figure 10-6 there is significant baseline drift (where the signal is not centred on a common line).

This phenomenon is also quite common in actual ECG signals (Bisson et al., 2012). If we consider the peaks in the final filtered output to be the R peaks in an ECG signal (Figure 10-5), finding the time interval between the two R peaks would give the time interval required. A thresholding method could be used to distinguish the R peaks from the rest of the filtered signal but only after the baseline drift has been minimized which otherwise could cause baseline fluctuations to be classified as R peaks. With the help of an algorithm presented in Chouhan & Mehta (2007) the baseline drift can be minimized using a Savitzky-Golay smoothing method described in section 2.2.5. The lower half in Figure 10-6 shows the result applying a fourth degree polynomial smoothing with the Savitzky-Golay method on the input signal in the second subfigure. When the smoothed signal is subtracted from the input to the baseline drift removal stage a baseline rectified signal shown in Figure 10-6 is obtained.

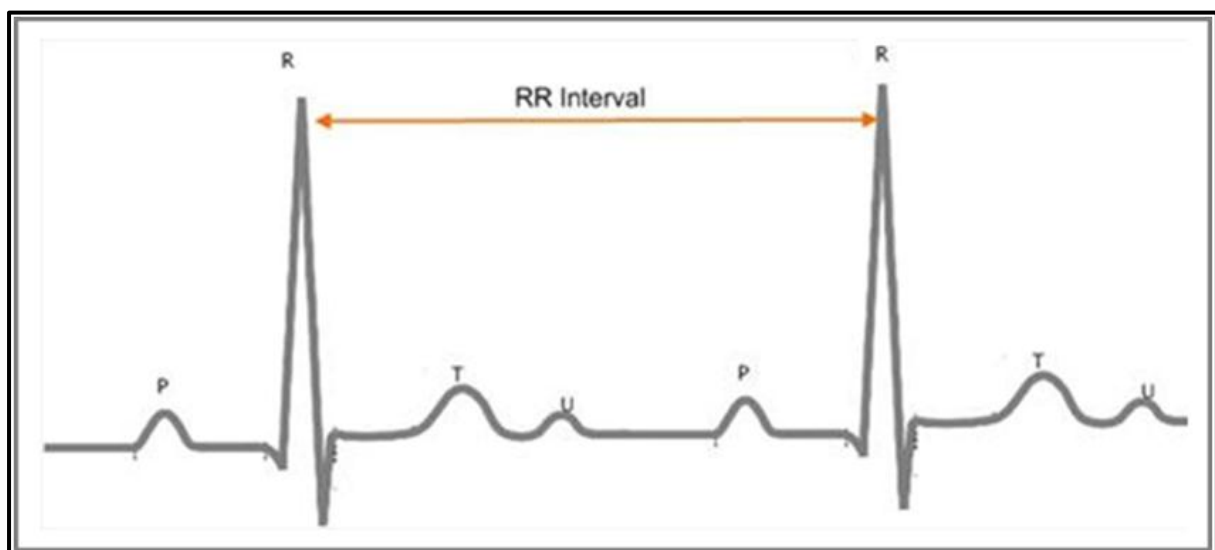


**Figure 10-5: Shows the R peaks of a real ECG signal, the time difference between the two R peaks is the time difference between two heart-beats.**

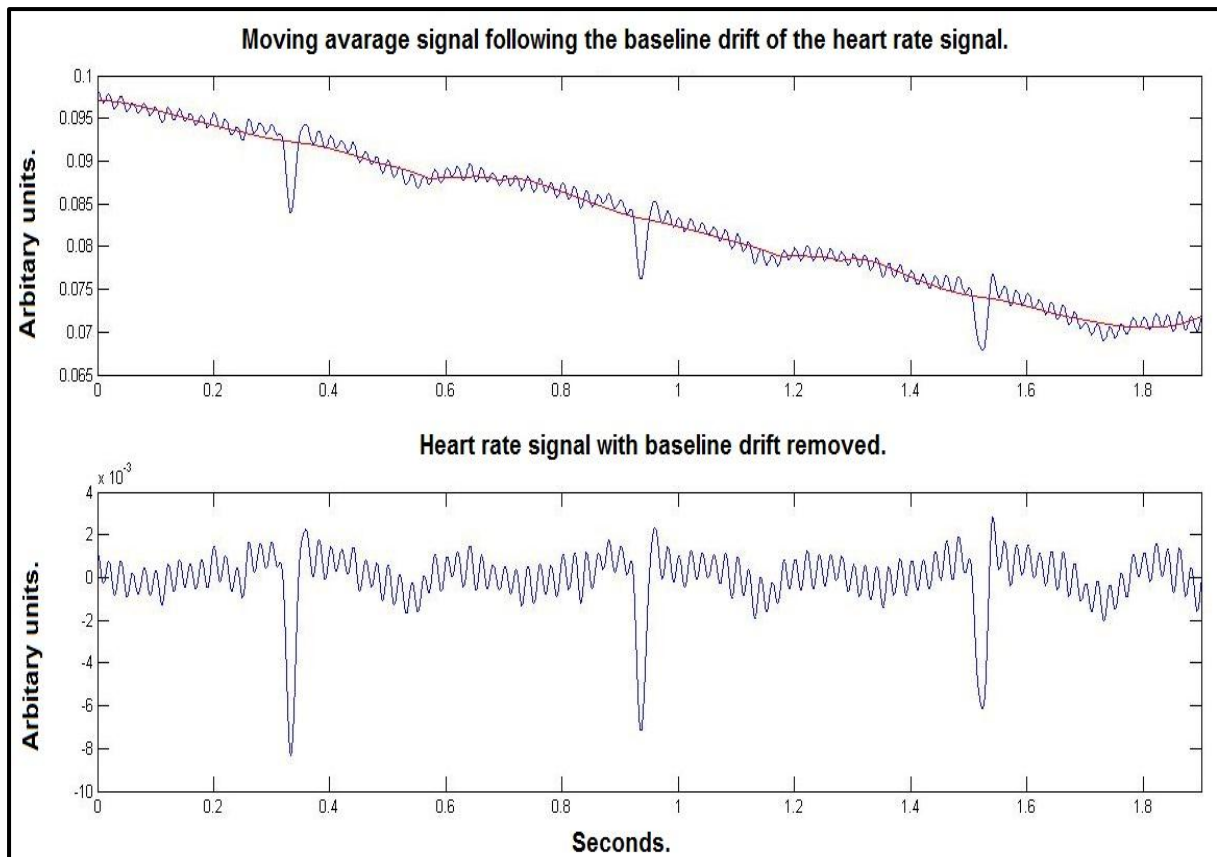


**Figure 10-6: Shows the smoothing procedure which generates a signal following the baseline drift of the original signal. After subtracting the smoothed signal from the input the baseline rectified signal is recovered as shown in the lower sub-figure.**

#### **10.2.4 Extracting the heart-rate from baseline rectified signal:**

After the baseline drift is removed the problem becomes finding the R peaks and their indices (sample number), then calculate the difference between the sample number corresponding to these R peaks. This has to be translated into time by dividing the difference with the sampling frequency (which after the first filtering stage stands at 10 kSa/Sec). The inverse of this time-difference would give the frequency in Hertz; this frequency when multiplied by 60 would give us the number of beats in one minute. Matlab functions 'findpeaks' and 'diff' conveniently help in this regard. The following two lines of Matlab code detect the R peaks are detected and determine the difference between the indices of detected peaks.

```
[pks1,locs1]=findpeaks(abs(ecg1),'minpeakdistance',5.7e3,'minpeakheight',0.6*max(abs(ecg1)));
```

```
x1=diff(locs1);
```

Starting from the left hand side 'pks1' and 'locs1' represent the magnitude and index of the R peak respectively in the two second period of the signal under examination. On the right hand side the 'findpeaks' function is supplied with its first argument which is the input to the function (the baseline rectified signal). The next argument is the 'minpeakdistance' argument which forces the function to look for peaks only after a certain time interval, the value of 5.7 kSa/sec translates to approximately 105 beats per minute (BPM), because we do not expect our healthy volunteers to have a heart rate above this during the measurement. The final argument is 'minpeakheight' which would classify a spike as an R peak only if its magnitude is 60% of the magnitude of the highest R peak in the input baseline rectified signal. The 'diff' function simply evaluates the difference in the indices of R peaks obtained in 'locs1' and puts these values in 'x1'. Upon analysis it was observed that the signals acquired to measure impedance of the left and right leg segments did not show any distinguishable R peaks, hence the signals from the other six segments were utilized to extract heart rate. Since acquisition time at each segment is two second it gives us a total of 12 seconds (2 seconds × 6 segments) worth of bio-electrical signals to determine heart rate.

**Results and conclusion:** When the above described procedure was applied to bio-electrical impedance signals from the first set of 14 volunteers the minimum and the maximum heart rate were found to be 68 BPM and 93 BPM. Hence the described method can be effectively be used to extract heart rate from six of the eight segmental bio-electrical signals acquired per person.

### **10.3 Estimating volume of body sections using the KinectFusion algorithm in PCL:**

As described in the introduction the KinectFusion algorithm can be used to reconstruct whole 3-D shapes of real world objects and save these reconstructed surfaces for further analysis. Obtaining the volume of these shapes involves extra steps as described in this section. Consider a real world object like the bust shown in Figure 10-7. When the Kinect camera is moved around the object with an approximate distance of 0.5 m from the object surface the KinectFusion (KinFu for short) program running on a computer reconstructs the object and allows the reconstructed 3-D surface which is saved as a polygon mesh (\*.ply) file or as a point cloud.



**Figure 10-7: The bust which was reconstructed using the KinectFusion algorithm.**

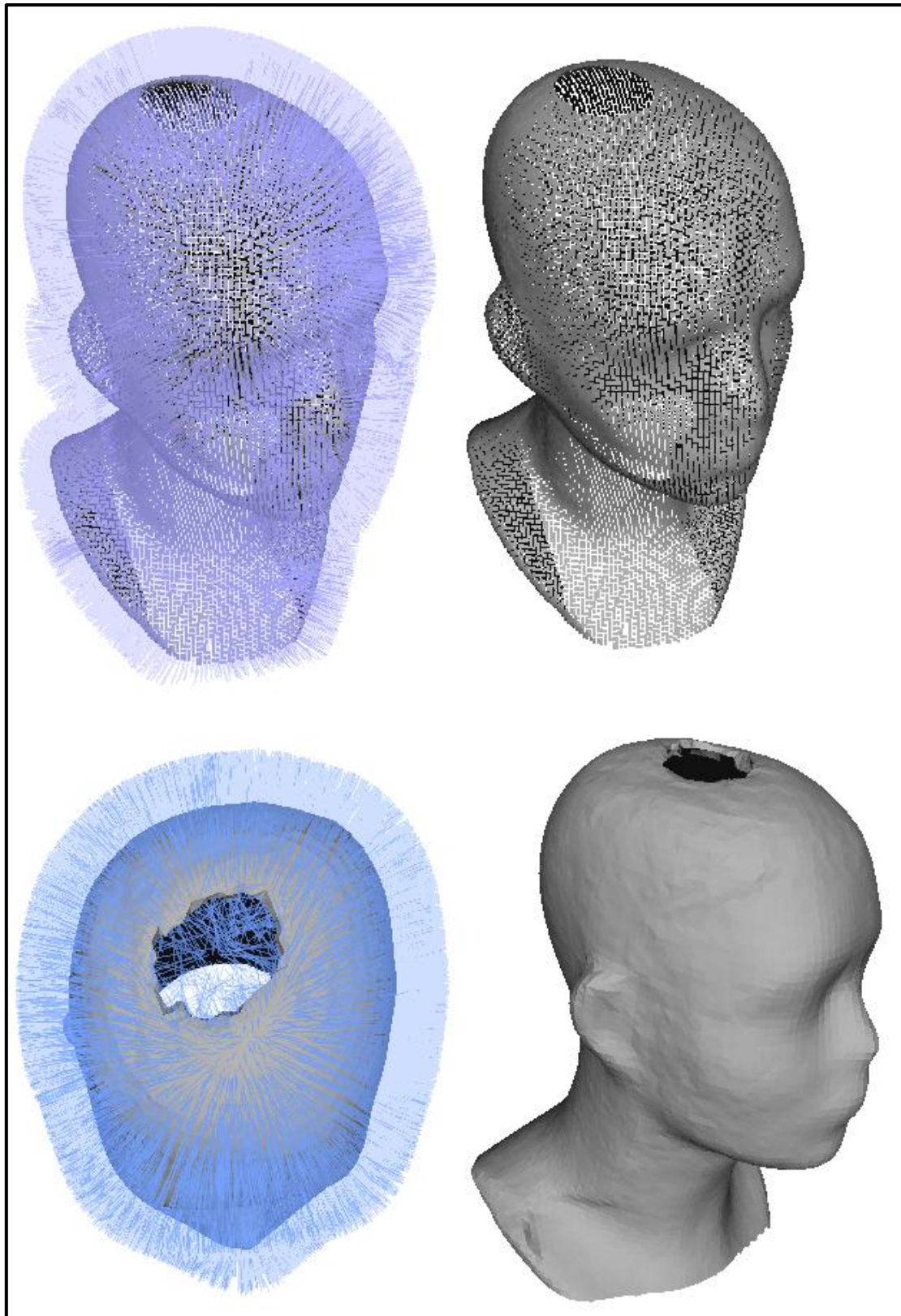


**Figure 10-8:** Shows the reconstructed bust as a point cloud and its point normal (upper two images) and as a mesh and face normals (lower two images). Notice there exist holes at the top and bottom of the bust.

Figure 10-8 shows the reconstructed bust as a point cloud and point normals (upper images) and as a mesh and face normals (lower images). These 3D surfaces need to be cleaned and separated from the remainder of the reconstructed surrounding surfaces. This is done manually Meshlab, which allows selection and removal of unwanted surfaces. Figure 10-8 shows the mesh and point cloud from the bust which has been cleaned using Meshlab. Meshlab also includes a feature which directly estimates the volume of objects if the surface is closed; i.e. it has no holes. But as can be seen in Figure 10-8 the model does have holes on the surface. Large holes can be avoided to an extent with precise camera movement around the surface but it is highly probable that a reconstructed surface will have a hole in it. To fill these holes Meshlab includes a surface reconstruction algorithm. The particular algorithm utilized in this study is called the Poisson surface construction which was proposed in Kazhdan et al. (2006), and is a feature of Meshlab used in the present analysis. This algorithm uses both the point or face location and their normals to reconstruct the entire surface. A good feature of Poisson surface reconstruction is that it always returns a closed surface. Figure 10-9 shows the bust point cloud reconstructed using the surface reconstruction algorithm.

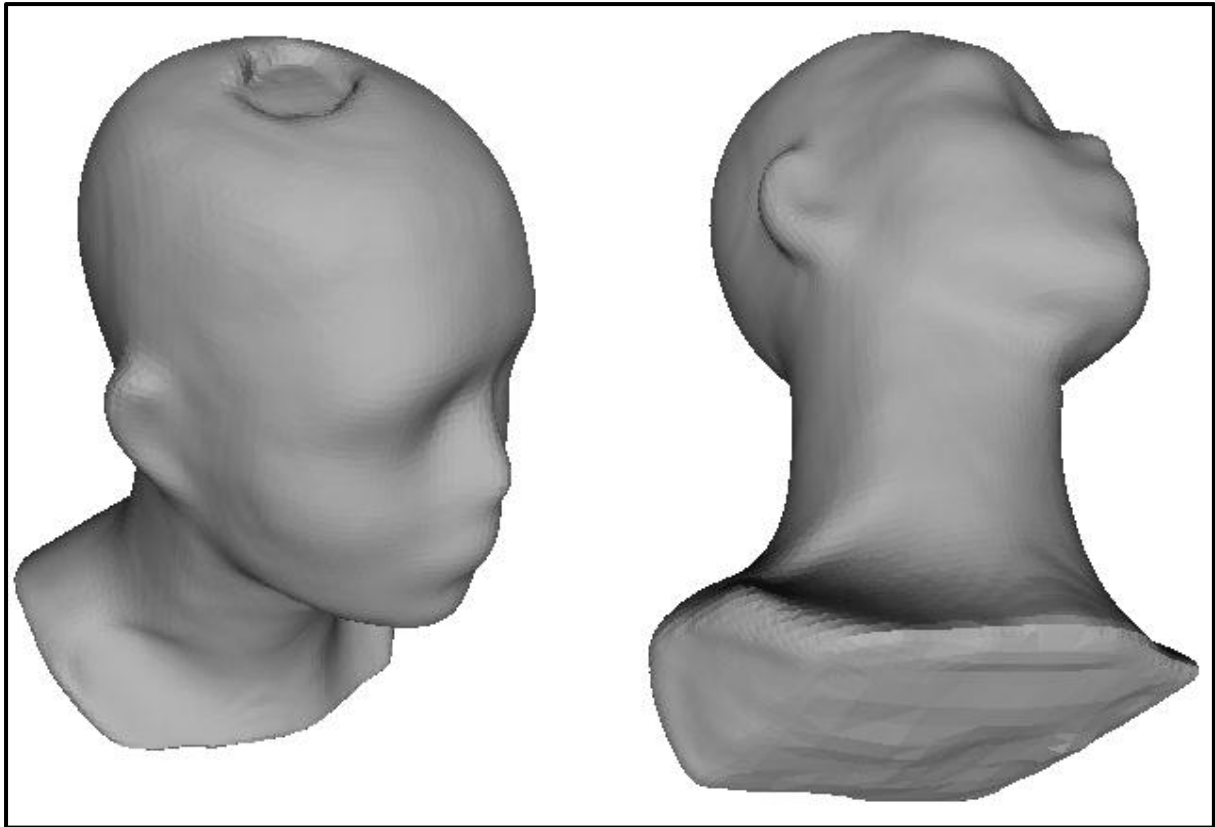


**Figure 10-9: Shows the bust surface reconstructed using the Poisson surface reconstruction. Notice that the holes in the previous figures have been successfully filled.**

**Results and conclusion:** Evaluating the volume of the bust was performed using a rigid bucket which was filled to the brim with water and the bust immersed into it. The volume of water displaced would be the volume of the bust. This was found to be approximately 5340 millilitres (ml). When the volume of the bust was predicted using the volume estimation feature in Meshlab it was found to be 5255 ml (average of 10 measurements, recorded SD was 17.38 ml). The error of 85 ml can be attributed to measurement error possibly in the immersion technique, and also the calibration of the input Microsoft Kinect camera. In this manner we have successfully employed the OpenSource KinectFusion algorithm to predict volumes of closed objects, and will be later used in later sections to extract body volumes.

## **10.4 Summary:**

This chapter demonstrated the extraction of heart rate signals from bio-impedance signals which involved the use of a three stage FIR LPF filtering procedure. Heart-rate signals were observed in signals of all four frequencies V4 was designed for i.e. 10kHz, 50kHz, 75kHz and 100kHz. Also illustrated in this chapter was the use of the KinectFusion algorithm to determine the volume of real world objects. This method is used in later chapters to determine the volume of human limbs.

## Chapter 11 Results

Previous chapters of this thesis have described the development and testing of a highly flexible multi-frequency segmental bio-electrical signal recording system. This section will focus on the outcome of studies to compare the bio-impedance measurements from this device (version 4) and body composition parameters obtained using DEXA scans (standard body composition evaluation technique). In addition to the original program two additional hypotheses were tested during the present studies. Firstly body-segment volumes estimated using a KinFu 3D scan was compared to bio-impedance measurements. Secondly change in bio-impedance with motion of the arm was evaluated and compared to arm tissue volumes. The description of these additional procedures and results are presented in subsequent sections in this chapter. However the results produced by a DEXA scan will be discussed briefly first. Following ethical approval and informed consent bio-electrical signals from 22 human volunteers were recorded and their body composition was acquired (on the same day) using a DEXA scan at the Heartlands hospital, Birmingham, U.K.

**Subjects:** 22 healthy volunteers (15 female, 7 male; age range 24 to 60 years; 7 Asian, 14 Caucasian, 1 Afro-Caribbean) underwent both the BIA and DEXA procedures. Table 11-1 lists the mean age, height, weight and BMI for the participants and also respective standard deviations.

**Table 11-1: Shows the mean and standard deviation for the age, height, weight and BMI for participants in this study.**

	<b>Age(years)</b>	<b>Height(cm)</b>	<b>Weight(kg)</b>	<b>BMI (kg/m<sup>2</sup>)</b>
<b>Mean ± SD</b>	34.50±10.62	167.8±9.63	67.74±16.1	23.82±4.1

**Protocol:** For bio-electrical measurements the volunteers were asked to step on the constructed bio-impedance device so that the 4 foot electrodes were in contact with the

underside of the foot. Volunteers were also asked to hold the two handheld electrode attachments (two electrodes per attachment, Figure 11-1). Proper contact was ensured before the measurements were taken and any defective contact would show on screen as the acquired signals were visually monitored. The radiologist responsible for taking the DEXA scan ensured the protocol for body composition measurements was strictly followed which guaranteed highly accurate body composition estimates. Table 11-2 shows the body composition results summary from a volunteer. As can be seen the scan provides an estimate of the bone mineral content (BMC), fat mass, lean mass, combined lean mass (assuming BMC is part of lean body mass) and percentage fat mass in each body section listed under the 'Region' column. Optical character recognition service provided within 'Google Drive' was used to convert the text within the pdf images to computer readable text format; this reduced the effort which would have to be put in for typing individual entry for 22 volunteers. The bio-impedance of these volunteers (8 segments at 4 different frequencies, 32 measurements per volunteer) was combined with their respective body composition from DEXA in a comma separated text file (CSV). Table 11-3 shows the mean and standard deviation of bio-impedance measurements taken at four input frequencies. These values are in agreement with those presented by (Organ & Bradham 1994). The text file containing this information (also including gender, age, height, weight and ethnicity) for all 22 volunteers was imported into statistical package R for analysis. Linear and multiple regression (discussed in section 0) is utilized to analyse this information. For a linear relationship to be scrutinized further a cutoff of 0.6 was set on the coefficient of determination ( $R^2$ ). These relationships were further refined by including parameters like age, height weight and gender. Capitalizing on the huge flexibility of R we were able to fit linear models between impedance and composition of respective sections. For example impedance from left arm was compared with the composition parameters (BMC, fat mass) etc. of the left arm alone, with exception of whole body impedance which was compared against composition of all segments. Figure 11-2 shows the split of a subject's body into various sections in a DEXA scan. The dividing lines separate the section and the composition of each section is reported

in Table 11-2. The mean and standard deviations of various body composition parameters measured from 22 volunteers is presented in Table 11-4.



**Figure 11-1: Shows a volunteer undergoing bio-impedance examination on device version 4. As stated in section 9.1 the internal circuitry of the Tanita device pictured is replaced with device V4.**

**Table 11-2: Shows the body composition summary from a DEXA. The 'Region' column lists the section of the body and the top row lists the body composition parameters in grams. Last column represents percentage fat in the particular region.**

<b>DXA Results Summary:</b>						
<b>Region</b>	<b>BMC (g)</b>	<b>Fat Mass (g)</b>	<b>Lean Mass (g)</b>	<b>Lean + BMC (g)</b>	<b>Total Mass (g)</b>	<b>% Fat</b>
L Arm	113	857.6	1533.4	1646.0	2503.6	34.3
R Arm	118	816.0	1666.6	1784.7	2600.7	31.4
Trunk	390	5292.6	14466.2	14856.6	20149.3	26.3
L Leg	309	2695.3	5401.7	5711.2	8406.5	32.1
R Leg	319	2730.2	5623.8	5942.8	8673.1	31.5
Subtotal	1250	12391.8	28691.8	29941.4	42333.2	29.3
Head	533	873.0	2400.2	2933.1	3806.1	22.9
<b>Total</b>	<b>1783</b>	<b>13264.8</b>	<b>31091.9</b>	<b>32874.5</b>	<b>46139.2</b>	<b>28.7</b>

TBAR102 - NHANES BCA calibration

**Table 11-3: Shows mean and standard deviation of bio-impedance measured from various body sections (from 22 volunteers) at four different frequencies, viz. 10,50,75,100 kHz.**

<b>Frequency (kHz)</b>	<b>Left arm</b>	<b>Trunk from left</b>	<b>Left leg</b>	<b>Whole-body from left</b>	<b>Right arm</b>	<b>Trunk from right</b>	<b>Right leg</b>	<b>Whole-body from right</b>
<b>10</b>	422 ±78.82	25.54 ±4.06	301.3 ±51.27	754.2 ±127.58	413.7 ±76.24	27.51 ±8.96	297.6 ±52.70	739.2 ±126.60
<b>50</b>	379 ±77.34	24.51 ±5.98	266.5 ±47.62	768.9 ±120.94	373.4 ±70.91	24.88 ±5.82	264.3 ±49.23	658 ±119.88
<b>75</b>	369.2 ±72.81	22.11 ±3.46	258.6 ±44.67	654.4 ±114.51	360.2 ±70.85	22.11 ±3.51	255.7 ±46.58	680.8 ±115.61
<b>100</b>	361.6 ±72.36	21.25 ±3.30	251.8 ±44.77	630 ±133.73	355 ±70.05	21.36 ±3.17	249.5 ±45.51	625.9 ±113.99

**Table 11-4: Shows the mean and standard deviations of body composition parameters measured using DEXA scan (22 volunteers).**

<b>Body composition parameter</b>	<b>Mean(kg)</b>	<b>SD (kg)</b>
Left arm bone mass	0.174779	0.055833
Left arm fat mass	1.027417	0.452226
Left arm lean mass	2.552639	0.996537
Left arm lean mass and bone mass	2.72745	1.045663
Left arm total mass	3.754856	1.172234
Left arm percentage fat	27.87778	9.660262
Right arm bone mass	0.182129	0.056113
Right arm fat mass	1.010367	0.436919
Right arm lean mass	2.701811	1.003736
Right arm lean mass and bone mass	2.883906	1.052032
Right arm total mass	3.894278	1.196158
Right arm percentage fat	26.33333	8.815828
Trunk bone mass	0.643133	0.186219
Trunk fat mass	7.322278	3.304493
Trunk lean mass	23.57907	6.516805
Trunk lean mass and bone mass	24.22218	6.673722
Trunk total mass	31.54447	8.813619
Trunk percentage fat	22.77222	6.286007
Left leg bone mass	0.477338	0.135808
Left leg fat mass	3.321094	0.966171
Left leg lean mass	7.981322	2.341136
Left leg lean mass and bone mass	8.458744	2.46038
Left leg total mass	11.77984	2.743485
Left leg percentage fat	28.70556	7.006591
Right leg bone mass	0.488337	0.142246
Right leg fat mass	3.288956	0.971204
Right leg lean mass	8.1478	2.369037
Right leg lean mass and bone mass	8.636067	2.498058
Right leg total mass	11.89725	2.847823
Right leg percentage fat	28.05	6.700593
Total bone mass	1.880217	0.705109
Total fat mass	15.97012	5.766857
Total lean mass	44.96264	13.00605
Total lean mass and bone mass	46.92836	13.51281
Total percentage fat	25.46111	6.345924

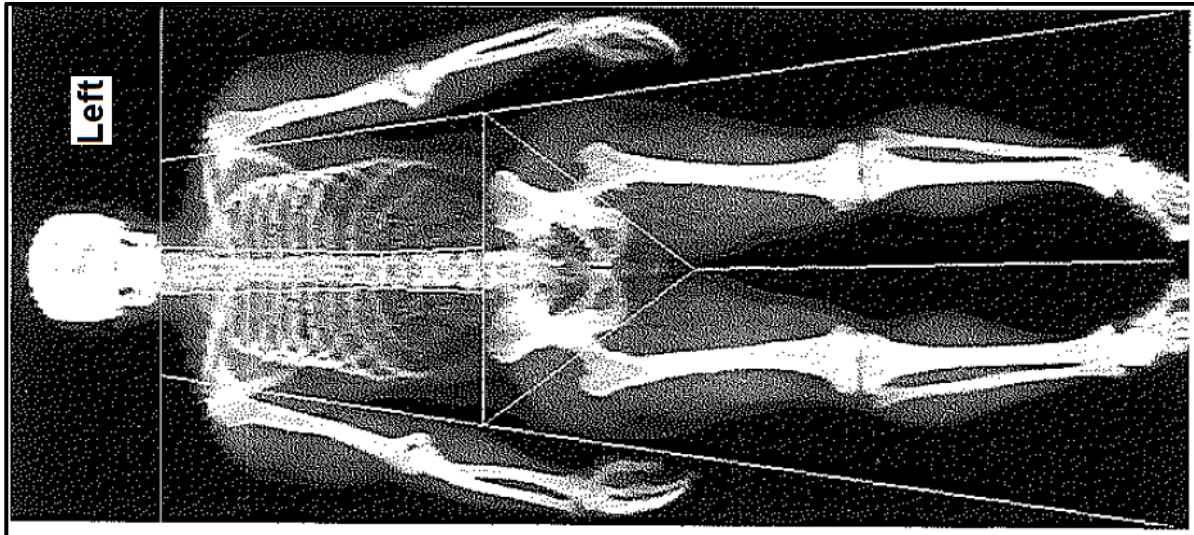


**Figure 11-2: Shows the typical split of a subject's body into left and right limbs and the trunk. The lines are used to separate different sections and body composition of each of these sections is presented in a DEXA result scan summary.**

As described in section 1.8 impedance coefficients are calculated for each impedance measurement and then used to develop linear models between impedance coefficients and various body composition parameters. The following sections and subsections describe the observed associations between impedance coefficient and composition of whole-body, arms, legs and body trunk.

## **11.1 Whole body composition:**

Here we look at whole-body composition and whole-body impedance coefficients, the parameters include lean mass, bone mass, fat mass and combined lean mass. Please note that throughout this chapter V4 of the device will be used to make segmental bio-impedance measurements. All bio-impedance measurements at all frequencies made in this chapter are made using V4 of the device.

### 11.1.1 Whole-body lean mass:

Figure 11-3 subsections (a) & (b) show the linear regression model between whole-body lean mass and whole-body impedance coefficient measured from the left and right at 10kHz and 100kHz. The Rsq values are 0.92 and 0.91 as shown in the figure. The Rsq value increases to 0.98 with the inclusion of height, weight and age in the regression model. The p value for each of this is presented in Table 11-5. Therefore measured impedance combined with height, weight and age can predict whole-body lean-mass accurately.

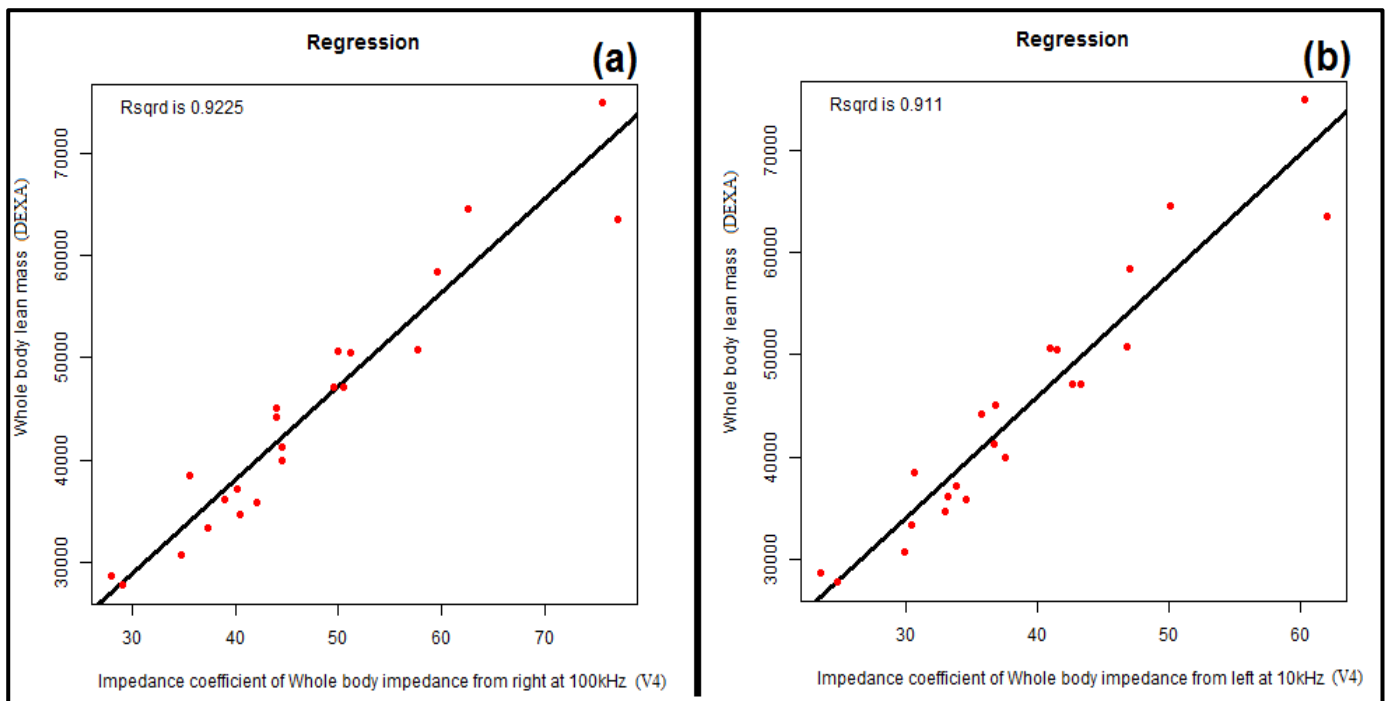


**Figure 11-3: Shows a linear model between whole-body lean mass and whole-body impedance coefficients measured at 10kHz and 100kHz. The whole-body lean mass is obtained from DEXA scan reports and is presented here in grams.**

**Table 11-5: Shows the significance value for body composition parameters in whole-body lean-mass linear regression model.**

<b>Composition parameter</b>	<b>P-value (&lt;0.05)</b>
<b>Weight</b>	7.76e-5
<b>Impedance coefficient of Whole body impedance from left at 10kHz</b>	0.0001
<b>Age</b>	0.0045
<b>Height</b>	0.0052
<b>F-statistic P-value for entire model</b>	6.723e-14

From the data obtained a clear trend between frequency of measurement and model accuracy could not be established. Improvements in Rsq values are observed with the inclusion of weight, height and gender. The significance of gender in this model is negligible and the significance values suggest that weight has a greater influence in predicting whole-body lean mass.

### **11.1.2 Whole-body bone mass:**

Findings from the present study suggested a linear relationship between whole-body impedance coefficient and whole-body bone mass with an Rsq value of 0.7. This relationship was optimised with the inclusion of height, gender and age. The Rsq value for this new multiple regression model was 0.89. Here again a fixed trend between measurement frequency and model improvement was not observed. Table 11-6 shows the significance value of various body composition parameters and whole-body bone mass; here the individual's height has a greater significance than the measured impedance coefficient. Hence with impedance coefficient combined with height, gender and age can be used to explain variation in whole-body bone mass across given population of subjects.

**Table 11-6: Shows the significance value for body composition parameters in a whole-body bone mass model. GenderM represents male volunteers.**

<b>Composition parameter</b>	<b>P-value (&lt;0.05)</b>
<b>Impedance coefficient of Whole body impedance from right at 100kHz</b>	0.000336
<b>Height</b>	0.000137
<b>GenderM</b>	0.001368
<b>Age</b>	0.055298
<b>F-statistic P-value for entire model</b>	6.08e-8

### **11.1.3 Whole-body fat mass (WBFM):**

WBFM is the difference between the individual's weight and whole-body combined lean-mass. Preliminary analysis showed that the weight of the head significantly affects the accuracy of the fat estimation model. Therefore we required a method to determine body weight excluding the head (BW-EH). In order to do this we used whole-body impedance (at 10kHz, other frequencies showed similar results) which gave an Rsq value of 0.77 when modelled with BW-EH. For each of the four frequencies when weight was included in the model the coefficients of determination improved to 0.99. Hence the BW-EH can be predicted with great accuracy with bio-impedance measurements combined with weight.

For predicting fat mass in the whole-body another quantity is required; the combined lean mass (lean-mass + bone-mass). Figure 11-4 shows a linear model between whole-body combined lean mass (WB-CLM) and whole-body impedance coefficient at 50kHz. This model was optimised by including height, weight and gender to improve the Rsq to 0.98. The BW-EH and WB-CLM were estimated using models described above and then subtracted to obtain WBFM. It is obvious that the WBFM estimate will inherit errors from estimated BW-EH and WB-CLM. When quantified using actual WBFM (obtained from the DEXA scan) the error was 9%. Therefore WBFM can be predicted with an accuracy of 91% using the procedure

above. This is in contrast to the WBFM estimated using individual's actual weight (including weight of head) which produced an error of 30.5%. This model is better than various models reported in (Kyle, De Lorenzo, et al. 2004) for estimating WBFM.

#### **11.1.4 Conclusion:**

Whole-body impedance coefficient correlations have been used to predict whole-body lean-mass, bone-mass and fat-mass. The whole-body lean mass multiple regression model which included height, weight and age had an  $R^2$  value of 0.98. It was also observed that weight had a higher significance in this model than impedance coefficient. The whole-body bone-mass model which included height, age and gender had an  $R^2$  value of 0.89: here height had a slightly higher significance than the impedance coefficient. To predict WBFM, estimates of BW-EH and WB-CLM were made which were later subtracted to obtain WBFM estimates. An error of 9% was observed in these estimates. An important result from estimation of BW-EH was BIA's ability to accurately predict BW-EH from body weight.

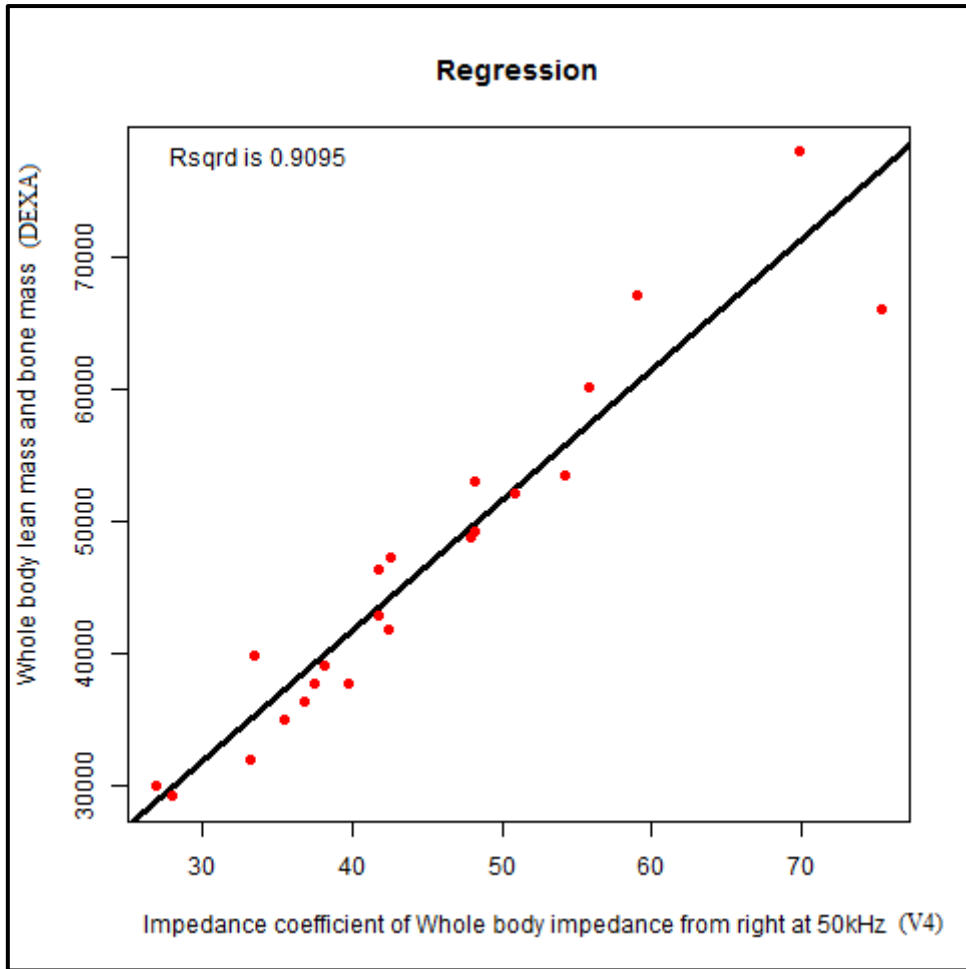


**Figure 11-4: Shows linear association between whole-body impedance coefficient and whole-body combined lean-mass. The whole-body lean-mass and bone-mass is obtained from DEXA scan reports and is presented here in grams.**

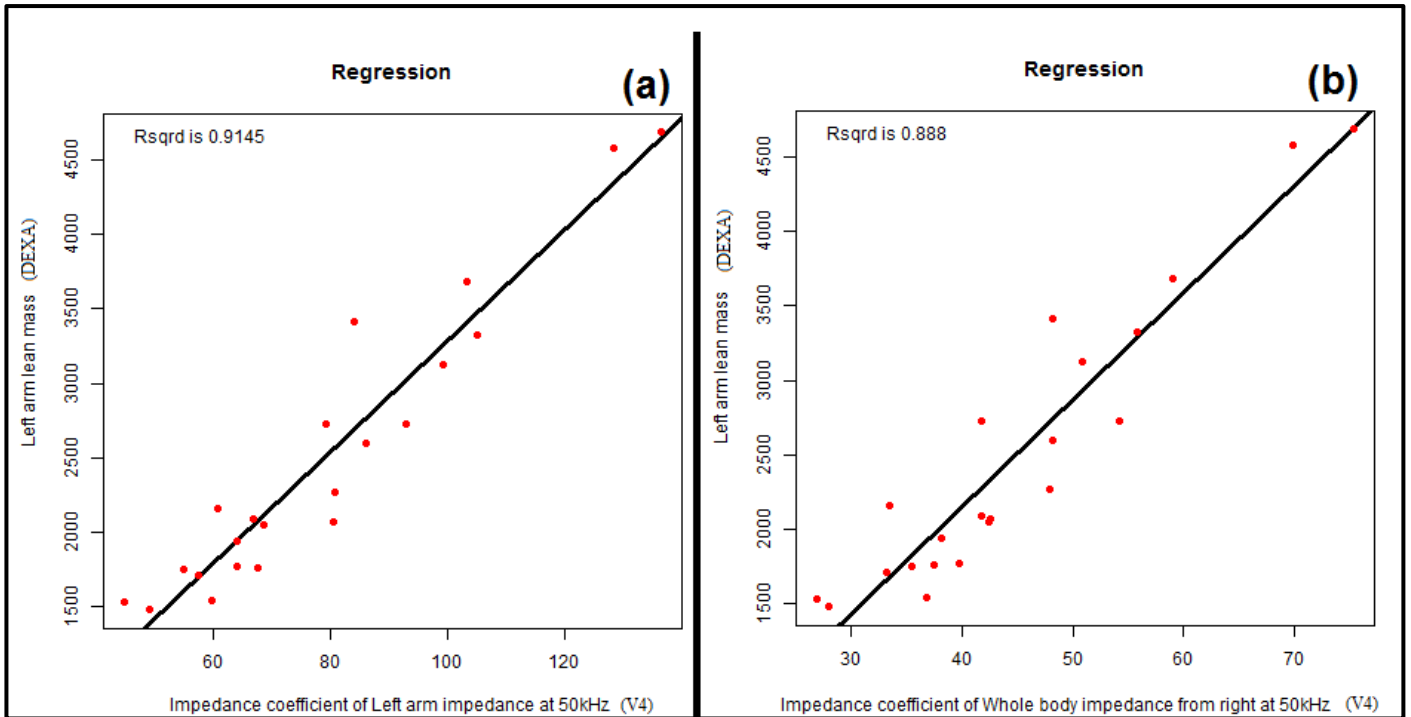


**Figure 11-5: Shows the scatter plot between impedance coefficient of left arm and the whole-body with the left arm lean mass. A linear trend can be observed in the two graphs. The left-arm lean-mass is obtained from DEXA scan reports and is presented here in grams.**

## **11.2 Composition of the arms:**

In this section relationships between measured impedance coefficients of the whole-body and arms (left and right) will be compared with the composition parameters of the arm viz. bone mass, lean mass and fat mass in the arms.

### **11.2.1 Lean mass:**

Figure 11-5 shows the scatter plot between the impedance coefficient of left arm at 50kHz and lean-mass in the left arm in subsection (a), here the Rsq is 0.92. However lean mass, when plotted against whole-body impedance at the same frequency has an Rsq value of 0.89. Therefore the impedance coefficient of the arm is better at predicting the lean mass of the respective arm (this was observed in both arms at all frequencies). When this model was optimised it was observed that gender was the only characteristic which contributed to the

model and improved the Rsq to 0.95 (see Table 11-7). This difference is probably due to larger muscle-mass in men when compared to women particularly the arms (Hager 1997).

**Table 11-7: Shows the significance value for body composition parameters in the left arm lean-mass model.**

<b>Composition parameter</b>	<b>P-value (&lt;0.05)</b>
<b>Impedance.coefficient.of.Left.arm.ampedance.at.50kHz</b>	1.29e-8
<b>GenderM</b>	0.0012
<b>F-statistic P-value for entire model</b>	3.27e-13

Here it was found that height and weight were not statistically significant and were therefore not included to simplify the model.

### **11.2.2 Bone mass:**

Analysis of the linear relationships between arm impedance coefficients and arm bone-mass revealed lack of statistical significance of impedance coefficients in determining arm bone mass. The Rsq value observed when left arm bone mass was fitted independently with impedance coefficient of the arm at 50kHz and height was 0.75 (for both cases). In a multiple regression model the p-value observed for impedance coefficient was 0.25; in contrast the p-value for height was 0.01. The model was optimised with the exclusion of impedance coefficient and inclusion of weight (age and gender were found to be statistically insignificant) which produced an Rsq value of 0.86. The significance of both height and weight were 0.0029 and 0.0009 respectively. This suggests that the bone-mass in the arm can be predicted accurately with an individual's height and weight alone.

### **11.2.3 Fat mass:**

Conventionally fat mass has been predicted indirectly by bio-impedance analysis systems. A slightly different approach is used to minimize the error in the model. When a linear model

was fitted between impedance coefficients of the arm at 75kHz (similar results observed at different frequencies) and combined lean mass of the right arm and Rsq of 0.94 was observed (Figure 11-6). This model was enhanced and optimized with the inclusion of weight and gender parameters which increased the Rsq to 0.96 (largest p-value of 0.011 was seen for gender in the model). Analysis of this combined lean-mass and right arm fat-mass showed an Rsq value of 0.85 when weight and height were included in the model. Therefore this model explained 85% of the variation in fat mass with the help of predicted combined lean-mass, height and weight. Another observation while attempting to predict arm fat-mass was the multiple-regression relationship between arm total-mass and weight, gender (both used for prediction) which returned an Rsq of 0.96. This shows the ability to estimate the volume of the arms accurately with the weight and gender.

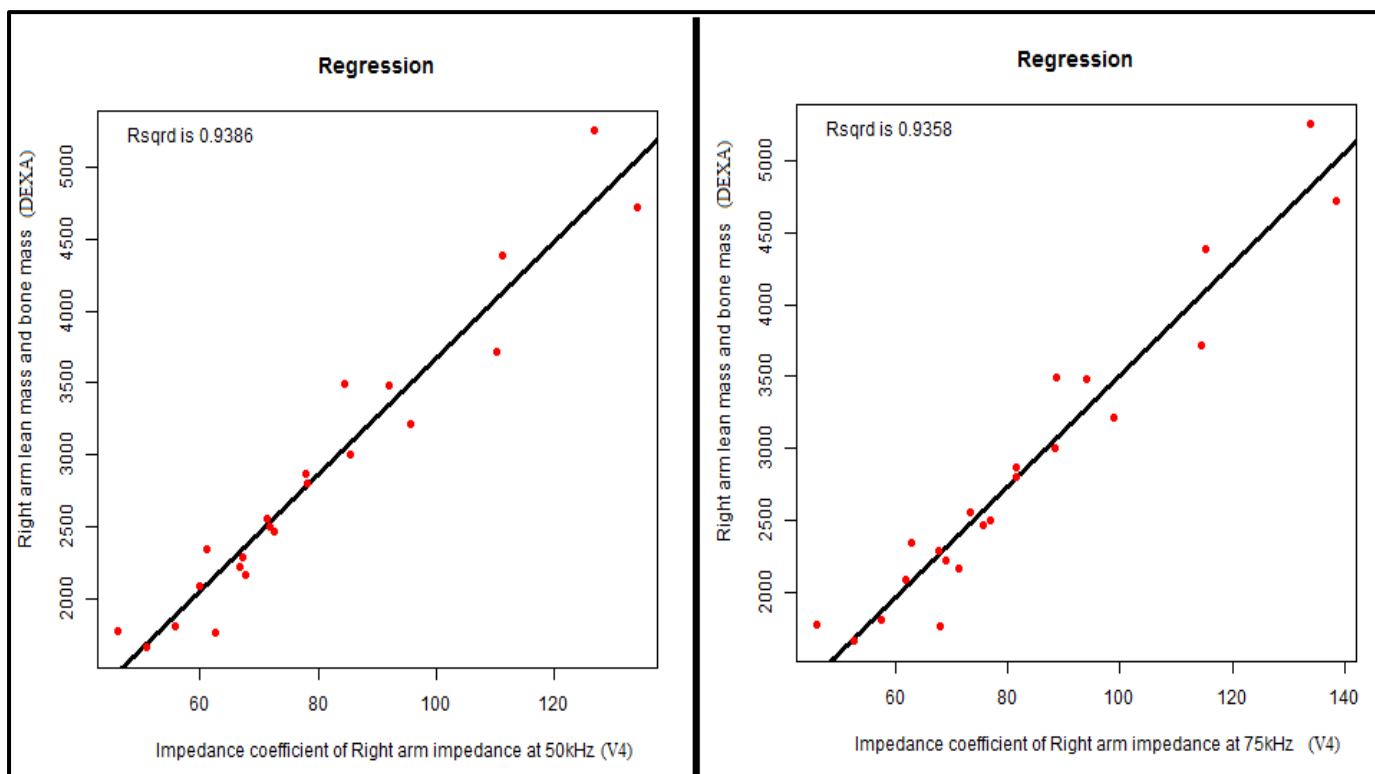


**Figure 11-6: Shows the scatter plot between the impedance coefficient of right arm at 50kHz and 75kHz and the combined right arm lean mass. The right-arm lean-mass and bone-mass is obtained from DEXA scan reports and is presented here in grams.**

#### **11.2.4 Conclusion:**

The section on composition of the arms showed that lean-mass could be accurately predicted with measured bio-impedance of the arm. The arm impedance better explained arm lean-mass than whole-body impedance, hence it is important to measure the impedance of individual limbs for better estimates of body composition. Also gender plays an important role in predicting arm lean mass. For predicting bone mass it was shown that the use of measured impedance coefficient is statistically insignificant and one could obtain arm bone mass estimates with the use of the individuals height and weight; weight being more statistically significant than height. Fat mass variation was explained with combined variation in combined arm lean mass, height and weight with an  $R^2$  of 0.85. Also a model using weight and gender explained the arm mass which (without the aid of bio-impedance measurements) is useful for body volume indexing.

### **11.3 Composition of the legs and measured bio-impedance:**

This section will illustrate the use of measured bio-impedance to predict the various composition parameters of the legs: first to be presented is a model to explain the lean mass followed by a model for bone mass and finally fat mass.

#### **11.3.1 Lean mass:**

Figure 11-7 shows the linearity between measured bio-impedance at 75kHz and leg lean-mass. As can be seen in subplot (b) the  $R^2$  (0.89) is greater when whole-body impedance is used in the model. This trend was observed across all frequencies therefore whole-body impedance better explains the variation in leg lean-mass. The model was enhanced with the inclusion of height and weight and the P-values are listed in Table 11-8. This multiple-regression model has an  $R^2$  of 0.94 and hence can predict lean mass in the legs efficiently.

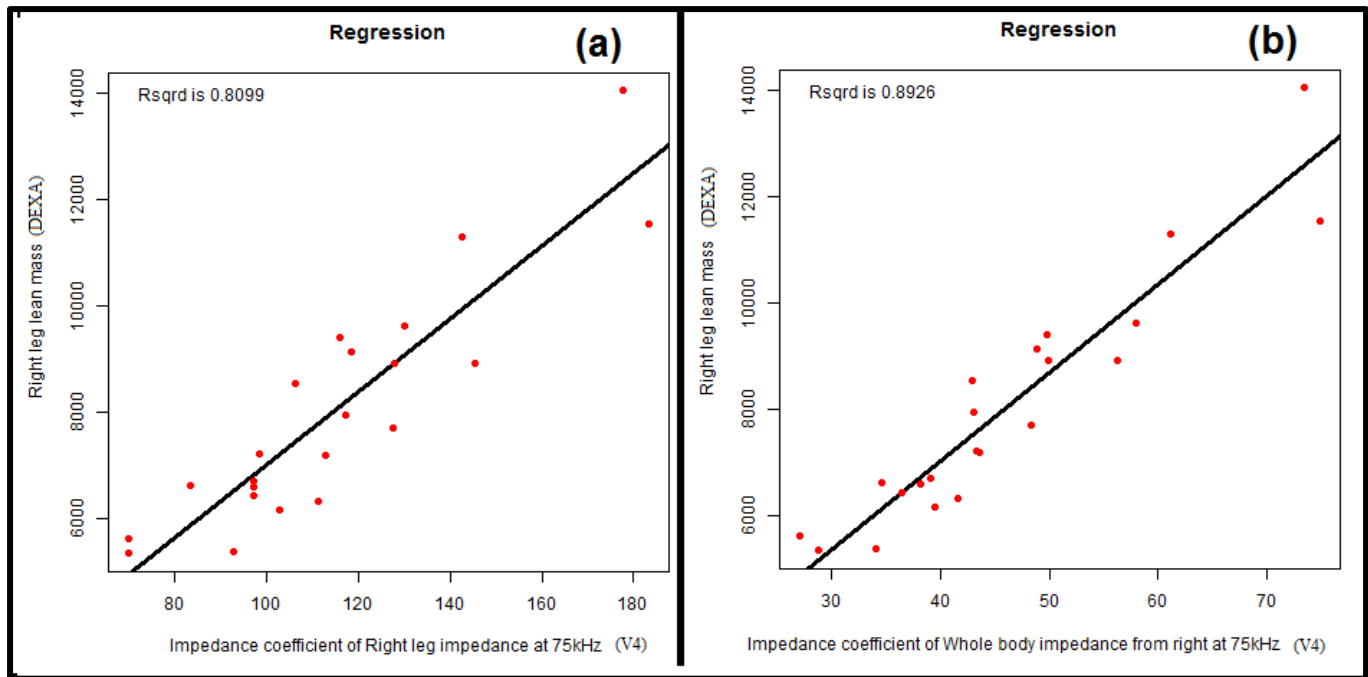


**Figure 11-7:** Shows the scatter plots between right leg lean mass and whole body impedance coefficient from right (a) and the impedance coefficient of the right leg (b) measured at 75kHz. The right-leg lean-mass is obtained from DEXA scan reports and is presented here in grams.

**Table 11-8:** Shows the P-values for the right leg lean mass predication model.

Composition parameter	P-value (<0.05)
Impedance coefficient of Whole body impedance from right at 75kHz	0.00055
Height	0.014
Weight	0.043
F-statistic P-value for entire model	2.84e-11

### 11.3.2 Bone-mass:

Table 11-9 shows an attempt to model left leg bone-mass with whole-body impedance coefficient at 50kHz. The p-values suggest that measured impedance coefficient is insignificant in this model and can be excluded with minimal effect on the model (the Rsq

value obtained was 0.89). The model was redesigned with the exclusion of impedance coefficient the p-values shown in Table 11-10.

**Table 11-9: Shows the P-value for the regression model to predict bone mass in the left leg. This model is to be optimized by excluding the non-significant parameters.**

Composition parameter	P-value (<0.05)
Whole body impedance from left at 50kHz	0.18
Height	1.42e-5
Weight	0.35
GenderM	0.0092
Age	0.016

**Table 11-10: Shows the optimised model to predict bone mass in the left leg with parameters and their significance.**

Composition parameter	P-value (<0.05)
Height	1.99e-5
Weight	0.019
GenderM	0.018
Age	0.018

Here it can be observed that the individual's height has the largest significant and the parameters height, weight, gender and age can be combined to predict bone mass in the legs without any further measurements. The relevance of gender in the model confirms that men have denser bones when compared to women (Hager 1997), similar trend was also observed in the whole-body bone mass model.

### **11.3.3 Fat mass:**

Variation in the fat-mass of the legs could not be satisfactorily explained with the parameters obtained from the subjects. The highest Rsq of 0.73 was observed when the right leg fat

mass was modelled with predicted whole-body fat mass (section 11.1.3) and gender with significance values of  $3.92e-6$  and  $0.016$  respectively. While attempting to explain fat-mass in the legs a model to explain the total mass of the leg was deduced. The total mass of the leg (hence its volume) was explained using combined model between height, weight and gender alone which returned an  $R^2$  of  $0.93$  with significance p-value of  $0.028$ ,  $3.9e-8$ ,  $0.071$  respectively.

#### **11.3.4 Conclusion:**

An attempt was made to accurately quantify the lean mass, bone mass and fat mass of the legs. It was found that whole-body impedance coefficient was a better at predicting lean-mass of the legs as compared to the leg impedance coefficient. A strong relationship between leg bone-mass and height was seen and this was further enhanced with inclusion of weight, gender and age. Hence a fair estimate of the bone-mass in the legs can be obtained without the aid of bio-impedance measurements. Fat-mass was best determined using whole-body fat-mass estimates and gender with an  $R^2$  of  $0.73$ . Also it was found that weight, height and gender can be used to predict the volume of the legs without the aid of bio-impedance measurements.

### **11.4 Composition of the body trunk:**

The following sub-sections will aim to explain the body composition of the body trunk based on measured bio-impedance and other physiological measurements.

### 11.4.1 Lean mass:

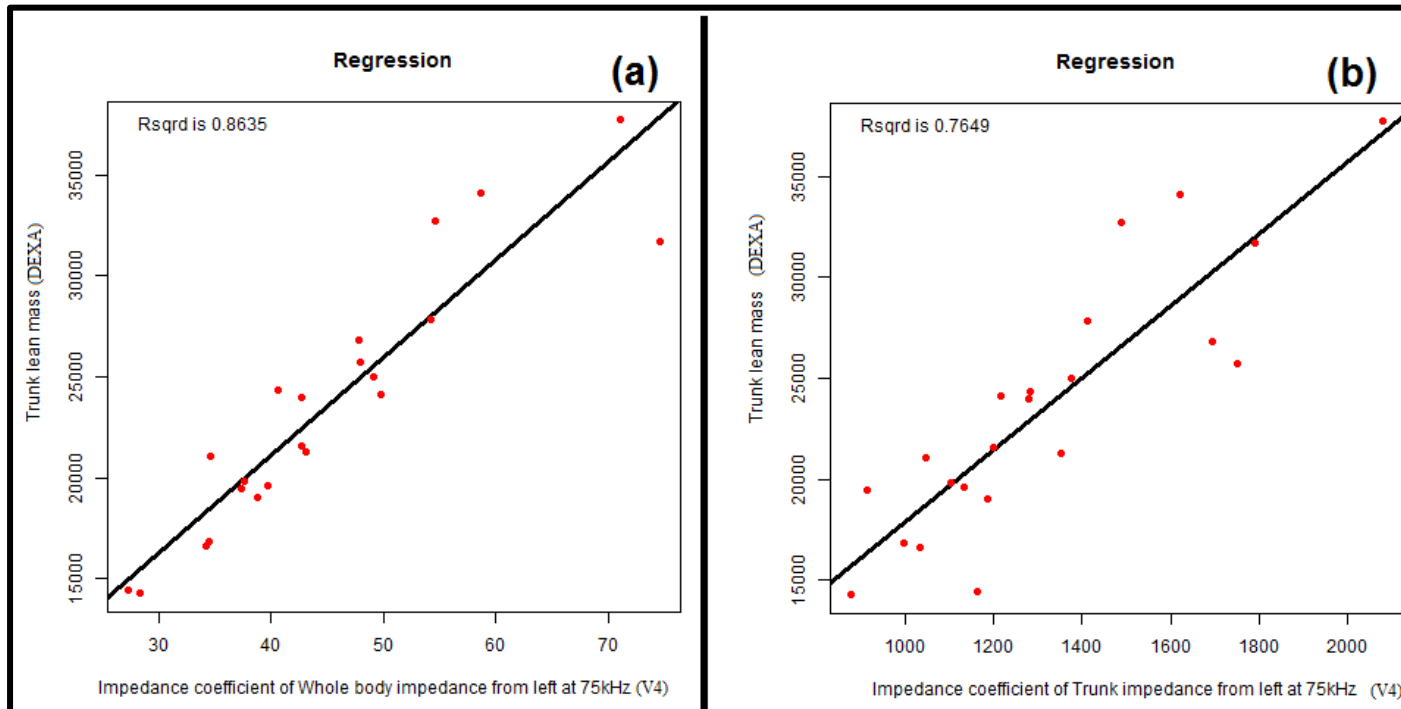


**Figure 11-8: Shows the correlation and Rsq values when lean-mass of the trunk is modelled with impedance of the trunk (b) and whole-body (a). The trunk lean-mass is obtained from DEXA scan reports and is presented here in grams.**

Figure 11-8 shows that whole-body impedance coefficient produces better fits for trunk as compared to trunk impedance coefficient since the Rsq values are 0.86 and 0.77 respectively. This pattern is also observed at different frequencies. Better estimates were obtained with inclusion of height and weight with Rsq improving from 0.86 to 0.95.

**Table 11-11: Shows the optimised linear model to fit lean-mass in the trunk with different parameters and their significance.**

<b>Composition parameter</b>	<b>P-value (&lt;0.05)</b>
<b>Weight</b>	0.000154
<b>Height</b>	0.003836
<b>Whole body impedance from left at 75kHz</b>	0.013676

Here it can be observed that the weight of the individual has the highest significance followed by height and measured impedance. In this case it can also be seen that parameters other than measured impedance coefficient take precedence in the model.

#### **11.4.2 Bone mass:**

Upon analysis it was found that trunk bone-mass variation across the subject population can be explained with the bio-impedance. Figure 11-9 shows the Rsq value of 0.62 when bone-mass of the trunk is modelled with impedance coefficient of the whole-body. When impedance coefficients of the trunk were used instead the Rsq values obtained were less than 0.6. Hence whole-body impedance coefficients are better suited in this case.

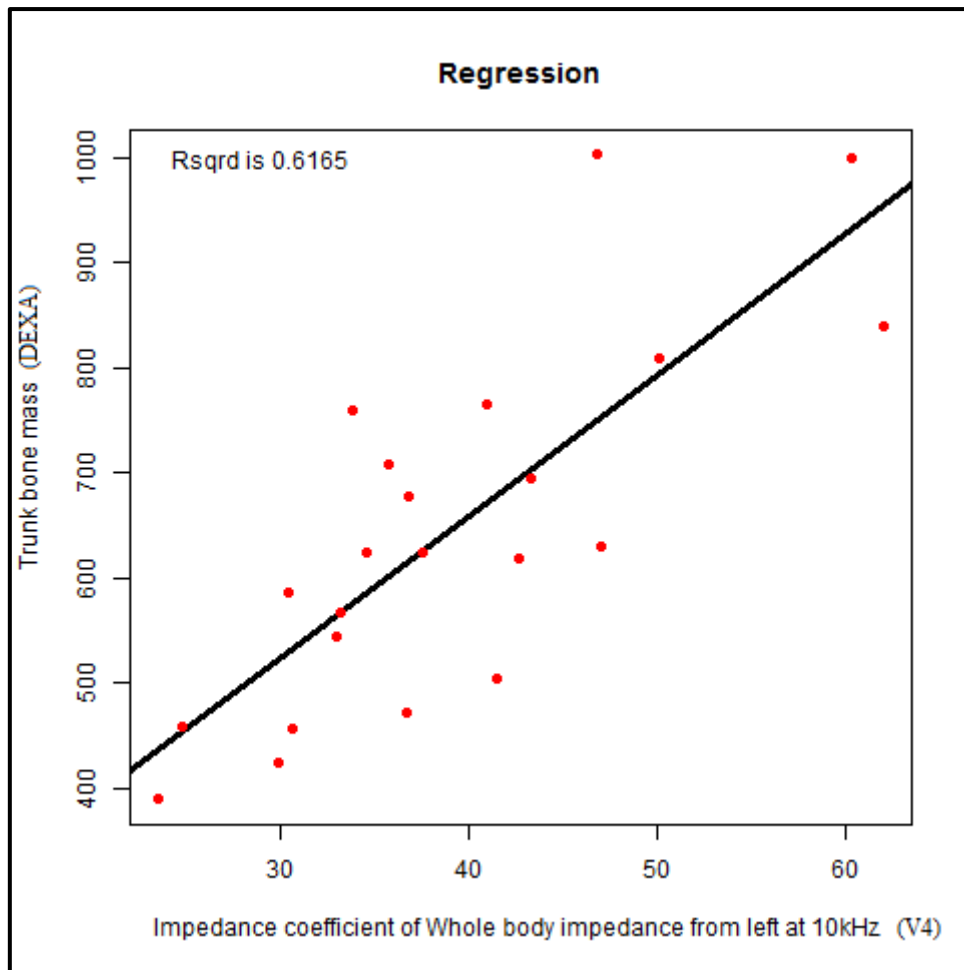


**Figure 11-9: Shows the correlation between trunk bone-mass and whole-body impedance coefficient measured at 10kHz. The trunk bone-mass is obtained from DEXA scan reports and is presented here in grams.**

The model was further enhanced with the inclusion of height and weight which resulted in an Rsq value of 0.76. Table 11-12 lists the significance of various parameters utilized to linearly model trunk bone-mass. 'GenderM' signifies the inclusion of male gender as a parameter in the model.

**Table 11-12: Shows the significance of the various parameters used to produce the linear model for the trunk bone mass. 'GenderM' stands for the inclusion of male gender as a parameter in the prediction model.**

<b>Composition parameter</b>	<b>P-value (&lt;0.05)</b>
<b>Height</b>	0.000131
<b>Whole body impedance from left at 75kHz</b>	0.001598
<b>GenderM</b>	0.011184

Here it can be observed that like the case of leg bone-mass height of the individual has a higher significance followed by measured bio-impedance and lastly gender.

### **11.4.3 Fat-mass:**

Trunk fat-mass is the difference between trunk total-mass and combined trunk lean-mass. Hence to find trunk fat-mass the two quantities above are to be determined. Analysis of the data showed that an individual's height and weight can explain the variation of trunk total-mass with an  $R^2$  of 0.97, the significance of weight being  $1.42e-15$  and that of height being 0.096. It was also found that the combined lean-mass when modelled with impedance coefficient of whole-body gave an  $R^2$  value of 0.87, this model was refined with the inclusion of height and weight to provide an  $R^2$  of 0.96. The significance of whole-body impedance coefficient, weight and height were 0.0025,  $6.44e-5$  and 0.08 respectively. Fat-mass calculated using these linear models was compared with the actual fat-mass of the trunk. The error between the predicted and actual value was 14.5%.

### **11.4.4 Conclusion:**

In the sub-sections above body composition compartments of the trunk were modelled with various measured parameters. Analysis of the data showed the ability of measured bio-impedance to model lean-mass of the trunk with  $R^2$  of 0.95, bone-mass with  $R^2$  of 0.76 and trunk fat-mass with an error of 14.5%. Additionally trunk total-mass was explained only

with subject weight and height, with an  $R_{sq}$  of 0.96. Trunk combined lean-mass variation was explained with  $R_{sq}$  of 0.96. Interestingly for predictions which utilized impedance coefficient it was found that whole-body impedance coefficients produced more accurate models. Here a fixed trend between frequency of measurement and model improvement was not observed.

## **11.5 Bio-impedance variation during motion and body composition:**

Capitalizing on the flexible nature of the constructed device and based on evidence in (Yunfei et al. 2009) the potential of changing bio-impedance during motion to predict body composition was explored. Equation (5) was used to develop this; upon observation it can be noted that impedance is an inverse function of area of cross-section. If one flexes an arm against a force the area of cross-section of the arm increases, ensuing generation of the hypothesis that the change in bio-impedance due to this increase in area of cross-section is linearly related to the composition of the arm. Another way of looking at this is; between two individuals, the individual with the larger amount of tissue mass in their arm will see a greater change in bio-impedance from flexing. This is due to larger change in area of cross-section (after flexing) as compared to individual with the lower amount of tissue mass in their arm. In order to record the change in bio-impedance 18 of the 22 volunteers who underwent the DEXA scan agreed to participate in this part of the study. As shown in Figure 11-10 the volunteers were requested to stand on the impedance measurement rig (V4) with an elastic band tied around their wrist; they were then asked to flex and relax their arm in a span of 5 seconds while the voltage and current through their arm was recorded for 5 seconds with the Agilent U2531A (sampling frequency of 1MSa/s to limit file size). This was later used to make an impedance profile of the arm during this flexing action. Figure 11-11 shows the change in impedance (impedance profile) of the arm as the arm is flexed and relaxed. Since impedance is inversely proportional to the area of cross-section the increase in area due to

flexing of the arm should decrease the impedance. This trend can be observed in the profile shown in Figure 11-11. In order to evaluate the change in bio-impedance first, an average value of five hundred samples belonging to the time intervals greater than 0.1 second and less than 0.5 seconds was taken. This ensured that impedance values are obtained during the relaxed state. Then an average of five hundred samples closest to the minimum value of the profile was taken to obtain the lowest impedance recorded during the flexing action. The difference between the two values gave the change in bio-impedance during the flexing action.

***Results and conclusion:*** After obtaining the change in bio-impedance during flexing from all 18 volunteers a linear regression model between the muscle mass in the arm and the change in bio-impedance was made, but this was relatively insignificant with an  $R^2$  of 0.54. The change in impedance was then normalized by division with impedance before flexing the arm. But a plausible linear relationship between normalized impedance-change and arm muscle mass could not be established. Therefore although we were able to record the reduction of impedance due to an increase in area of cross-section of the arm during flexing, a credible relationship between this and the composition of the arm could not be established.



**Figure 11-10: Shows the volunteer undergoing impedance measurement while his arm is flexed. Note the elastic band around the wrist and the change in area of cross section of the arm before and after flexing the arm. The procedure utilized V4 of the bio-impedance device and the signals are recorded using Agilent U2531A.**

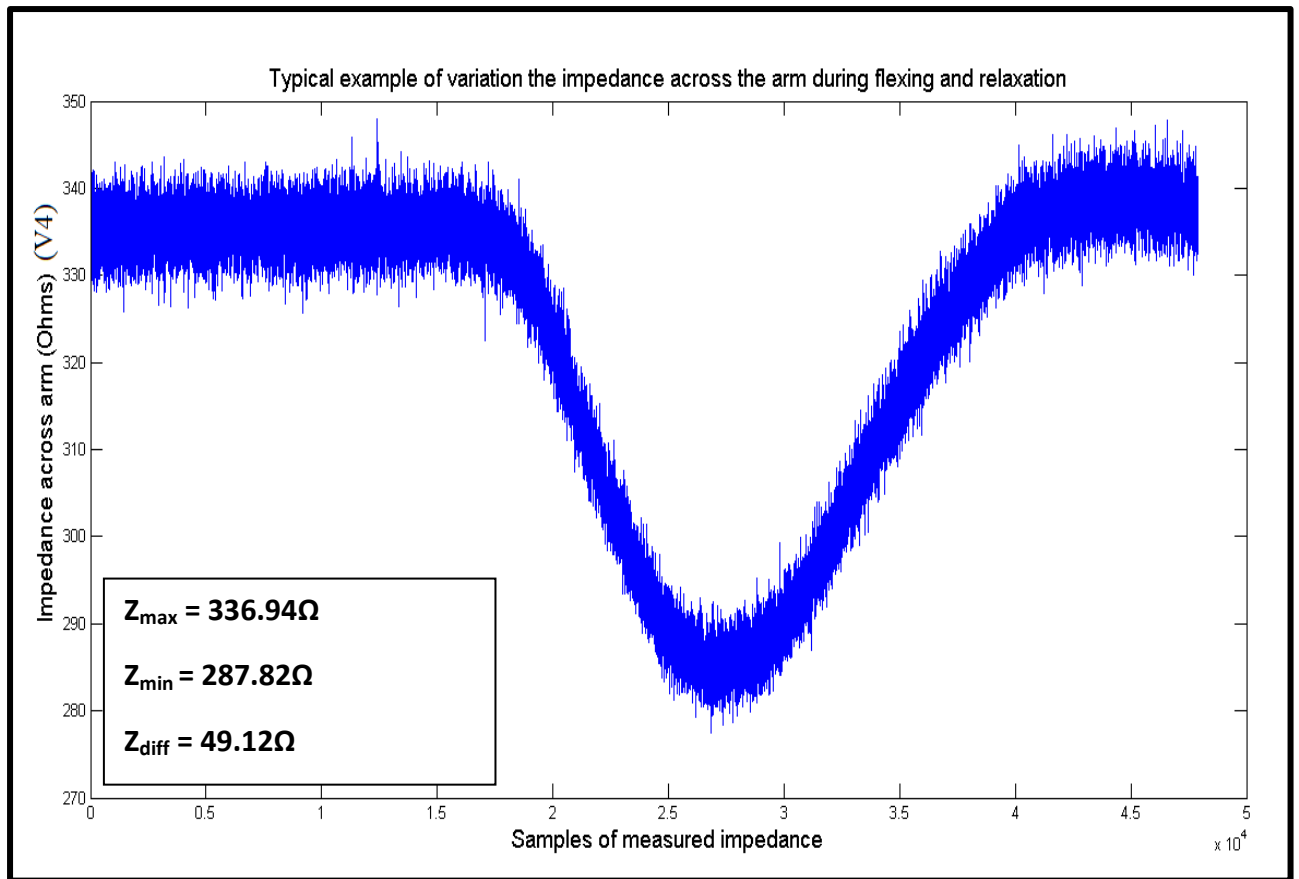


**Figure 11-11: Shows a typical example of variation of impedance across a subject’s arm as the subject flexes and relaxes his/her arm.  $Z_{max}$  is the maximum value of impedance before start,  $Z_{min}$  is the minimum value of impedance after flexing,  $Z_{diff}$  is the change in impedance due to flexing. The signal is sampled at 1MSa/s using the U2531A for duration of 5 Seconds.**

## **11.6 3D body volume and bio-impedance:**

A strong relationship between measured segmental body-mass (using DEXA) and bio-impedance has been described in the previous sections. The body section mass was determined during the DEXA scan (Table 11-2). Using the KinectFusion technology lower halves (below waste line) of nine subjects who underwent the DEXA were scanned to get a 3D image of their legs (whole-body scans made the algorithm unstable due to large number of calculations). The volunteers were dressed in skin-tight clothing to ensure the silhouette of their leg was revealed during the scan. The left leg of the volunteers was truncated manually

in Meshlab at the plane where the leg is truncated in Figure 11-2 to ensure similar volume estimates.

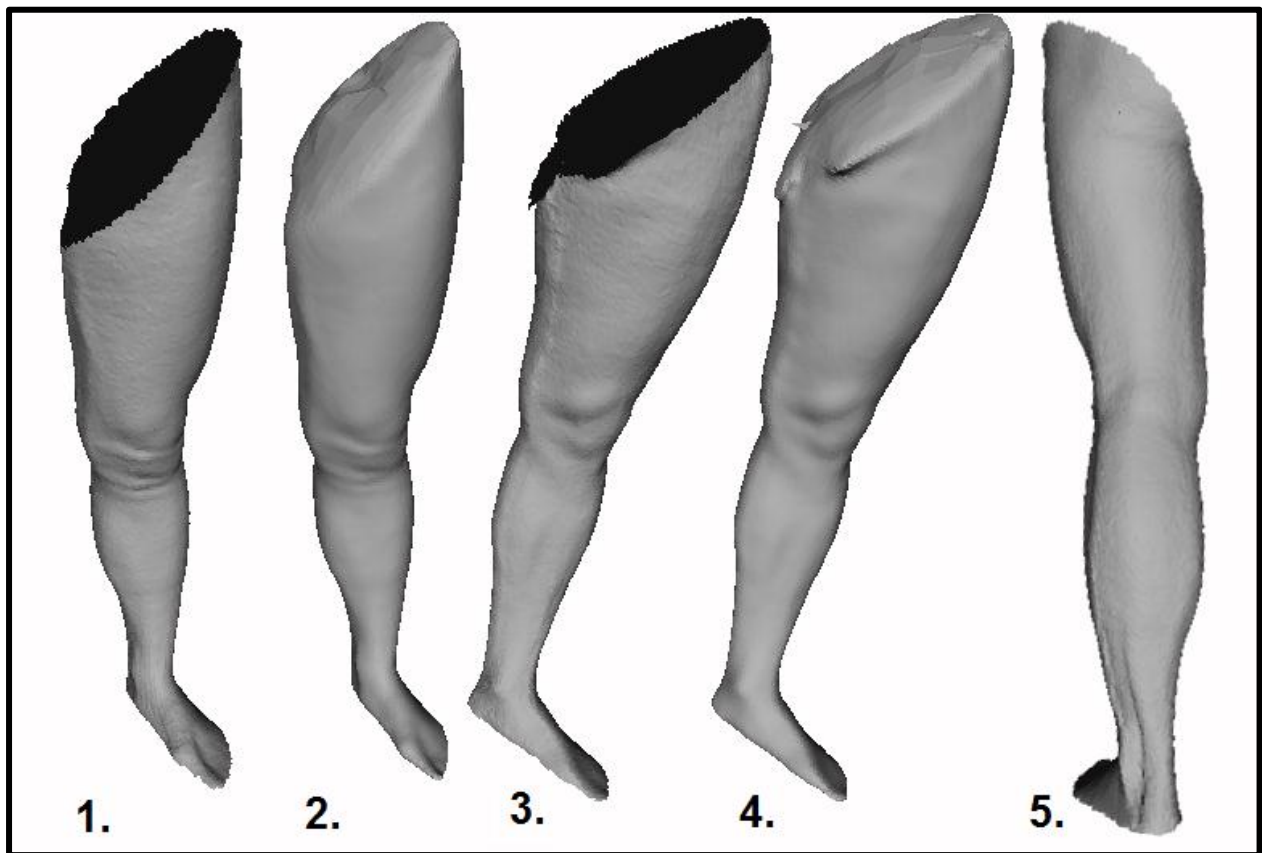


**Figure 11-12: Subfigure 1, 2 and 3, 4 show the original and reconstructed (with no holes) legs of two volunteers, whereas subfigure 5 shows the rear view original leg in 3.**

**Results and conclusion:** The volume of the isolated legs was determined using Meshlab software as described in section 10.3. When volume of the left-leg was compared to the impedance of the left-leg at 10kHz (similar results seen at other frequencies) an  $R_{sq}$  of 0.61 was observed between the two as shown in Figure 11-13. This improved to  $R_{sq}$  of 0.68 with the inclusion of weight and height in the model, with weight having highest significance followed by impedance coefficient and height. Such a relationship between measured bio-impedance and limb volume has not been reported in the past and this thesis notes this for the first time. Manual truncation errors of the 3D scan and inaccuracies in the Kinfu algorithm could have affected the accuracy of the model. However in essence this is an effective way

of determining body section volumes and with further refinements (which would negate the need for manual truncation of 3D model) its accuracy can be improved.

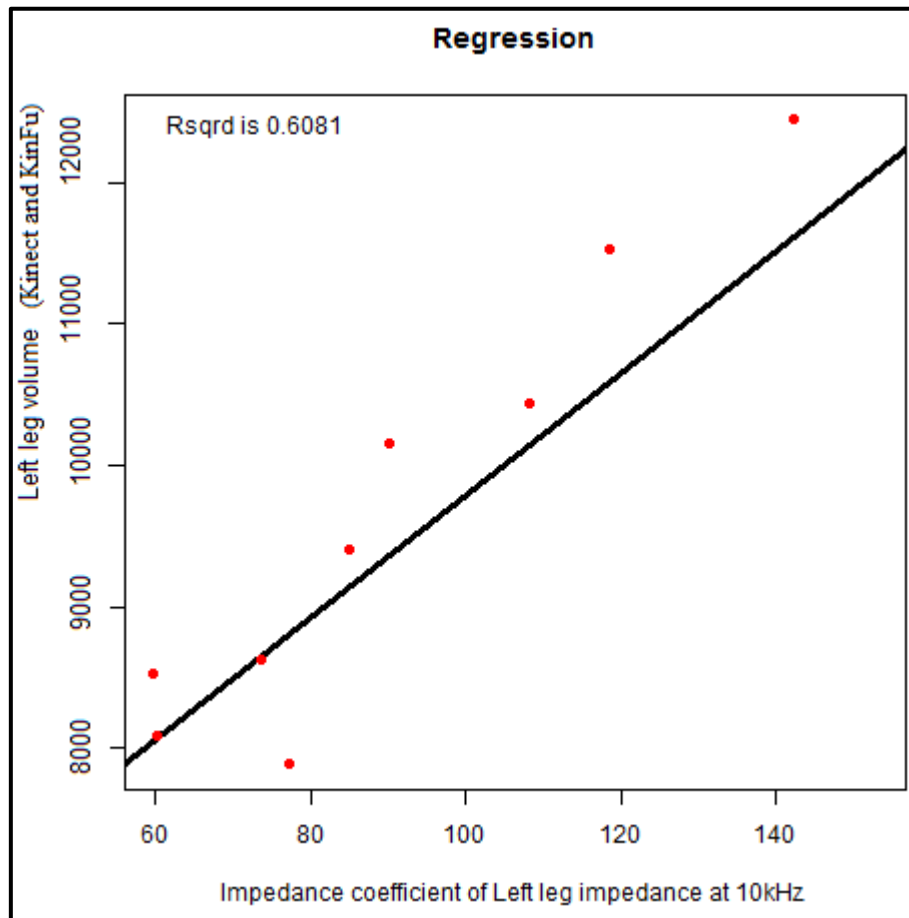


**Figure 11-13: Shows scatter plot between left-leg volume measured using KinFu algorithm and impedance coefficient of the left-leg.**

## **11.7 Neural-networks to learn from BIA data:**

Neural-networks provide an effective method for creating data-fitting models, which can later be used to predict outcomes for new data (data not used for modelling)(Witten et al. 2011). Since BIA data from 81 volunteers acquired using the Tanita BC-545 (in a previous study) and DEXA scan data from 22 volunteers (collected for present project, also available was Tanita body composition for these 22 volunteers) was available, a neural-network using this data was sought which could predict body lean-mass. Also of interest was the effect of DEXA scan data would have on a neural-network model built using BIA data. Neural-network

algorithms were studied as part of the literature review to be able to apply this technique on a larger collection of DEXA scan data, but time constraints restricted the dataset to 22 DEXA scans. Some ideas applied here are not detailed in this thesis, further information could be found in Bishop (2007) and Witten et al. (2011). For simplicity functions available in the Matlab neural-network toolbox are used for the modelling.

### **11.7.1 Data pre-processing:**

The existing data was divided into three, the training data, the validation data and the test data (section 2.4). Since actual body composition data was available from DEXA scan it was appropriate to use this information to test the network. But in order to check if inclusion of DEXA scan data within bio-impedance data would enhance the predictions of a network the DEXA data (from 22 volunteers) was split into two equal halves. One half was used to test the designed network and the other half was included in the BIA dataset (81+11=92, with the inclusion of 11 DEXA scan results). Therefore for the final network design there was a fixed test dataset of 11 DEXA scan results. Also required was another training set (which also included validation with 92 entries) which replaced the 11 DEXA scan entries in the first training set with Tanita lean-mass estimates for the same 11 volunteers. These two training sets of 92 entries were used to independently train the same network; this enabled the quantification of any improvements in the model due to inclusion of 11 DEXA scan entries. To summarize a neural-network structure was trained independently using two dataset of body composition data, one dataset included body composition results from a DEXA scan for 11 volunteers and the other dataset included Tanita BC-545 body composition results for the same 11 volunteers. Both training sets had Tanita lean-mass estimates for 81 volunteers in common.

### **11.7.2 Network structure and training:**

Since this was a preliminary study a two layer neural-network with one hidden layer was chosen since this is a simple configuration. Initially the hidden layer contained 10 neurons

(which is the default set by Matlab) this was later reduced to 5; results to both these configurations are presented here. The input (predictors) to the network was the age, height, weight and gender of each of the 92 individuals. The target (predicted) value for the network was whole-body lean-mass. Before training commenced both datasets were symmetrically shuffled and the first 80 entries of the 92 were used for training the network. The next 12 were used for validation during training (refer section 2.4.4). DEXA scan results from the remaining 11 volunteers was used to test (evaluate performance) of the trained network.

### **11.7.3 Results**

Figure 11-14 shows the performance metrics of the neural network designed with 5 neurons in the hidden layer. The second dataset which was comprised of Tanita body composition results for 92 volunteers was used for training. It can be seen from the regression plot that the network fits the training and validation very convincingly with an R value of 0.96 and 0.93 respectively when regression between the predicted and actual values was performed. When presented with fresh data for 11 volunteers the network predicted the lean-mass with an R of 0.96. The validation performance graph shows the reduction of mean squared error as the training progresses. An epoch is completed when the all of the training data has been used to train the data once. After 12 epochs no significance improvement on the validation set was seen and the network training was halted. But a consistent reduction in error can be seen for all three datasets as the training progresses. Now when the second dataset which included lean-mass entries for 11 volunteers collected using DEXA was used to train the network similar R values were seen for training and validation sets but the test data R value was reduced slightly to 0.95. This suggests that when given DEXA scan lean-mass data to network the performance of the network is slightly reduced. This cannot be the case and the slight reduction in performance could be due to the low number of DEXA scan entries. Figure 11-15 shows the performance of a network with 10 neurons in the hidden layer trained using the dataset which included the DEXA scan results. It can be seen that the R value on the training and validation sets are higher than that for the network with 5 neurons

in the hidden layer. However when it comes to the test dataset the regression R value is lower than that for the 5 neuron network. This is an example of the network over-fitting the training data and not being a good generalised network whose performance does not degrade significantly when new data is presented to the network. It can be therefore concluded that a 5 neuron network is better than a 10 neuron network for this dataset.

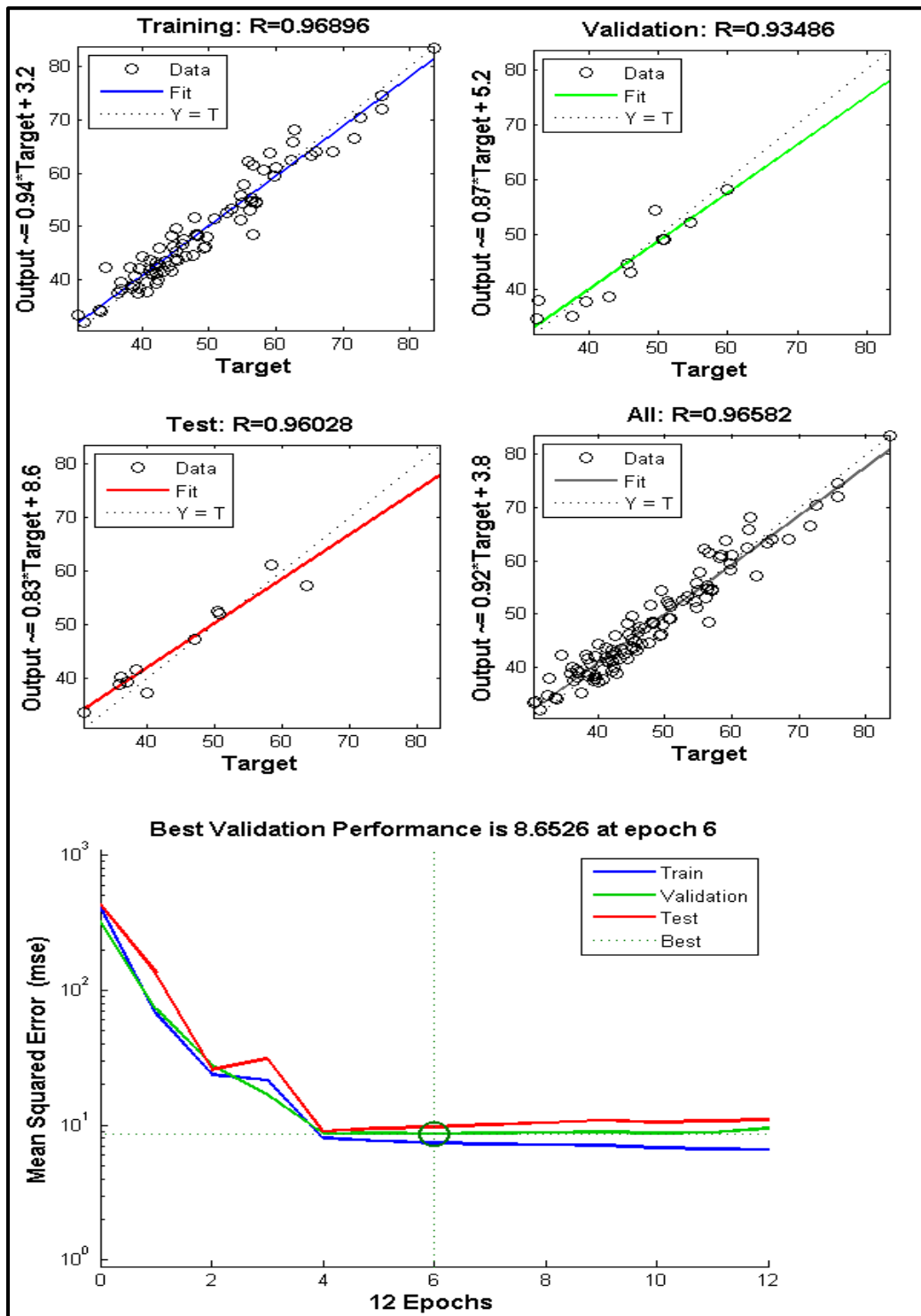


Figure 11-14: Shows the performance metrics of a neural-network with 5 neurons in the hidden layer.

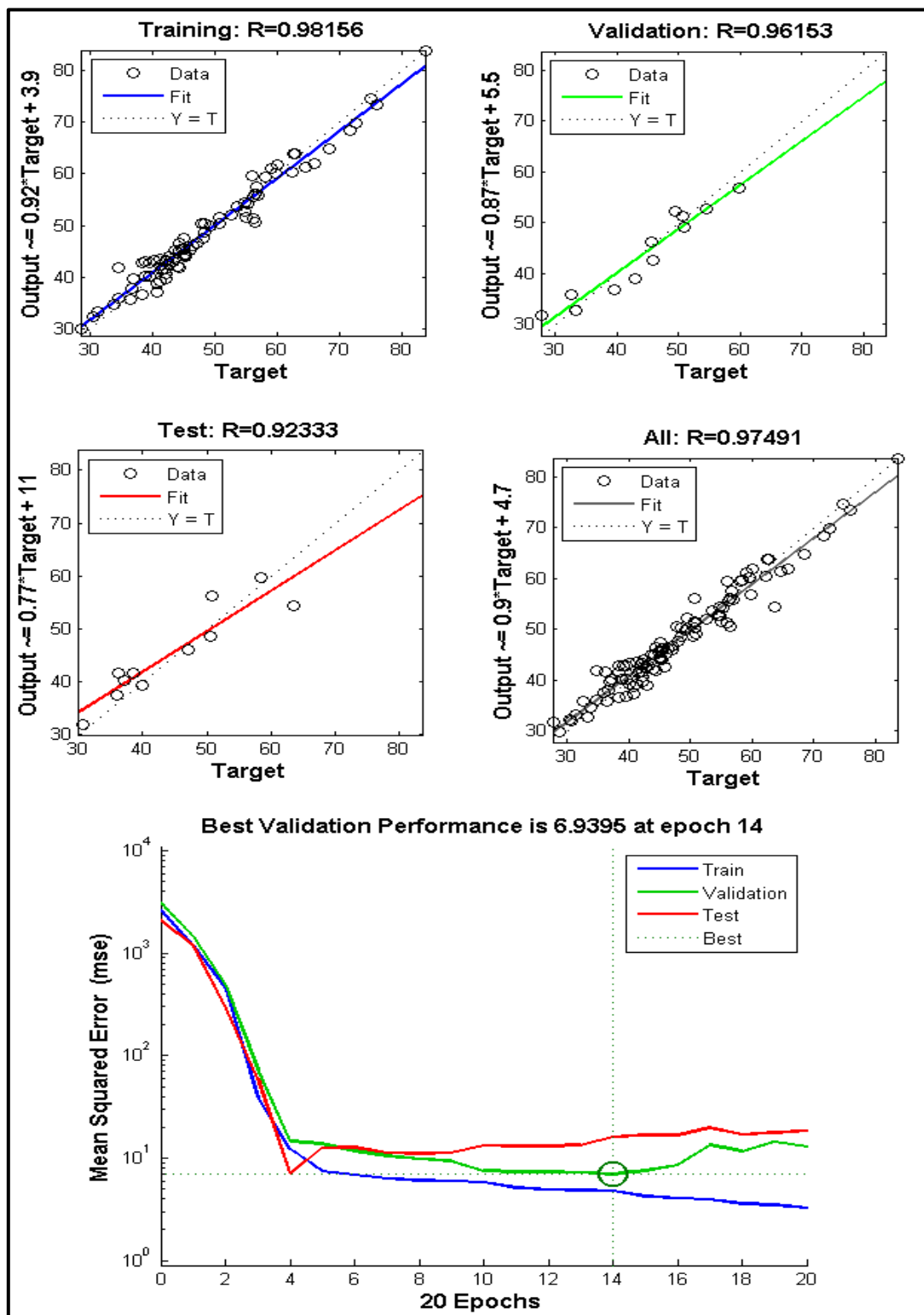


Figure 11-15: Shows the performance metrics of a neural-network with 5 neurons in the hidden layer.

## **11.8 Summary:**

Discussed in this chapter was the ability of segmental bio-impedance measured using V4 to predict the composition of the segments. Measured bio-impedance as has been reported previously (Kyle, De Lorenzo, et al. 2004) is a good predictor of lean muscle-mass. In case of the leg and trunk composition it was found that the whole-body impedance is a better predictor of lean-mass than the impedance of the individual limbs. Also presented is the reduction in bio-impedance with the flexing of the arm, also detailed is the ability of bio-impedance to predict limb volumes. Lastly using neural network topologies body composition data from two different sources; viz. Tanita BC-545 and DEXA scan; were fused to produce whole-body lean-mass with a test set accuracy of 96%.

## Chapter 12 Discussion

Numerous scientific studies have explored the potential use of BIA for clinical purposes particularly during the last two decades (Kyle, Bosaeus, et al. 2004). The rapid advancements in the field during this time have been due to refinements in the underlying technology and instrumentation. Therefore work on the basic body impedance measurement systems has now reached a new level of opportunity and recent BIA devices have been introduced commercially (such as Tanita MC-780, InBody770 and RJL Quantum IV) which are variants of the basic body impedance measurement set up shown in Figure 1-10. Many studies have used BIA to examine body composition under normal circumstances and in certain disease conditions, while some studies have explored population based applications of this technology (Kyle, De Lorenzo, et al. 2004; Kyle, Bosaeus, et al. 2004). In essence BIA is a method for assessing body composition; it is a quick body composition estimation technique with other clinically relevant advantages. Moreover it is non-invasive, since it passes a high frequency electric current through the subject (whose magnitude is in accordance with the BS EN 60601 standard to satisfy MDD 93/42) and produces results in a few seconds. Standard clinical body composition estimation techniques such as MRI, CT or DEXA scan take much longer to be undertaken, and require specialized (expensive) equipment which in turn call for trained personnel for operation and generally involve one or another form of ionising radiation or electromagnetic exposure which precludes repeated use.

The primary disadvantage of BIA is that it is an indirect method and it involves an element of 'prediction' to estimate body composition. Since it relies on measured body impedance and extrapolates an individual's body impedance on to a larger population dataset to derive body composition estimates, the results are not as accurate and have a degree of associated variability compared with DEXA, MRI and CT. Also another prominent limitation of BIA is that

most BC prediction equations are derived using linear regression. Since most of the commercial BIA device manufacturers use undisclosed datasets to produce body composition prediction equations, their devices are based on variable 'functions' which leads to differences in results for the same individual on different devices. The same occurs when independent research studies across the world study BIA for body composition estimation, because ethnic differences as well as gender, age, somatotype and health related variables are involved. Although merging bio-impedance prediction equations from various publications surrounding BIA was an initial aim of this project, a later feasibility analysis revealed this to be beyond the scope of the project which has focused on making BIA implementation easier and more flexible for future studies.

The present study aimed towards improving BIA predictions and reproducibility. Over the past two decades studies have examined multiple variants of BIA, three of the pronounced BIA variants are whole body BIA, segmental BIA and multi-frequency BIA. These variants are reported to predict one BC parameter better than the other. However there was a lack of a unified system which could bring these three variants together. A study which utilizes a standard BC method along with impedance measurements from all these variants of BIA could provide a unique dataset which would aid more accurate predictions for an individual. Therefore in this research programme I aimed to develop a safe BIA measurement system capable of determining whole-body and segmental BIA at varied frequencies. This novel device was tested by recruiting volunteers. These volunteers also underwent a standard BC estimation technique (DEXA in present study) to access their BC information along with various body impedance measurements. Another important component of this study was the level of scrutiny given to the data interpretation and the use of linear regression for BIA predictions. An appreciation of the dependence on linear regression for body composition estimates is a major shortcoming of the application of present technology. Multiple and linear regression are basic prediction methods and as the name suggests only establish linear relationships between two quantities. Hence the need for better prediction methods was

sought. It was planned to collect data from a larger cohort of volunteers than time actually permitted. Then analyse the dataset initially with linear/ multiple regression and later moving onto more elaborate prediction schemes like neural networks and statistical pattern recognition. This would enable us to explore any disease patterns which could be observed (Hsieh et al. 2008). This diversity of approach was to be envisaged to aid in improving BIA in two different aspects primarily by integrating three BIA variants in one system and later by using prediction methods which are more advanced than linear regression. However this plan was impeded by delays in obtaining ethical clearance to conduct this study which resulted in a reduced number of participants (22 volunteers only). Neural-networks was however used to analyse a large set of bio-impedance measurements from another study conducted in the same research group, this is discussed in the section 11.7. Additionally we also explored the ability of BIA to predict body volume and the usability of bio-impedance variation during motion to predict body composition.

## **12.1 Chronology of the presented study:**

In order to accomplish the aforementioned objectives the project under went several stages and iterations of refinement. After initial study of BIA technology and an extensive literature search and review the first step was to construct a body impedance measurement device at least comparable in accuracy to the advanced commercially available BIA devices. Commercially available options were not used since we were also interested in analysing the bio-electrical signals for other physiological measures. To do this initially the functioning of a commercially available BIA device the Tanita BC-545 was evaluated because this was an advanced device at that time and the findings are presented in section 3.1. After establishing that fixed electrode positions and large electrode areas on this device attained reproducible results, and comparing other electrode types, the decision was made to utilize the electrodes from the BC-545. Recognising the need for a segmental BIA device to expand the utility of BIA for clinical purposes, the project design was directed to the construction of a segmental,

multi-frequency BIA device. This was achieved in three major stages. Firstly a whole body impedance measurement system was constructed, tested and characterised, the results of this are presented in section 1.6. After this a segmental bio-impedance measurement device capable of evaluating impedance from the four limbs, trunk and the whole body was taken from an original theoretical design to a functional device. The design of this system is described in Chapter 4 and Chapter 5. The first prototype of this design idea was made on a prototype evaluation board as shown in section 6.4. This prototype was to be transferred onto a PCB board to produce a device that could be used with volunteers to measure their body impedance. In order to achieve this, the entire circuit design was transferred onto Proteus ISIS (circuit simulation software) and then a dual-layer PCB designed using Proteus ARES. A dual-layer design ensured that the circuit was compact; the entire circuit development stage and results are presented in section 6.4. Foreseeing the need to measure body impedance at different frequencies, the capability to measure segmental body impedance at different frequencies was added to the device as described in Chapter 7. This whole system was then re-optimized to produce the final version of the device which was much more compact as described in section 7.1. The final design incorporates segmental bio-impedance measurement protocol similar to that described by Organ & Bradham 1994 and takes this a step further allowing the storage of bioelectrical signals for further analysis, such as extracting heart rate as explained in section 10.2. Another major process with regard to testing this device with volunteers was to obtain ethics approval from both local and NHS ethics committees which would allow testing this device on both volunteers at Aston University and the Heart of England NHS trust, Birmingham, U.K. The major part of this procedure which spanned over 12 months is described in section 1.11.

In order to evaluate impedance, the acquired signals had to be transferred to a computer and analysed using Matlab. The instrumentation to perform this and the testing procedure described in section 5.2 and section 9.2. Also described therein is the use of the signal acquisition system to execute control over the designed device which enabled it to switch

between different body sections and separately evaluate the impedance from each of these sections. A specialist application was coded in Matlab to collect volunteer information and save bioelectrical signals from the 8 body regions and this is described in section 8.5. This unified program with its various functions encrypted volunteer names using AES algorithm, compared his/her names against existing names to classify the entry as update or new volunteer. After this the program allowed recording of physiological characteristics, notably height, weight and body composition results from Tanita BC-545 to be stored. It also executed control over the designed bio-electrical signal recording device and saved the acquired signals for further analysis. Each of the program features and their operation is explained in 0. A three stage digital filtering scheme was also designed in Matlab which successfully extracted heart rate signals from six of the eight bio-electrical signals recorded per individual. This method is illustrated in section 10.2.

At the time of writing and to the best of my knowledge the presented system is the only unified multi-frequency, segmental and whole-body impedance measurement setup with the added convenience of stand-on and hand-held electrodes. Generally other similar systems do not have all of these features and require stick on Ag-AgCl electrodes which have limitations. The device was tested with 0.01% precision resistors and the results are presented in section 9.2. Since a decision was made to utilize the 8 electrodes from the Tanita BC-545, the characteristics of these electrodes had to be evaluated because the afore mentioned device operated only at 50 kHz the performance of the electrodes at lower and higher frequencies was evaluated since the final device operated at varied frequencies and these tests have been conducted between 50 Hz and 200kHz . The analysis and results to these tests are presented in section 0. In order to extract impedance from the saved data a specialist digital filtering scheme was developed. Upon further exploration a more efficient procedure to extract impedance from the unfiltered signals using FFT was introduced as described in section 8.2; this made the filtering method redundant. As detailed in section 8.2 relationships between measured BIA and body 3D volumes were also explored. A

convincing linear relationship was found with a  $R^2$  of 0.68 but this needs to be refined further for better results.

The major steps undertaken during the project can be summarized as follows:

1. Design and testing of a whole-body bio-impedance measurement system version 1.
2. Designing and testing segmental bio-impedance measurement system version 2.
3. Designing and testing a multi-frequency segmental bio-impedance measurement system version 3.
4. Re-optimizing version 3 for an improved multi-frequency segmental bio-impedance measurement system version 4.
5. Testing involved characterizing various Howland current circuit topologies for frequency range and load bearing capabilities and constructing a reliable VCCS using an instrumentation amplifier and a single resistor in version 4.
6. Also tested was the suitability of electrodes from Tanita BC- 545 for current bio-electrical signal acquisition system.
7. The design and testing was performed alongside ethical approval applications which were required to test this device on volunteers.
8. Schematics of different versions of the device transferred to a PCB board after dual-layer PCB design were made for version 2 through to version 4. The PCB was later manufactured and tested before the components were soldered on.
9. Matlab programs were written to control and acquire signals from the subject through the designed device. Matlab programs were also written to extract bio-impedance using FFT, extract change in impedance due to motion and also to extract heart rate from the bio-electrical signals

10. The final device was tested on volunteers and a 3D scan of legs of some volunteers was performed to evaluate relationship between measured bio-impedance and body tissue volume.

## **12.2 Major challenges addressed:**

Constructing a safe, flexible bio-electrical measurement device was a major step addressed by this project. The device was capable of acquiring bio-electrical signals from eight anatomical regions of the subject, store them and extract bio-impedance measurements using electrodes from a commercial device. We also addressed the issue of standardizing electrode positions; this is a major concern when making bio-impedance measurements (Cornish et al. 1999; Bogonez-Franco 2009). Large electrode areas ensured low electrode-impedance and low electrode-impedance mismatch which made the current device very stable. It also enabled the device to produce reliable and repeatable impedance measurements. Another common problem addressed in the duration of this project was the design of a stable current source. Stability of the VCCS has been identified previously as a potential source of inaccuracy with BIA (Hong et al. 2007). Although initially tightly matched resistors were used to produce a stable VCCS, a standard instrumentation amplifier package was used in order to achieve this in later stages. The major advantage of using an instrumentation amplifier was the ease with which the VCCS could be designed with a single resistor. This simplified the circuit and negated the dependence on close resistor matching to ensure high CMRR. Better performance was also achieved with the use of this VCCS design with improvements seen in both frequency range and load bearing capabilities (section 7.2). Making PCB circuit boards using pre-sensitised boards was time consuming and involved several steps. Adopting the toner-transfer method theoretically was much easier, was relatively inexpensive and was also quicker. This method was primarily used for single-layer PCB boards, but by slightly modifying this method, dual-layer PCB boards were successfully manufactured and used in this project. Given the difficulties that arose with manufacturing

PCB boards for this project, PCBs for future versions of the device, PCB manufacturing firms such PCBtrain or Multi-cb would be preferred. Extracting heart rate from bio-impedance signals previously involved the use of extensive hardware (González-Landaeta et al. 2008); in this thesis an easier way of performing this using a three-stage signal filtering process is presented.

### **12.3 Major advances and findings:**

In this study a bio-impedance measurement system was presented which made bio-impedance measurements more accurate and easier to perform in a research setting. The system provided an easy to construct segmental multi-frequency bio-electrical measurement method. This was not only used to measure bio-impedance but also stored the signals for further analysis. The use of metal electrodes ensured the bio-electrical signal acquisition procedure was straightforward while ensuring good repeatability (section 5.4). When measured bio-impedance was compared with body composition estimates from a DEXA scan, a mixed trend in the ability of segmental bio-impedance measurement to predict body composition was observed. It was sometimes found that whole-body impedance measurements are better at predicting body composition parameters in certain cases as reported by several studies (Cornish et al. 1996). In most models used to describe body-composition in the results chapter it can be noted that use of other physiological parameters such as height and weight improved the prediction model. It was also seen that measured bio-impedance was better at predicting lean-mass rather than fat mass as can be seen in several equations presented in Kyle, De Lorenzo, et al. 2004. The  $R_{sq}$  value obtained for the model that predicts whole-body lean mass from whole-body impedance was 0.98 and it was revealed that weight had higher significance than measured bio-impedance. Lean-mass in the limbs and trunk returned  $R_{sq}$  values close to 0.95 with the aid of physiological measures such as height and weight. Such a high degree of agreement shows that bio-impedance along with basic physiological measures can predict lean-mass with high accuracy in

contrast to studies which use other physiological measures like limb-length or limb circumference to make composition predictions. An exhaustive list of such equations can be found in the literature (Kyle, De Lorenzo, et al. 2004; Kyle, Bosaeus, et al. 2004). Similarly a whole-body bone-mass linear model produced an  $R_{sq}$  of 0.89 but here measured bio-impedance has higher significance compared to physiological measures. Measured bio-impedance had very little significance in the model used to predict bone-mass in the arms and legs. These models returned  $R_{sq}$  close to 0.9 without the aid of bio-impedance. However the trunk bone-mass model utilized whole-body bio-impedance to produce an  $R_{sq}$  of 0.76. Fat mass in all cases had to be predicted indirectly i.e. as the difference between predicted lean-mass and predicted total-mass. It was found that the inclusion of the mass of the head severely affected the fat prediction model and contributed to an error of 31% between predicted whole-body fat-mass and its actual value (obtained from DEXA scan). It was proposed to predict body-mass (excluding the weight of the head; BW-EH refer section 11.1.3) using a linear model and using BW-EH to predict WBFM. This gave a reduced error of 9% in WBFM as opposed to 31% when actual weight was used. Fat-mass in the arms was explained using predictions of combined lean-mass in the arms which showed an  $R_{sq}$  of 0.85.

Another aspect this project explored was the ability of measured bio-impedance to predict body-segment masses. A good degree of agreement was found in linear models between measured bio-impedance and mass of the whole-body, the trunk and the limbs with  $R_{sq}$  in every case close to 0.95. Leg volumes were also estimated with the KinFu 3D scanning technology which is a freely available tool. Linear models between limb volumes and measured bio-impedance provided a positive correlation of 0.68. Estimation of volume enclosed by a body segment adds a 'visual aspect' to bio-impedance which could have implications in body composition estimation accuracy. Fat is lower in density than muscle and the 'visual aspect' would allow clear differentiation between muscular people and people with more body-fat who are of the same weight, because their body segments would occupy

more space. Hence using body-volume in the model could enable the estimation accuracy of bio-impedance to improve. Thus KinFu has a potential to be used as a body-volume scanning technology with further refinement. The flexibility of the device allowed measurement of the change in bio-impedance of the arm when the arm was flexed and relaxed. It was noted that the impedance of the arm decreased when the arm was flexed. This is expected, since flexing increases the area of cross-section of the arm which decreases impedance. Although it was hypothesised that this 'change in bio-impedance' could better predict arm composition as compared to bio-impedance measured in normal condition (when arm is relaxed) enough evidence could not be gathered in order to prove this. Additionally, as mentioned previously, heart-rate peaks were extracted from six of the eight segmental measurements taken per subject and could be used as a health indicator when making bio-impedance measurements. Heart-rate is a valuable clinical marker of cardiac function which can be used in conjunction with body-composition data to enhance the overall appreciation of disease risk in older individuals (Liberato et al. 2013). Neural-network models were created with BIA data and DEXA data to predict body lean-mass. It was found that the model predicted lean-mass with a accuracy of 96% when compared with lean-mass with DEXA scan. This suggests that provided enough data body lean-mass can be predicted with high precision in healthy volunteers with their gender, height, age and weight. Influence of other parameters such ethnicity is to be explored further.

## **12.4 Major shortcomings:**

A major drawback of this study was considered to be the phase insensitivity of the constructed device, i.e. the phase change between the input sinusoid and the output sinusoid (response to the input) could not be measured. Studies in the past have used phase difference in their models to predict body composition (Roubenoff et al. 1997). Also phase difference is used to deduce resistance and reactance (refer section 1.7.2) which together form impedance. Some studies have used the resistance and reactance deduced

from measured impedance and phase angle for their body composition predictions models (Roubenoff et al. 1997; Organ & Bradham 1994; Baumgartner et al. 1989). Although an attempt was made to deduce phase difference in this study it was concluded that the device was unable to preserve change in phase probably due to the use of switch ICs, which introduce an error in the original phase when the signals are routed through them. Ideally the device would be tested on a larger cohort of subject's but time constraints restricted the testing of the device (version 4) on 22 volunteers.

## **12.5 Future work:**

Bio-impedance device development has remained the focus of this study and there is scope for further refinement of the constructed device. Sinusoid function generation in version 2 through to version 4 of the device was done using the XR2206 function generation IC. This meant that the output frequency had to be tuned using analog components. Tuning different frequencies in version 4 was done using variable resistors. This can be replaced with direct digital synthesis (DDS) ICs in the future versions of the device. Direct digital synthesis makes selection and tuning of various frequencies much easier, and with the use of appropriate output the filtering stages generally produce sinusoids with lower noise as compared to its analog counterparts. Using DDS could also improve the repeatability of impedance measurements. Deducing resistance and reactance from measured impedance is another feature that could be added. Previous studies have used complex circuits in order to do this. Some studies have used Cole-Cole circuit elements which are deduced by extrapolating measurements made at different frequencies to low and high frequency resistance equivalents. Some studies have used these equivalents in their prediction models. Elwakil & Maundy (2010) have recently proposed a simple method to do this using a unity gain amplifier. Inclusion of these two features would enable the BIA device to make most bio-impedance related parameters with a unified device. This could be very useful to the scientific community as a unified bio electrical measurement system. The current source

can also undergo further enhancements to improve the frequency range by manufacturing dedicated ICs with highly precision matched resistors as proposed in Hong et al. (2007).

There is also scope for improvements in body composition prediction measured by bio-impedance. As discussed earlier use of prediction methods like neural networks can improve bio-impedance predictions as proposed by Hsieh et al. (2008). In this thesis it was shown that body lean-mass predictions can be reliably made using subject morphological measures. This could be taken a step forward and combined with BIA to predict abnormalities in body composition if there is a large variability between body composition predicted by the two methods. Once a relevant prediction model is devised pattern recognition methods could be used to pinpoint abnormalities like risk of osteoporosis in individuals with low-bone mass. This would improve BIAs profile as a diagnostic tool. A hybrid system which uses both KinFu 3D scanning technology and bio-impedance could be a valuable body composition evaluation method. This adds a 'visual aspect' to bio-impedance and would help identify different characteristics of an individual such as abnormalities of limb volume/surface area, and help with better body-composition predictions. For doing this automatic truncation of various body segments from a KinFu 3D scan would need to be implemented as in the case of a DEXA scan Figure 11-2. PCL provides open source tools to perform this but needs further exploration. Change in bio impedance due to limb movement is another aspect this thesis explored but needs further investigation. Further research into this method could potentially be used as a predictor of full body composition. To conclude this project aimed to produce a highly flexible bioelectrical signal acquisition system and looked at some of its potential applications. Using standard body composition estimates from DEXA scans it provides evidence for alternate BIA body composition prediction methods which are accurate in predicting body composition particularly body lean-mass.

## 12.6 Conclusion:

. The clinical advantages of BIA led to the rapid development of the method in the last two decades. Firstly, it is a non-invasive body composition estimation technique. This along with low equipment, operation and maintenance costs makes it a repeatable method to estimate body composition. The work of several researchers has made BIA the most cost effective body composition estimations method. However the accuracy of predictions made using BIA is poor when compared to standard body composition methods. This thesis presents the following contributions to BIA methodologies in order to expand its applicability in a clinical setting:

- A plausible relationship between measured bio-impedance and limb volumes is established here for the first time.
- Also presented herein is a digital signal filtering scheme which enables extraction of heart rate signals from measured bio-impedance signals.
- Neural network models were utilized to fuse body composition data from DEXA scans and Tanita BC-545 and such models can be used to fuse data in a similar manner to make BIA predictions better.
- Additionally, a reduction in measured impedance with increase in cross-sectional area of the arm (flexing) is reported.
- Using the DEXA scan data collected from volunteers multiple regression models to predict segmental composition of body compartments is presented.

## ❖References:

- Alvarez, O., 1978. Voltage-dependent capacitance in lipid bilayers made from monolayers. *Biophysical Journal*, 21(1), pp.1–17.
- Anon, 2013. Kinect.
- Anon, Microsoft Kinect Teardown.
- Anon, 2010. OpenNI | The standard framework for 3D sensing.
- Anon, Safe Design, Constuction and Modification of Electromedical Equipment: Guidelines for the Application of BS EN 60601-1 to Clinical Instrumentation: Amazon.it: Libri in altre lingue.
- Aroom, K. & Harting, M., 2009. Bioimpedance analysis: a guide to simple design and implementation. *Journal of Surgical ...*, 153(1), pp.23–30.
- Batra, P. & Kapoor, R., 2010. A Novel Method for Heart Rate Measurement Using Bioimpedance. In pp. 443–445.
- Baumgartner, R., Chumlea, W. & Roche, A., 1989. Estimation of body composition from bioelectric impedance of body segments. *Am J Clin Nutr*, 50(2), pp.221–226.
- Bedogni, G. et al., 2002. Accuracy of an eight-point tactile-electrode impedance method in the assessment of total body water. *European Journal of Clinical Nutrition*, 56(11), pp.1143–1148.
- Bedogni, G. et al., 2003. Comparison of bioelectrical impedance analysis and dual-energy X-ray absorptiometry for the assessment of appendicular body composition in anorexic women. *European Journal of Clinical Nutrition*, 57(9), pp.1068–1072.
- Besl, P.J. & McKay, N.D., 1992. A method for registration of 3-D shapes. *IEEE Transactions on Pattern Analysis and Machine Intelligence*, 14(2), pp.239–256.
- Bird, J.O., 2010. *Electrical and electronic principles and technology* ISBN: 9780080890562 0080890563, Oxford: Newnes.

- Bishop, C.M., 2007. *Natural networks for pattern recognition* ISBN: 9780198538646 0198538642, Oxford [u.a.]: Oxford Univ. Press.
- Bisson, J. et al., *ECG Interpretation & Rhythm Recognition*,
- Bogonez-Franco, P., 2009. Measurement errors in multifrequency bioelectrical impedance analyzers with and without impedance electrode mismatch. ... *measurement*, 30(7), p.573.
- Boslaugh, S.W.P.A., 2008. *Statistics A Desktop Quick Reference* ISBN: 9780596510497 0596510497, Cambridge; LaVergne: O'Reilly Media, Incorporated Ingram Publisher Services [Distributor].
- Bushberg, J.T., 2012. *The essential physics of medical imaging* ISBN: 9780781780575 0781780578, Philadelphia: Wolters Kluwer Health/Lippincott Williams & Wilkins.
- Carlton, R.R., Adler, A.M. & Frank, E.D., 2006. *Principles of radiographic imaging: an art and a science* ISBN: 1401871941 9781401871949 9781439080795 1439080798, Clifton Park, NY: Thomson Delmar Learning.
- Chouhan, V.S. & Mehta, S.S., 2007. Total Removal of Baseline Drift from ECG Signal. In pp. 512–515.
- Cole, K.S. & Cole, R.H., 1941. Dispersion and Absorption in Dielectrics I. Alternating Current Characteristics. *The Journal of Chemical Physics*, 9(4), p.341.
- Cooley, J.W. & Tukey, J.W., 1965. An algorithm for the machine calculation of complex Fourier series. *Mathematics of Computation*, 19(90), pp.297–301.
- Cornish, B.H. et al., 1996. Evaluation of multiple frequency bioelectrical impedance and Cole-Cole analysis for the assessment of body water volumes in healthy humans. *European journal of clinical nutrition*, 50(3), pp.159–164.
- Cornish, B.H. et al., 1999. Optimizing electrode sites for segmental bioimpedance measurements. *Physiological measurement*, 20(3), p.241.
- Dalziel, C.F. & Lee, W.R., 1968. Reevaluation of Lethal Electric Currents. *IEEE Transactions on Industry and General Applications*, IGA-4(5), pp.467–476.

- Despres, J.-P. & Lemieux, I., 2006. Abdominal obesity and metabolic syndrome. *Nature*, 444(7121), pp.881–887.
- Deurenberg, P., Andreoli, A. & deLorenzo, A., 1996. Multi-frequency bioelectrical impedance: A comparison between the Cole-Cole modelling and Hanai equations with the classical impedance index approach. *Annals of Human Biology*, 23(1), pp.31–40.
- Dey, D.K. & Bosaeus, I., 2003. Comparison of bioelectrical impedance prediction equations for fat-free mass in a population-based sample of 75 y olds:: The NORA study. *Nutrition*, 19(10), pp.858–864.
- Dittmar, M. & Reber, H., 2001. New equations for estimating body cell mass from bioimpedance parallel models in healthy older Germans. *Am J Physiol Endocrinol Metab*, 281(5), pp.E1005–1014.
- Donadio, C. et al., 2008. Single- and multi-frequency bioelectrical impedance analyses to analyse body composition in maintenance haemodialysis patients: comparison with dual-energy x-ray absorptiometry. *Physiological Measurement*, 29(6), pp.S517–S524.
- Ellis, K.J. & Wong, W.W., 1998. Human hydrometry: comparison of multifrequency bioelectrical impedance with  $2\text{H}_2\text{O}$  and bromine dilution. *Journal of Applied Physiology*, 85(3), pp.1056–1062.
- Elwakil, A.S. & Maundy, B., 2010. Extracting the Cole-Cole impedance model parameters without direct impedance measurement. *Electronics letters*, 46(20), pp.1367–1368.
- Fricke, H., 1925. A mathematical treatment of the electric conductivity and capacity of disperse systems II. The capacity of a suspension of conducting spheroids surrounded by a non-conducting membrane for a current of low frequency. *Physical Review*, 26(5), p.678.
- De González, A.B. & Darby, S., 2004. Risk of cancer from diagnostic X-rays: estimates for the UK and 14 other countries. *The Lancet*, 363(9406), pp.345–351.
- Gonzalez, C.H. et al., 2002. Total body water measurement using bioelectrical impedance analysis, isotope dilution and total body potassium: a scoring system to facilitate intercomparison. *European journal of clinical nutrition*, 56(4), pp.326–37.

- González-Landaeta, R., Casas, O. & Pallàs-Areny, R., 2008. Heart rate detection from plantar bioimpedance measurements. *Biomedical Engineering, IEEE Transactions on*, 55(3), pp.1163–1167.
- Goovaerts, H.G. et al., 1998. Extra-cellular volume estimation by electrical impedance - phase measurement or curve fitting: a comparative study. *Physiological Measurement*, 19(4), pp.517–526.
- Grimnes, S. & Martinsen, O.G., 2014. *Bioimpedance and Bioelectricity Basics* ISBN: 0124115330, Academic Press.
- Grimnes, S. & Martinsen, Ø.G., 2008a. Chapter 4 - PASSIVE TISSUE ELECTRICAL PROPERTIES. In New York: Academic Press, pp. 93–137.
- Grimnes, S. & Martinsen, Ø.G., 2008b. Chapter 5 - EXCITABLE TISSUE AND BIOELECTRIC SIGNALS. In New York: Academic Press, pp. 139–159.
- Grimnes, S. & Martinsen, Ø.G., 2008c. Chapter 7 - INSTRUMENTATION AND MEASUREMENT. In New York: Academic Press, pp. 205–281.
- Grimnes, S. & Martinsen, Ø.G., 2008d. Chapter 9 - CLINICAL APPLICATIONS. In New York: Academic Press, pp. 333–409.
- Gudivaka, R., 1999. Single-and multifrequency models for bioelectrical impedance analysis of body water compartments. *Journal of Applied ...*, 87(3), pp.1087–1096.
- Guyton, A.C., 1981. *Textbook of medical physiology* ISBN: 9780721643946, Saunders.
- Haapala, I. et al., 2002. Anthropometry, bioelectrical impedance and dual-energy X-ray absorptiometry in the assessment of body composition in elderly Finnish women. *Clinical Physiology and Functional Imaging*, 22(6), pp.383–391.
- Hager, L., 1997. *Women In Human Evolution* ISBN: 9780203973103, Routledge.
- Hannan, W.J. et al., 1998. Proximal and distal measurements of extracellular and total body water by multi-frequency bio-impedance analysis in surgical patients. *Applied radiation and isotopes : including data, instrumentation and methods for use in agriculture, industry and medicine*, 49(5-6), pp.621–2.

- Hickman, I., 1999. *Analog electronics* ISBN: 0750644168 9780750644167, Oxford; Boston: Newnes.
- Hoffer, E., 1969. Correlation of whole-body impedance with total body water volume. *Journal of applied ...*, 27(4), p.531.
- Hong, H. et al., 2007. Floating voltage-controlled current sources for electrical impedance tomography. In pp. 208–211.
- Hsieh, K.-C. et al., 2008. Application Adaptive Linear Neural Network Algorithm for Assessment of Body Fat in Elderly Taiwanese Men. *Journal of Nan Kai*, 5(2), pp.21–26.
- Izadi, S. et al., 2011. KinectFusion: real-time 3D reconstruction and interaction using a moving depth camera. In *UIST '11*. New York, NY, USA: ACM, pp. 559–568.
- Jackson, A.S. et al., 1988. Reliability and validity of bioelectrical impedance in determining body composition. *Journal of Applied Physiology*, 64(2), p.529.
- Jaffrin, M.Y. et al., 1997. Extra-and intracellular volume monitoring by impedance during haemodialysis using Cole-Cole extrapolation. *Medical and Biological Engineering and Computing*, 35(3), pp.266–270.
- Jaffrin, M.Y. & Morel, H., 2008. Body fluid volumes measurements by impedance: A review of bioimpedance spectroscopy (BIS) and bioimpedance analysis (BIA) methods. *Medical engineering & physics*, 30(10), pp.1257–1269.
- Kanai, H., Haeno, M. & Sakamoto, K., 1987. Electrical measurement of fluid distribution in legs and arms K. Atsumi et al., eds. *Medical progress through technology*, 12(3-4), pp.159–170.
- Kazhdan, M., Bolitho, M. & Hoppe, H., 2006. Poisson surface reconstruction.
- Kotler, D.P. et al., 1996. Prediction of body cell mass, fat-free mass, and total body water with bioelectrical impedance analysis: effects of race, sex, and disease. *The American Journal of Clinical Nutrition*, 64(3 Suppl), p.489S–497S.
- Kyle, U.G., De Lorenzo, A.D., et al., 2004. Bioelectrical impedance analysis--part I: review of principles and methods. *Clinical Nutrition*, 23(5), pp.1226–1243.

- Kyle, U.G., Bosaeus, I., et al., 2004. Bioelectrical impedance analysis—part II: utilization in clinical practice. *Clinical Nutrition*, 23(6), pp.1430–1453.
- Kyle, U.G. et al., 2001. Reliable bioelectrical impedance analysis estimate of fat-free mass in liver, lung, and heart transplant patients. *JPEN. Journal of parenteral and enteral nutrition*, 25(2), pp.45–51.
- Liberato, S.C. et al., 2013. The relationships between body composition and cardiovascular risk factors in young Australian men. *Nutrition Journal*, 12(1), p.108.
- Losada, R.A., 2008. Digital Filters with MATLAB®. *Online]. <http://www.mathworks.com/matlabcentral/fileexchange/19880> (<http://www.mathworks.com/matlabcentral/fileexchange/19880>).*
- Lukaski, H.C.H. et al., 1985. Assessment of fat-free mass using bioelectrical impedance measurements of the human body. *American Journal of Clinical Nutrition*, 41(4), p.810.
- Marquez, J.C., Seoane, F. & Lindecrantz, K., 2011. Skin-electrode contact area in electrical bioimpedance spectroscopy. Influence in total body composition assessment. In pp. 1867–1870.
- MathWorks, I., 2002. *Signal processing toolbox for use with MATLAB: user's guide*, The MathWorks.
- McAdams, E.T. et al., 1996. Factors affecting electrode-gel-skin interface impedance in electrical impedance tomography. *Medical and Biological Engineering and Computing*, 34(6), pp.397–408.
- McCulloch, W.S. & Pitts, W., 1943. A logical calculus of the ideas immanent in nervous activity. *The bulletin of mathematical biophysics*, 5(4), pp.115–133.
- Medicines and Healthcare products Regulatory Agency (MHRA), [www.mhra.gov.uk](http://www.mhra.gov.uk), 2007. Safety Guidelines for Magnetic Resonance Imaging Equipment in Clinical Use - DB 2007(03).
- Minsky, M.L., 1988. *Perceptrons: an introduction to computational geometry* ISBN: 0262631113 9780262631112, Cambridge, Mass.: MIT Press.
- Mohr, U. et al., 1999. Possible carcinogenic effects of X-rays in a transgenerational study with CBA mice. *Carcinogenesis*, 20(2), pp.325–32.

- Morel, H. & Jaffrin, M.Y., 2008. A bridge from bioimpedance spectroscopy to 50 kHz bioimpedance analysis: application to total body water measurements. *Physiological Measurement*, 29(6), pp.S465–S478.
- Newcombe, R.A. et al., 2011. KinectFusion: Real-time dense surface mapping and tracking. In UIST '11. New York, NY, USA: ACM, pp. 127–136.
- Nunez, C. et al., 1999. Bioimpedance analysis: potential for measuring lower limb skeletal muscle mass. *Journal of Parenteral and Enteral Nutrition*, 23(2), pp.96–103.
- Oppenheim, A. V, 1975. *Digital signal processing* ISBN: 0132146355 9780132146357 0132141078 9780132141079, Englewood Cliffs, N.J.: Prentice-Hall.
- Organ, L. & Bradham, G., 1994. Segmental bioelectrical impedance analysis: theory and application of a new technique. *Journal of Applied ...*, 77(1), pp.98–112.
- Pease, R., 2008. A Comprehensive Study of the Howland Current Pump, National Semiconductor Inc.
- Pietrobelli, a et al., 1998. Appendicular skeletal muscle mass: prediction from multiple frequency segmental bioimpedance analysis. *European journal of clinical nutrition*, 52(7), pp.507–11.
- Roubenoff, R. et al., 1997. Application of Bioelectrical Impedance Analysis to Elderly Populations. *The Journals of Gerontology Series A: Biological Sciences and Medical Sciences*, 52A(3), pp.M129–M136.
- Schipper, L. et al., 2011. Hip fracture prognosis: could bioimpedance be an alternative to conventional nutritional assessment? *Nutrición Hospitalaria*, 26(4), pp.904–906.
- Schoeller, D. & Santen, E. Van, 1980. Total body water measurement in humans with <sup>18</sup>O and <sup>2</sup>H labeled water. *The American journal ...*, (December), pp.2686–2693.
- Schwenk, A. et al., 2000. Phase angle from bioelectrical impedance analysis remains an independent predictive marker in HIV-infected patients in the era of highly active antiretroviral treatment. *The American Journal of Clinical Nutrition*, 72(2), pp.496–501.

- Shankar, T.M.R., Webster, J.G. & Shao, S., 1985. The Contribution of Vessel Volume Change and Blood Resistivity Change to the Electrical Impedance Pulse. *IEEE Transactions on Biomedical Engineering*, BME-32(3), pp.192–198.
- Slavicek, G. & Forsdahl, G., 2009. Ethics and regulatory aspects in medical research. *international journal of stomatology & occlusion medicine*, 2(1), pp.45–49.
- Spach, M.S. et al., 1966. Skin-electrode impedance and its effect on recording cardiac potentials. *Circulation*, 34(4), pp.649–656.
- Surhone, L.M., Timpledon, M.T. & Marseken, S.F., 2010. *Savitzky-Golay Smoothing Filter* ISBN: 9786131156755, VDM Publishing.
- Thomas, B.J., Ward, L.C. & Cornish, B.H., 1998. Bioimpedance spectrometry in the determination of body water compartments: accuracy and clinical significance. *Applied radiation and isotopes*, 49(5), pp.447–455.
- Witten, I.H., Frank, E. & Hall, M.A., 2011. *Data mining: practical machine learning tools and techniques* ISBN: 9780123748560 0123748569, Burlington, MA: Morgan Kaufmann.
- Yanovski, S.Z. et al., 1996. Bioelectrical impedance analysis in body composition measurement: National Institutes of Health Technology Assessment Conference Statement. In *The American Journal of Clinical Nutrition*. American Society for Nutrition, p. 524S–532S.
- Yoo, H.-J., 2011. *Bio-Medical CMOS ICs*, Springer.
- Yunfei, H. et al., 2009. Development of a bioimpedance-based human machine interface for wheelchair control. In pp. 1032–1035.

## ***Appendix 1: Ethics documents.***

---

## NRES Committee West Midlands - Coventry & Warwickshire

The Old Chapel  
Royal Standard Place  
Nottingham  
NG1 6FS

Tel: 0115 8839309  
Fax: 0115 8839294

28 August 2012

Professor Clifford J Bailey  
MB 354B, School of Life and Health Sciences  
Aston University  
Aston street, Birmingham  
B4 7ET

Dear Professor Bailey

<b>Study title:</b>	<b>Trends in body composition and markers of energy regulation in adults</b>
<b>REC reference:</b>	<b>08/H1210/17</b>
<b>Amendment number:</b>	<b>3</b>
<b>Amendment date:</b>	<b>14 August 2012</b>

The above amendment was reviewed at the meeting of the Sub-Committee held on 24 August 2012 in correspondence.

### Ethical opinion

The members of the Committee taking part in the review gave a favourable ethical opinion of the amendment on the basis described in the notice of amendment form and supporting documentation.

### Approved documents

The documents reviewed and approved at the meeting were:

Document	Version	Date
Notice of Substantial Amendment (non-CTIMPs)	3	14 August 2012
Covering Letter		
Participant Information Sheet	4	14 August 2012

### Membership of the Committee

The members of the Committee who took part in the review are listed on the attached sheet.

### R&D approval

All investigators and research collaborators in the NHS should notify the R&D office for the relevant NHS care organisation of this amendment and check whether it affects R&D approval of the research.

## Statement of compliance

The Committee is constituted in accordance with the Governance Arrangements for Research Ethics Committees and complies fully with the Standard Operating Procedures for Research Ethics Committees in the UK.

08/H1210/17:

Please quote this number on all correspondence

Yours sincerely

pp: W Rees

**Dr Helen Brittain**  
**Chair**

E-mail: Wendy.Rees@nottspct.nhs.uk

Enclosures:

*List of names and professions of members who took part in the review*

**NRES Committee West Midlands - Coventry & Warwickshire**

**Attendance at Sub-Committee of the REC meeting on 24 August 2012**

<i>Name</i>	<i>Profession</i>	<i>Capacity</i>
Dr Helen Brittain	Clinical Psychologist Retired	Lay
Mr Roger Cross	Senior Clinical Pharmacist	Expert

## **Participant information Sheet**

**Study Title:** Trends in body composition and markers of energy regulation in adults

### **Information and consent form**

Please take time to read this information leaflet. Please feel free to raise any questions with the team member who gave you this sheet.

*It is up to you to decide. We will describe the study and go through this information sheet, which we will then give to you. We will then ask you to sign a consent form to show you have agreed to take part. You are free to withdraw at any time, without giving a reason. This would not affect the standard of care you receive.*

### **Background and Purpose**

Aston University and Heart of England NHS Trust are collaborating in a research programme to study the manner in which body fat is stored. As a part of this study we wish to discover when people gain fat fastest and if there are differences between men and women. We are building a database of body composition and blood analysis to see where fat is stored and whether we can predict who will get fat.

### **What will happen to you?**

*You are only asked to participate once in this study, after your involvement ends you will not have to return for any further activity.*

You will be asked to step onto a body composition analysis unit, which looks like a bathroom scales. The analyser will send a harmless very low pulse of current through your body which you will not feel. This will enable the machine to calculate your body fat and the amount of water, muscle, and bone in your body. You will also be asked if you would like to give a blood sample so that we can analyse it later and see how your body composition compares with certain blood proteins. You do not have to give a blood sample to be a part of the study. The average time for us to do this is given in the table below.

**You will receive DXA scans of your spine, hip and whole body so that we can measure your bone mineral density and body fat. Some patients would have had the spine and hips scans as part of their routine care but the whole body scan will be additional. DXA scanning involves using very small doses of radiation. For healthy volunteers, who would not normally be receiving any of these scans, the total extra dose received will be less than 7 days of average background radiation in the UK. For patients, the additional dose will be less than 1 day of background radiation. The risk from this radiation dose is negligible.**

*You do not have to personally receive your results but if you would like a copy of them and the chance to discuss them with a team member you are able to request this service.*

Service	Approximate time
Body scan	4min
Waist measurement	1 min
Medical history	10 min
Blood samples	5 min
DEXA scan	20 min
Optional discussion and questions	5 min
Approximate total time	35min

### **What will happen to any sample I give?**

The blood tests will measure the amounts of fats and the amount of some proteins that are produced by fat cells and found in the blood. The tests will be used to see if the amounts of the blood fats and proteins can tell us how much “hidden” fat is stored inside your abdomen (tummy). The amount of blood to be taken is 10 ml (2 teaspoons). The tests will NOT provide any other information about your state of health.

### **What happens to the blood?**

The blood you donate will be analysed at Aston University, for different proteins involved in storing fat and sugar. Some of the analysis may be undertaken at other universities which have specialised equipment.

### **What will happen to the results of the research study?**

We hope this research will find a way to check, predict and detect how and when you are likely to become fat. Our study will show where in your body you are storing fat, and this information will enable healthcare professionals to better take care of you and help you look after your body.

*The information is confidential and your name will not be attached to any of the results. Researchers analyzing the results will not be able to identify your details.*

If you have any further questions about the study please feel free to discuss them with:

Dr Sri Bellary, Heartlands Hospital, [srikanth.bellary@heartofengland.nhs.uk](mailto:srikanth.bellary@heartofengland.nhs.uk)

If you are unhappy with this study please contact Professor C. J Bailey, Diabetes Research Group, Aston University, [c.j.bailey@aston.ac.uk](mailto:c.j.bailey@aston.ac.uk)

### **Confidentiality**

*The samples will normally be analysed by a team member. No sample will be stored after analysis, and results will not be able to be traced back to you.*

*As a voluntary participant you have the right to withdraw at any time. You do not have to give a reason and it will not be held against you in any way. You can withdraw your consent by emailing [subashj1@aston.ac.uk](mailto:subashj1@aston.ac.uk) or by telling any team member.*



Dear Participant,

You have been invited to take part in a study to discover more about body composition.

Our research team at Aston University is working with local healthcare providers to learn more about where fat is stored in your body and how much is in each store.

For instance;

People who look thin might have more “hidden” fat around their organs than people who look overweight?

People can be wrongly classified as overweight or obese by the Body Mass Index (BMI) scale because they have a lot of muscle?

This study is designed to find out if we can accurately

Detect the amount of body fat

How this fat is distributed around the body in people of different gender, ethnicity and with exercise

If the amount of fat relates to the amount of certain proteins in the blood.

Thank you for considering this invitation to participate. If you wish to join the study you will be given your body analysis details at the end of the session absolutely free. All of this information will be used entirely anonymously in our research programme.

If you are interested, please contact the research team on 0121 204 3914. They will be pleased to answer any questions and demonstrate the simple analyses using bioimendace and DEXA scan, and a short consultation to determine your body composition.

Best wishes

Professor Cliff Bailey



## ***Appendix 2: Datasheets.***

---

Page removed for copyright restrictions.

### ***Appendix 3: DEXA results from 22 subjects.***

---

**DXA Results Summary:**

<b>Region</b>	<b>BMC (g)</b>	<b>Fat Mass (g)</b>	<b>Lean Mass (g)</b>	<b>Lean + BMC (g)</b>	<b>Total Mass Mass (g)</b>	<b>% Fat</b>
L Arm	164.64	935.5	3123.4	3288.1	4223.5	22.1
R Arm	162.23	912.4	3317.1	3479.3	4391.7	20.8
Trunk	504.54	7067.2	24964.6	25469.1	32536.4	21.7
L Leg	446.63	2828.7	9681.3	10127.9	12956.6	21.8
R Leg	437.58	2709.4	9410.1	9847.7	12557.1	21.6
Subtotal	1715.62	14453.3	50496.5	52212.1	66665.4	21.7
Head	520.49	1095.5	3027.5	3548.0	4643.5	23.6
<b>Total</b>	<b>2236.11</b>	<b>15548.8</b>	<b>53524.0</b>	<b>55760.1</b>	<b>71308.9</b>	<b>21.8</b>

TBAR102 - NHANES BCA calibration

**DXA Results Summary:**

<b>Region</b>	<b>BMC (g)</b>	<b>Fat Mass (g)</b>	<b>Lean Mass (g)</b>	<b>Lean + BMC (g)</b>	<b>Total Mass (g)</b>	<b>% Fat</b>
L Arm	125	954.2	1546.6	1671.9	2626.1	36.3
R Arm	135	1023.8	1632.8	1767.6	2791.4	36.7
Trunk	544	5161.1	19043.0	19586.8	24747.9	20.9
L Leg	378	3123.0	6333.0	6711.3	9834.3	31.8
R Leg	395	3113.4	6166.2	6560.8	9674.2	32.2
Subtotal	1577	13375.5	34721.6	36298.5	49674.0	26.9
Head	666	949.7	2595.1	3261.0	4210.7	22.6
<b>Total</b>	<b>2243</b>	<b>14325.2</b>	<b>37316.7</b>	<b>39559.5</b>	<b>53884.7</b>	<b>26.6</b>

FBAR102 - NHANES BCA calibration

**DXA Results Summary:**

<b>Region</b>	<b>BMC (g)</b>	<b>Fat Mass (g)</b>	<b>Lean Mass (g)</b>	<b>Lean + BMC (g)</b>	<b>Total Mass (g)</b>	<b>% Fat</b>
L Arm	150	630.2	2730.4	2880.8	3511.0	17.9
R Arm	145	624.2	2654.3	2799.4	3423.6	18.2
Trunk	472	5360.6	21278.6	21750.3	27110.9	19.8
L Leg	398	2387.9	7364.4	7761.9	10149.8	23.5
R Leg	415	2377.1	7214.8	7629.5	10006.6	23.8
Subtotal	1580	11380.0	41242.4	42822.0	54202.0	21.0
Head	414	1119.4	3109.2	3523.0	4642.4	24.1
<b>Total</b>	<b>1993</b>	<b>12499.4</b>	<b>44351.7</b>	<b>46345.0</b>	<b>58844.4</b>	<b>21.2</b>

**DXA Results Summary:**

<b>Region</b>	<b>BMC (g)</b>	<b>Fat Mass (g)</b>	<b>Lean Mass (g)</b>	<b>Lean + BMC (g)</b>	<b>Total Mass (g)</b>	<b>% Fat</b>
L Arm	201	1451.8	2076.4	2277.6	3729.5	38.9
R Arm	209	1343.9	2294.0	2503.3	3847.2	34.9
Trunk	677	8888.9	23952.7	24630.0	33518.9	26.5
L Leg	515	4027.9	8290.5	8805.6	12833.5	31.4
R Leg	532	3838.1	8538.1	9069.8	12907.9	29.7
Subtotal	2135	19550.6	45151.7	47286.4	66836.9	29.3
Head	706	1073.1	2929.8	3636.0	4709.1	22.8
<b>Total</b>	<b>2841</b>	<b>20623.6</b>	<b>48081.5</b>	<b>50922.4</b>	<b>71546.0</b>	<b>28.8</b>

TBAR102 - NHANES BCA calibration

**DXA Results Summary:**

<b>Region</b>	<b>BMC (g)</b>	<b>Fat Mass (g)</b>	<b>Lean Mass (g)</b>	<b>Lean + BMC (g)</b>	<b>Total Mass (g)</b>	<b>% Fat</b>
L Arm	247	979.7	3687.8	3934.7	4914.4	19.9
R Arm	259	956.0	4127.5	4386.1	5342.2	17.9
Trunk	809	6979.4	34090.2	34898.9	41878.3	16.7
L Leg	668	2814.9	11365.8	12034.2	14849.0	19.0
R Leg	671	2750.9	11308.5	11979.3	14730.3	18.7
Subtotal	2653	14480.9	64579.9	67233.3	81714.2	17.7
Head	742	1127.2	3085.4	3827.8	4955.0	22.7
<b>Total</b>	<b>3396</b>	<b>15608.1</b>	<b>67665.3</b>	<b>71061.0</b>	<b>86669.2</b>	<b>18.0</b>

TBAR102 - NHANES BCA calibration

**DXA Results Summary:**

<b>Region</b>	<b>BMC (g)</b>	<b>Fat Mass (g)</b>	<b>Lean Mass (g)</b>	<b>Lean + BMC (g)</b>	<b>Total Mass (g)</b>	<b>% Fat</b>
L Arm	140	830.8	2056.4	2196.6	3027.4	27.4
R Arm	168	864.6	2301.3	2469.6	3334.2	25.9
Trunk	625	5581.6	21532.1	22156.9	27738.5	20.1
L Leg	437	3206.4	6939.2	7376.3	10582.7	30.3
R Leg	457	3211.1	7198.0	7655.0	10866.1	29.6
Subtotal	1827	13694.5	40027.0	41854.4	55548.9	24.7
Head	514	949.2	2612.3	3126.2	4075.4	23.3
<b>Total</b>	<b>2341</b>	<b>14643.7</b>	<b>42639.2</b>	<b>44980.6</b>	<b>59624.3</b>	<b>24.6</b>

TBAR102 - NHANES BCA calibration

**DXA Results Summary:**

<b>Region</b>	<b>BMC (g)</b>	<b>Fat Mass (g)</b>	<b>Lean Mass (g)</b>	<b>Lean + BMC (g)</b>	<b>Total Mass Mass (g)</b>	<b>% Fat</b>
L Arm	228.36	1218.6	2732.8	2961.2	4179.8	29.2
R Arm	242.20	1241.0	2972.0	3214.2	4455.3	27.9
Trunk	1002.78	10573.7	27832.9	28835.7	39409.4	26.8
L Leg	652.78	4191.5	8290.9	8943.7	13135.2	31.9
R Leg	694.01	4167.8	8918.9	9612.9	13780.7	30.2
Subtotal	2820.14	21392.7	50747.5	53567.7	74960.3	28.5
Head	788.37	1112.7	3028.8	3817.2	4929.9	22.6
<b>Total</b>	<b>3608.51</b>	<b>22505.4</b>	<b>53776.3</b>	<b>57384.8</b>	<b>79890.2</b>	<b>28.2</b>

**DXA Results Summary:**

<b>Region</b>	<b>BMC (g)</b>	<b>Fat Mass (g)</b>	<b>Lean Mass (g)</b>	<b>Lean + BMC (g)</b>	<b>Total Mass (g)</b>	<b>% Fat</b>
L Arm	217	956.2	3412.0	3629.2	4585.4	20.9
R Arm	219	989.1	3277.3	3495.9	4485.0	22.1
Trunk	766	8234.1	25709.4	26475.7	34709.9	23.7
L Leg	648	3370.4	9132.4	9780.2	13150.7	25.6
R Leg	592	3350.1	9136.9	9728.9	13079.0	25.6
Subtotal	2442	16900.0	50668.0	53110.0	70009.9	24.1
Head	577	1113.0	3065.1	3642.5	4755.5	23.4
<b>Total</b>	<b>3019</b>	<b>18012.9</b>	<b>53733.1</b>	<b>56752.5</b>	<b>74765.5</b>	<b>24.1</b>

TBAR102 - NHANES BCA calibration

**DXA Results Summary:**

<b>Region</b>	<b>BMC (g)</b>	<b>Fat Mass (g)</b>	<b>Lean Mass (g)</b>	<b>Lean + BMC (g)</b>	<b>Total Mass (g)</b>	<b>% Fat</b>
L Arm	175	936.5	2094.5	2269.5	3206.0	29.2
R Arm	194	962.7	2360.1	2554.1	3516.9	27.4
Trunk	709	4909.4	24352.7	25061.8	29971.2	16.4
L Leg	516	3924.5	7460.5	7976.5	11901.0	33.0
R Leg	531	3994.9	7959.4	8489.9	12484.8	32.0
Subtotal	2125	14728.0	44227.2	46351.9	61079.9	24.1
Head	767	1028.2	2814.5	3581.7	4609.9	22.3
<b>Total</b>	<b>2892</b>	<b>15756.2</b>	<b>47041.7</b>	<b>49933.6</b>	<b>65689.8</b>	<b>24.0</b>

TBAR102 - NHANES BCA calibration

**DXA Results Summary:**

<b>Region</b>	<b>BMC (g)</b>	<b>Fat Mass (g)</b>	<b>Lean Mass (g)</b>	<b>Lean + BMC (g)</b>	<b>Total Mass Mass (g)</b>	<b>% Fat</b>
L Arm	151.03	2035.5	2270.9	2421.9	4457.4	45.7
R Arm	169.44	2070.8	2701.1	2870.5	4941.3	41.9
Trunk	618.28	15332.7	26800.9	27419.2	42751.8	35.9
L Leg	391.24	4356.5	7597.3	7988.5	12345.1	35.3
R Leg	420.19	4256.0	7708.9	8129.1	12385.1	34.4
Subtotal	1750.18	28051.4	47079.0	48829.2	76880.6	36.5
Head	663.27	960.9	2615.7	3279.0	4239.8	22.7
<b>Total</b>	<b>2413.45</b>	<b>29012.3</b>	<b>49694.7</b>	<b>52108.2</b>	<b>81120.4</b>	<b>35.8</b>

**DXA Results Summary:**

<b>Region</b>	<b>BMC (g)</b>	<b>Fat Mass (g)</b>	<b>Lean Mass (g)</b>	<b>Lean + BMC (g)</b>	<b>Total Mass (g)</b>	<b>% Fat</b>
L Arm	174	1437.2	1944.0	2117.7	3554.9	40.4
R Arm	177	1405.8	2045.6	2222.4	3628.2	38.7
Trunk	759	7285.6	19831.5	20590.3	27875.9	26.1
L Leg	441	4521.3	6615.4	7055.9	11577.3	39.1
R Leg	452	4666.1	6717.4	7169.4	11835.5	39.4
Subtotal	2002	19316.0	37153.9	39155.8	58471.8	33.0
Head	519	945.3	2600.5	3119.5	4064.8	23.3
<b>Total</b>	<b>2521</b>	<b>20261.3</b>	<b>39754.4</b>	<b>42275.3</b>	<b>62536.6</b>	<b>32.4</b>

TBAR102 - NHANES BCA calibration

**DXA Results Summary:**

<b>Region</b>	<b>BMC (g)</b>	<b>Fat Mass (g)</b>	<b>Lean Mass (g)</b>	<b>Lean + BMC (g)</b>	<b>Total Mass (g)</b>	<b>% Fat</b>
L Arm	115	493.7	1749.1	1863.9	2357.6	20.9
R Arm	132	488.1	1960.4	2092.0	2580.1	18.9
Trunk	586	3243.7	16863.7	17449.6	20693.3	15.7
L Leg	390	2039.4	6317.8	6707.5	8746.9	23.3
R Leg	379	2005.2	6447.6	6826.7	8831.8	22.7
Subtotal	1601	8270.0	33338.5	34939.7	43209.7	19.1
Head	591	910.7	2499.1	3090.4	4001.1	22.8
<b>Total</b>	<b>2192</b>	<b>9180.7</b>	<b>35837.6</b>	<b>38030.1</b>	<b>47210.7</b>	<b>19.4</b>

TBAR102 - NHANES BCA calibration

**DXA Results Summary:**

<b>Region</b>	<b>BMC (g)</b>	<b>Fat Mass (g)</b>	<b>Lean Mass (g)</b>	<b>Lean + BMC (g)</b>	<b>Total Mass Mass (g)</b>	<b>% Fat</b>
L Arm	141.77	1366.4	2162.0	2303.8	3670.2	37.2
R Arm	145.74	1347.6	2204.4	2350.2	3697.7	36.4
Trunk	456.30	10761.9	21038.2	21494.6	32256.5	33.4
L Leg	363.05	4133.2	6412.6	6775.7	10908.9	37.9
R Leg	356.95	3936.1	6638.5	6995.4	10931.6	36.0
Subtotal	1463.81	21545.2	38455.8	39919.6	61464.8	35.1
Head	534.88	869.9	2380.7	2915.6	3785.5	23.0
<b>Total</b>	<b>1998.68</b>	<b>22415.1</b>	<b>40836.5</b>	<b>42835.2</b>	<b>65250.4</b>	<b>34.4</b>

TBAR102 - NHANES BCA calibration

**DXA Results Summary:**

<b>Region</b>	<b>BMC (g)</b>	<b>Fat Mass (g)</b>	<b>Lean Mass (g)</b>	<b>Lean + BMC (g)</b>	<b>Total Mass (g)</b>	<b>% Fat</b>
L Arm	113	857.6	1533.4	1646.0	2503.6	34.3
R Arm	118	816.0	1666.6	1784.7	2600.7	31.4
Trunk	390	5292.6	14466.2	14856.6	20149.3	26.3
L Leg	309	2695.3	5401.7	5711.2	8406.5	32.1
R Leg	319	2730.2	5623.8	5942.8	8673.1	31.5
Subtotal	1250	12391.8	28691.8	29941.4	42333.2	29.3
Head	533	873.0	2400.2	2933.1	3806.1	22.9
<b>Total</b>	<b>1783</b>	<b>13264.8</b>	<b>31091.9</b>	<b>32874.5</b>	<b>46139.2</b>	<b>28.7</b>

TBAR102 - NHANES BCA calibration

**DXA Results Summary:**

<b>Region</b>	<b>BMC (g)</b>	<b>Fat Mass (g)</b>	<b>Lean Mass (g)</b>	<b>Lean + BMC (g)</b>	<b>Total Mass (g)</b>	<b>% Fat</b>
L Arm	183	1359.1	3322.1	3505.3	4864.4	27.9
R Arm	186	1352.0	3525.8	3711.6	5063.5	26.7
Trunk	631	15692.3	32717.5	33348.3	49040.6	32.0
L Leg	426	3349.0	9219.0	9645.0	12994.0	25.8
R Leg	444	3427.3	9616.8	10060.9	13488.2	25.4
Subtotal	1870	25179.7	58401.1	60271.0	85450.7	29.5
Head	575	1370.3	3654.3	4229.6	5599.9	24.5
<b>Total</b>	<b>2445</b>	<b>26550.0</b>	<b>62055.4</b>	<b>64500.6</b>	<b>91050.6</b>	<b>29.2</b>

TBAR102 - NHANES BCA calibration

**DXA Results Summary:**

<b>Region</b>	<b>BMC (g)</b>	<b>Fat Mass (g)</b>	<b>Lean Mass (g)</b>	<b>Lean + BMC (g)</b>	<b>Total Mass (g)</b>	<b>% Fat</b>
L Arm	118	724.5	1482.8	1600.4	2324.9	31.2
R Arm	122	691.5	1544.1	1666.4	2357.9	29.3
Trunk	459	4119.2	14272.3	14731.2	18850.4	21.9
L Leg	353	2791.3	5134.4	5487.9	8279.2	33.7
R Leg	356	2806.1	5356.9	5713.1	8519.1	32.9
Subtotal	1408	11132.6	27790.5	29198.9	40331.5	27.6
Head	546	914.4	2513.1	3059.4	3973.7	23.0
<b>Total</b>	<b>1955</b>	<b>12047.0</b>	<b>30303.6</b>	<b>32258.2</b>	<b>44305.2</b>	<b>27.2</b>

TBAR102 - NHANES BCA calibration

**DXA Results Summary:**

<b>Region</b>	<b>BMC (g)</b>	<b>Fat Mass (g)</b>	<b>Lean Mass (g)</b>	<b>Lean + BMC (g)</b>	<b>Total Mass Mass (g)</b>	<b>% Fat</b>
L Arm	147.10	1706.1	1767.1	1914.2	3620.3	47.1
R Arm	154.80	1590.7	2134.7	2289.5	3880.2	41.0
Trunk	568.16	10800.5	19464.4	20032.5	30833.0	35.0
L Leg	350.11	4873.2	6160.6	6510.7	11383.8	42.8
R Leg	347.44	5157.3	6598.1	6945.6	12102.9	42.6
Subtotal	1567.61	24127.8	36124.8	37692.5	61820.2	39.0
Head	670.22	939.2	2562.1	3232.4	4171.6	22.5
<b>Total</b>	<b>2237.83</b>	<b>25067.0</b>	<b>38687.0</b>	<b>40924.8</b>	<b>65991.8</b>	<b>38.0</b>

### DXA Results Summary:

Region	BMC (g)	Fat Mass (g)	Lean Mass (g)	Lean + BMC (g)	Total Mass (g)	% Fat
L Arm	102	351.1	1711.9	1814.1	2165.3	16.2
R Arm	103	341.0	1710.7	1813.8	2154.8	15.8
Trunk	424	3204.1	16650.3	17074.0	20278.1	15.8
L Leg	289	2072.1	5217.4	5506.7	7578.8	27.3
R Leg	300	2071.5	5401.2	5701.7	7773.1	26.6
Subtotal	1219	8039.8	30691.6	31910.3	39950.1	20.1
Head	549	937.0	2576.4	3125.3	4062.4	23.1
<b>Total</b>	<b>1768</b>	<b>8976.8</b>	<b>33268.0</b>	<b>35035.6</b>	<b>44012.4</b>	<b>20.4</b>

TBAR102 - NHANES BCA calibration

**DXA Results Summary:**

<b>Region</b>	<b>BMC (g)</b>	<b>Fat Mass (g)</b>	<b>Lean Mass (g)</b>	<b>Lean + BMC (g)</b>	<b>Total Mass Mass (g)</b>	<b>% Fat</b>
L Arm	248.22	691.1	4684.4	4932.6	5623.7	12.3
R Arm	229.72	705.2	4485.1	4714.8	5420.0	13.0
Trunk	839.49	4841.4	31665.7	32505.2	37346.6	13.0
L Leg	576.39	2013.4	11202.1	11778.5	13791.9	14.6
R Leg	595.34	2054.7	11547.1	12142.5	14197.2	14.5
Subtotal	2489.16	10305.8	63584.4	66073.5	76379.3	13.5
Head	598.19	1148.9	3183.0	3781.2	4930.1	23.3
<b>Total</b>	<b>3087.36</b>	<b>11454.7</b>	<b>66767.4</b>	<b>69854.7</b>	<b>81309.4</b>	<b>14.1</b>

**DXA Results Summary:**

<b>Region</b>	<b>BMC (g)</b>	<b>Fat Mass (g)</b>	<b>Lean Mass (g)</b>	<b>Lean + BMC (g)</b>	<b>Total Mass (g)</b>	<b>% Fat</b>
L Arm	141	799.9	1772.3	1913.3	2713.1	29.5
R Arm	160	797.3	2009.6	2169.7	2966.9	26.9
Trunk	624	6047.5	19637.3	20261.0	26308.5	23.0
L Leg	410	3770.3	6145.0	6555.2	10325.5	36.5
R Leg	433	3646.6	6327.9	6761.2	10407.9	35.0
Subtotal	1768	15061.6	35892.1	37660.3	52721.9	28.6
Head	532	944.4	2595.4	3127.7	4072.1	23.2
<b>Total</b>	<b>2300</b>	<b>16006.0</b>	<b>38487.5</b>	<b>40787.9</b>	<b>56793.9</b>	<b>28.2</b>

TBAR102 - NHANES BCA calibration

**DXA Results Summary:**

<b>Region</b>	<b>BMC (g)</b>	<b>Fat Mass (g)</b>	<b>Lean Mass (g)</b>	<b>Lean + BMC (g)</b>	<b>Total Mass (g)</b>	<b>% Fat</b>
L Arm	290	1133.5	4575.8	4865.7	5999.1	18.9
R Arm	304	1042.1	4944.2	5248.2	6290.3	16.6
Trunk	1000	10991.9	37704.3	38704.3	49696.2	22.1
L Leg	744	3633.4	13632.1	14376.4	18009.8	20.2
R Leg	809	3617.7	14042.8	14851.5	18469.2	19.6
Subtotal	3147	20418.6	74899.1	78046.1	98464.6	20.7
Head	725	1302.9	3584.3	4309.7	5612.6	23.2
<b>Total</b>	<b>3872</b>	<b>21721.5</b>	<b>78483.4</b>	<b>82355.8</b>	<b>104077.2</b>	<b>20.9</b>

TBAR102 - NHANES BCA calibration

**DXA Results Summary:**

<b>Region</b>	<b>BMC (g)</b>	<b>Fat Mass (g)</b>	<b>Lean Mass (g)</b>	<b>Lean + BMC (g)</b>	<b>Total Mass (g)</b>	<b>% Fat</b>
L Arm	218	1977.5	2601.0	2819.4	4796.8	41.2
R Arm	229	1833.9	2771.3	3000.1	4834.0	37.9
Trunk	695	10791.6	24100.3	24795.2	35586.8	30.3
L Leg	544	5606.0	8684.6	9228.5	14834.5	37.8
R Leg	554	5775.4	8912.8	9466.4	15241.8	37.9
Subtotal	2240	25984.4	47070.0	49309.6	75294.0	34.5
Head	979	1212.0	3282.0	4261.2	5473.2	22.1
<b>Total</b>	<b>3219</b>	<b>27196.4</b>	<b>50352.0</b>	<b>53570.8</b>	<b>80767.2</b>	<b>33.7</b>

TBAR102 - NHANES BCA calibration

## ***Appendix 4: CD with Matlab programs.***

---